The effect of carbon and silicon-based additives on the hydrogen storage properties of Lithium Borohydride

by

Joshua Edwin Vines

A thesis submitted to the University of Birmingham
For the degree of

DOCTOR OF PHILOSOPHY

School of Metallurgy and Materials
College of Engineering and Physical Sciences
University of Birmingham

September 2016

Synopsis

A vast range of different materials have been studied for their hydrogen storage properties, however, borohydrides offer some of the highest gravimetric and volumetric storage densities, with $LiBH_4$ boasting the highest H_2 storage capacity of 18.36 wt%. In this work $LiBH_4$ is added to a number of different non-reactive additives in order to investigate their influence on the hydrogen storage properties of $LiBH_4$.

Graphite is a cheap and abundant material that has been used to destabilize hydrogen storage materials such as LiH. In this work graphite was ball milled under argon (Ar) and hydrogen (H_2) atmospheres before being added to $LiBH_4$. Milling under Ar led to a higher amorphous content in the graphite compared to that milled under H_2. Graphite milled under Ar resulted in a reduction of 102 °C in the decomposition temperature of $LiBH_4$. Pawley refinement of XRD measurements on the dehydrided graphite+$LiBH_4$ samples provided evidence of lithium intercalation, with graphite milled under Ar forming the more lithium rich compound LiC_{36}. $LiBH_4$ was successfully reformed at 350 °C and 100 bar H_2 confirmed by XRD, however, the both samples suffered serious degradation over 5 cycles.

The effect of porous additives was investigated through the incorporation of $LiBH_4$ into zeolite templated carbon (ZTC) and porous silicon via melt-infiltration. Confinement of $LiBH_4$ in these scaffolds resulted in a decrease in the decomposition temperature of $LiBH_4$ by over 125°C. The smaller pore size of ZTC was found to have the greatest effect on the H_2 onset and cyclic stability of $LiBH_4$. The pre-melting of $LiBH_4$ mixed with the porous hosts was found

to eliminate the release of B_2H_6 during decomposition. No correlation between the surface area of the additives and decomposition temperature of $LiBH_4$ was observed.

Unfortunately none of the materials studied in this work meet the Ultimate Fleet targets set out by the United States DoE (Section 1.6), however, the confinement of $LiBH_4$ in porous structures was shown to best enhance the H_2 storage properties of $liBH_4$. Adjustments to the ratio of additive to $LiBH_4$ along with the fine tuning of pore size of porous scaffolds should be explored in order to optimize the H_2 content in $LiBH_4$ + additive mixtures.

ACKNOWLEDGEMENTS

I would like to thank the EPSRC for their financial support over the 3 years of research. Thank you to Intrinsiq Materials and Nicholas M. Musyoka (Council for Scientific and Industrial Research (CSIR), South Africa) for the kind donation of Porous Silicon and Zeolite Templated Carbon for investigation in this work.

Thank you to Professor David Book for his supervision and support throughout the duration of my postgraduate studies in the Hydrogen Materials Group especially his attention to detail during the writing of this thesis.

A special thank you must be extended to Dr Daniel Reed for his continued support, guidance and help with experimental measurements. Thank you to my fellow peers who have provided me with many laughs and wise words: Matt Farr, Sheng Guo, Rich Murray, Christos Paterakis, Luis Fernandez and Rich Sheridan for keeping me fuelled with coffee and snacks.

Thank you to my partner in crime, Dr Luke Hughes. It is safe to say without you I would have spent much less time on the golf course and more time in the lab destroying things… although we did get pretty good at fixing everything we broke before anyone found out. Thank you to yourself, Jen, Rupert and Nala for always providing me with a home away from home during my write up.

Thank you to my amazingly supportive and inspiring family. Mum and Dad your support both financially and emotionally has been integral to my success, I thank you for everything you have done and continue to do for me. Thank you to Adam for always being there and especially for the low interest rates you charged on every loan you gave me in my hour of need.

Finally, but most importantly, thank you to Jasmine. You never doubted me and were always there to slap the sense back into me every time I wanted to throw in the towel. Without you I would never have completed this thesis, I can never thank you enough.

CONTENTS

LIST OF FIGURES

1 Introduction

1.1 Current Energy Situation

In the past 12 years the world's population has grown by one billion and is predicted to reach 9.7 billion by 2050 and 11.2 billion by 2100 (UN, 2015), requiring more energy than ever before. In July 2013, the United States Energy Information Administration (EIA) projected that the global energy demand would increase by 56% between 2010 and 2040 (EIA, 2013).

Currently, nearly 80 % of global energy consumed is produced from fossil fuels (coal, oil and natural gas), with only 19 % being generated from renewable sources, as shown in

Figure 1.1, (REN21, 2011). However, rapidly depleting fossil fuels reserves will lead to a supply short fall. Estimates on reserve sizes vary, but it is believed that oil and gas will be the first to run out after 40 and 60 years respectively, followed finally by coal in 120 years (Nersesian, 2015).

The combustion of fossil fuels for energy conversion (into energy we can use, such as electricity or mechanical in an engine) leads to the release of large quantities of carbon dioxide (CO_2) and other harmful greenhouse gases into the atmosphere. Energy and transport sectors are responsible for one third of global CO_2 emissions (IPPC, 2007).

Although fossil fuels do form naturally, they are not considered renewable due to their long formation periods over millions of years. Consequently, finding a sustainable, efficient and

economically viable energy conversion mechanism is vital to overcoming the issues of increasing energy demand, dwindling fuel stocks and large CO_2 emissions that face us today.

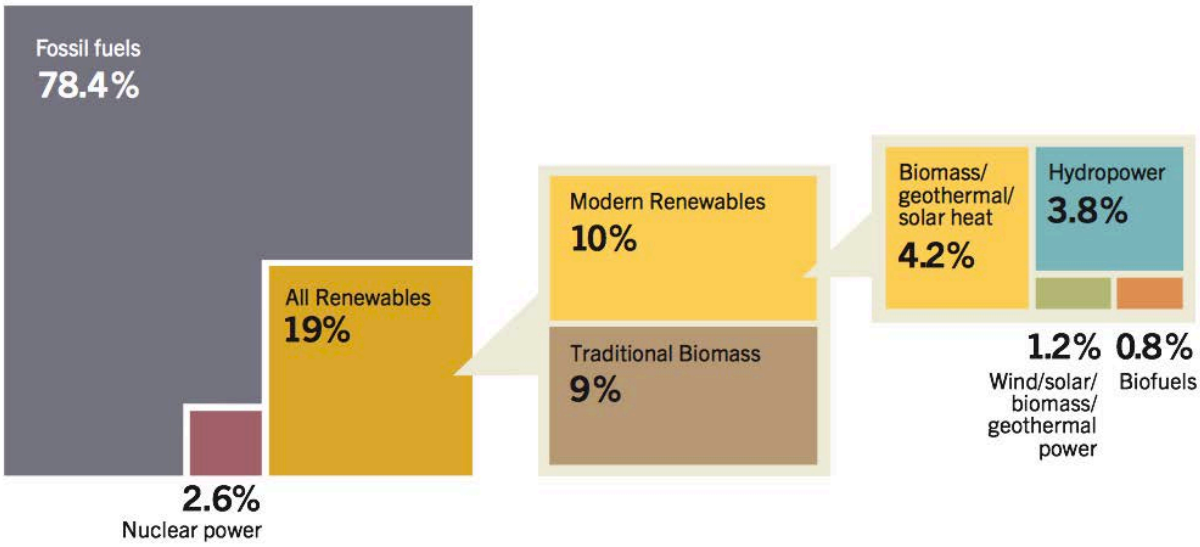

Figure 1.1 Breakdown of Global Energy Consumption 2012 (REN21, 2011)

Renewable energy sources such as wind turbines and solar photovoltaic cells offer a solution to the energy production crisis, reducing/removing the need for fossil fuels and reducing CO_2 emissions. These renewable energy sources are able to produce electricity with a relatively small carbon footprint (associated with the initial production and installation of the infrastructure), however, their greatest limiting factor is the varying and uncontrollable levels of wind and sunlight. Consequently, a mismatch between real-time energy demand and production is created.

To combat this, the renewable energy generated during periods of low demand must be stored and utilised to fill the void when production cannot meet demand. The excess energy during periods of low demand can be used to produce hydrogen from electrolysis that may later be converted back to energy in a fuel cell or by combustion. Hydrogen can therefore be considered as a possible energy vector to replace traditional fossil fuels as an energy storage mechanism for use in both the grid-scale and transport sectors.

The use of renewable energy technology can also increase a nation's political energy security. Hydrogen generation within the host country removes a nation's dependence on the importation of fossil fuels. This eradicates the risk of a country's energy supply being affected by political or military instability in the supply nation, as well as limiting the effect of high price increases due to instability in the global economy.

1.2 What makes hydrogen a viable energy vector?

Hydrogen is the most abundant element in the universe, existing on earth mainly as water (H_2O) covering an impressive 70% of the planet's surface. Since H_2 molecules have the highest energy per unit mass of any known compound, hydrogen contains almost three times as much as energy per unit mass compared to petrol (142 $MJkg^{-1}$ and 47 $MJkg^{-1}$, respectively) (Schlapbach and Züttel, 2001).

Hydrogen can be easily produced via electrolysis of water and combusted to form water and heat closing the cycle allowing hydrogen to truly be referred to as a clean fuel. Equation 1.1 shows the chemical equation for the combustion of hydrogen.

$$2H_2 + O_2 \rightarrow 2H_2O \qquad (\Delta H = -484\ kJmol^{-1}) \qquad (1.1)$$

Although gravimetrically hydrogen's energy capacity is remarkable, volumetrically it is rather poor with an energy per unit volume far less than that of gasoline when stored at standard pressures and temperatures (11.8 MJm^{-3} and 34,800 MJm^{-3} respectively (Dunlap, 2013)). As a result, finding a cheap and efficient storage mechanism for hydrogen is critical to allowing the introduction of a renewable and sustainable hydrogen economy. The potential of a hydrogen storage mechanism will vary depending upon its intended use. For transport applications, the potential of a storage mechanism will be directly affected by its weight and volume limitations, whereas grid-scale storage mechanisms do not face the same limitations. This thesis will focus on hydrogen storage mechanisms for vehicular applications.

1.3 Hydrogen Production

For hydrogen to succeed as an energy vector, it must be produced sustainably. Currently 90 % of global hydrogen produced (Dolan, 2010), is generated via steam methane reforming (SMR), which although cheap and efficient uses unsustainable natural gas as the basis of the

reaction pathway. In this section, the current technique of steam methane reforming will be discussed and alternate cleaner production methods discussed.

1.3.1 Steam Methane Reforming

Steam methane reforming (or steam reforming of natural gas) has been used for decades to produce hydrogen for the refining of petroleum and for ammonia production; hence, it has become increasingly efficient (60-75 %) and cost-effective (Holladay et al., 2009). The technique involves heating the natural gas up to temperatures of 700 – 900 °C and reacting it with steam in the presence of a catalyst, often made of Nickel or Iron. The endothermic reaction produces carbon monoxide (CO) and Hydrogen, as shown in equation 1.2.

$$CH_4 + H_2O \rightarrow CO + 3H_2 \qquad (700\text{-}900\ ^\circ C) \qquad (1.2)$$

The CO produced in the first step can then be reacted with steam at lower temperatures (250 – 450 °C) to produce hydrogen and carbon dioxide. This step is known as the water-gas shift and is shown in equation 1.3.

$$CO + H_2O \rightarrow CO_2 + H_2 \qquad (250\text{-}450\ ^\circ C) \qquad (1.3)$$

The gas is then purified using a technique called pressure swing absorption (PSA). At elevated pressures, impurities are adsorbed into adsorbent beds, which then release the impurities at lower pressure. As the hydrogen is not absorbed in the process, purity levels of up to 99.99 % can be achieved. Other less common purification techniques used are

cryogenic distillation and membrane separation, yielding purities of up to 95 % and 99.99 %, respectively (Adhikari and Fernando, 2006).

SMR relies heavily on the availability of natural gas, and even with the recent discovery of shale gas, is not a sustainable way to produce hydrogen.

1.3.2 Electrolysis

Electrolysis of water (H_2O) results in the production of pure oxygen and hydrogen, however, currently electrolysis only accounts for 4 % of global hydrogen production (Kothari et al., 2008).

The reaction (Equation 1.6) is endothermic requiring the process to be electrically or thermally driven, a schematic diagram can be seen in

Figure 1.2, the corresponding reactions that occur at the cathode and anode are shown in Equations 1.4 and 1.5 respectively. In order to the process a zero CO_2 hydrogen production technique, the reaction may be driven by renewable energy sources, such as wind or solar.

Cathode: $H_2O \rightarrow H^+ + OH^-$ (1.4)

Anode: $4OH^- \rightarrow O_2 + 2H_2O + 4e^-$ (1.5)

Complete Reaction: $2H_2O \rightarrow O_2 + 2H_2$ ($\Delta H = -586\ kJmol^{-1}$) (1.6)

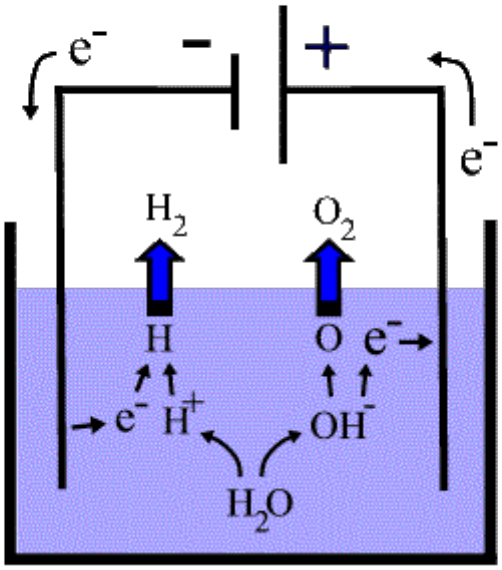

Figure 1.2 Schematic diagram showing the electrolysis of water (NMSEA, 2015)

Since hydrogen and oxygen gas are the only reaction products, the levels of purification required are much less than for SMR; dehumidification is required to remove any trace water from the gas stream. The overall efficiency of the process is comparable to SMR, with low temperature electrolysers achieving efficiencies of 56-73 % (Holladay et al., 2009). Providing solutions to SMR's greatest drawbacks, electrolysis presents itself as an ideal candidate for future hydrogen production.

1.3.3 Thermal Splitting of water

Thermal splitting of water is an energy intensive method in which water is physically split into hydrogen and oxygen, requiring temperatures of greater than 2000 °C which are not

considered practical in current commercial conditions (Speight, 2011). Consequently, research efforts have been focused on reducing the temperatures required through the introduction of thermochemical cycles. Thermochemical splitting of water is defined as *"the conversion of water into hydrogen and oxygen by a series of thermally driven reactions"* (IEA, 2006). Thermochemical cycles are able to produce hydrogen within the temperature ranges associated with nuclear reactors (Speight, 2011), allowing greater efficiencies to be achieved. However, this would require extreme safety and inspection procedures to monitor degradation of the nuclear reactor.

1.3.4 Biohydrogen

Biohydrogen is defined as hydrogen generated via biological machinery or thermochemical treatment of biomass (Mohan and Pandey, 2013), a breakdown of the associated production techniques is shown in Figure 1.3. Biomass, defined as renewable organic materials such as food waste, wood or crops, can be thermochemically treated to produce hydrogen through a process similar to SMR. The biomass feedstock is first subject to gasification of pyrolysis in the absence of oxygen converting the biomass into a combustible gas, referred to as syngas (a mixture of carbon monoxide and hydrogen). The syngas is then reformed via the same processes associated with SMR, the water-gas shift followed by purification via PSA producing high purity hydrogen Gas. Although the process is efficient (52 % (Balat, 2010)) and can be considered a closed CO_2 cycle, the growth of crops for fuel will present moral issues in 3rd world countries where alleviating hunger may be considered a higher priority.

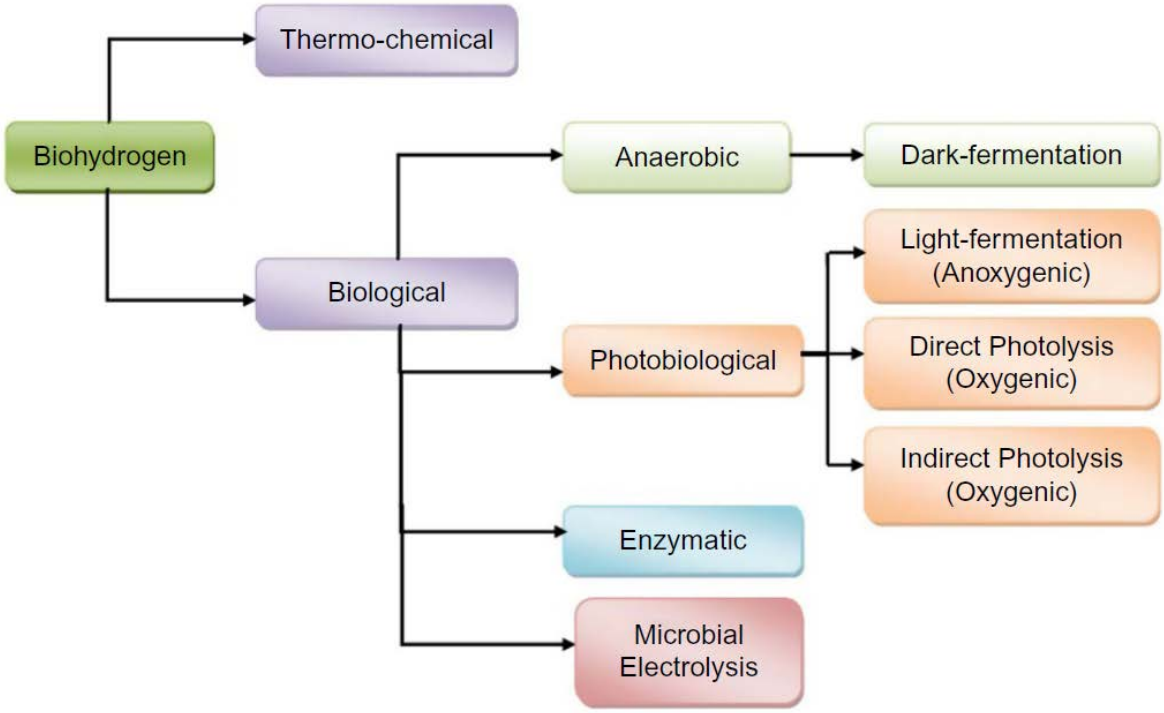

Figure 1.3 Schematic diagram showing a breakdown of the hydrogen production techniques associated with biohydrogen (Mohan and Pandey, 2013)

The production of hydrogen via biological processes (Figure 1.3) is another alternative in which hydrogen is produced as a by-product of various microbial-driven bio-chemical reactions. The various biological production techniques can be broken down into two categories: light dependant photosynthetic reactions and dark (light independent) fermentation reactions. As suggested by the name, light dependant photosynthetic reactions are driven by sunlight, whereas dark fermentation is an anaerobic process in the absence of oxygen. Other biological hydrogen production techniques include enzymatic and microbial electrolysis, further information can be found in (Mohan and Pandey, 2013).

1.4 Hydrogen as a fuel

Similar to petrol and liquefied petroleum gas (LPG), hydrogen can be used in an internal combustion engine (ICE) to produce energy (kinetic and thermal), however, hydrogen can also be used chemically in a fuel cell to produce electricity (and heat) cleanly which can be used to power a motor or charge a battery. The eradication of CO_2 emissions upon consumption of hydrogen, coupled with the benefits mentioned in Section 1.2, renders hydrogen one of the most promising future energy carriers.

1.4.1 Internal Combustion

The conversion technology of conventional hydrocarbon ICE's to hydrogen is readily available and offers many benefits over its fossil fuelled counterpart. The combustion of hydrogen leaves no carbon residues or sediments as created in conventional engines, thus the engine requires less maintenance and a longer potential life. As with combustion of hydrocarbons in air, the combustion of hydrogen in air also results in the production of nitrogen oxides (NO_x) (Speight, 2011) responsible for smog and acid rain. As a consequence, although traditional hydrocarbon ICEs can be converted easily to run on the hydrogen, greatly reducing the quantity of harmful emission produced, they are seen as more of an intermediate step between traditional fossil fuel engines and fuel cells.

1.4.2 Fuel Cells

A fuel cell may be described as an electrochemical energy conversion system. Chemical reactions occurring at the anode and cathode give rise to an electric current across the two; this current may be used immediately or stored for later use. The principal is much the same as a traditional battery that converts chemical energy to electricity until all the original chemicals have reacted. At this point the battery is either recharged or disposed of. In contrast, a fuel cell does not store the chemicals within, the reactants (hydrogen and oxygen) are instead flowed over either side of the cell.

The proton exchange membrane (PEM) fuel cell shows the greatest promise for an on-board vehicular fuel cell, where weight, temperature and start up time are all critically important.

The chemical reaction taking place in a PEM fuel cell is the inverse of electrolysis (Equation 1.6) and is demonstrated in Figure 1.4. Air/oxygen and hydrogen are flowed over the cathode and anode respectively. Hydrogen molecules are dissociated at the anode and split into protons and electrons. The electrolyte/membrane separating the electrodes allow the flow of proton across the physical barrier, whilst the electrons flow through an external circuit generating a current. Once the protons and electrons arrive at the cathode they combine with the O_2 to finish the reaction producing water and heat. Efficiencies as high as 80% are possible, however, in practice only 60% is achieved due to heat loss (Speight, 2011). Compared to conventional ICE efficiencies (35%) (Fronasiero and Graziani, 2011), PEM fuel cells are almost twice as efficient which means a H_2-ICE vehicle requires double the quantity of H_2 to achieve the same range as its PEM-FC - electric motor equivalent.

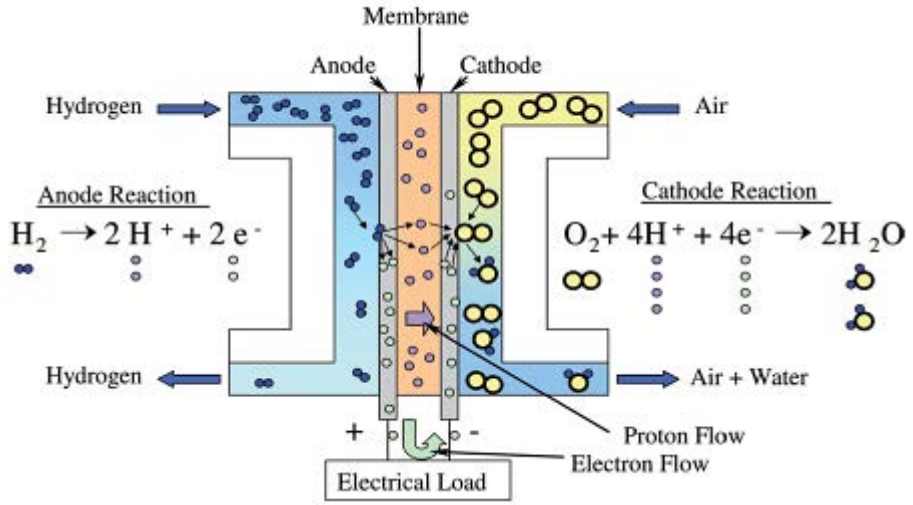

Figure 1.4 Schematic diagram of a PEM fuel cell (Speight, 2011)

The low operating temperature of PEM fuel cells of between (80 °C - 100 °C) (Busby, 2005) allow for quick start up times and remove the need for complex engineering and safety restraints associated with high temperatures (Busby, 2005). In vehicular applications the weight of the fuel cell system is critical in ensuring both the driving experience and range are comparable to current expected standards, the light weight of PEM fuel cells (e.g. Toyota Mirai fuel cell stack = 56 kg) further boost their potential as a viable alternative to ICEs.

1.5 A Brief comparison of Battery and Fuel Cell powered cars

Batteries and fuel cells convert chemical energy into electrical energy that can be used to power any electrical device such as a motor in a car. Their difference lies in the way their fuel stock is stored, a battery contains the chemical reactants internally, and once all the

chemical energy has been converted, the battery must be recharged. On the other hand, the chemical reactants for a fuel cell (hydrogen and air/oxygen) are stored externally from the cell.

Battery electric vehicles (BEVs) or Battery electric hybrid vehicles (BEHV)s have been seen as possible replacements to convention ICE vehicles (Lebeau et al., 2012) with models such as the Toyota Prius, Nissan Leaf and Chevrolet Volt being particularly successful . Their greatest draw back lies in the weight of the energy storage system, lithium ion batteries which although have an energy density four times greater than traditional lead acid batteries (Khaligh, 2010), are still very large and heavy and consequently greatly limit the driving range and performance capabilities that can be achieved. Another major drawback of lithium ion batteries is their life time (1000 charge cycles (Chalk and Miller, 2006)) requiring batteries to be replaced every three years. In situations that do not require considerable commutes, such as city driving, BEVs and BEHVs provide viable zero/low CO_2 emission options.

Figure 1.5 shows the relative volume and weight for different energy storage systems capable of providing a car with enough energy to travel 500 km. The current benchmark set by a diesel system can be seen to be very impressive with a system weight and volume of 43 kg and 46 L respectively. Comparatively, the volumetric and gravimetric energy storage density of lithium ion batteries is much poorer in comparison to a diesel system, with a total system weight almost twenty times greater.

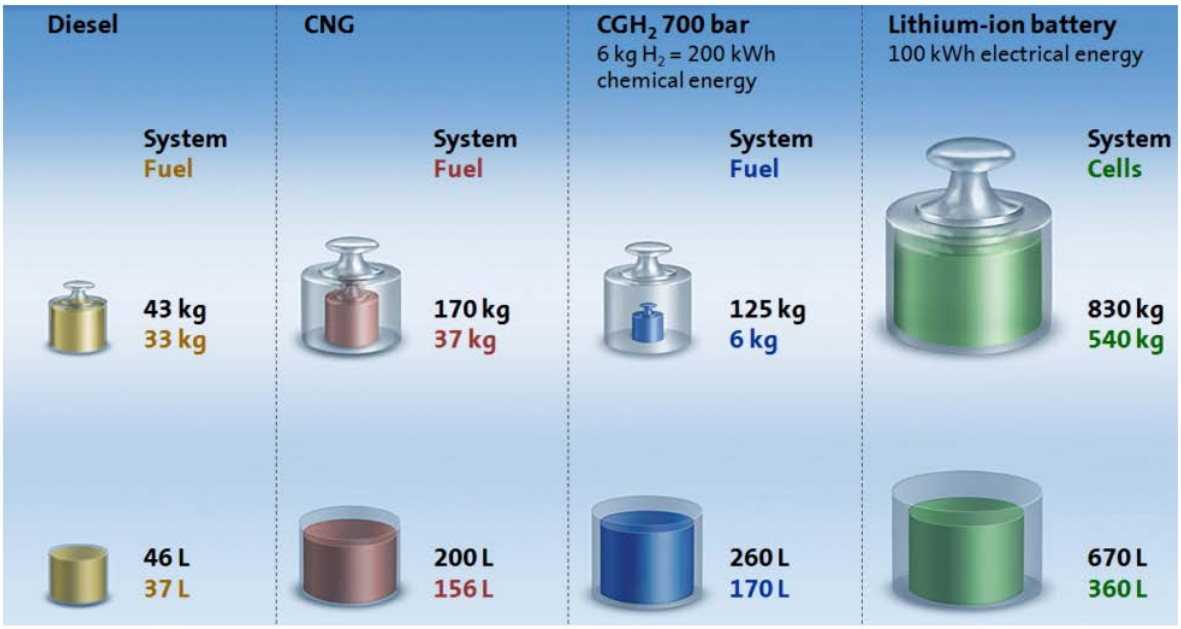

Figure 1.5 Schematic diagram showing relative fuel tank volumes and weights for different storage materials for a vehicle with a 500km range. CNG = compressed natural gas, CGH_2 = compressed gaseous hydrogen (Brinkman et al., 2012)

On the contrary, a fuel cell electric vehicle (FEV) fed by a 700 bar compressed hydrogen storage tank shows greater promise with system weight and volume of 125 kg and 260 L respectively. The Toyota Mirai is one of the latest hydrogen vehicles to go to mass market and boasts an impressive 300 mile range with a two tank system capable of storing 5.7 wt% H_2 with a refuel time of 5 minutes. The Toyota Mirai is the first FEV to offer a comparable driving experience to ICE vehicles, however, the H_2 is stored at 700 bar which presents inherent engineering and safety challenges.

Since the technology for both hydrogen production and conversion to energy are both well established, the key to unlocking hydrogen's full potential as the energy vector of the future, is finding a safe low-pressure storage system with a range comparable to traditional

hydrocarbon vehicles. This work focuses on solid-state storage of hydrogen inside of complex hydrides.

1.6 Properties of an Ideal Storage Material

The United States Department of Energy (DoE) has set out a series of targets for a storage system on light-duty vehicles capable of storing a total of 5 kg of hydrogen, giving a vehicle range of over 300 miles comparable to that achieved by current ICE vehicles. Table 1.1 shows a list of current and previous revised targets set by the DoE; the 'Ultimate Full Fleet' refers to targets suitable not just for small compact cars, but a range of vehicle types including sport utility vehicles (SUVs).

The 2015 and ultimate full fleet targets also include a cyclic lifetime of 1500 cycles, with the storage capacities of the system still able to meet the targets after the last cycle.

Table 1.1 US DoE targets for a hydrogen storage system for applications on light-duty vehicles (DoE, 2015)

Target	2010	2015 (New)	2015 (old)	Ultimate Full Fleet
Gravimetric H_2 Density (wt%)	4.5	5.5	9	7.5
Volumetric H_2 Density (gL^{-1})	28	40	81	70
Refill Time ($kgmin^{-1}$)	4.2	3.3	2.5	2.5

From these targets it is possible to outline the key properties of an ideal hydrogen storage medium, which will:

- Be capable of storing >7.5 wt% H_2, since this target includes the weight of the entire system (tank, cooling, valves, regulators, etc..)
- Release hydrogen at low-moderate temperatures achievable on-board vehicles
- Absorb hydrogen with fast kinetics at moderate pressures and temperatures
- Be stable over 1000s of cycle with no short term degradation or loss in storage hydrogen capacity
- Release high purity hydrogen, with no/minimal release of impurity gases such as Diborane (B_2H_6) which can be poisonous to the catalysts in fuel cells (Kostka et al., 2007))
- Be cheap, abundant and cost effective to manufacture

2 Literature Review

2.1 The Hydrogen Storage Problem

The DoE targets (see Section 1.6) for hydrogen storage on light-duty vehicles require the storage of 5 kg of hydrogen to achieve a driving range of 500 km (DoE, 2015). Under standard temperature and pressure (STP) conditions 1 kg of gaseous hydrogen has a density of 0.089866 kgm^{-3} occupying a volume of 11 m^3 (Züttel, 2011); a 55 m^3 tank would be required to store the required quantity of fuel. To decrease the required tank volume the hydrogen density must be increased. This may be achieved through a number of techniques that will be discussed in this literature review: compressed gas, cryogenic storage, physisorption and chemisorption.

2.2 Traditional Hydrogen Storage Techniques

2.2.1 Compressed Gaseous Hydrogen

Gas compression technology is well established and as such the most common storage method for hydrogen has been as a pressurised gas (up to 200 bar) in high pressure cylinders (Züttel, 2011). To store enough hydrogen for a vehicle range of 400 km, five 200 bar hydrogen bottles would be required which although may be practical for larger vehicles such as buses, is not an option for light duty vehicles.

High pressure light weight composite tanks have been developed capable of storing hydrogen gas under pressures of up to an impressive 800 bar with a volumetric storage density of 36 kgm^{-3} (Züttel, 2003). These tanks are made from three layers, an inner corrosive resistant liner, a reinforced carbon fibre shell and a reinforced protective shell with impact resistant domes covering the top and bottom, a schematic diagram is shown in Figure 2.1 (IEA, 2006).

Health and safety standards for vehicles are always under assessment and development, however, until human error can be removed from the equation collisions and accidents will continue to occur. The storage of gas under high pressures (700 bar) can pose both significant safety risks if the tank integrity is compromised and difficult engineering issues when incorporating a cylindrical tank into a light duty vehicle, although has been shown to be a possible by Toyota (Toyota Mirai).

When storing hydrogen as a gas it is also vital to account for hydrogen embrittlement; the "loss of ductility of a metal resulting from the absorption of hydrogen" (Davis, 2001). Hydrogen embrittlement of steel tanks may lead to the development of faults and cracks, causing the tank to fail. Lightweight composite tanks contain hydrogen impermeable membranes to limit the effect of hydrogen embrittlement, as shown in Figure 2.1.

The low volumetric storage density and customer perceived safety concerns of sitting on top of a 700 bar tank of hydrogen present significant drawbacks to this storage method.

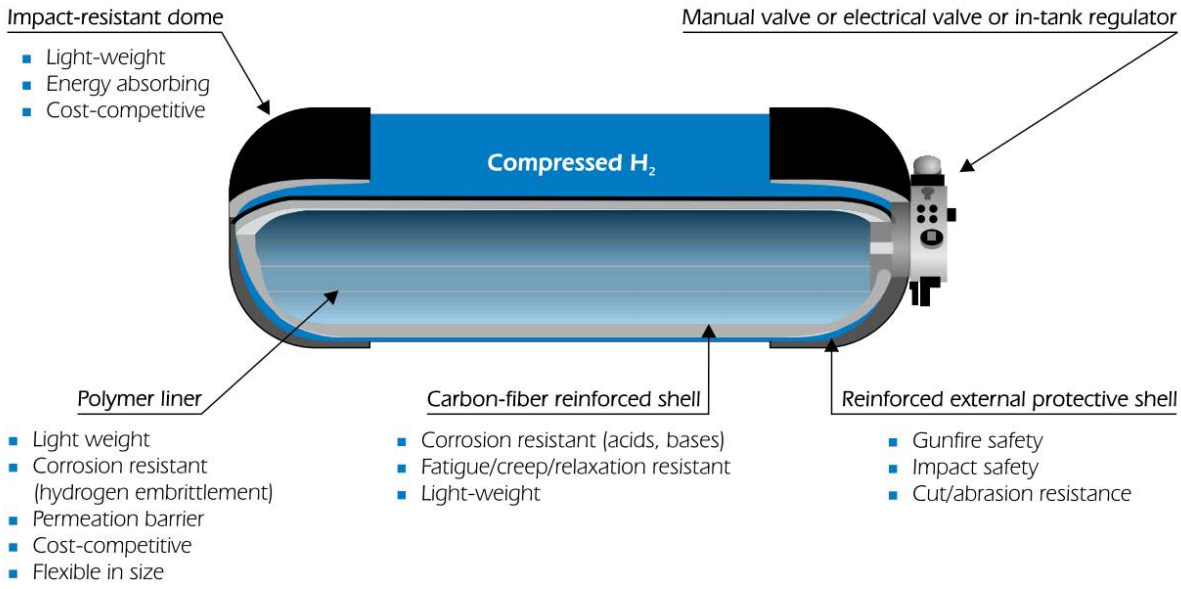

Figure 2.1 Schematic diagram of a high pressure light weight composite hydrogen storage tank (IEA, 2006)

2.2.2 Liquefaction of Hydrogen- Cryogenic Storage

Condensation of a gas into liquid is an effective way to increase the density of gas per unit volume. Liquid hydrogen has a density of 70.8 kgm^{-3} and must be stored at -253 °C under atmospheric pressure due to the low critical temperature of hydrogen (-241 °C), above which hydrogen exists in gas form (Schlapbach and Züttel, 2001). A consequence of this low critical temperature is that cryogenic storage vessels must exist as open systems to avoid large build-ups of hydrogen gas, pressures of up to 10^4 bar are possible (Züttel, 2003). As a result any heat transfer into the vessel results in boil-off of the liquid hydrogen. The surface area to volume ratio is therefore a critical factor in the rate of boil off that is experienced by a storage vessel. Spherical storage vessels offer the lowest surface area to volume ratio but are expensive to manufacture and not easily incorporated into current vehicle designs. Double walled vacuum insulated spherical storage vessels experience boil of losses of 0.4%, 0.2% and 0.06% per day for 50 m^3, 100 m^3 and 20,000 m^3 respectively (Züttel, 2011).

The liquefaction of hydrogen is a very energy intensive process requiring up to 40% of the total energy of the hydrogen being storage.

The combination of continuous boil off and the large amount of energy required for liquefaction limit the possible applications for cryogenic storage of hydrogen. Instances where hydrogen is used quickly and process cost is less of an issue (e.g. space), cryogenic storage offers a suitable storage technology, however for light duty vehicles these issues are too significant and thus it cannot be considered a suitable storage technique.

2.2.3 Hydrolysis

Hydrolysis is defined as a "reaction of the substance with water to liberate hydrogen" (Fakiolu, 2004). Large quantities of hydrogen can be released through hydrolysis however stable compounds are often formed during the reaction. The formation of these compounds render reversible hydrolysis systems extremely complex, consequently, hydrolysis can only be considered for specific situations requiring rapid release of in a 'one-shot desorption'. Such applications may include military or space operations.

2.3 Solid State Hydrogen Storage

A vast array of different storage materials have been investigated and developed over many years. As discussed in Section 1.6 the ideal storage material has a high volumetric and gravimetric hydrogen storage density and is subsequently located in the top right hand corner of Figure 2.2 showing volumetric and gravimetric storage densities for a variety of hydrogen storage materials (Parker, 2010). From Figure 2.2 the potential of solid-state hydrogen storage materials is clear. Their higher gravimetric and volumetric hydrogen capacities are far superior compared to the traditional methods of cryogenic storage (the blue horizontal line at 71 kg H_2 m^{-3}) and pressurised gaseous storage (the two purple lines located towards the bottom left).

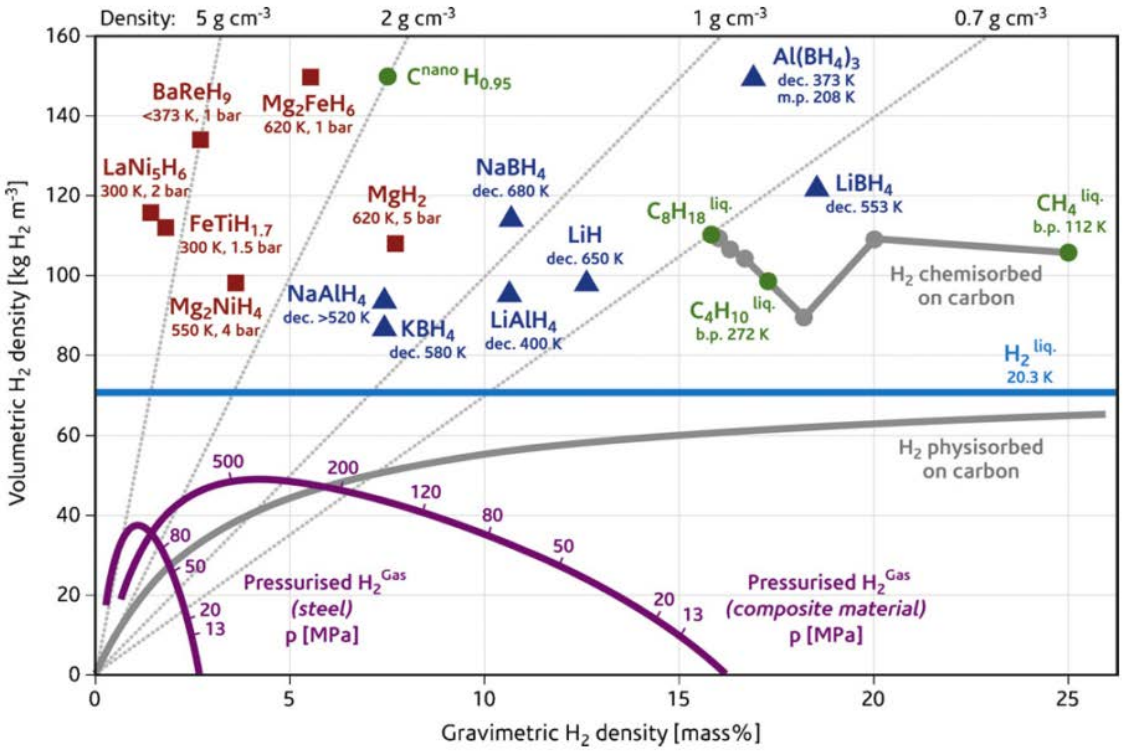

Figure 2.2 Gravimetric vs. Volumetric hydrogen storage densities of a variety of hydrogen storage materials and the temperate at which H_2 is released (Parker, 2010)

Solid-state hydrogen storage materials contain hydrogen in one of two states, physically bound to the surface of a high surface area material as an adsorbate (physisorption), or chemically bound to a compound (chemisorption). Both methods have their own inherent advantages and drawbacks. Physisorption benefits from higher efficiencies alongside quick adsorption/desorption times while chemisorption allows for higher concentrations of H_2 to be stored but suffers from higher desorption temperatures (Lim et al., 2010).

2.3.1 Physisorption

Physisorption occurs when gas molecules interact with surface atoms of a material through Van der Waals interactions. The Van der Waals forces occur between any gas molecule and surface combination however due to the low energy nature of these interactions (4-10 $kJmol^{-1}$ of H_2, (Walker, 2008)) low temperatures are required to achieve respectable gravimetric storage densities; liquid nitrogen is often used to achieve temperatures of -195 °C.

The lack of activation energy required for physisorption allows for rapid adsorption/desorption of hydrogen and since physisorption is an interaction that occurs between a surface and a gas molecule, it follows that the quantity of H_2 that may be adsorbed is highly dependent upon the surface area of the material.

High surface area materials such as activated carbons, carbon nanotubes, Metal organic frameworks (MOFs), Zeolites and Zeolite templated carbons (ZTCs) have all been subject to extensive research due to their high surface areas and for the later three their highly tuneable pore sizes.

2.3.1.1 Carbons

Carbon allotropes have received a lot of interest in hydrogen adsorption due to their low densities, availability of carbon, high porosities and large specific surface areas.

Activated carbon has a porous structure dependant up on the fabrication conditions used, the pore size and distribution can vary as a result (Broom, 2011). Consequently there has been a variety of different adsorption values published, the largest of which is 5.5 wt% H_2 at -196 °C (Yürüm et al., 2009).

Dillon et al. (1997) were the first to study carbon nanotubes (CNTs) for hydrogen storage, claiming storage capacities of up to 10 wt% H_2 possible at room temperature, however, these results have never been successfully replicated by other research groups.

Broom, (2011) concluded that since calculated hydrogen capacities of CNTs were no greater than values for activated carbon, CNTs did not offer any significant advantage over other forms of carbon which can be synthesised much more viably in large quantities.

Carbon nanofibers constructed of layers of graphene stacked in various orientations have also been considered for hydrogen storage. (Chambers et al., 1998) reported extremely high hydrogen storage capacities of up to 67.55 wt% that have never been replicated. More realistic values of between 4 wt% and 6.5 wt% under 121.6 bar H_2 were reported by (Browning et al., 2002).

2.3.1.2 Metal Organic Frameworks

MOFs are built up of inorganic building units connected by organic bridges that result in highly ordered inorganic-organic hydrid solids with large surface areas and pore volumes (Felderhoff et al., 2007). Rosi et al. (2003) were the first to investigate the potential of MOFs for use in hydrogen storage reporting MOF-5 $Zn_4O(bdc)$, where bdc = 1,4-benzenedicarboxylate (Broom, 2011)), to have a capacity of 4.5 wt% at -196 °C and 0.7 bar H_2, however, this was later reduced (Rowsell et al., 2004). One of the highest hydrogen capacities reported is for MOF-177 in work by Wong-Foy et al. (2006) who reported a total H_2 capacity of 7.5 wt% at -196 °C and 70 bar H_2.

The low cryogenic temperatures required to store H_2 inside metal organic frameworks are not suitable for light vehicle applications due to the highly energy intensive process required to both achieve and maintain these temperatures on a per vehicle basis.

2.3.1.3 Zeolites

Traditional zeolites are highly ordered structures constructed of SiO_4 and AlO_4 tetrahedral units. However, the term is often also used to describe similar structures formed by other elements called zeolites. There are 176 different possible reported crystallographic structures (Baerlocher et al., 2007). The nature of their structure creates uniform cavities and pores within the zeolite framework resulting in a rigid microporous material with large pore volumes and high specific surface areas (Broom, 2011). Although at first glance zeolites appear to have a lot of potential as hydrogen storage materials, their low hydrogen storage

capacities (limited to 2.86 wt% by geometric constraints e.g. framework flexibility) render them unfavourable options (Felderhoff et al., 2007).

2.3.1.4 Zeolite Templated Carbons

ZTCs are highly ordered porous carbon structures synthesised through the introduction of a carbon precursor such as acetonitrile into a chosen zeolite material followed by carbonisation and the removal of the zeolite framework (Yang et al., 2007a; Broom, 2011). The synthesis process is shown in the schematic diagram in Figure 2.3. The resulting ZTC has a large pore volume and surface areas of up to 4000 m^2g^{-1} (Nishihara et al., 2009) with a highly defined pore size dependant upon the choice of host zeolite, such as 1.2 nm for a ZTC synthesised from zeolite Y (Matsuoka et al., 2005). This defined pore size preserves the long-range ordering in the (111) plane of zeolite Y of 1.4 nm, seen as a singular peak by X-Ray diffraction at the corresponding 2θ value of 6.2 ° (Paredes et al., 2005). ZTCs have been shown to hold up to 7 wt% H_2 at -196 °C under 20 bar H_2 (Yang et al., 2007b).

The structure of ZTCs consists of a 3-dimensional network of Buckyball-like nanographenes as shown in Figure 2.4. Figure 2.5 shows TEM images of commercial zeolite X and the subsequent derived ZTC published by Musyoka et al., 2007. It was observed that the structure of the ZTC showed similar morphological features as the parent zeolite X. The aligned fringes visible in the bottom right image of Figure 2.5 was consistent with the observed XRD reflection at 7° 2θ. The diffraction halo indicated the ZTC was amorphous by nature.

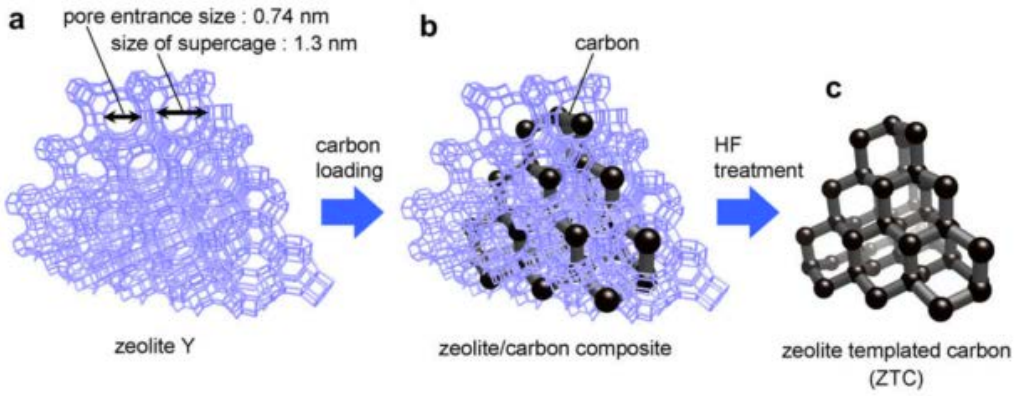

Figure 2.3 Schematic diagram of the synthesis of a zeolite templated carbon, (a) crystal structure of zeolite Y, (b) illusion of zeolite/carbon composite and (c) framework structure of the final ZTC after washing (Nishihara et al., 2009)

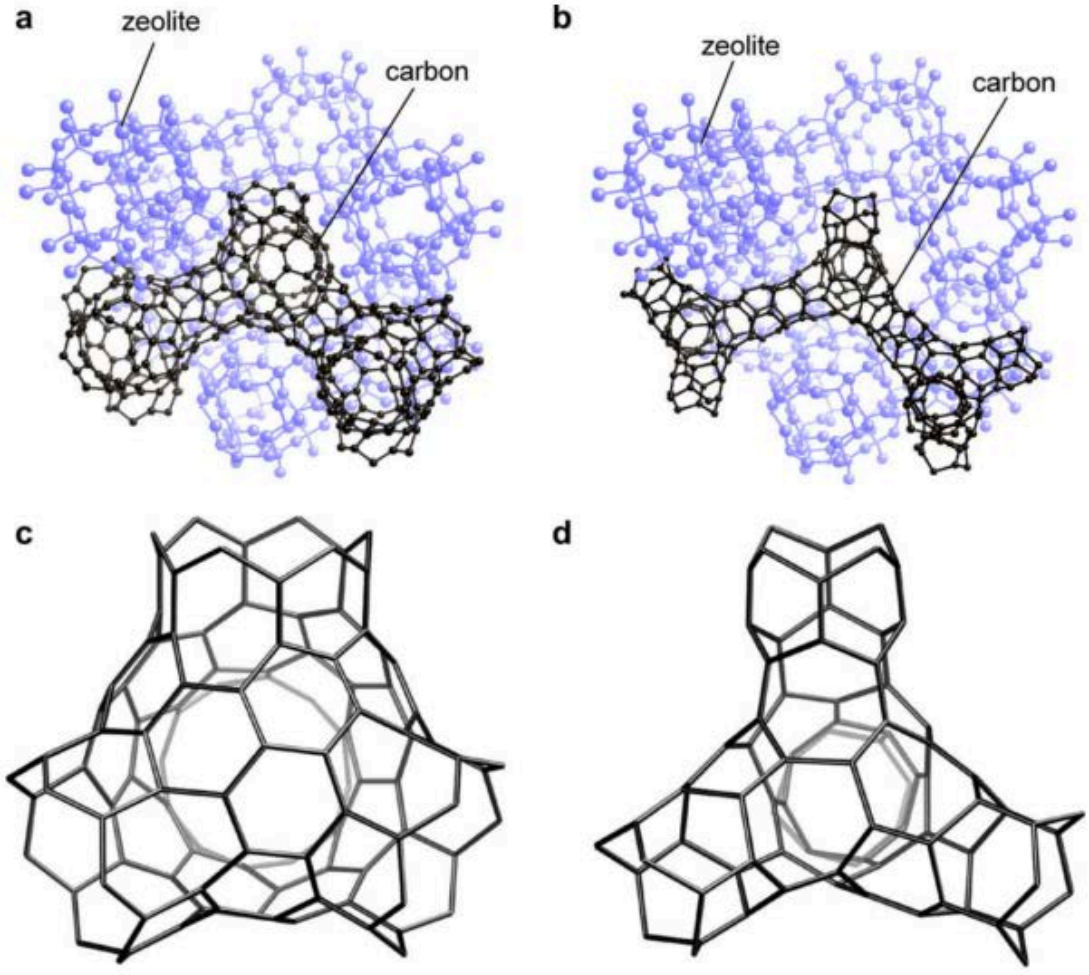

Figure 2.4 Two hypothetical ZTC structures fitted into a zeolite Y framework (a) and (b), where (c) and (d) are the encased ZTC structures comprised of C_{88} and C_{68} building units respectively (Nishihara et al., 2009)

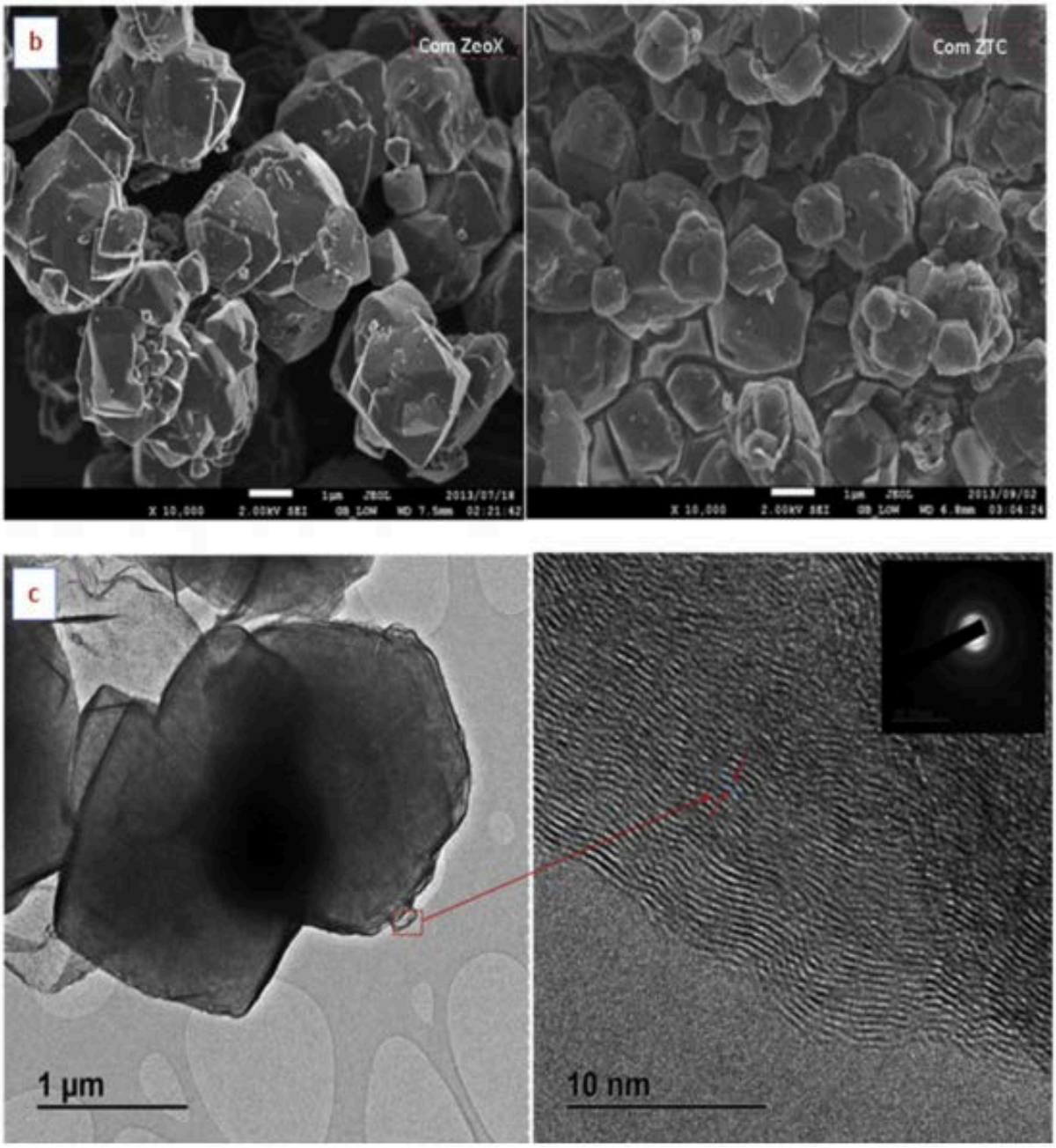

Figure 2.5 TEM images of (b) Commercial Zeolite X and its ZTC derivative and (c) high and low resolution images of the derived ZTC (Musyoka et al., 2007)

2.3.2 Chemisorption (Metal Hydrides)

As previously mentioned, chemisorption is the process by which atomic hydrogen bonds to the host metal forming a compound opposed to sitting as a molecule on its surface. For chemisorption of hydrogen to take place H_2 molecules must first be physisorbed onto the surface of the metal after which they must overcome an activation barrier allowing the disassociation of the molecules into atomic hydrogen which then bonds to the surface of the metal (Züttel, 2003). At sufficiently high coverages, chemisorbed hydrogen atoms may then form surface phases before being able to jump into the subsurface layer and diffusing through the metal on interstitial sites eventually forming a hydride. This process is shown in Figure 2.6.

A variety of simple and complex metal hydrides such as MgH_2, $NaAlH_4$ and $LaNi_5H_6$ have been investigated as hydrogen storage materials (Lim et al., 2010). MgH_2 offers the greatest gravimetric hydrogen capacity with a theoretical content of 7.6 wt% (Zaluska et al., 1999) however slow absorption/desorption kinetics demand high temperatures for H_2 release. Nano-sizing (see Section 2.7.4.2) of MgH_2 has been shown to be an effective way to reduce the temperatures required by minimising diffusion distances within the sample (Huot et al., 1999).

Other metal hydrides such as $LaNi_5H_5$ (located in the upper left corner of Figure 2.2) can readily absorb and desorb hydrogen at room temperatures with fast diffusion rates, however the their gravimetric performance of 1.37 wt% is too poor to be considered for on-board vehicular storage (Schlapbach and Züttel, 2001). In applications in which weight is not

considered an issue/drawback such as ballast in a canal boat (Bevan et al., 2011), such metal hydrides have been shown to be viable options.

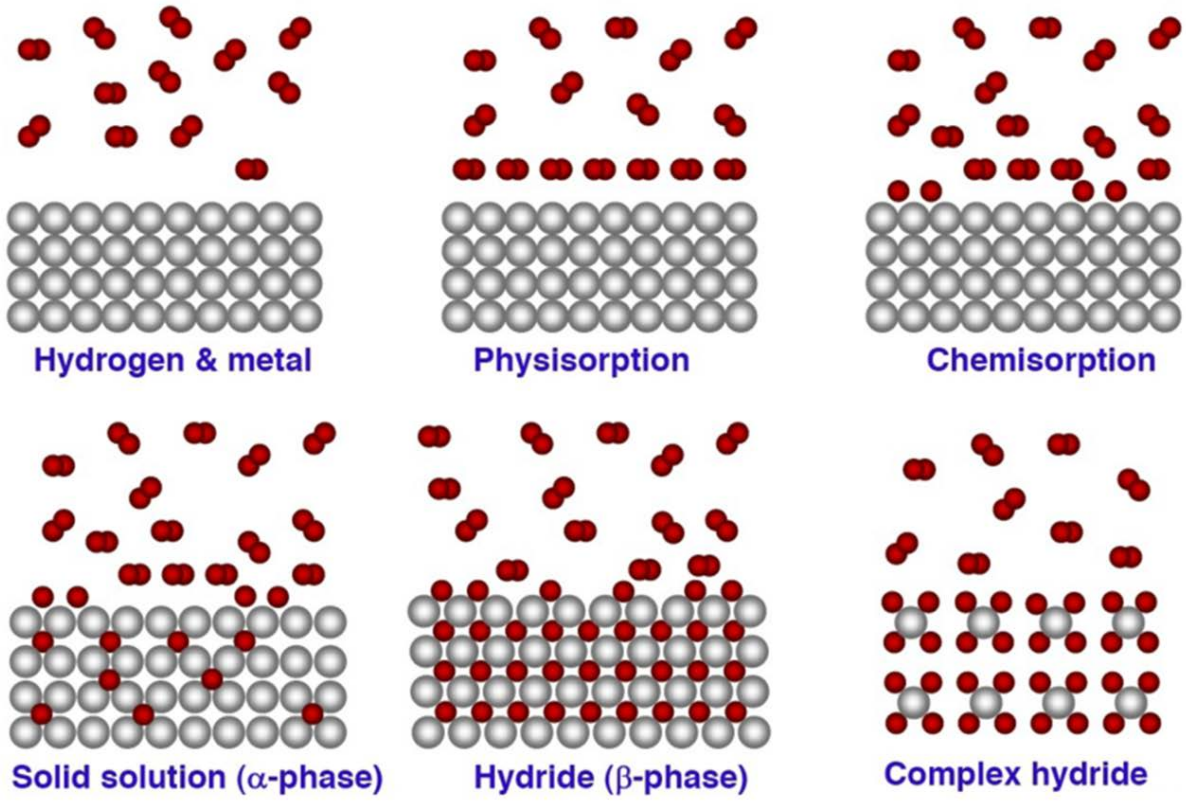

Figure 2.6 Schematic diagram of different hydrogen bonding states possible in hydrogen storage materials (Züttel and Borgschulte, 2007)

2.4 Carbon Based Storage Materials (Chemisorbed H_2)

A stated in Section 2.3.1.1 (in which carbons used in the physical storage of hydrogen are discussed) carbon allotropes have been subject to a lot interest due to their low densities

and chemical inertness. This section provides a review on carbon allotropes used for the chemical storage of hydrogen.

2.4.1 Characterisation of Graphite

2.4.1.1 Raman Spectroscopy

Raman Spectroscopy is an extremely effective way to characterise carbon materials. This non-destructive characterisation technique (the theory behind Raman Spectroscopy is discussed in Section 4.3.2.1) is sensitive to highly symmetric covalent bonds with little to no natural dipole moment, properties possessed by C-C bonds found in carbon allotropes (Hodkiewicz, 2010). Raman spectroscopy probes the vibrations of these C-C bonds permitting any tiny structural changes to be detected.

Graphene consists of a sheet of carbon atoms (one atom thick) arranged in a hexagonal honeycomb formation with each carbon atom in sp^2 configuration (Zhang, 2012). Graphene sheets are the fundamental building blocks for all graphitic materials such as fullerenes, single and multiwall carbon nanotubes and graphite.

In graphite, graphene sheets stacked on top of one another are held in place by weak Van der Waals interactions allowing the planes to slide over one another with ease; the reason behind graphite's use as a lubricator (Shriver et al., 1994).

The Raman Spectrum of graphene exhibits two peaks, the G band (graphite) located at 1582 cm^{-1} and the G' band located around 2700 cm^{-1}. Disordered (defective) graphite exhibits two addition peaks, the D band (diamond) located near 1350 cm^{-1} (close to half the wavenumber of the G' band) and the D' band at 1620 cm^{-1} (Malard et al., 2009). Peak locations correspond to an excitation laser wavelength of 514 nm. Figure 2.7 shows the Raman spectrum of a graphene edge and all subsequent Raman bands discussed above.

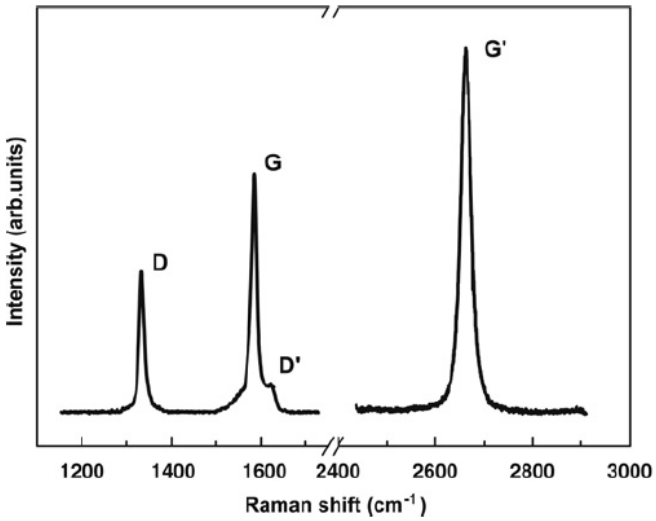

Figure 2.7 Raman Spectrum of a graphene edge showing the location of the D, G, D' and G' bands (514 nm excitation laser wavelength) (Malard et al., 2009)

The G band is a result of the doubly degenerate (internal Transverse Optical (iTO) and Longitudinal optical (LO)) phonon modes that exhibit E_{2g} symmetry and is the only first order Raman scattering process observed in graphene.

Contrary to the G band, both the G' and D bands are a result of second order Raman scattering processes. The D band is result of Raman scattering involving one iTO and one defect (as seen in defective graphite) in the form of a sp^3 hybridised carbon atom. As a

result, the greater the number of sp^3 hybridised carbon atoms the more defects within the graphite.

The G' band originates from two iTO phonons near the K point and produces photons at frequencies close to twice the D band and is therefore sometimes referred to as the 2D band. However the 2D/G' band is permitted by Raman selection rules in defect free graphite and thus calling it the 2D band is somewhat misleading.

The final band in defective graphite it the D' peak and is a result of an intra-valley resonance process. The origins of each band discussed above are shown in Figure 2.8 (Malard et al., 2009).

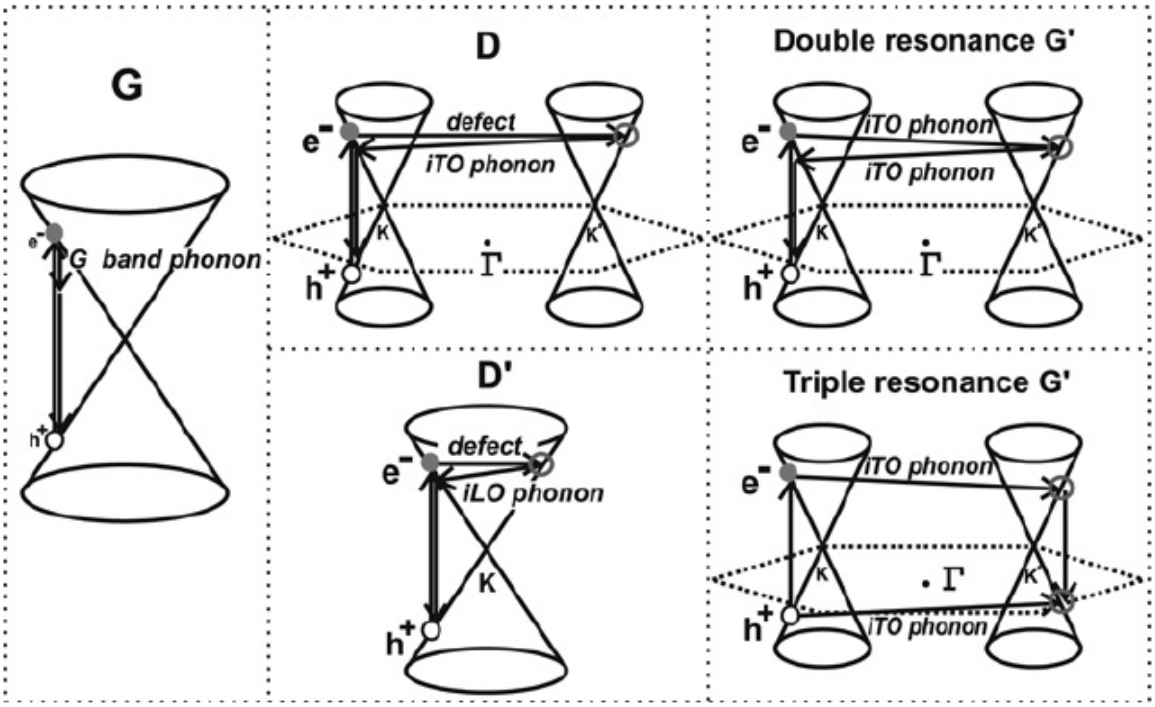

Figure 2.8 Schematic diagram showing the different Raman scattering process for each possible graphitic band. G band (left) is a first order process, D (middle top) is a inter-valley single phonon second order double resonance process, D' (middle bottom) is an intra-valley single phonon second order double resonance process, G' (right) two photon second order double and triple resonance processes (Malard et al., 2009)

Ferrari et al. (2006) have shown that for Bernal AB stacked graphene, the characteristics of the G' peak can be interpreted to quantify the number of graphene layers present. The G' band for graphene exhibits a single lorentzian peak below 2700 cm^{-1}. Stacking of additional graphene layers causes both an up shift and a splitting of the G' band, with highly order pyrolytic graphite (HOPG) being described by two lorentzian peaks, as shown in Figure 2.9.

In the case turbostractic graphite (graphite in which each layer is in a random rotation along the c-axis) a single G' peak is observed similar to that of single layer graphene. This is a result of the structure of the graphite in which the electronic structure is very similar to that of graphene. Key differences are an upshift to above 2700 cm^{-1} and broadening of the FWHM from 24 cm^{-1} to up to ~46-60 cm^{-1} for turbostratic graphite (Malard et al., 2009; Cançado et al., 2002, 2008). The ratio of the intensities of the G' to G peak is also much larger for mono layer graphene that that of turbostratic graphite (Malard et al., 2009).

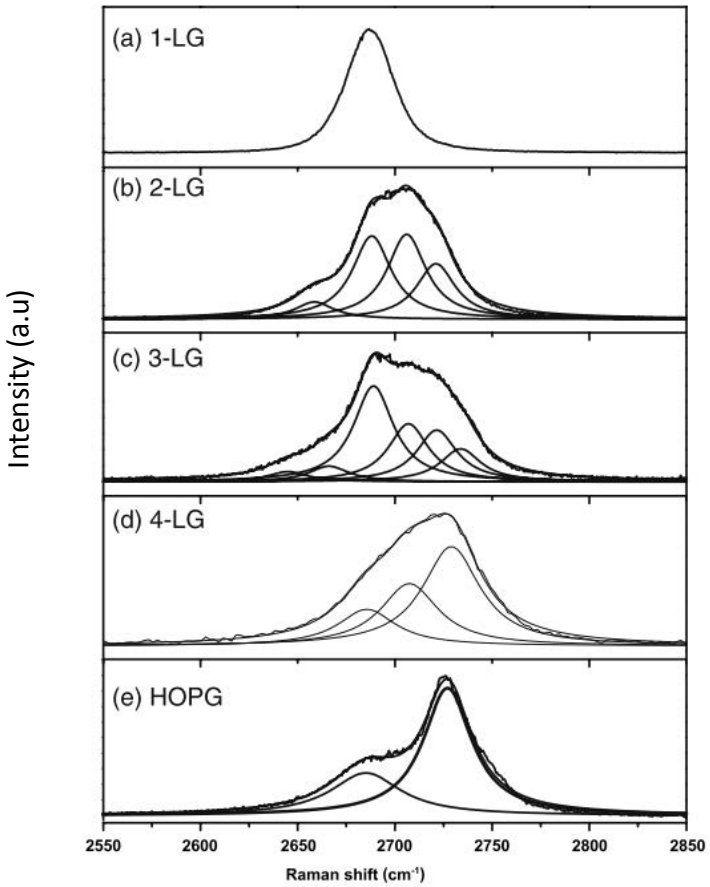

Figure 2.9 G' Raman band of (a) 1, (b) 2, (c) 3, (d) 4 and (e) highly order pyrolytic graphite (measured using a 514 nm excitation wavelength) (Malard et al., 2009)

2.4.1.2 X-Ray Diffraction

X-ray diffraction (XRD) is a non-destructive method of characterising crystalline graphite, however since XRD relies on long-range order within the sample and regular crystal structure, diffraction patterns for carbon materials that lack these properties such as graphene, amorphous or nano-crystalline graphite cannot offer much insight into their microstructures (the theory behind XRD is discussed in Section 4.3.1.1). Since not all parts of

a sample may be amorphous, XRD patterns can complement Raman spectra and help build an understanding of the microstructure of the sample.

2.4.1.3 Calculation of Crystallite size from Raman Spectroscopy

Tuinstra and Koenig (1970) demonstrated that the ratio of the D and G bands in graphite was inversely proportional to the average crystallite size (L_a) for graphite measured with a 514 nm excitation wavelength. Knight and White (1989) later derived a formula to calculate the crystallite size based on the ratio of intensity of the D and G bands.

However, Mernagh et al. (1984) were able to show that the intensity of the G and D bands relied heavily on the wavelength of the excitation laser, resulting in Knight and Whites' formula only being valid of samples studied using 514 nm excitation lasers.

A generalised formula was produced by Cancado et al. (2006) which incorporated the wavelength of the laser used allowing the calculation of L_a for a minimum of the 5 excitation wavelengths used in the study (647 nm, 568 nm, 514.5 nm, 488nm and 457.9 nm). This generalised formula calculates the constant as 13.5 nm for a 488 nm laser which is almost 3 times greater than the value calculated for a 514 nm equivalent (4.4 nm).

$$L_a\,(\mathrm{nm}) = \frac{560}{E_l^4}\left(\frac{I_D}{I_G}\right)^{-1} \qquad E_l = \text{excitation laser energy in eV} \qquad (2.1)$$

It should also be noted that in the general formula proposed by Cançado et al., I_D and I_G are the integral intensities (peak area) of the D and G bands opposed to the peak intensities for the relationship proposed by Knight and White.

2.4.1.4 Calculation of Crystallite size from X-Ray Diffraction

In 1948 Paul Scherrer developed an equation to calculate the average crystallite size (L_c) perpendicular to a chosen plane (hkl) within nano-crystalline materials by measuring the diffraction angle and full width half maximum (FWHM) of the corresponding hkl reflections, shown in Equation (2.2); K = shape factor, λ = X-ray wavelength in nm, β = FWHM and θ = diffraction (Bragg) angle. When calculating the crystallise size, it is necessary to account for intrinsic broadening of the measurement, as such, $\beta = \beta_{observed} - \beta_{intrinsic}$.

$$L_c = \frac{K\lambda}{\beta cos\theta} \qquad (2.2)$$

Some important factors must be considered when using the Scherrer equation to evaluate the average crystallite size within a sample. The Scherrer equation is only valid for crystallite sizes in the range of 200 nm and smaller as such large crystallite sizes correspond to small peak width making it hard to separate the broadening of peaks as a result of crystallite size from broadening from other factors (Holzwarth and Gibson, 2011).

The equation must be used with caution since effects such as stress, strain and defects that can effect both the FWHM and measured diffraction angle of reflections, therefore caution must be used when applying the formula. It was reported by (Aladekomo and Bragg, 1990) that the calculated crystallite size would be roughly 22% larger than the actual value.

The shape factor K is a dimensionless constant with a value close to unity, for spherical particles a value of 0.89 is used and 0.94 for cubic particles, in general K = 0.9 is used for particles of unknown shape.

2.4.2 Ball Milled Graphite

Ball milling of graphite is an effective way of creating nanostructured graphite inducing nano-crystallinity, defects and dangling carbon bonds (Orimo et al., 1999; Huang et al., 2007; Chen et al., 2003; Zhang et al., 2009; Fukunaga et al., 2004).

Hydrogenated milled graphite was first investigated by Orimo et al. (1999). Ball milling of graphite was found to rapidly reduce crystallinity and long-ranger order in the graphite. The hydrogen content in graphite reached 7.4 wt% (milled under 10 bar H_2 for 80 h at 400 rpm). Radial distribution function spectra confirmed the presence of C-H bonding within the sample confirming that ball milling under hydrogen is an effective way to form hydrogenated nanostructured graphite. Hydrogen was reported to be released over a broad range of temperatures between 327 °C and 727 °C under a hydrogen atmosphere (Orimo et al., 2001)

2.4.2.1 Effect of Hydrogen Milling Pressure

Chen et al. (2003) demonstrated that H_2 milling pressures above 3 bar resulted in a decrease in the total H_2 absorbed during milling, postulating that this was a result of H_2 atoms being trapped at sheet edges and between graphene layers, thus suppressing defect formation.

2.4.2.2 Effect of Milling Time

Orimo et al. (1999) reported that the hydrogen concentration of ball-milled graphite was proportional to the milling time for milling times up to 80 h, however, Temperature Desorption Mass Spectrometry (TPS) revealed hydrogen release between 327 °C and 727 °C

with two main peaks around 475 °C and 675 °C. Methane and ethane were also detected alongside the first hydrogen desorption (Orimo et al., 2001).

Zhang and Book, (2011a) studied the effect of milling time on the desorption of hydrogen and methane from milled graphite. Milling under 3 bar hydrogen for 10 h was found to release 5.5 wt% hydrogen and no methane within detectable limits. Longer milling times resulted in desorption of methane and a reduction in the quantity of desorbed hydrogen.

2.4.2.3 Effect of milling mode on H_2 uptake

The choice of milling mode used during the ball milling process has been shown to directly affect the hydrogen content of the graphite (Huang et al., 2007). Graphite samples were milled for 100 h under 5 bar H_2 using two different milling processes, shear milling resulted in a final H_2 concentration of 0.613 wt% compared to 2.718 wt% for impact milling.

2.4.2.4 Effect of milling under H_2 vs. Ar

Ogita et al. (2004) investigated the effect on graphite when milled under Ar and H_2 through Raman and Infrared (IR) spectroscopy. Milling under 1 bar H_2 was found to preserve crystallinity, whereas milling under Ar was found to induce nanostructure randomness more rapidly.

Francke et al. (2005) observed the same effects when milling under Ar and H_2. Hydrogen was found to preserve the microstructure with greater milling pressures resulting in greater preservation. However, BET calculations indicated that milling under hydrogen does not

increase the maximum surface area that can be achieved compared to milling under Ar, after 60 h samples milled under both H_2 and Ar had similar calculated surface areas. Due to the slowed rate of destruction in the hydrogen sample, the rate of surface area increase for the sample milled under Ar is greater. A maximum surface area for the Ar sample was achieved after 5 h after which the surface area began to decrease due to particle agglomeration.

Figure 2.10 shows high resolution transmission electron microscopy (HRTEM) images of graphite samples milled under Ar and H_2 published by Francke et al., 2005. Stacking packages (crystalline graphitic particles embedded in an amorphous matrix) were observed for samples milled under Ar for between 1 and 10 h after which the structure is best described as "balls of wool" as shown in the left hand image of Figure 2.10. Conversely stacking packages were visible in graphite milled under H_2 after 15 h. The middle image in Figure 2.10 shows examples an example of stacking packages in which graphite layers were observed to be bent up to 180 °. After 50 h of milling TEM measurements displayed no long range order in the graphite layers.

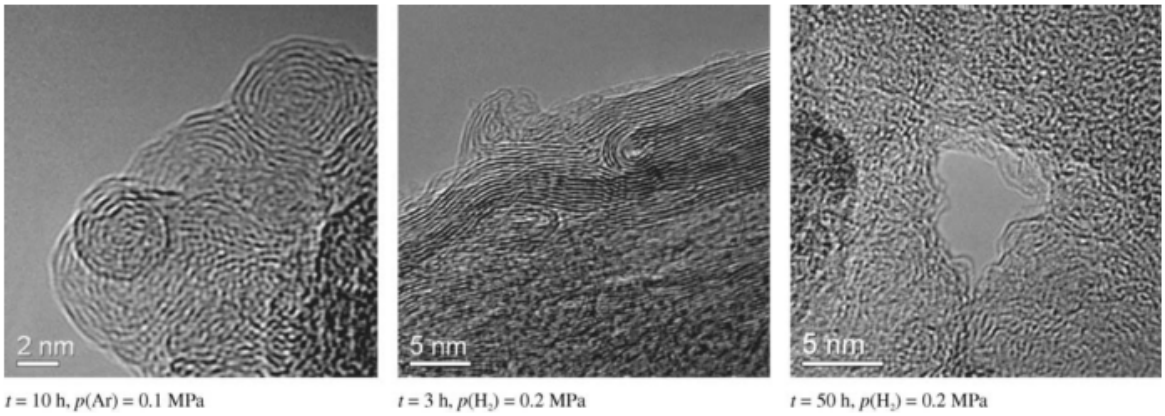

Figure 2.10 HRTEM images of graphite samples with an amorphous nanostructure milled for various durations under Ar and H_2 (Francke et al., 2005)

Down shifts in the location of the (002) reflections for each graphitic sample indicated an expansion in the crystal lattice consistent with destruction of graphitic planes and the introduction of defects as explained by (Chen et al., 2000; Huang, 1999).

2.4.2.5 C-H bonding in hydrogenated graphite

The ball milling of graphite under a hydrogen atmosphere has been shown to result in the chemisorption of hydrogen to dangling C bonds located at graphene edges and defects (Smith et al., 2009; Fukunaga et al., 2004; Ogita et al., 2004).

Ogita et al. (2004) investigated the nature of C-H bonding in the hydrogenated graphite using IR. C-H stretching modes were observed around 2900 cm^{-1}, the concentration of CH_2 to CH_3 bonds was estimated to be 93-30% for CH_2 and 7-10% CH_3 for graphite milled for 20 h and 85% and 15% respectively for graphite milled for 8 h. CH_2 was identified as the most dominant hydrogen configuration.

Although not seen in visible light Raman spectroscopy, C-H stretching vibrations have been observed using Surface Enhanced Raman Spectroscopy (SERS) (Ushizawa et al., 1999) and ultra violet Raman Spectroscopy (UV-RS) (Ferrari and Robertson, 2001) indicating that although very weak, the C-H stretching modes in hydrogenated carbon is Raman active.

2.4.3 Ball Milled Graphite + Additions

As discussed in Section 2.4.2, hydrogenated ball milled graphite is capable of storing up to 7.4 wt% of H_2, however the extremely high temperatures required for its release (400-

900 °C) are far too high for vehicular applications and reversibility is not possible. In an effort to lower H_2 desorption temperatures and induce reversibility, additions such as iron and lithium hydride have been added to graphite.

2.4.3.1 Ball Milled Graphite + Fe

Ichikawa et al. (2004) identified that Fe contamination which occurred during milling led to a two stage H_2 desorption profile during heating, with the first step commencing at the same temperature as Fe_3C crystal growth, 300 °C.

Zhang and Book (2011) observed similar results, through the addition of Fe, reducing the H_2 desorption temperature of pure graphite down to 350 °C whilst increasing the total H_2 absorbed during milling to 9.6 wt% by milling graphite with 0.5 wt% Fe. XRD measurements identified no crystalline Fe in the milled sample. Peaks consistent with iron carbide were identified indicating the improvement in storage capacity was due to the presence of iron carbide formed during milling.

2.4.3.2 Ball Milled Graphite + LiH

Ichikawa et al. (2011) showed that 5 wt% H_2 could be reversibly desorbed and re-absorbed over 5 cycles using milled graphite with the addition of LiH at a molar ratio of 2:1, graphite:LiH. Hydrogen release is observed between 473 K and 773 K, with peak desorption at 350 °C. It was proposed that the presence of LiH destabilized the C-H bonds of the hydrogenated graphite. XRD results indicated Li_2C_2 was found to form during desorption

which was believed to accountable for the induced reversibility. Only the 1st dehydrogenation released methane, all of the rehydrided samples only released hydrogen indicating that the composition of the as-prepared sample was different to that of the rehydrided samples. A reduction of storage capacity over cycling was deduced to be a consequence of hydrocarbon production; a result of the decomposition of Li_2C_2 during rehydrogenation.

2.5 Porous Silicon

Porous silicon (PS) was discovered accidently in the 1950s at Bell Laboratories in attempts to produce silicon wafers via electrochemical processing (Sailor, 2011a). Under certain conditions, the electrochemical processing of silicon wafers resulted in the formation of holes (pores) in the (001) direction (Uhlir, 1956).

The fabrication of PS involves the etching of crystalline silicon wafers in hydrofluoric acid (HF) solutions resulting in the propagation of long open nanopores along with the formation a hydrogen terminated surface (Sailor, 2011a) originating from the fabrication process.

Since the term nanoporous refers to a large range in pore size ($999 \geq x \geq 1$ nm), nanopores are broken down into three sub categories shown in Table 2.1, as defined by the International Union of Pure and Applied Chemistry (IUPAC) (Rouqerol et al., 1994):

Table 2.1 Types of nanopores as defined by the IUPAC (Rouqerol et al., 1994)

Name	Range of Pore Diameter (nm)
Micropores	< 2
Mesopores	50 < x < 2
Macropores	> 50

The level of doping in the silicon wafer used in the manufacturing process determines the range of pore sizes that can be achieved during fabrication, p-type, p^{++}-type and n-type silicon wafers results in microporous, mesoporous and macroporous silicon respectively (Sailor, 2011b). Varying the current density, temperature and electrolyte composition can also impact the pore size and porosity. As expected for porous materials, porous silicon has a high surface area, typically between 20 and 1000 m^2cm^{-3} (Petrova et al., 2000) or between 9 and 429 m^2g^{-1}.

Figure 2.12 shows a cross-sectional SEM image of a porous silicon wafer published by (Dian et al., 2004), the elongated pores resulting from the electrochemical etching fabrication process are clearly visible, SEM images were also published showing the surface of porous silicon wafers clearly showing the open end of the pores, shown in Figure 2.11.

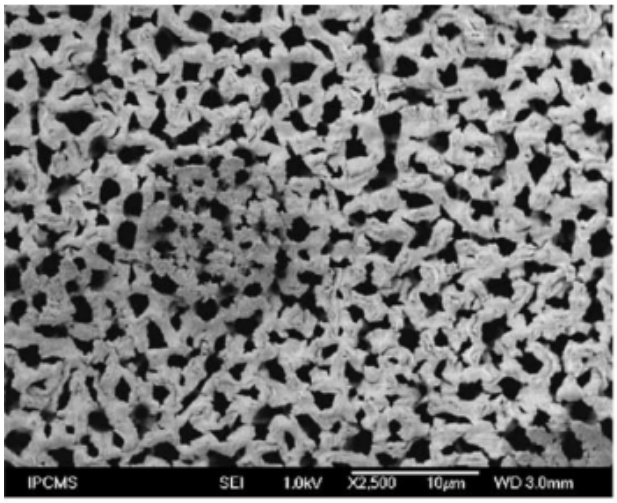

Figure 2.11 SEM image of the surface of a porous silicon wafer (12.5 %HF solution, anodization current of 10 mAcm^{-2}) (Dian et al., 2004)

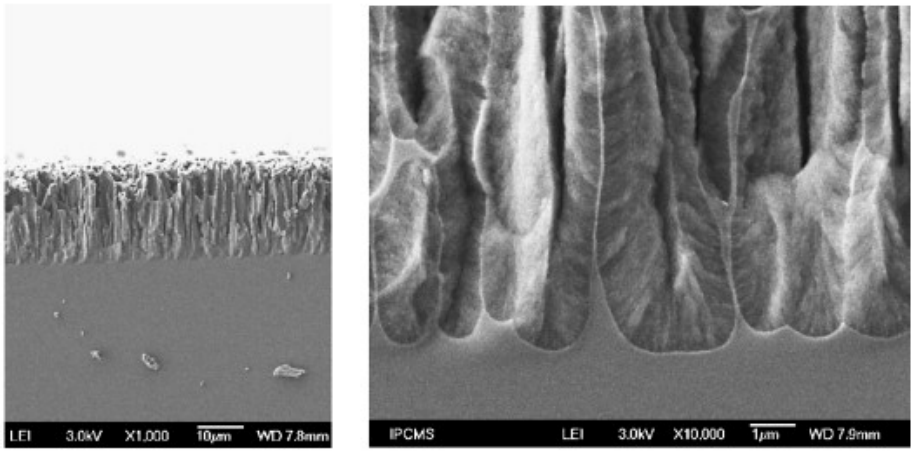

Figure 2.12 Cross-sectional SEM image of a porous silicon wafer created by electrochemical etching (Dian et al., 2004)

2.5.1 Characterisation of Porous Silicon

The profile of silicon's Raman spectrum is indicative of its long rang ordering. Figure 2.13 shows the Raman spectra of 4 silicon samples with increasing amorphous content. Crystalline silicon has cubic crystal structure leading to uniform bond strength and energy, as such its Raman spectrum exhibits an intense symmetric peak ca. 520 cm^{-1} originating from the transverse optical TO mode of Si-Si bond (Veprek et al., 1981). On the other hand, this uniformity is not present in amorphous silicon, and as such the Raman spectrum of amorphous silicon (red line) exhibits a broad peak ca. 480 cm^{-1}. The green and blue lines in Figure 2.13 show the Raman spectra of silicon samples with some degree of crystallinity remaining, but with large amorphous contents, indicated by a reduction of intensity and downshift in the TO mode at 520 cm^{-1} and an increase in the broad amorphous peak ca. 480 cm^{-1}.

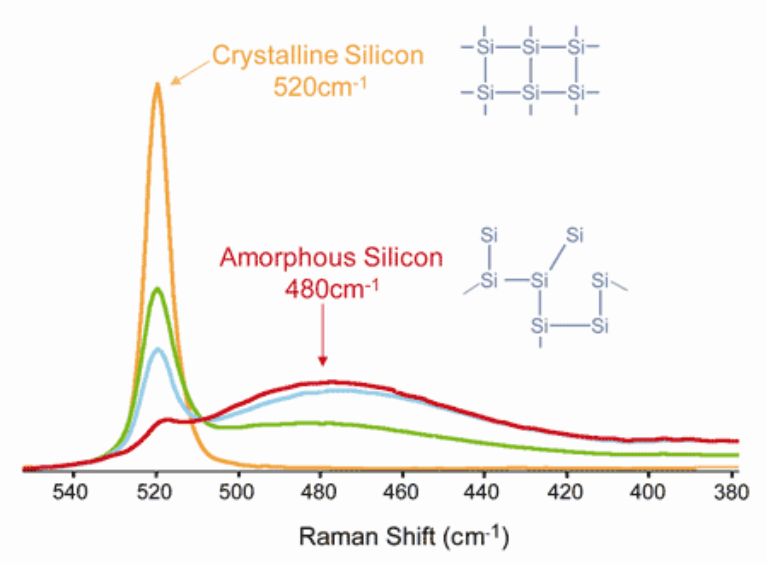

Figure 2.13 Raman spectra of Silicon samples with varying quantities of amorphous content. The orange line shows the spectrum of crystalline silicon, the red, blue and green lines show Raman spectra of amorphous silicons (Semrock, 2016)

The Raman spectrum of porous silicon differs slightly to that for crystalline silicon. The location of the TO mode of silicon is broadened and downshifted to lower energy indicating the presence of nano-scale features (Dubey and Gautam, 2009). As the size of the nanocrystallites reduces the TO mode moves to lower frequencies becoming broader asymmetrically (Dubey and Gautam, 2009). Thus for higher porosity silicon a greater down shift is observed.

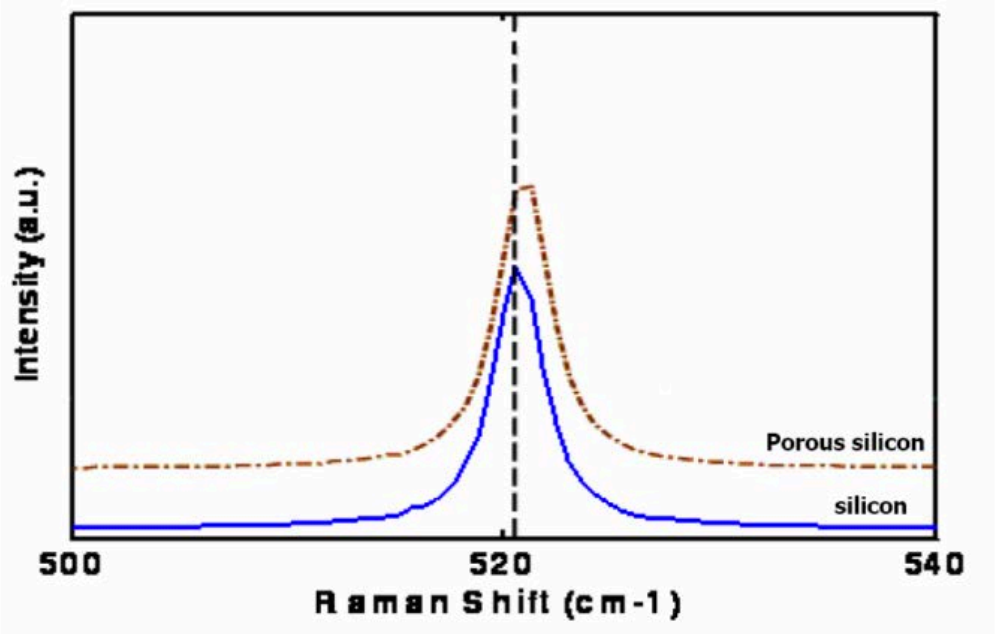

Figure 2.14 Raman spectrum of Porous and crystalline silicon with an excitation wavelength of 488 nm
(Dubey and Gautam, 2009)

The hydrogen terminated surface of porous silicon consists of three different SiH_x species: SiH, SiH_2 and SiH_3. SiH is most common on flat surfaces, whilst SiH_2 and SiH_3 require more Si dangling bonds for their formation and as such are believed to exist on pore edges and defects, as demonstrated in Figure 2.15.

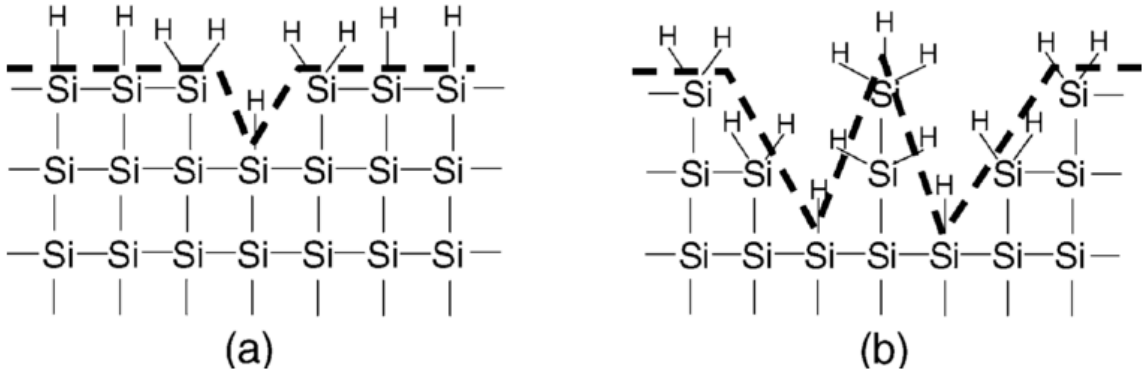

Figure 2.15 Schematic diagram of SiHx bonding present on the surface of porous silicon. a) the surface of a low porosity PS (<60%) b) the surface of a high porosity (>60%). The dashed lines represent the surface (Lysenko et al., 2004)**.**

SiH, SiH_2 and SiH_3 are all Raman and IR active and can be observed in the Raman spectra of porous silicon. Figure 2.16a shows the IR Spectra or porous silicon in the range of 2040 cm^{-1} and 2190 cm^{-1}. The three peaks ca. 2088 cm^{-1}, 2110 cm^{-1} and 2137 cm^{-1} correspond to stretching modes of SiH, SIH_2 and SiH_3 bonds respectively. Their relative intensities are dependant upon the degree of porosity within the sample. As shown in Figure 2.15, higher porosity silicon will contain a larger proportion of SiH_2 and SiH_3 species compared to low porosity silicon.

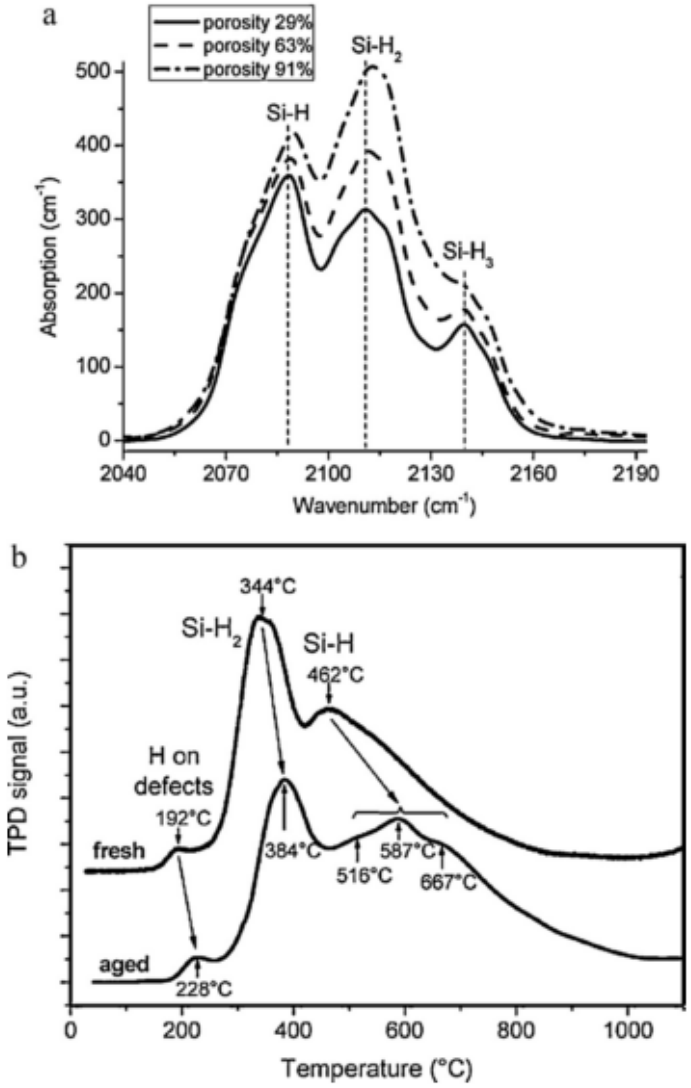

Figure 2.16 a) Infrared Spectra of meso-porous silicon with varying porosity b) TPD profile showing hydrogen desorption with increasing temperature (Manilov and Skryshevsky, 2013; Lysenko et al., 2005)

2.5.2 Thermal decomposition

Lysenko et al. 2005 studied the thermal decomposition of PS via temperature programmed desorption (TPD), their results can be seen in Figure 2.16b. Hydrogen was observed to desorb in the in a 3 main steps from both freshly prepared and aged (50 days) PS. Traces of silane (SiH_4) were detected but at an intensity 2 orders of magnitude lower than the observed H_2 desorption and was subsequently considered negligible.

The observed increase in hydrogen desorption temperature of 40 °C from the aged PS compared to its freshly made counterpart was attributed to the partial oxidation believed to have occurred during storage

2.6 Lithium Borohydrides

Borohydrides are a type of complex hydride which are defined as salt like materials consisting of a complex anion built of hydrogen atoms covalently bonded to a central atom (in the case of borohydrides, the central atom is Boron) and a light metal cation (Weidenthaler and Felderhoff, 2010). The anion in borohydrides is a tetrahedral $[BH_4]^-$ structure, hence borohydrides are also given the name tetrahydroborates (Stavila et al., 2013). Since borohydrides contain such light elements, they show great promise as hydrogen storage materials, with $LiBH_4$ boasting the highest H_2 storage capacity of 18.36 wt% and 122.5 kgm^{-3}.

$LiBH_4$ was the first synthesised by Schlesinger and Brown (1940) via the reaction of ethyl lithium and diborane, however, it was not investigated as a hydrogen storage material until 2003 when Züttel et al. (2003) investigated the thermal decomposition of $LiBH_4$ and successfully lowered the decomposition temperature through the addition of SiO_2.

Recently, another application of $LiBH_4$ has been investigated, its high conductivity makes $LiBH_4$ a potential solid-state electrolyte for use in batteries (Matsuo et al., 2007; Maekawa et al., 2009; Takahashi et al., 2013; Blanchard et al., 2015), however, this work will focus on its use as a hydrogen storage medium.

2.6.1 Structure of $LiBH_4$

$LiBH_4$ is comprised of a Li^+ cation ionically bound to a $[BH_4]^-$ anion. The tetrahedral structure of the $[BH_4]^-$ unit is very similar to that of methane and as such the vibrational modes in $LiBH_4$ are referred to by their CH_4 equivalents.

At room temperature $LiBH_4$ possesses an orthorhombic crystal structure (o-$LiBH_4$), however, upon heating to around 113 °C $LiBH_4$ under goes a reversible polymorphic transformation from o-$LiBH_4$ to a hexagonal crystal structure (h-$LiBH_4$) (Shao et al., 2014).

2.6.2 Thermal Decomposition

$LiBH_4$ melts at 285 °C releasing a small amount of H_2 followed by the decomposition of $LiBH_4$ with peak hydrogen release at 467 °C (Shao et al., 2014) (reaction temperatures were calculated for bulk $LiBH_4$ heated at a 5 $C.min^{-1}$ under 50 $ml.min^{-1}$ Ar as shown in Figure 2.17).

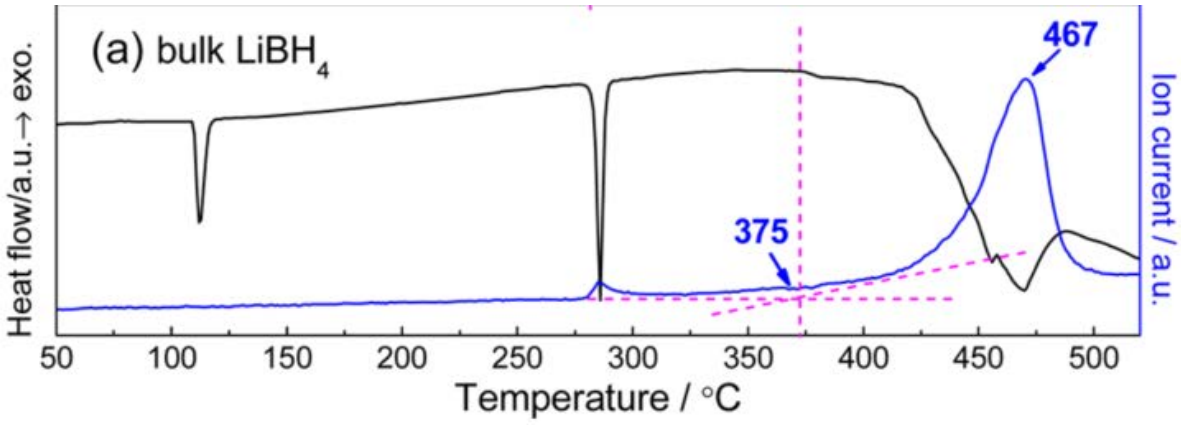

Figure 2.17 DSC-MS profile of bulk $LiBH_4$ heated to 550 °C at 5 $°C.min^{-1}$ under 50 $ml.min^{-1}$ Ar (Shao et al., 2014)

When heated $LiBH_4$ decomposes into LiH, amorphous boron (α-B) and hydrogen following an overall decomposition pathway shown in Equation (2.3), recombination of reaction products has been successful under 600 °C and 155 bar H_2 (Mauron et al., 2007).

A number of intermediate phases have been proposed such as $Li_2B_{12}H_{12}$ and B_2H_6 (Ohba et al., 2006; Kato et al., 2010).

$$LiBH_4 \leftrightarrow LiH + B + {}^3/_2H_2 \qquad (14\ wt\%) \qquad (2.3)$$

Ohba et al. (2006) conducted first principle studies investigating the stability of different intermediate compounds in the decomposition of $LiBH_4$. Lithium dodecaborane ($Li_2B_{12}H_{12}$) comprised of two Li^+ cations and a $[B_{12}H_{12}]^{2-}$ anion was predicted as the most thermodynamically stable reaction product, with the decomposition reaction following Equations (2.4a) and (2.4b).

$$LiBH_4 \leftrightarrow {}^1/_{12}Li_2B_{12}H_{12} + {}^5/_6LiH + {}^{13}/_{12}H_2 \qquad (10\ wt\%) \qquad (2.4a)$$

$$\leftrightarrow LiH + B + {}^3/_2H_2 \qquad (4\ wt\%) \qquad (2.4b)$$

Shortly after Orimo et al. (2006) confirmed the presence of $Li_2B_{12}H_{12}$ in the decomposition of $LiBH_4$ by Raman spectroscopy measurements. Thermo-gravimetric (TG) measurements indicated a rapid weight loss of ~11 wt% between 427 °C and 457 °C followed by a further gradual weight loss of ~3 wt% by 625 °C, suggesting decomposition progressed through Equation 2.4a followed by Equation 2.4b. XRD results did not show any reflections consistent with $Li_2B_{12}H_{12}$ indicating a lack of long-range order; only reflections of LiH were observed.

Reed et al. (2009) studied the decomposition of $LiBH_4$ through in-situ Raman spectroscopy. Results showed the formation of $Li_2B_{12}H_{12}$ at 350 °C with the formation of α-B at 380°C. Both

α-B and $Li_2B_{12}H_{12}$ are present during heating suggesting that $LiBH_4$ may decomposes directly into LiH, α-B and H_2 (Equation 2.3) as well as through the intermediate compound $Li_2B_{12}H_{12}$ (Equation 2.4); the two decomposition pathways may be simultaneous.

Another decomposition pathway was proposed by Kato et al. (2010) due to the detection of B_2H_6 during the decomposition of $LiBH_4$, the reaction pathway is summarised in Equation (2.5).

$$LiBH_4 \rightarrow LiH + {}^{1}/_{2}B_2H_6 \rightarrow LiH + B + {}^{3}/_{2}H_2 \qquad (2.5)$$

Friedrichs et al. (2010) produced $Li_2B_{12}H_{12}$ via the reaction of B_2H_6 and $LiBH_4$ which along with the detection of B_2H_6 by Kato et al. (2010) gives rise to the decomposition pathway described in Equation (2.6).

$$2LiBH_4 + 5B_2H_6 \rightarrow Li_2B_{12}H_{12} + 13H_2 \qquad (2.6)$$

The icosahedral $[B_{12}H_{12}]^{2-}$ cages in closo-boranes such as $Li_2B_{12}H_{12}$ are extremely stable as a result of the aromatic character of bonding in the cage (Stavila et al., 2013), and as such are unlikely to further decompose through Equation 2.3b. Consequently, avoiding the formation of B_2H_6 and $Li_2B_{12}H_{12}$ are highly important if $LiBH_4$ is to be used in hydrogen storage. B_2H_6 can poison fuel cell stacks and along with $Li_2B_{12}H_{12}$ both act like boron sinks, reducing the quantity of boron free to reform $LiBH_4$ during rehydriding reactions (Yan et al., 2012).

The decomposition pathway for bulk $LiBH_4$ has been shown to be dependent upon the decomposition conditions and as such can be influenced by an applied H_2 over pressure (Yan et al., 2012). The decomposition of $LiBH_4$ at 600 °C under 50 bar H_2 overpressure and at 427 °C under 10 bar H_2 yields the formation of $Li_2B_{12}H_{12}$ only (Equation 2.3a). Decomposition

under the lower H_2 pressure range of 0.1 to 10 bar at 600 and 527 °C leads to simultaneous decomposition mechanisms; decomposition into $Li_2B_{12}H_{12}$ (Equation 2.4a) and direct decomposition into α-B (Equation 2.3).

2.6.3 Hydrolysis of $LiBH_4$

Hydrolysis of $LiBH_4$ has been studied due to its high theoretical H_2 'storage' capacity of 8.6 wt% (Kojima et al., 2004) and the intensely exothermic nature of the reaction which can result in the reaction chamber reaching temperatures in excess of 200 °C (Weng et al., 2011b).

Experimentally no more than 60 wt% of the theoretical hydrogen generation has been achieved due to the formation of impermeable solids clogging the reaction vessels formed by a combination of reacted and un-reacted $LiBH_4$ (Weng et al., 2011b). Weng et al. (2011a) found that full hydrolysis could be achieved with addition of 7wt% multi-wall carbon nanotubes (MWCNTs) through prevention of agglomeration of reactants and products. However formation of stable reaction products such as $LiOB_2$ make reversibility complex.

2.7 Destabilisation $LiBH_4$

As previously discussed $LiBH_4$ requires non-practical conditions (for on-board vehicles) for de/re-hydrogenation. Consequently a vast quantity of research has been focused on reducing the temperatures and pressures required (Saldan, 2011; Li et al., 2011). There are

three main approaches that may be used: catalysts, reactive hydride composites and size interface reactions (Fichtner, 2011).

2.7.1 Effect of Oxidation on the decomposition of $LiBH_4$

Kato et al. 2010 studied the effect of surface oxidation on decomposition pathway of $LiBH_4$. The formation of LiO_2 on the surface layer of $LiBH_4$ resulted in a reduction in the quantity of B_2H_6 released and improved H_2 desorption kinetics indicating B_2H_6 desorption is determined by a surface process. It was reported that when oxygen chemosorbs to the surface of $LiBH_4$, boron rich oxide compounds are formed before the more stable and lithium rich LiO_2 forms resulting in segregation of Li onto the surface. LiO_2 suppressed the release of B_2H_6 by hindering its formation, resulting in enhanced H_2 desorption.

2.7.2 Catalysts

A wide range of catalysts have been added to $LiBH_4$ in order to influence the decomposition pathway of $LiBH_4$ with the aim of reducing temperatures and pressures required for re/de-hydrogenation of $LiBH_4$, a few of the most prominent additions are discussed in this section.

2.7.2.1 $LiBH_4 + SiO_2$

$LiBH_4$ was first destabilized via the addition of SiO_2 as a catalyst by Züttel et al. 2003 who observed a significant reduction in the decomposition temperature of $LiBH_4$ to 200 °C, with the release of hydrogen occurring in three stages all below 400 °C. The $LiBH_4$ was found to

desorb 13.5 wt% H_2 by 500 °C corresponding to complete desorption with the production of B and LiH. Molten $LiBH_4$ has been shown to react with SiO_2 and forming Li_2SiO_3 and Li_4Sio_4 during decomposition (Mosegaard et al., 2008) preventing the possibility for reversibility.

2.7.2.2 $LiBH_4$ + $TiCl_3$

Mosegaard et al. 2008 investigated the effect of $TiCl_3$ on the decomposition of $LiBH_4$. The hand-mixed sample containing 2 mol% $TiCl_3$ was found to partially react with $LiBH_4$ at room temperature forming LiCl as observed by XRD.

2.7.2.3 $LiBH_4$ + TiO_2

Yu et al. 2010 ball milled $LiBH_4$+TiO_2 with varying weight ratios, the most promising was determined to be 1:4 ($LiBH_4$:TiO_2) whose onset of H_2 release was 150 °C with peak H_2 release ca. 245 °C. The sample was found to desorb 3.65 wt% H_2 by 600 °C, however, the majority of H_2 was released below 220 °C. The proposed reaction pathway (equation 2.7) for decomposition is shown below. Rehydrogenation attempts under 400 °C and 100 bar H_2 were unsuccessful.

$$LiBH_4 + TiO_2 \rightarrow LiTiO_2 + B + 2H_2 \qquad (2.7)$$

A few months later, Au et al. 2008 reported that ball-milled $LiBH_4$+TiO_2 (75:25 wt%) desorbed 9wt% H_2 between 100 °C and 600 °C and could resorb an impressive 8 wt% at 600 °C under 70 bar H_2. The decomposition pathway was reported as below (equation 2.8),

giving a theoretic capacity of 10 wt%. Over 5 re/de-hydrogenation cycles the capacity was found to reduce from 9 wt% to 2 wt%, accredited to the formation of stable Li_3BO_3.

$$LiBH_4 + 0.09TiO_2 \rightarrow 0.18LiOH + 0.82LiH + 0.82B + 0.09TiB_2 \quad (2.8)$$

2.7.2.4 $LiBH_4 + Li_3BO_3$

Ma et al., 2016 ball milled $LiBH_4$ with porous lithium borate (Li_3BO_3) (fabricated by balling milling LiH and $LiBO_2$) to form a mixture of $LiBH_4$ scattered within the Li_3BO_3 pores (characterised by TEM). The decomposition and recombination kinetics of $LiBH_4$ were found to be enhanced for the $LiBH_4$ ball milled with Li_3BO_3 compared to milled $LiBH_4$ on its own, with composite samples desorbing 8 wt% H_2 just above 600 °C (100 °C lower compared to milled $LiBH_4$). The $LiBH_4 + Li_3BO_3$ sample was shown to desorb three times as much H_2 by 350 °C (1.5 wt%) compared to ball milled $LiBH_4$ and adsorb 2.1 wt% H_2 after 500s at 400 °C under 50 bar H_2 compared to 1.5 wt% for milled $LiBH_4$. XRD results of the $LiBH_4 + Li_3BO_3$ at various stages of de/re-hydrogenation revealed no change in the intensity of reflections of Li_3BO_3 and no additional intermediate phases indicating the Li_3BO_3 acts as an additive without chemically reacting with the $LiBH_4$, as depicted in Equation 2.9.

$$LiBH_4 \quad Li_3BO_3 \quad LiH + B + {}^3/_2H_2 \quad (2.9)$$

A combination of the Li^+ ions, positively charged active B sites and highly electronegative oxygen atoms in Li_3BO_3 were speculated to reduce the activation enthalpies for de/re-hydrogenation of $LiBH_4$.

2.7.3 Reactive Hydride Composites

Reactive hydride composites (RHCs) include the addition of a second compound hydride based compound to $LiBH_4$ resulting in the formation of new compounds with different thermodynamic properties. The addition of a second compound can lead to a reduction in the H_2 content of the system hence the H_2 capacity of the individual compounds must be considered in order to minimise any overall loss in H_2 storage capacity of the system. A number of promising RHCs are discussed below.

2.7.3.1 $LiBH_4 + MgH_2$

$LiBH_4$ mixed with MgH_2 has a theoretical H_2 capacity of 11.4 wt% and decomposes via a two-stage reaction shown in equations 2.10a and 2.10b. The formation of MgB_2 acts to stabilize the decomposition of $LiBH_4$ resulting the destabilisation of $LiBH_4$ (Vajo et al., 2005). The reformation of $LiBH_4$ is achieved in a single reaction step under 100 bar H_2 at 350 °C shown in equation 2.10c. The addition of $TiCl_3$ was found to catalyse the reaction resulting in a reversible storage capacity of > 9 wt%.

$$LiBH_4 + {}^1/_2MgH_2 \rightarrow LiBH_4 + {}^1/_2Mg + {}^1/_2H_2 \qquad (2.10a)$$

$$LiBH_4 + {}^1/_2Mg + {}^1/_2H_2 \rightarrow LiH + {}^1/_2MgB_2 + 2H_2 \qquad (2.10b)$$

$$LiH + {}^1/_2MgB_2 + 2H_2 \rightarrow LiBH_4 + {}^1/_2MgH_2 \qquad (2.10c)$$

The limiting factor on $LiBH_4 + MgH_2$ systems is the incubation period between the two decomposition steps of 12 h (Fang et al., 2010b).

2.7.3.2 $LiBH_4 + CaH_2$

$LiBH_4$ + CaH_2 has a theoretical H_2 capacity of 11.7 wt% and follows the decomposition pathway described by equation 2.11.

$$6LiBH_4 + CaH_2 \leftrightarrow 6LiH + CaB_6 + 10H_2 \qquad (2.11)$$

As reported for the $LiBH_4$ + MgH_2 system, TiCl3 has been shown to catalyse the de/re-hydrogenation reaction of a $LiBH_4$ + CaH_2 system (Pinkerton and Meyer, 2008). A $LiBH_4$ + CaH_2 + $TiCl_3$ (6:1:0.25 molar ratio) composite was prepared via ball milling for 1 h. The sample was able to reversibly store 9.1 wt% over 3 cycles which corresponds to 95% of its theoretical capacity when rehydrided under 83 bar H_2 at 400 °C for 10 h, only H_2 was detected by mass spectroscopy.

2.7.3.3 $LiBH_4 + YH_3$

Shim et al. 2010 ball milled YH_3 with $LiBH_4$ forming a mixture of $LiBH_4$, YH_3 and YH_2 (indicating partial decomposition of YH_3 during ball-milling). The application of a 3 bar H_2 back-pressure on the decomposition of $LiBH_4$ + YH_3 was shown to alter the decomposition pathway of the mixture through the formation of LiH and YB_4 resulting in the desorption of over 7 wt% H_2 after 6 h at 350 °C. A 4 h incubation period was observed before the mixture started to rapidly release hydrogen, which was attributed to surface oxidation of YH_3 particles acting as a kinetic barrier in the reaction between $LiBH_4$ and YH_3. Rehydrogenation of the sample under 90 bar H_2 at 350 °C resulted in the reformation of $LiBH_4$, YH_3 and YH_2 and a H_2 uptake of 5.2 wt% (72% of its original capacity).

The application of a H_2 back pressure has been shown to promote the formation of metal borides and thus lower hydrogen desorption temperatures for YH_3, CaH_2, CeH_2 (Shim et al., 2010) and MgH_2 (Vajo et al., 2005; Nakagawa et al., 2007) mixed with $LiBH_4$.

2.7.3.4 $LiBH_4$ + NbF_5

Kou et al. 2014 ball milled a variety of ratios of $LiBH_4$ and NbF_5 at 400 rpm for 1 min under an Ar atmosphere. After ball-milling of $5LiBH_4$ + NbF_5 a new phase was observed by XRD along with reflections from LiF, indicating anew phase was formed during the milling process. FTIR measurements confirmed the presence of B-H bending and stretching bonds in the milled sample indicating the formation of a new borohydride. The milled $5LiBH_4$ + NbF_5 sample was shown to begin H_2 desorption at an incredibly 60 °C and desorb 4 wt% by 255 °C. $20LiBH_4$ + NbF_5 was shown to desorb a total of 7 wt% H_2 by 400 °C, only losing 37% of that capacity after 5 re/de-hydrogenation cycles; rehydrogenation was carried out under 100 bar H_2 at 600 °C.

2.7.3.5 $LiBH_4$ + $LiNH_2$

Aoki et al. 2005 investigated the potential of a $LiBH_4$ + $LiNH_2$ system created via ball milling of $LiBH_4$ and $LiNH_2$ under an Ar atmosphere for 1 h (2:1 molar ratio) resulting in the formation of an unknown phase. This phase was found to desorb 89 % (10.6 wt%) of its H_2 capacity at 250 °C forming Li_3N-BN and Li_3BN_2, almost 40 °C below the melting temperature for pure $LiBH_4$.

2.7.3.6 $LiBH_4$ + $MgBH_4$

Z.-Z. Fang et al. 2010 balled milled $LiBH_4$ with $Mg(BH_4)_2$ with a molar ration of 1:1 for 10 h. The resultant material was found to a mixture of the starting materials long with a new phase believed to be a dual cation borohydride. The resultant mixture was found to desorb H_2 at 240 °C, 30 °C and 170 °C lower than expected for $Mg(BH_4)_2$ and $LiBH_4$ respectively, over 9 wt% H_2 was desorbed by between 200 and 370 °C. However, complete rehydrogenation could not be achieved under 100 bar H_2 at 400 °C. The rehydrided sample exhibited a capacity of 2.5 wt% corresponding to the formation of MgH_2 as confirmed by XRD.

2.7.4 Size and Interface Reactions

The introduction of nano-sizing in hydrogen storage materials has been shown to be an effective way of reducing the temperatures and pressures required for re/de-hydrogenation arising from smaller diffusion distances and a greater influence from surface energy effects (Roduner, 2006; Fichtner, 2011; de Jongh et al., 2013) In this section the effect of high surface area additives, nano-sizing and nano-confinement on the re/de-hydrogenation of $LiBH_4$ are examined.

2.7.4.1 High surface area additives

A number of high surface carbon based materials have been added to $LiBH_4$ successfully lower the decomposition temperature of $LiBH_4$ and are discussed below.

2.7.4.1.1 Carbon Nanotubes

MWCNTs (C_{nano}) were ball milled with $LiBH_4$ for 1 h under an Ar atmosphere with various $LiBH_4$:C_{nano} ratios. A ratio of 2:1 was found to be optimum. The onset of H_2 desorption of $LiBH_4$ was decreased from 380 °C to 250 °C with 100% of H_2 content being desorbed by 600 °C. XRD patterns of dehydrided samples showed reflections consistent with Li_2C_2, LiOH and C. The formation of Li_2C_2 indicated that MWCNTs destabilise both $LiBH_4$ and LiH, since the decomposition temperature of LiH is around 600 °C. Similar results were seen by Ichikawa et al. (2005) as discussed in Section 2.4.3.2. Partial recombination to LiH was achieved under 100 bar H_2 at 400 °C equating in a decrease in storage capacity of over 75%. Reformation of $LiBH_4$ could not be achieved under the stated conditions.

2.7.4.1.2 Activated Carbon

Cahen et al. 2009 pre-melted $LiBH_4$ into activated carbon with a pore size < 2 nm at 280 °C under an Ar atmosphere (no evidence was supplied to support the claim of successful melt-infiltration) as a comparison material for their study of $LiBH_4$ in porous carbons, reporting a total of 2 wt% H_2 desorbed by 600 °C with a loss of over 30% of this total capacity after three re/de-hydrogenation cycles. Rehydrogenation was carried out under 100 bar H_2 at 400 °C.

2.7.4.1.3 C_{60}

Wellons et al. 2009 studied the addition of C_{60} on the de/re-hydrogenation reaction of $LiBH_4$. C_{60} and $LiBH_4$ (1.6 mol%) was mixed with tetrahydrofuran (THF) and stirred for one hour. The solvent was then removed under vacuum producing a C_{60} + $LiBH_4$ composite, this ball-mill free method of mixing was chosen to preserve the structure of the C_{60}. The hydrogen

desorption temperature of $LiBH_4$ was shown to be 80 °C lower compared to pure $LiBH_4$, the sample desorbed over 9 wt% after 2 h at 350 °C. Rehydrogenation was carried out under 120 bar H_2 at 350 °C resulting in a capacity of 4.2 wt%, the large reduction in capacity was speculated to be a result of the formation of stable intermediates.

2.7.4.1.4 Nanostructured Graphite + $LiBH_4$

Zhang et al. 2012 reported the potential of a hydrogenated nanostructured graphite + $LiBH_4$ sample prepared via ball milling under a hydrogen atmosphere that was capable of desorbing 9.3 wt% by 500 °C.

(Zhang et al., 2013) investigated the influence of milling graphite with $LiBH_4$ through density-functional theory calculations, predicting a favourable reaction between $LiBH_4$ and graphite nano-fragments. Unsaturated sites introduced by graphite nano-fragments (e.g. chains or rings of carbon atoms) inserted into the interstitial sites in $LiBH_4$ are favourably occupied by BH_3 complexes and H atoms, the dehydrogenation energy of BH_3 – C complexes (1.99 eV for carbon rings inserted into $LiBH_4$) was calculated to be lower than that for pure $LiBH_4$ (2.54 - 2.69 eV).

During the writing of this thesis, Wang et al., 2016 published a study on nanostructured graphite mixed with $LiBH_4$. Graphite was first ball milled under 10 bar Ar for 8 h resulting in the formation of nano-crystalline graphite and an increase in the surface area (calculated by BET) from 3.9 m^2g^{-1} to 324 m^2g^{-1} both of which are consistent with this work. $LiBH_4$ was then added at weight ratio of 1:1 and re-milled, no duration was given for this second milling procedure. The resulting graphite + $LiBH_4$ mixture begin to desorb H_2 above 250 °C with

peak H_2 desorption ca. 350 °C, however, both CH_4 and B_2H_6 were detected at 275 °C. The presence of CH_4 during decomposition clearly shows an interaction between the nano-structured graphite and $LiBH_4$. It was concluded that nano-sized graphite may act as a milling aid in the reduction of $LiBH_4$ particle size during ball milling and that an interaction between $LiBH_4$ and nano-sized graphite gave rise to impurity gas release (B_2H_6 and CH_4). Pristine graphite was shown to not have the same effect upon the decomposition temperature of $LiBH_4$ as nanostructured graphite suggesting it the structure of the additive that influences the decomposition reaction, not the material itself.

2.7.4.2 Nano-sizing

Nano-sizing of metal particles is known to change the physicochemical properties of a material (de Jongh et al., 2013; Roduner, 2006; Fichtner, 2011; Shao et al., 2012), an example of which is gold which changes from an inert metal to an excellent catalyst when its particle size is reduced to <3 nm (Roduner, 2006).

The effects of nano-sizing are a result of the large increase in the fraction of atoms at the surface of the particle, known as the dispersion. The number of atoms (N) in a sphere of radius r is directly proportional to the volume of the sphere (V), whereas the surface area is proportional to the r^2 and the volume to r^3. However the dispersion is proportional to the surface area divided by the volume and is thus abides by the relation $N^{-1/3}$ (Roduner, 2006).

In nano-sized particles, the majority of atoms are located on the surface with interior atoms located near to the surface. This arrangement of atoms allows for rapid H_2 uptake and release kinetics since diffusion distances are minimal (de Jongh et al., 2013).

Nano-sizing of MgH_2 has been shown to be an effective way of reducing temperatures required for de/re-hydrogenation (Huot et al., 1999). Ball milling Mg_2H_2 for 20 h was found to lower its desorption by 64 °C. The ball-milled sample was also able to fully absorb (at 300 °C) and desorb (at 350 °C) H_2 five times quicker than the unmilled sample.

2.7.4.3 Nano-confinement

Nano-confinement is another way of inducing the nano-scale effects discussed above. The nano-confinement of hydrogen storage materials has been shown to be an effective route to lowering the required temperatures and pressures required for de/re-hydrogenation (Vajo, 2011; Liu et al., 2010; de Jongh et al., 2013). The reasoning behind these effects originates from the increase in surface energy which is inversely proportion to particle size (Fichtner, 2011) (as explained above). Interactions between the scaffold and material surface may also interact chemically affecting to the total energy of the system along with elastic restraints imposed upon the confined material (Fichtner, 2011; Baldi et al., 2009).

2.7.4.4 Melt-infiltration

Melt-infiltration is the process by which a material (A) is heated above its melting temperature in the presence of a porous host material (B). The melted material then fills the pores through capillary action. The result is a host material (B) with material (A) confined within its pores. Nano-confinement of metal hydrides has been shown to be an effective way of altering the thermodynamics of a confined material, resulting in reduced decomposition

temperatures (Fang et al., 2010b; Ngene et al., 2010; Liu et al., 2011; Shao et al., 2014; Capurso et al., 2012).

2.7.4.5 Nano-confinement of $LiBH_4$

Nano-confinement of $LiBH_4$ can be achieved through melt-infiltration. $LiBH_4$ is heated to just above it's melting temperature (~285 °C) under an over pressure of hydrogen. The application of a 3 bar H_2 over pressure during heating is known to suppress the decomposition of $LiBH_4$ (Pinkerton et al., 2007), molten $LiBH_4$ is then drawn into the pores of the scaffold material via capillary action (Gross et al., 2008), resulting in the confinement of $LiBH_4$ within a host material.

The successful confinement of $LiBH_4$ within the porous host is inferred from a loss in long-range ordering of $LiBH_4$, seen as the disappearance of reflections from o-$LiBH_4$ at room temperature after melt-infiltration (Gross et al., 2008) along with a large decrease in the measured surface area and pore volume of the host scaffold (Ngene et al., 2010; Liu et al., 2010, 2011; Shao et al., 2014).

2.7.4.5.1 Porous Silica + $LiBH_4$

As discussed in section 2.7.2.1, SiO_2 has been shown to destabilize the decomposition of $LiBH_4$. Ngene et al. (2010) investigated the confinement of $LiBH_4$ within a porous silica scaffold (SBA-15), a reduction in the pore volume of the SBA-15 was observed after melt-infiltration under 180 bar H_2 at 295 °C inferred the possible confinement of $LiBH_4$ within the

porous structure, which kept its original structure as indicated by XRD. Decomposition of the melt-infiltrated sample showed an impressively low onset of hydrogen release of 150 °C, however the formation of Li_2SiO_3 and Li_4SiO_4 eliminated the possibility for reversibility. The proposed decomposition pathway is shown below in equation 2.11.

$$6LiBH_4 + SiO_2 \rightarrow 2Li_2SiO_3 + Si + 4B + 2LiBH_4 + 8H_2 \quad (2.11a)$$

$$\rightarrow {}^{3}/_{2}Li_4SiO_4 + {}^{1}/_{2}Si + 2B + 4H_2 \quad (2.11b)$$

2.7.4.5.2 Porous Carbons + $LiBH_4$

(Zhang et al., 2007) combined nano-sizing and nano-confinement of $LiBH_4$ and subsequently were able to lower the decomposition of $LiBH_4$ through ball milling with a mesoporous templated carbon (CMK-3) (1:1 weight ratio), an ordered mesoporous carbon, for 5 h at 450 rpm under 30 bar H_2. TEM analysis of the milled sample indicated complete destruction of the porous framework, with $LiBH_4$ nanoparticles (~ 5 nm in diameter) embedded within the collapsed carbon framework. The composite desorbed over 7 wt% H_2 by 600 °C with bulk desorption occurring at 332 °C, 83 °C lower than they reported for pure $LiBH_4$. Rehydrogenation was demonstrated as being feasible under 30 bar H_2, a reported 3 wt% was absorbed within 500 min. Li_2C_2 was observed by XRD in the dehydrided phase, leading to a proposed dehydrogenation pathways shown in Equation 2.12.

$$LiBH_4 \rightarrow LiH + B + H_2 \quad (2.12a)$$

$$LiBH_4 + C \rightarrow Li_2C_2 + B + H_2 \quad (2.12b)$$

$$LiH + C \rightarrow Li_2C_2 + H_2 \quad (2.12c)$$

Zhang et al concluded there were two key mechanisms responsible for the improvement observed in the re/de-hydrogenation of $LiBH_4$ mixed with mesoporous carbon. Nano-dispersion was reported to influence thermal stable tailoring of $LiBH_4$ and reduce diffusion distances whilst the mesoporous carbon framework served as a reactive agent for decomposition.

Gross & Vajo 2008 melt-infiltrated 25-30 wt% and 45-50 wt% $LiBH_4$ into carbon aerogels with pore sizes of 13 nm and 25 nm respectively, calculated from Brunauer-Emmett-Teller (BET) and Barrett-Joyner-Halenda (BJH) methods (Lowell et al., 2004). The dehydrogenation rate was found to be 50 times greater for the 13 nm sample, with the sample desorbing 3.7 wt% H_2 by 400 °C (corresponding to 91% of the samples total H_2 capacity), < 0.2 wt% CH_4 was detected during decomposition but no B_2H_6 was found to be released. $LiBH_4$ was successfully recombined under 100 bar H_2 at 400 °C as confirmed by the reappearance of reflections from o-$LiBH_4$ in XRD measurements, however, the cyclic capacity was found to reduce by 40 % after 3 cycles possibility resulting from the degradation of the carbon scaffold.

Mesoporous carbon (manufactured by templating of SBA-15 resulting in a pore size of 4 nm) impregnated by $LiBH_4$ via incipient wetness method was studied by Cahen et al. 2009. The sample was found to desorb 4 wt% H_2 by 500 °C (82% of the theoretical capacity based on the formation of LiH and B) with decomposition ca. 335 °C. No diborane was detected. Rehydrogenation attempts under 100 bar H_2 and 300 °C were unsuccessful.

Liu et al. 2010 melt-infiltrated $LiBH_4$ into highly order porous carbon with a pore size of 2 nm under 60 bar H_2 at 300 °C, BET analysis of the sample showed a significant decrease in the

surface area of the carbon (594 m^2g^{-1} to 116 m^2g^{-1}) after the melt-infiltration process suggesting $LiBH_4$ was successfully confined within the pores of the scaffold material. The onset of hydrogen desorption was found to reduce to 220 °C with no DSC peaks consistent with the orthorhombic to hexagonal phase change or melting of $LiBH_4$ observed, suggesting a high level of disorder was induced as a result of nano-confinement. No attempts at rehydrogenation were reported.

2.7.4.5.3 Zeolite templated carbon + $LiBH_4$

(Shao et al., 2015) successfully nano-confined $LiBH_4$ inside of a densified zeolite template carbon. ZTC with a surface area of 3596 m^2g^{-1} was synthesised from zeolite 13X and densified under 750 MPa for 20 min resulting in a surface area of 3309 m^2g^{-1}. The resulting ZTC was then hand ground before being melt-infiltrated at 300 °C under 140 bar H_2 for 30 min. The densified ZTC+$LiBH_4$ was calculated to have a hydrogen content of 6.92 wt%, releasing hydrogen 181 °C lower than pure $LiBH_4$. Rehydrogenation was achieved at 260 °C under 120 bar H_2 for 12 h, with the reformation of $LiBH_4$ confirmed by XRD and FTIR. The composite was subjected to 5 re/de-hydrogenation cycles; the H_2 capacity after the 5th cycle was measured to be 56% of the original capacity of the composite. This reduction was speculated to be a result of the formation of $Li_2B_{12}H_{12}$ as seen by NMR.

2.7.4.5.4 Effect of nano-confinement of $LiBH_4$ on diborane

The nano-confinement of $LiBH_4$ within porous carbon with a pore size of < 15 nm has been shown to reduce the quantity of diborane released during decomposition of $LiBH_4$ (Liu et al., 2011), with pores <2nm reported to fully suppress/eliminate the evolution of B_2H_6 during

decomposition (Liu et al., 2010), however, the same sample was shown to release B_2H_6 when not subject to the melt-infiltration process.

Diborane release was also found to be suppressed during the decomposition of $LiBH_4$ confined within porous carbons with pore sizes of 13 nm (Gross et al., 2008) and 3.8 nm (Cahen et al., 2009).

Kostka et al. 2007 reported diborane release from porous silica gel (3 nm pore size) milled with $LiBH_4$ but found the addition of 5 mol% of $LaCL_3$ or $TiCl_3$ to $LiBH_4$ prior to ball milling with the silica gel greatly reduced the quantity of B_2H_6 released during decomposition of $LiBH_4$.

2.7.4.6 Porous carbons + $LiBH_4$ + Additives

2.7.4.6.1 $LiBH_4$ + MgH_2

Fang et al. 2010 studied the potential of a $LiBH_4$ + MgH_2 + Activated Carbon (AC) composite prepared by ball-milling with the aim of reducing the incubation period associated with the decomposition of $LiBH_4$ + MgH_2 systems, discussed in Section 2.7.3.1. The addition of AC was found to promote the decomposition of the system reducing the wait time between the two decomposition steps by a factor of 4 to 3 h, this time could be further reduced to 2 h by melt-infiltrating $LiBH_4$ into the AC during fabrication of the composite. Isothermal desorption at 350 °C lead to 4.5 wt% H_2 being desorbed during the first decomposition step indicating partial decomposition of the $LiBH_4$ (the theoretical capacity from the MgH_2 in the system was 2.85 wt%). The cyclic capacity was shown to be stable with a total of 9 wt% H_2 storage

capacity achieved after 3 cycles, rehydrogenation was carried out under 100 bar H_2 at 350 °C. From these results it can be concluded that the infiltration of hydrides within activated carbon can greatly improve decomposition kinetics.

2.7.4.6.2 $LiBH_4 + Mg(BH_4)_2$

Capurso et al. 2012 investigated the effect of confinement on $LiBH_4$ and $Mg(BH_4)_2$ mixtures to see if the decomposition temperature could be further reduced when mixed with nano-structured graphite produced via ball-milling, concluding that graphite milled for 10 h had the greatest impact in reducing the hydrogen desorption temperatures of the mixtures.

2.7.4.6.3 $LiBH_4 + NbF_5$ nano-particles

As discussed in section 2.7.3.4, NbF_5 has been shown to be an effective catalyst in the decomposition of $LiBH_4$. As such, Shao et al. 2014 investigated the effect of confining $LiBH_4$ within a meso-porous carbon (with a pore size of 3.8 nm formed as an inverse replica of SBA-15 as described by Zhao et al. 1998) impregnated with 10 wt% NbF_5. SEM images along with a drastic reduction in the BET surface area of the porous carbon from 1321 m^2 to 33.58 m^2 indicated $LiBH_4$ was successfully melt-infiltrated and confined within the nano-pores under 140 bar H_2 at 300 °C. The onset of hydrogen desorption was found to be 225 °C than that of pure $LiBH_4$ occurring at 150 °C with peak H_2 release ca. 309 °C. No peak indicative of the melting of $LiBH_4$ was observed by DSC inferring the high lever of disorder induced by nano-confinement of $LiBH_4$. Reversibility of the sample was successful under 200 °C and 50 bar H_2, the reformation of $LiBH_4$ was confirmed by FTIR. The remarkable improvement on both the

decomposition and recombination conditions of $LiBH_4$ within the sample was attributed to a combination of the active species NbH_x and NbB_2 in the decomposition reaction (shown in equation 2.13) along with the function of F anions, high surface area carbon and nano-sized $LiBH_4$ particles.

$$2LiBH_4 + NbH_x \rightarrow 2LiH + NbB_2 + (3+{}^{x}/_{2})H_2 \qquad (2.13)$$

2.8 The Challenge

As discussed in this section $LiBH_4$ shows great promise as a H_2 storage material and the addition of high surface and porous carbon species are an effective way to reduce the decomposition temperatures and pressures/temperatures associated with reformation. Additional research is needed to further improve these required conditions and unlock the full potential of $LiBH_4$.

3 Aims

As outlined in the previous chapter $LiBH_4$ shows great promise as a hydrogen storage material with reduced decomposition temperatures and improved reversibility achieved via the addition of both high surface and high porosity materials. The key to unlocking $LiBH_4$'s full potential is reducing its decomposition temperature closer to that achievable on-board a vehicle (100 °C, opposed to those required for bulk $LiBH_4$ of >400 °C) and improving its hydrogen capacity over cycling. The aim of this thesis is to investigate the effect of stable additives with varying microstructures and compositions on the storage properties of $LiBH_4$. This thesis will focus on the gravimetric storage capacity of these samples with the aim of understanding the additives influences and effect on the decomposition pathway of $LiBH_4$.

The research objectives are as follows:

- To investigate the effect of cheap and abundant ball milled graphite on the hydrogen storage properties of $LiBH_4$.
- To investigate the differing effect, if any, of $LiBH_4$ ball milled with graphite under Ar compared to graphite milled under H_2.
- To investigate the effect of different porous materials on hydrogen storage properties of $LiBH_4$.
- To investigate the different effects of porous vs non-porous additives to $LiBH_4$.
- To investigate the effect of non-reactive additives on the suppression of B_2H_6 evolution during the decomposition of $LiBH_4$.

4 Experimental Methods

This chapter presents an overview of the experimental methods used for the work presented in this thesis along with a brief description of the underlying theories.

The experimental procedure can be broken down into 4 sections as shown in Figure 4.1, the experimental methods used at each stage are indicated. All measurements were repeated at least twice to ensure presented results were accurate and replicable. Results presented are from single measurements. Reported errors originate from the larger of intrinsic measurement errors and an average of discrepancies between multiple measurements such as a ± 0.1 wt% variance in weight loss between multiple measurements.

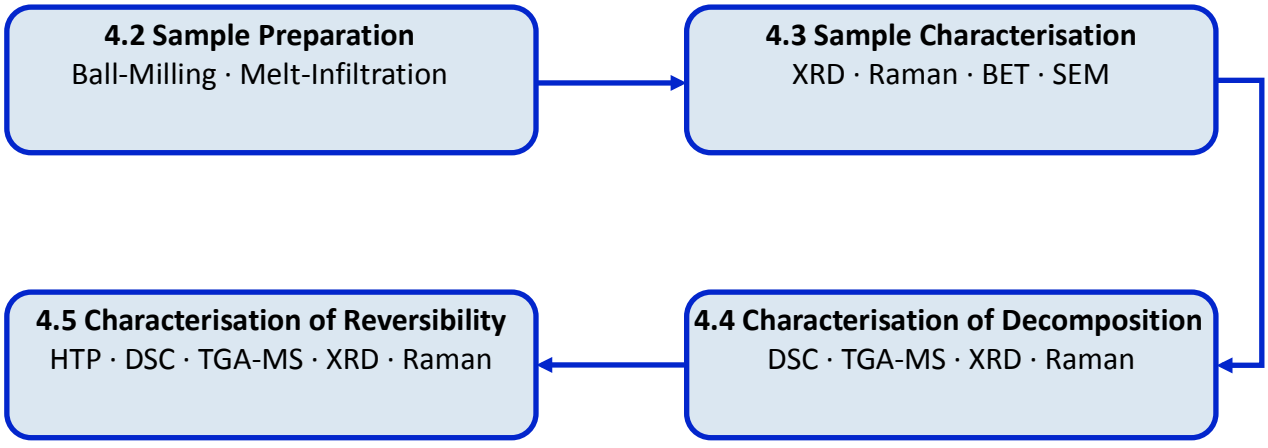

Figure 4.1 Schematic Diagram of Characterisation Process

All handling of samples was carried out inside a glove box with an inert argon (Ar) atmosphere (<2 ppm O_2) to try to avoid any reactions with oxygen or moisture in the air.

Samples were stored inside sealed Kilner jars inside the glove box. All samples were loaded/unloaded inertly (under and Ar atmosphere) into each instrument for measurements to be carried out.

4.1 Starting Materials

Table 1.1 shows a list of all starting materials including purity and particle size if known.

Table 4.1 List of starting materials used in this work

Material	Particle Size	Source	Purity	Notes
Graphite	325 mesh	Sigma Aldrich	>99.99%	Two different batches were used for the Ar and H_2 milled samples.
Activated Carbon (YAO)	325 mesh	Eurocarb		
Zeolite Templated Carbon	-	CSIR*, SA		1-2nm pore size (Musyoka et al., 2015)
Porous Silicon	Wafers 1-5mm long	Intrinsiq Materials		Porous silicon wafers created using electro chemical etching
Silicon nano powder	<100 nm	Sigma Aldrich	>98%	
$LiBH_4$	-	Sigma Aldrich	>95%	

*Council for Scientific and Industrial Research, South Africa.

4.2 Sample Preparation

All additives were first heated to 250 °C under a dynamic vacuum (10^{-6} bar) for 8 h to remove any moisture within the as-received samples.

Two samples were fabricated using the ball-milling preparation process, one milled under a 3 bar Ar atmosphere (as-prepared graphite Ar + $LiBH_4$) and one milled under a 3 bar H_2 atmosphere (as-prepared graphite H_2 + $LiBH_4$). The two samples used two different batches of Sigma Aldrich graphite (m325, >99.99%). Three samples were fabricated using the following method, activated carbon+$LiBH_4$, Zeolite templated carbon+$LiBH_4$ and porous silicon+$LiBH_4$. All samples were hand-mixed for 5 min inside an Ar filled glove box to create a mixture of additive+$LiBH_4$. A molar ration of 2:1 (additive:$LiBH_4$ was used for all samples).

4.2.1 Ball Milling

Impact ball milling of graphite has been shown to be an effective way of producing nanostructured hydrogenated graphite (Orimo et al., 1999; Chen et al., 2003; Fukunaga et al., 2004; Huang et al., 2007; Zhang et al., 2009). In this work a Retsch Planetary PM400 Ball Mill was used. Impact ball milling is a high energy process that provides an effective way of both reducing particle size and forming hydrogenated graphite (Orimo et al., 1999; Zhang et al., 2009). The planetary ball mill works by rotating the sun wheel in the opposite direction to the rotation of the milling pots, (a schematic of the milling process can be seen in Figure 4.2) resulting in a high-energy impacts on the sample in between the milling ball and the wall of milling pot.

Tungsten carbide (WC) was chosen as suitable milling media due to its inherent hardness, giving rise to less contamination during milling, consequently only WC and cobalt (used as a binder in the milling balls) can be considered as possible contaminants. As mentioned in Section 2.4.3.1, contaminants from milling such as Fe can affect the storage capacity of

graphite. To allow for a controlled study of the additives to $LiBH_4$ in this work, WC was used to eliminate the possibility of Fe contamination. The 250 ml milling pot is fitted with a pressure transducer allowing the pressure inside of the milling pot to be monitored. Figure 4.3 shows a photograph of the Tungsten Carbide milling pot.

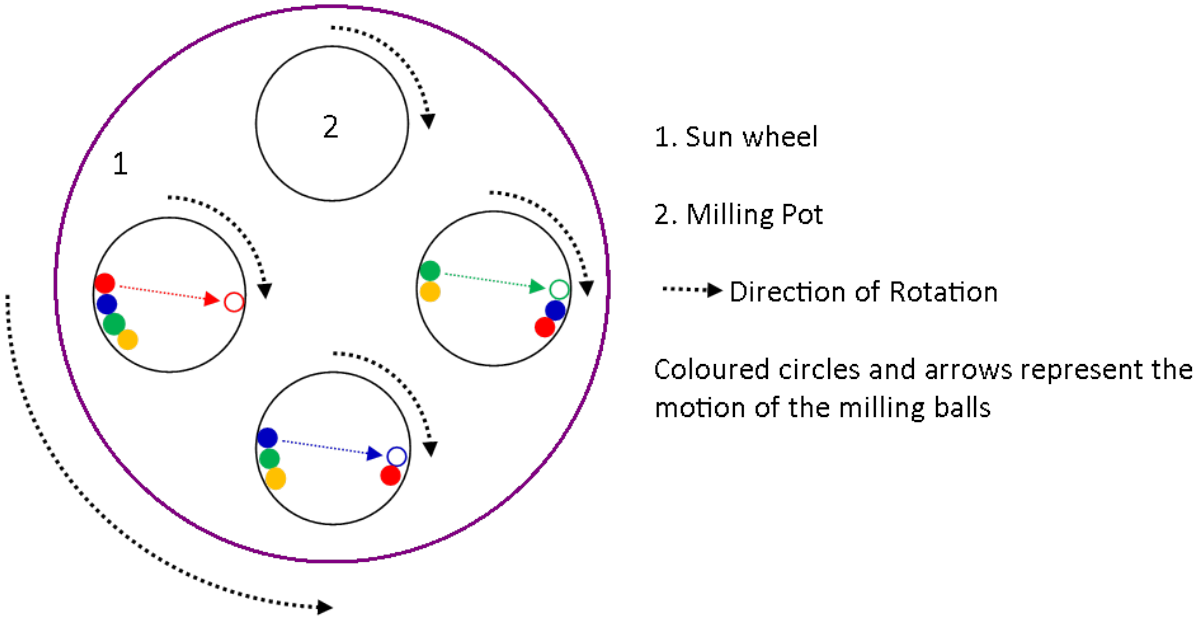

Figure 4.2 Schematic Diagram of Planetary Ball Mill and Motion of Milling Pots and Balls

The milling conditions chosen for the graphitic samples were those used by (Zhang et al., 2009) in order to maximise H_2 content whilst minimising CH_4 release (as discussed in Section 2.4.2). The graphite was weighed using a micro-balance accurate to ±0.001 mg and sealed inside the milling pot along with WC milling balls and removed from the glovebox; a mass ratio of the milling balls to sample was 13:1. The pot was charged with 3 bar of H_2 or Ar. The graphite was then subsequently milled for a total of 8 h at 280 RPM, however, in order to avoid temperature build up from the energy intensive milling process the sample was milled

periodically; 15 min of milling followed by 15 mill of rest. After each hour of milling, the pressure inside of the pot was checked using a pressure transducer, if the pressure had decreased to below 2.75 bar the pot was recharged to 3 bar.

After the graphite had been milled or 8 h, $LiBH_4$ was added to the graphitic samples at a molar ratio of (2:1) and the sample milled under for a further 2 h under the same conditions.

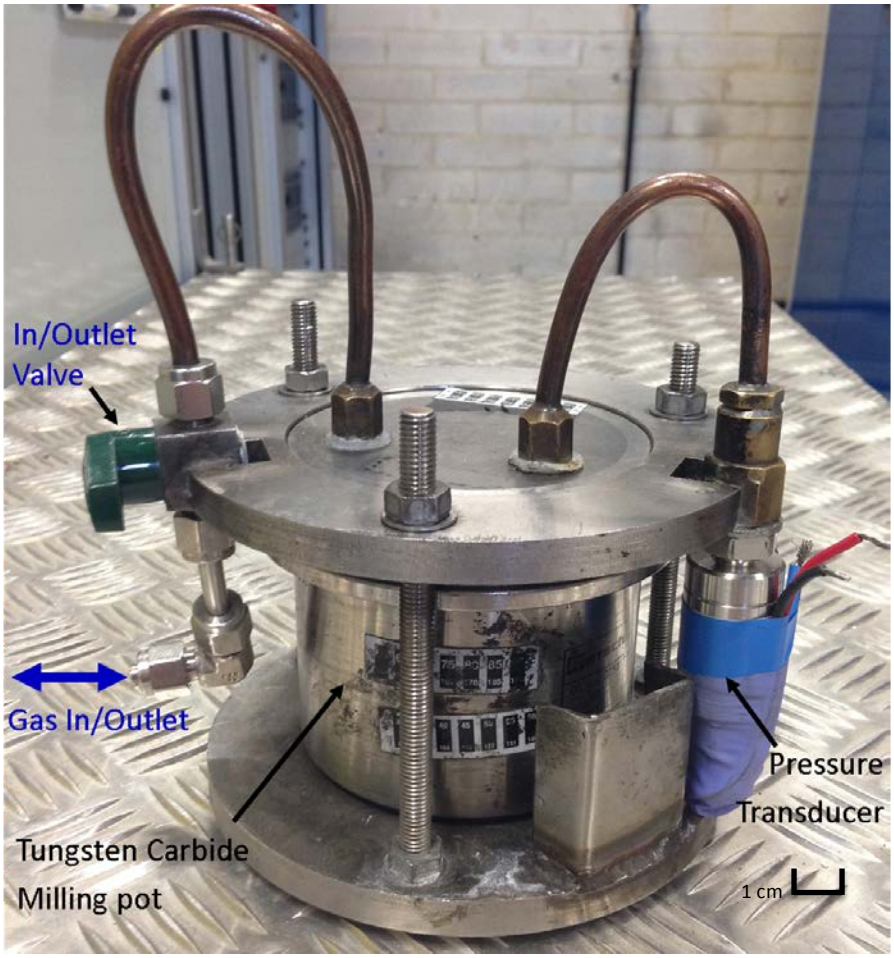

Figure 4.3 Tungsten Carbide Milling Pot and Pressure Transducer with approximate scale bar

4.2.2 Pre-Melting

The pre-melting of $LiBH_4$ into porous materials was carried out by first mixing $LiBH_4$ and the porous material together in a pestle and mortar. The mixed sample was then sealed inside a steel furnace tube and charged with 10 bar H_2. The sample was then heated to 300 °C at 2 °C.min^{-1} and held isothermally for 30 min before being cooled to room temperature. A 10 bar H_2 over pressure was chosen due to equipment limitations, however, a 3 bar H_2 over pressure has been shown to suppress the deocmposition of $LiBH_4$ (Pinkerton et al., 2007). Figure 4.4 shows a schematic diagram of the melt-infiltration apparatus. A 10 bar H_2 over pressure acts to suppress the decompostion of $LiBH_4$ to ensure the sample does not start to decompose during the melt-infiltration process . In this work “melt-infiltration” will refer to the process in which $LiBH_4$ is pre-melted under an over pressure of H_2 and cooled back to room temperature in order to form an intimate mixture of $LiBH_4$ and a host material. Melt-infiltration will not infer the successful confinement of $LiBH_4$ within the pores of a host material.

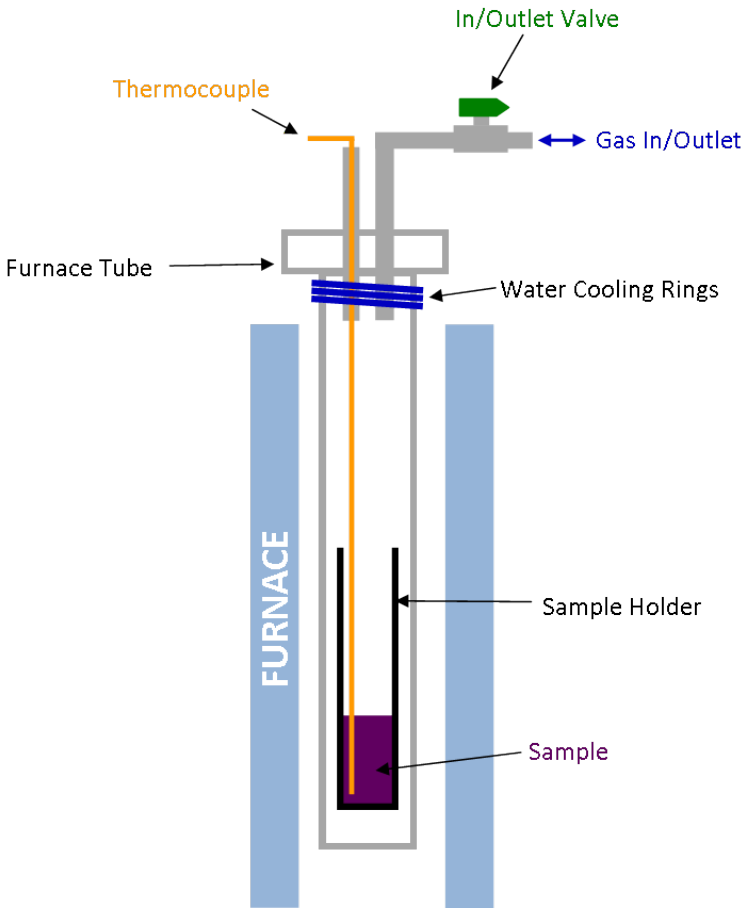

Figure 4.4 Schematic Diagram of the Melt-Infiltration Setup

4.3 Sample Characterisation

4.3.1 X-Ray Diffraction

4.3.1.1 Theory of X-Ray Diffraction and Bragg's Law

Solid-state matter can be grouped into two broad categories: crystalline materials and amorphous (non-crystalline) materials based upon the degree of long-range order. In an amorphous material atoms are arranged in random positions, thus lacking any long-range order. On the other hand, in crystalline structures atoms are arranged in a regular pattern,

and can be described by the unit cell, the smallest repeating volume/arrangement of atoms. Since the unit cell can be used to describe the atomic arrangement of any part of the crystalline material, the crystal lattice can be constructed through translational stacking of the unit cell.

X-ray diffraction is a non-destructive characterisation method that allows identification of crystalline phases within a sample. X-rays are a high-energy form of electromagnetic radiation with a wavelength comparable to that of the inter-planar distances of atoms (~1 Å). An incident beam of monochromatic X-rays can be elastically scattered (diffracted) from planes of atoms on the surface of a sample if the conditions of Bragg's Law are met, Equation 4.1; where λ = wavelength of incident X-ray, d = inter plane separation and θ = incident angle, as shown Figure 4.5.

$$n\lambda = 2d\sin\theta \qquad \textbf{(4.1)}$$

Consider two X-rays incident upon a sample (A and A') reflected by two adjacent planes of atoms, constructive interference will occur if the two waves are in phase (i.e. the extra distance travelled by A' is equal to a an integer multiple of the wavelength, $n\lambda$).

X-ray diffraction patterns are unique to each compound and thus can be used to identify what phase(s) is present in a sample.

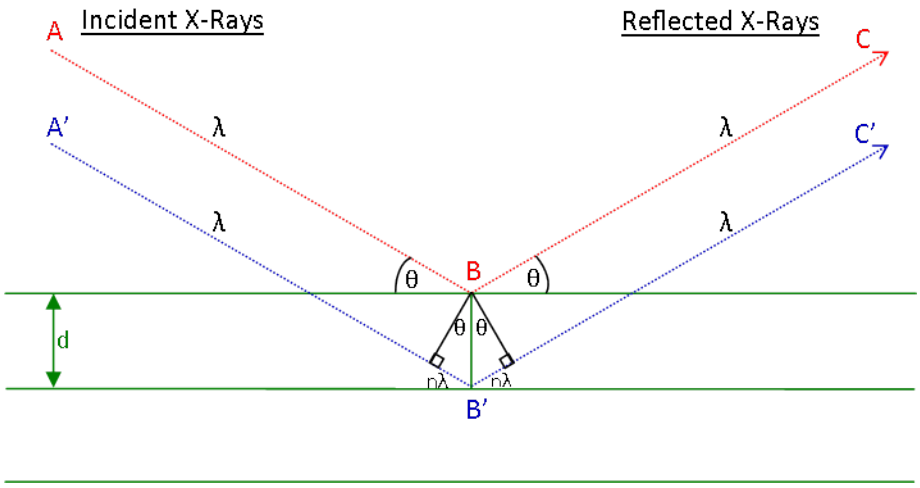

Figure 4.5 Bragg's Law

4.3.1.2 Room Temperature Powder X-Ray Diffraction

Powder X-ray Diffraction (PXRD) allows X-ray diffraction patterns of samples in powder form to be obtained. In the powder the crystallites can be orientated in any direction, therefore it is assumed that are an infinite number of crystallites are orientated in an infinite number of directions. Based on this assumption, all planes are orientated such that they can give rise to X-ray diffraction. Analysis of XRD patterns allows both qualitative and quantitative phase analysis, however, if the powder contains amorphous content, an internal standard must be used to account for the undetectable phase(s).

All PXRD measurements in this work were carried out using a Bruker D8 Advance Spectrometer with monochromatic Cu kα radiation (0.154 nm) and a Göbel mirror. Samples were rotated during measurements to reduce the impact of a non-level surface. The X-ray beam and detector both move around the sample as shown in Figure 4.6.

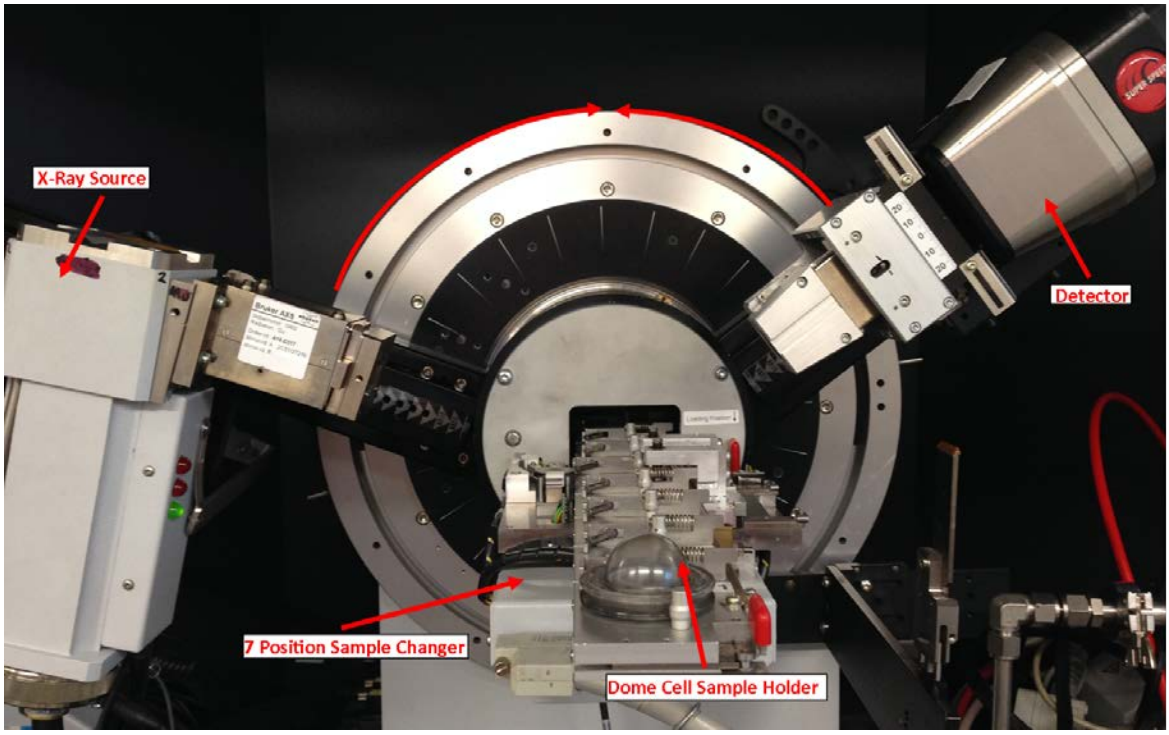

Figure 4.6 Bruker D8 Advance diffractometer with a 7-position sample changer and dome cell sample holder

For room temperature measurements samples were sealed inside of an X-ray transparent dome cell sample holder (as shown in Figure 4.6) whilst inside of the glovebox to eradicate sample exposure to moisture and air. Scan times ranged from 25 min to 210 min depending on the signal to noise ratio achievable for each sample due to amorphous/nanocrystalline content. The alignment of the D8 diffractometer was checked daily before samples were measured using an Al_2O_3 standard and the system re-aligned if necessary, ensuring an error margin of ± 0.005 ° 2θ.

For XRD measurements of as-received PS, the sample was first ground by hand for 30 sec to reduce the large flakes (~2 mm in diameter) to a finer powder which could be made flatter allowing for a better quality of measurement. An uneven sample leads to sample height

variation across the surface resulting in artificial peak shifts and intensities (the ideal average particle size for XRD analysis is 10-50 µm (Pecharsky and Zavalij, 2009).

4.3.1.3 In-situ Powder X-ray Diffraction

The decomposition pathway of samples was studied using in-situ PXRD allowing XRD patterns to be collected at increasing temperatures. An Anton Paar XRK900 XRD cell capable of heating samples from room temperature to 900 °C under helium or hydrogen at pressures ranging from 0 to 10 barg was used. The setup is shown in Figure 4.7. Typically, in-situ decomposition measurements were carried out under 3 barg He with a proportional-integral-derivative (PID) controlled flow with a heating rate of 2 °C.min^{-1}.

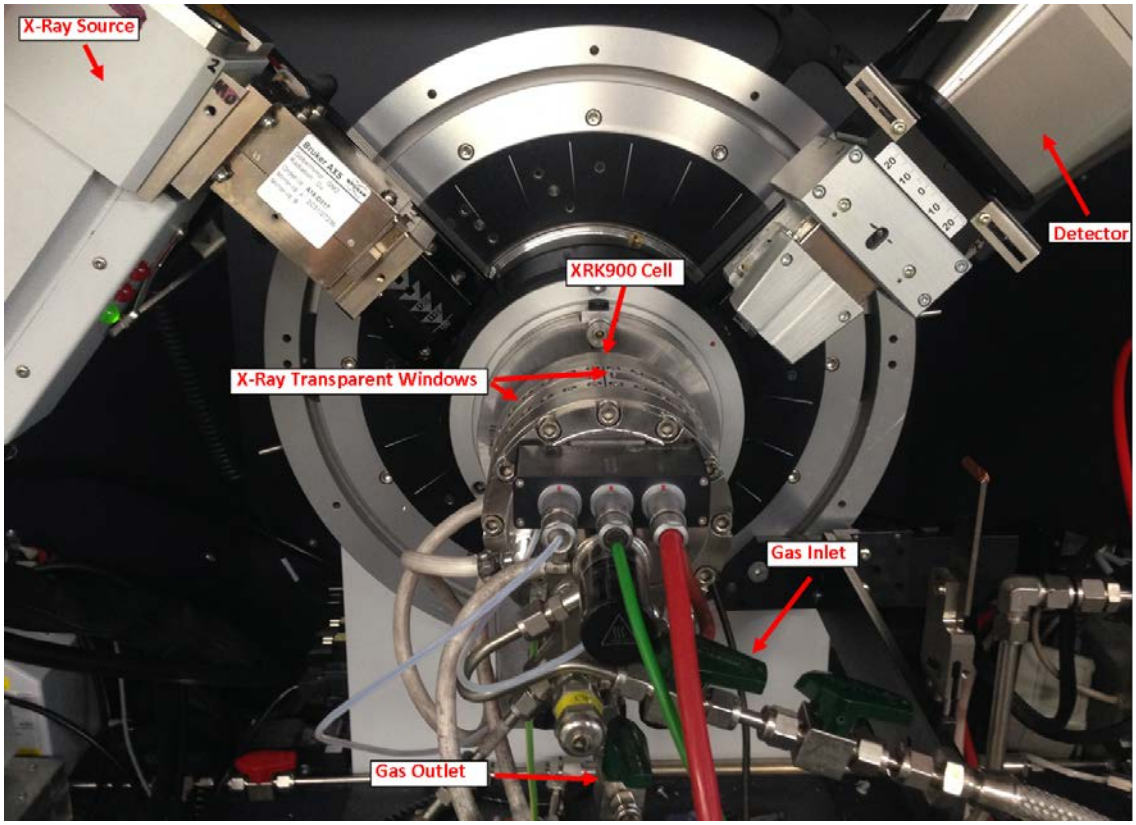

Figure 4.7 Bruker D8 Advance diffractometer with a XRK900 sample cell

4.3.1.4 Phase Identification

Phase analysis and identification was carried out using the software package EVA in conjunction with the PDF2 X-ray diffraction pattern database.

4.3.1.5 Crystallite Size

The crystallite sizes of graphite samples were calculated using the Scherrer equation discussed in Section 2.4.1.4. The intrinsic broadening was calculated by measuring the X-ray diffraction pattern of a highly crystalline corundum (Al_2O_3) sample used for calibration, the FWHM was calculated using peak fitting function in IGOR PRO. This value was subtracted

from the FWHM calculated using the same fitting software for all graphite samples. The 002 peak was used to determine the crystallite size due to its dominant intensity proving a high goodness of fit.

4.3.1.6 Partial Rietveld Refinement

Once phases have been identified Pseudo Rietveld refinement was carried out to calculate the lattice parameters of each phase present. Partial Rietveld refinement can also give quantitative phase analysis (Young, 1995), however this requires all phases in the sample to be crystalline and thus detectable by XRD. In this work it is believed amorphous phases may form upon decomposition of the samples (Reed and Book, 2009) and thus quantitative phase analysis could not be considered accurate.

4.3.1.7 Pawley Refinement

Unlike a partial Reitveld refinement in which intensity is bound to the structure, in a Pawley refinement the intensity is a free parameter and is not part of the fit (Cockcroft, 2006). A Pawley refinement allows the determination of lattice parameters but since intensity is not calculated, quantitative information cannot be inferred. For samples where obtaining a good partial Reitveld fit is not possible due to over lapping peaks, Pawley refinement offers an option to more accurately calculate the lattice parameters of phases present.

4.3.2 Raman Scattering Spectroscopy

4.3.2.1 Theory of Raman Scattering Spectroscopy

Raman scattering spectroscopy (Raman Spectroscopy for short) is a non-destructive spectroscopic technique that provides identification of phases and information on the bond

energies present in a sample and unlike XRD, Raman spectroscopy can be used to measure samples in a variety of states such as liquid, amorphous or nanocrystalline (Zhang, 2012).

Raman spectroscopy is based on the premise of interactions between photons and matter, which can result in either the photon being absorbed or scattered. Absorption spectroscopy occurs when the energy of an incident photon is equal to that of the band gap between the ground state and an excited state. If the energy of the photon is not equal to that of the band gap then scattering may occur.

Infrared absorption spectroscopy uses a beam of photons with a range of frequencies that can be absorbed whereas Raman spectroscopy uses a single wavelength laser. Raman scattering occurs when an incident photon interacts with a molecule distorting (polarizing) the electronic cloud around the nuclei forming a “virtual” short-lived state (Smith and Dent, 2005). Since the virtual state is instable, the electron cloud relaxes and emits a photon, it is changes in the energy of the scattered photon relative to the incident photon that is measured.

Most photons only polarize the electron cloud which requires a small amount of energy resulting in the release of a photon with an energy equal to that of the incident photon, this elastic scattering process is called Rayleigh scattering and is by far the most common.

If, however, the photon transfers enough energy to distort the electron cloud and induce motion into the nuclei, then the energy of the scattered photon will differ relative to the incident photon. This is referred to as Raman Scattering and is much weaker than Rayleigh scattering with one in every 10^6-10^8 photons scattering through this process.

If the virtual state decays to a state above the initial ground state, then the emitted photon will have a lower energy than the incident photon and is known as Stokes Raman scattering. The opposite occurs when an excited molecule decays to a state below the initial state resulting in the emission of a photon with a greater energy compared to that of the incident photon and is called Anti-Stokes Raman scattering. A diagram of the different types of scattering is shown in Figure 4.6.

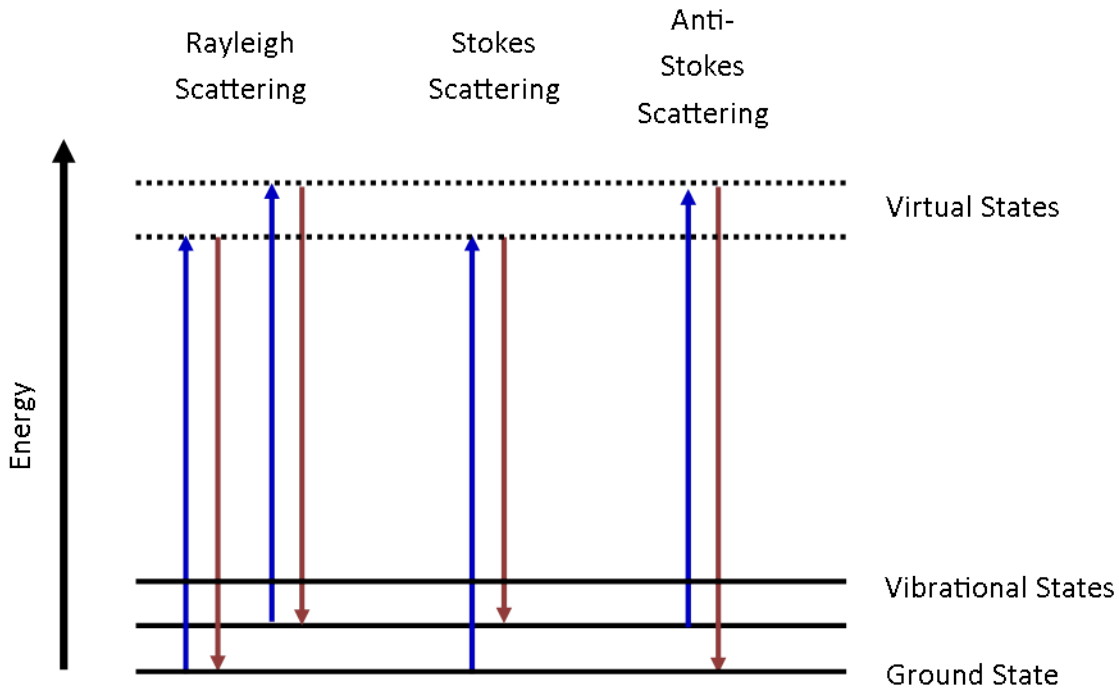

Figure 4.8 Schematic diagram of the Rayleigh and Raman Scattering Processes

Conventionally, photons are characterised by their wavelength, however in vibrational spectroscopy it is the interaction with the nuclei that is of interest hence it is easier to characterise the detected photons by their wavenumber or frequency which is directly proportional to their energy.

4.3.2.2 Raman Spectroscopy

In this work, a Renishaw InVia Reflex Raman Spectrometer was used with a 488 nm wavelength coupled with a 2400 lines/mm diffraction grating, a laser power of approximately 2 mW (on the sample) was used. The laser is focused through a series of high quality optics with the detected photons passing through a holographic notch filter removing any photons with a wavenumber of < 100 cm^{-1}. Each day the system was aligned prior to use with an internal neon light source and a silicon reference sample resulting in a measurement error of ± 0.01 cm^{-1}.

Samples were sealed inside of an Instec HCS621V sample cell inside of the glovebox. The cell was then transferred to the spectrometer and an Ar flow of 100 $ml.min^{-1}$ introduced to the cell. This process helps to avoid sample exposure to air to avoid any reactions with oxygen or moisture.

4.3.2.3 In-situ Raman Spectroscopy & Temperature Calibration

The Instec HCS6271V sample cell contains a heating stage used to heat samples at a rate of 2 $°C.min^{-1}$. The actual temperature experienced by the samples was calibrated by measuring materials with a well-defined and characterised phase change. The measured temperature vs. 'real' was then plotted and a conversion equation calculated and applied to all in-situ data.

4.3.3 BET Specific Surface Area (N_2 Adsorption Isotherms)

The Brunauer-Emmett-Teller (BET) method (Brunauer et al., 1938) is a widely used approach for the characterisation of Specific Surface Area (SSA) of powders and porous materials (Broom, 2011).

The BET method is an extension on the Langmuir theory in which an adsorbate is physically adsorbed (for more on physisorption see Section 2.3.1) onto a surface of an adsorbent, but instead of monolayer adsorption multilayer adsorption is simulated under the following assumptions:

1. No interaction between neighbouring molecules with an infinite number of layers possible
2. Adsorption occurs onto a flat energetically homogeneous surface

BET SSA measurements are typically made using N_2 adsorption isotherms at liquid nitrogen temperatures (77 K). The shape of the adsorption isotherms is indicative of the surface morphology and the number of layers adsorbed and can be characterised into 5 types of isotherm (Branauer, 1945).

N_2 adsorption isotherms were measured using a Hiden Analytical Intelligent Gravimetric Analyser (IGA) with BET SSA calculations carried out using the system software. Since the IGA could not be loaded inertly. Samples were transferred from the glovebox in a sample vial and only opened immediately before loading. Samples were sealed inside of the IGA furnace tube and heated to 150 °C at 5 °C.min^{-1} before being held isothermally for 60 min under a vacuum (~10^{-6} mbar) to remove any moisture that may have been adsorbed onto the sample surface during loading. The furnace was then removed and replaced with a liquid nitrogen

Dewar allowing the sample to be cooled to -195 °C (78 K) and the N_2 adsorption isotherms to be measured. Typical sample sizes ranged between 100-190 mg dependent upon the density of the measured sample.

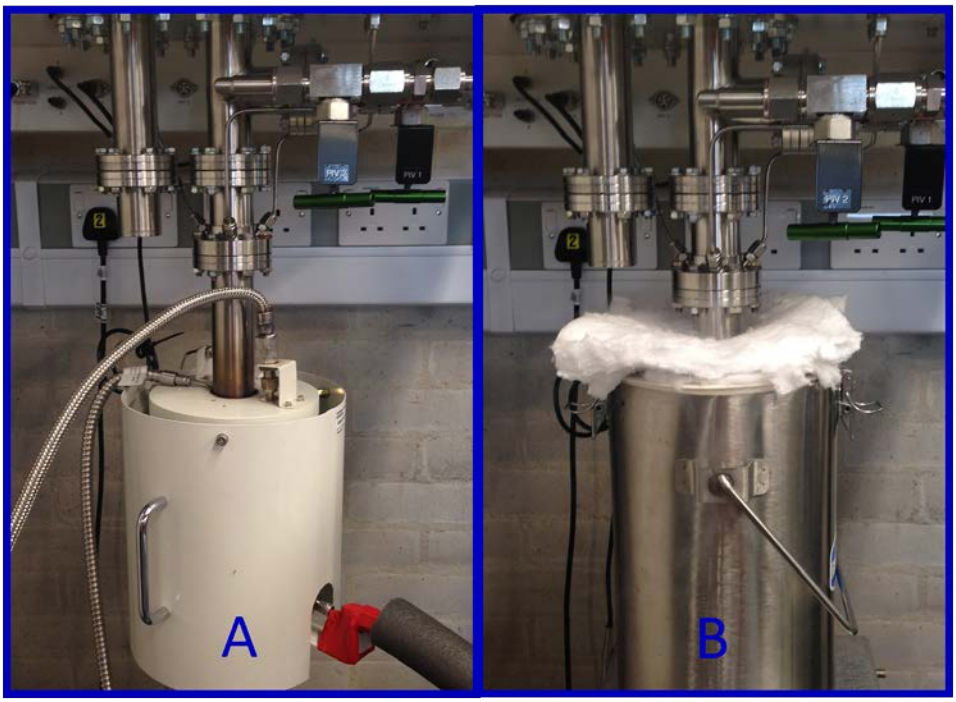

Figure 4.9 Hiden Analytical IGA setup for A) heating with furnace attached B) cooling with liquid nitrogen Dewar attached

Software provided by Hiden Analytical was used to calculate the BET surface area and associated errors, using a P/P_0 range of between 0.05 and 0.3; considered to be a valid range for the BET equation (Broom, 2011).

4.3.4 Scanning Electron Microscopy – Energy Dispersive (X-ray) Spectroscopy

Scanning Electron Microscopy is a type of electron microscopy in which a focused beam of electrons is focused on the surface of a sample. The electrons interact with the electron clouds of atoms on the surface of the sample and are subsequently scattered. The scattered electrons are detected and as the electron beam is scanned across the surface of a material, it is possible to build an image of the topology of the sample surface based on the intensity of detected scattered electrons at each point on the sample. The electron beam can cause charge build up on the surface of the sample and as such only conductive samples can be measured. Non-conditioning materials are coated with a thin conducting layer such as carbon, gold, palladium or platinum prior to measurement (Watt, 1997).

When an incident electron hits an electron in an inner shell transferring enough energy to eject the electron from the atom, a vacancy in the inner shell is left behind. An electron in a higher energy state (an outer shell) is then permitted to relax, dropping down to fill the vacancy in the inner shell and in the process it releases its excess energy in the form of an X-ray (Goldstein, 2003). Since the atomic structure (and thus the discrete electron energy levels) of each element is unique, the energy of emitted X-rays during electron bombardment of the sample can be used to fingerprint what elements are present in a material.

Since Energy dispersive X-ray Spectroscopy (EDS) relies on the interaction between incident electrons and those in the electron cloud surrounding an atom, the size of the electron cloud directly affects the probability of an interaction occurring. This means that light elements

such as H and Li which have 1 and 3 electrons in their clouds respectively, are much harder to observe via EDS than Si which has 14.

A JEOL 7000F SEM with Oxford Inca EDS was used examine the surface and edge morphology of porous silicon (PS). PS wafers were mounted on an aluminium stub using double-sided carbon tape inside of an Ar filled glove box. In order to study the edge of a PS wafer, samples were stuck perpendicular to the carbon tape and a minimal quantity of superglue used to fix them in place, this step could not be carried out under inside of the glove box so samples were prepared and transferred to the SEM as soon as the glue dried.

An Inca Oxford Energy Dispersive (x-ray) Spectrometer (EDS) was used in conjunction with a JEOL 7000F SEM to probe the elemental composition of the porous silicon samples.

4.4 Characterisation of Decomposition

4.4.1 Thermo-Gravimetric Analysis

Thermo-gravimetric analysis (TGA) is a thermal analysis technique that measures the mass of a sample as a function of temperature, allowing quantification of mass loss during a reaction such as decomposition. TGA was used in conjunction with Mass Spectroscopy (Section 4.4.2 for further information) to identify the evolution of gases corresponding to the mass loss.

In this work a Netzsch Iris 209 TGA was used inside of an Ar filled glovebox (O_2 < 10 ppm). The sample is placed inside of an Al_2O_3 sample holder and lid and placed onto the microbalance, the lid contains a pin-size hole allowing any gas evolved from the sample to

exit the system and flow to the MS for analysis. The system lid is then closed and Ar gas flowed over the sample at 40 ml.min^{-1}. Samples were heated to varying temperatures at a heating rate of 5 °C.min^{-1} unless stated otherwise. Figure 4.10 shows a schematic diagram of the TGA.

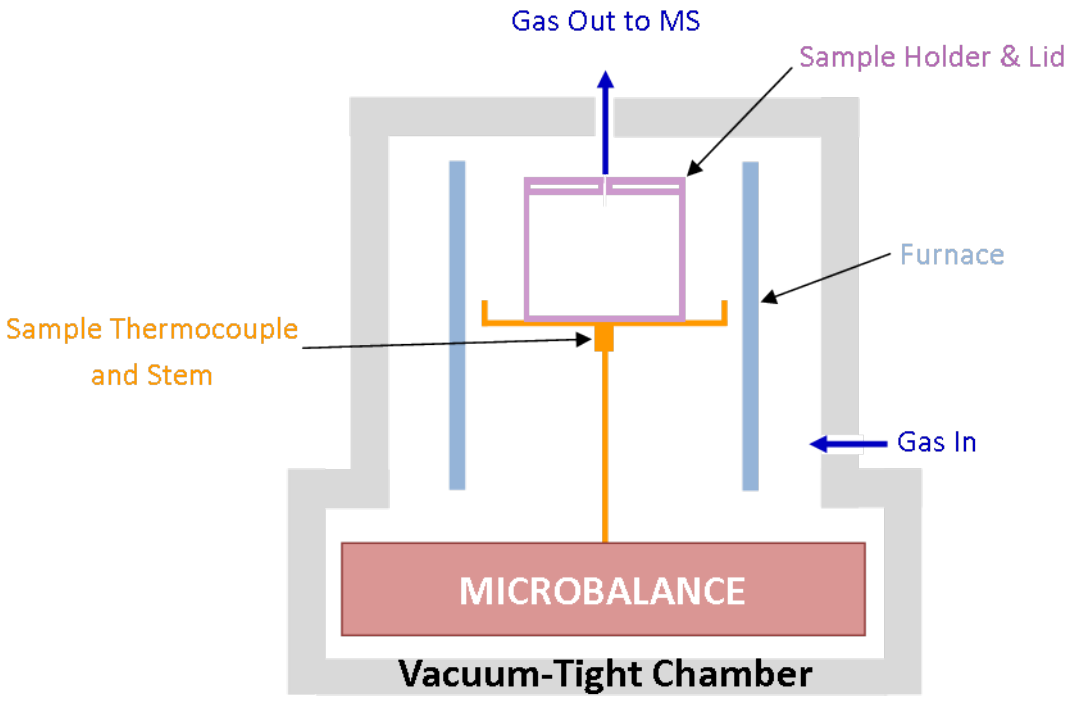

Figure 4.10 Schematic diagram of Netzsch 209 TGA setup

The TG thermocouple was calibrated using high purity metals: KNO_3, In, Bi, Sn, Pb and Zn. CaC_2O_4 was used to validate the thermocouple calibration (± 2 °C) and calibrate the microbalance to ± 0.01 mg. To minimise the effect of background signals and increase the sensitivity that can be achieved by the system, baseline measurements were taken under the same heating conditions to be experienced by a sample and the result subtracted from the measured run of the sample.

4.4.2 Mass Spectrometry

Mass spectrometry (MS) allows for the identification of gas phases through the measurement of the mass to charge ratio (m/z) of gas ions. In this work a Hiden Analytic HAL IV Quadrupole Mass Spectrometer was used in conjunction with a TGA (see section 4.4.1) to investigate what gases were released as function of temperature.

4.4.2.1 Quadrupole Mass Spectrometry

A quadrupole MS contains four rods each applied with a combination of a direct current (DC) and a radio frequency (RF) alternating current (AC). The rods are arranged in such that they can be considered as two sets of adjacent rods, with either set having the opposite polarity to the other, as seen in Figure 4.11. By altering the magnitude of the AC and DC currents applied to each set of rods, the electromagnetic field in between the rods can be manipulated such that only specific ions with an m/z value within a set range may pass through the quadrupole filter and continue to the detector, permitting the detection of pre-selected gas ions.

The Hiden Analytic HAL IV Quadrupole Mass Spectrometer contains two types of detectors, a Faraday cup and a Secondary Electron Multiplier. The Faraday cup is used for the detection of large concentrations of gas such as the carrier gas Ar, whereas the Secondary Electron Multiplier is much more sensitive and is used to detect lower concentrations of gas ions such as H_2 and B_2H_6.

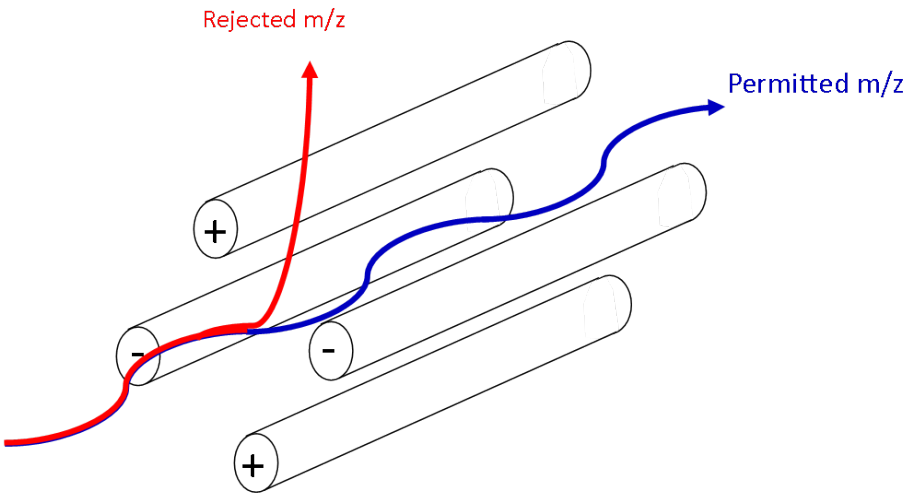

Figure 4.11 A schematic diagram of a quadrupole mass filter

In this work the following gas ion levels were monitored; hydrogen (m/z = 2, secondary electron multiplier (SEM) detector), diborane (m/z = 26, SEM detector), oxygen (m/z = 32, SEM detector), argon (m/z = 40, Faraday detector), water (m/z = 18, Faraday detector), methane (m/z = 16, SEM detector) for graphitic samples and silane (m/z = 30, SEM detector) for silicon based samples.

4.4.3 Differential Scanning Calorimetry

Differential scanning calorimetry (DSC) is a thermal analytical technique that measures the heat flow to sample allowing investigation into phase transitions within a sample and calculation of activation energies and enthalpies.

A reference sample and the sample to be measured are loaded into Al sample pans and placed onto sensitive heat flow sensors connected to thermocouples. As the temperature of the furnace is increased the temperatures of the two samples are measured. The

temperature measured for the empty reference sample will increase linearly as expected, however when a phase transition such as melting occurs in the sample, a process in which energy is required to break bonds, the temperature will appear to remain constant as the heat is used to break the bonds. After the phase transition is complete the temperature of the sample increases. Based on the difference in temperature profiles of the sample and reference the heat flow to the sample can be calculated. An exothermic peak will be seen for transitions that release energy such as crystallisation. Figure 4.12 shows a simplified diagram of the DSC setup.

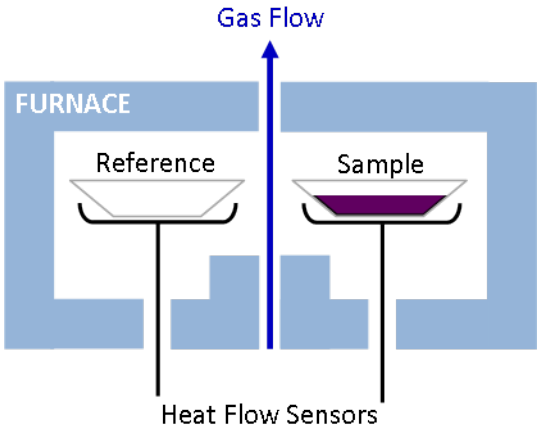

Figure 4.12 Schematic diagram of differential scanning calorimetry setup

In this work a Netzsch Phoenix 204 HP DSC was used. The gas flow to the sample was controlled using two mass flow controllers that allow a pressure gradient to be achieved across them, such that the sample can be measured at fixed pressures under a constant flow rate. Decomposition of samples was measured under 3 bar Ar with a constant flow rate of 100 $ml.min^{-1}$. A constant flow is required to ensure no hydrogen over pressure develops during the measurement, since this has been shown to suppress the decomposition process

of $LiBH_4$ (Pinkerton et al., 2007). Samples were heated to a variety of temperatures at a constant heating rate of 5 °C.min^{-1}. The DSC is located inside of an Ar filled glove box (O_2 < 10 ppm) allowing inert loading/unloading of the sample. Samples were placed into an aluminium sample holder and weighed prior to loading using a mass balance with a sensitivity of ± 0.001 mg.

Due to the high sensitivity of the DSC system, calibration must be carried out regularly. This is achieved by heating a series of high purity calibration samples that have a well-defined polymorphic phase transformation (In, Bi, Sn, Pb and Zn) from which both the sample temperature and heat flow sensitivity was calibrated resulting in a measurement error of ± 2 °C. In order to remove any background artefacts from the measured runs, baseline measurements were taken using an empty sample pan under the same conditions required for the sample measurement. Baselines were then subtracted from the measured run.

The bulk decomposition of $LiBH_4$ could not be studied in this work using DSC-TG-MS due to the foaming effect during decomposition. For comparison the DSC results published by Shao et al. (2014) of the decomposition of bulk $LiBH_4$ heated to 550 °C at a heating rate of 5 °C.min^{-1} are used for comparison (see Figure 2.17). The onset of H_2 desorption was identified to be 375 °C with peak H_2 desorption at 467 °C, no B_2H_6 evolution was observed during decomposition in this work.

4.5 Characterisation of Reversibility

4.5.1 Sieverts Method

The Sieverts method is a manometric method which uses the real gas law (Equation 4.2) to calculate a change in volume from the de/increase in pressure of the system where p is the pressure (Pa), V is the volume (m^3), T is the temperature (K), Z is the gas compressibility, n is the number of moles (mol) and R is the molar gas constant ($JK^{-1}mol^{-1}$) (Broom, 2011).

$$pV = nZRT \quad (4.2)$$

Figure 4.13 shows a schematic diagram of the Sieverts apparatus. The system is first evacuated by opening valves B and C, these valves are then closed and valve A opened, pressurising V_1 (of a known volume) to a set value that is measured by the manometer. Valve A is then closed and valve B opened leading to decrease in the pressure read by the manometer. This decrease in pressure is used to calculate the associated increase in volume and thus the volume of the sample. The Sieverts apparatus allows for isothermal decomposition and uptake measurements as a function of hydrogen over pressure, since H_2 uptake/release can be measured as at a series of different pressures.

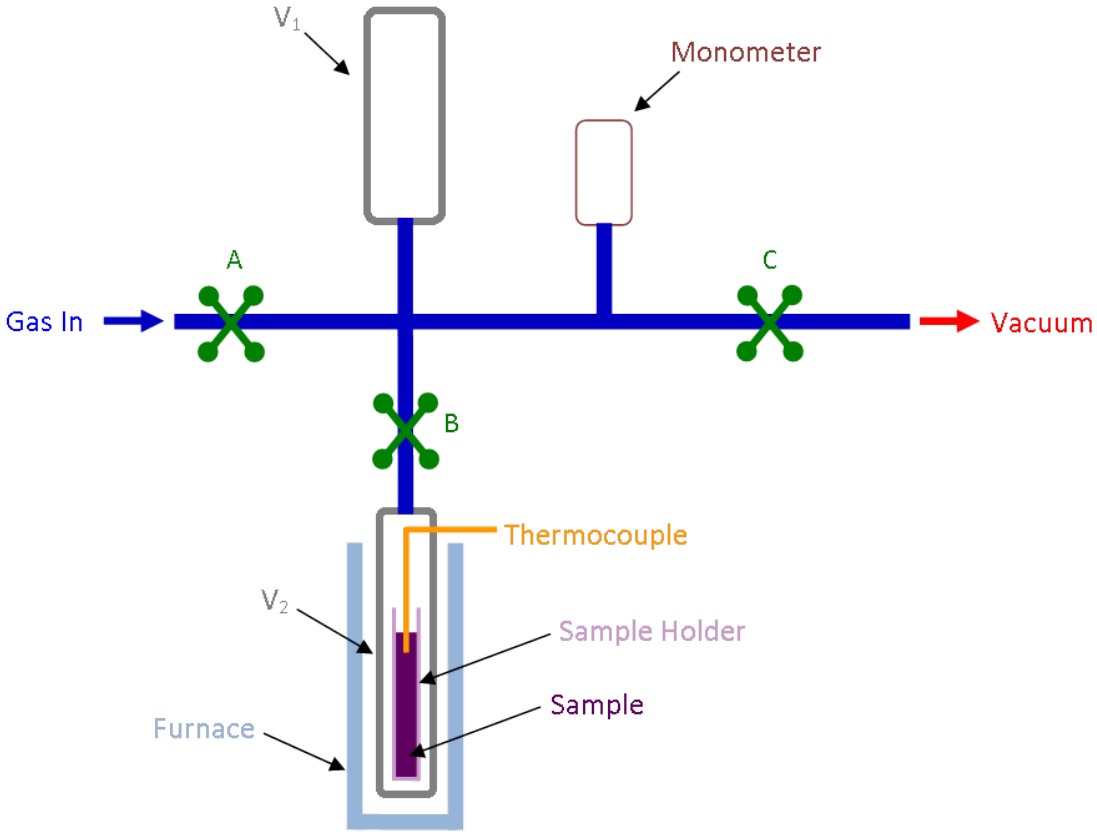

Figure 4.13 A Schematic diagram of a Sieverts apparatus

4.5.2 Isothermal H_2 desorption/uptake

In this work a Hiden Analytical HTP was used to carried out isothermal desorption and uptake measurements under hydrogen gas. Samples were placed inside a stainless steel sample holder and weighed before being transferred into an inert carrier. The carrier was placed inside of a portable glovebox that attaches to the HTP. The portable glovebox was flushed with Ar for 1 h prior to the sample being removed from the inert carrier and loaded into the HTP.

After the volume of the sample had been measured, the sample chamber was charged with 100 bar H_2 and heated to 350 °C. Isothermal H_2 desorption isotherms were then recorded as a function of decreasing pressure.

Hydrogen uptake measurements were carried out by first heating the samples to 350 °C and the H_2 pressure increased in steps.

4.5.3 Cyclic uptake/degradation

The cyclic storage capacity of the samples was investigated by repeating isothermal uptake/desorption measurements over 5 cycles. Samples were then removed from the HTP using the portable glovebox for further analysis such as XRD (see section 4.3.1) and Raman spectroscopy (see section 4.3.2). H_2 uptake measurements are accurate to ± 0.1 wt%.

5 Graphite (Ar) + $LiBH_4$

In this chapter the hydrogen storage potential of $LiBH_4$ added to nanostructured graphite ball milled under an Ar atmosphere is evaluated.

5.1 Characterisation of Graphite (Ar) + $LiBH_4$

The starting materials, 8 h milled graphite (Ar) and as-prepared graphite (Ar) + $LiBH_4$ were characterised by XRD, Raman Spectroscopy and N_2 adsorption isotherms (BET).

5.1.1 X-Ray Diffraction

Room temperature XRD patterns of the as-received materials, 8 h milled graphite (Ar) and as-prepared graphite (Ar) + $LiBH_4$ are shown in 5.1. The XRD pattern of as-received graphite (5.1a) exhibits an intense peak 26.4° 2θ due to reflections from the (002) plane within graphite. The (002) peak is characteristic of crystalline graphite due to the stacking of graphene layers perpendicular to the (002) direction.

After 8 h of ball milling the structure of the graphite can be seen to have changed, 5.1b. The (002) peak can be seen to broaden and decrease in intensity as a result of milling under Ar, this is a result of the reduction in the crystallite size of graphite and introduction of a

nanocrystalline structure. This was confirmed by calculation of the average crystallite size in the (002) direction via the Scherrer equation, results are shown in Table 5.1. It was not possible to determine the crystallite size for the as-prepared graphite (Ar) + $LiBH_4$ sample due to the number of $LiBH_4$ reflections in the region of the (002) graphite reflection making peak fitting highly inaccurate with the software available.

A very small downshift shift in the location of the (002) peak is also observed corresponding to an increase in the interlayer graphite separation which is associated with an increase in the inter-layer spacing in graphite, however, Pawley refinements of as-received graphite, 8 h milled graphite (Ar) and as-prepared graphite (Ar) + $LiBH_4$ are shown in Table 5.1 indicate no change within errors in the size of the c parameter as a result of milling. Since these calculations take into account alignment offsets, this small down shift is believed to be due to an error in the alignment of the equipment. Ball milling for longer periods of time (40 – 150 h) has been shown to result in expansion of the graphite layers as discussed in Section 2.4.2.

As-received $LiBH_4$ (5.1c) showed reflections consistent with the low temperature orthorhombic phase of $LiBH_4$ and no crystalline impurities.

The XRD pattern of as-prepared graphite (Ar) + $LiBH_4$ exhibits reflections from nanostructured graphite and orthorhombic $LiBH_4$ only indicating no additional phases were formed as a result of the high energy ball milling process. No crystalline contamination such as WC or Co was observed by XRD after the ball-milling process was detected via lab-based XRD in any of graphite samples milled under Ar, inferring any contamination that did occur was amorphous in nature or very low in quantity. Other experimental techniques with a

greater level of sensitivity such as NMR would be required to rule out contamination in this form. (Zhang et al., 2009) only saw WC contamination by lab based XRD after milling graphite for 40 h using the same milling media under the same conditions.

The lack of new phases suggests ball milling of graphite+$LiBH_4$ does not result in a solid-state chemical reaction between the two phases offering an effective way of producing nanostructured graphite and $LiBH_4$ mixture.

Table 5.1 Calculated c-direction lattice sizes from Pawley refinements and crystallite sizes calculated from the Scherrer equation using a *shape factor of K = 0.9

Sample	c-direction lattice parameter (Å)	*Crystallite size (nm)
As-received graphite	6.721 ± 0.001	52.3 ± 1.1
8 h milled graphite (Ar)	6.722 ± 0.002	13.0 ± 3.7
As-prepared graphite (Ar) + $LiBH_4$	6.727 ± 0.005	-

5.1.2 Raman Spectroscopy

The room temperature Raman spectra of the as-received materials, 8 h milled graphite (Ar) and as-prepared graphite (Ar) + $LiBH_4$ are shown in Figure 5.2.

The as-received graphite (Figure 5.2a) shows two prominent features, the G band located at 1580 cm^{-1} and a split peak above 2700 cm^{-1} known as the G' band. Both features are consistent with highly ordered pyrolytic graphite (Ferrari et al., 2006).

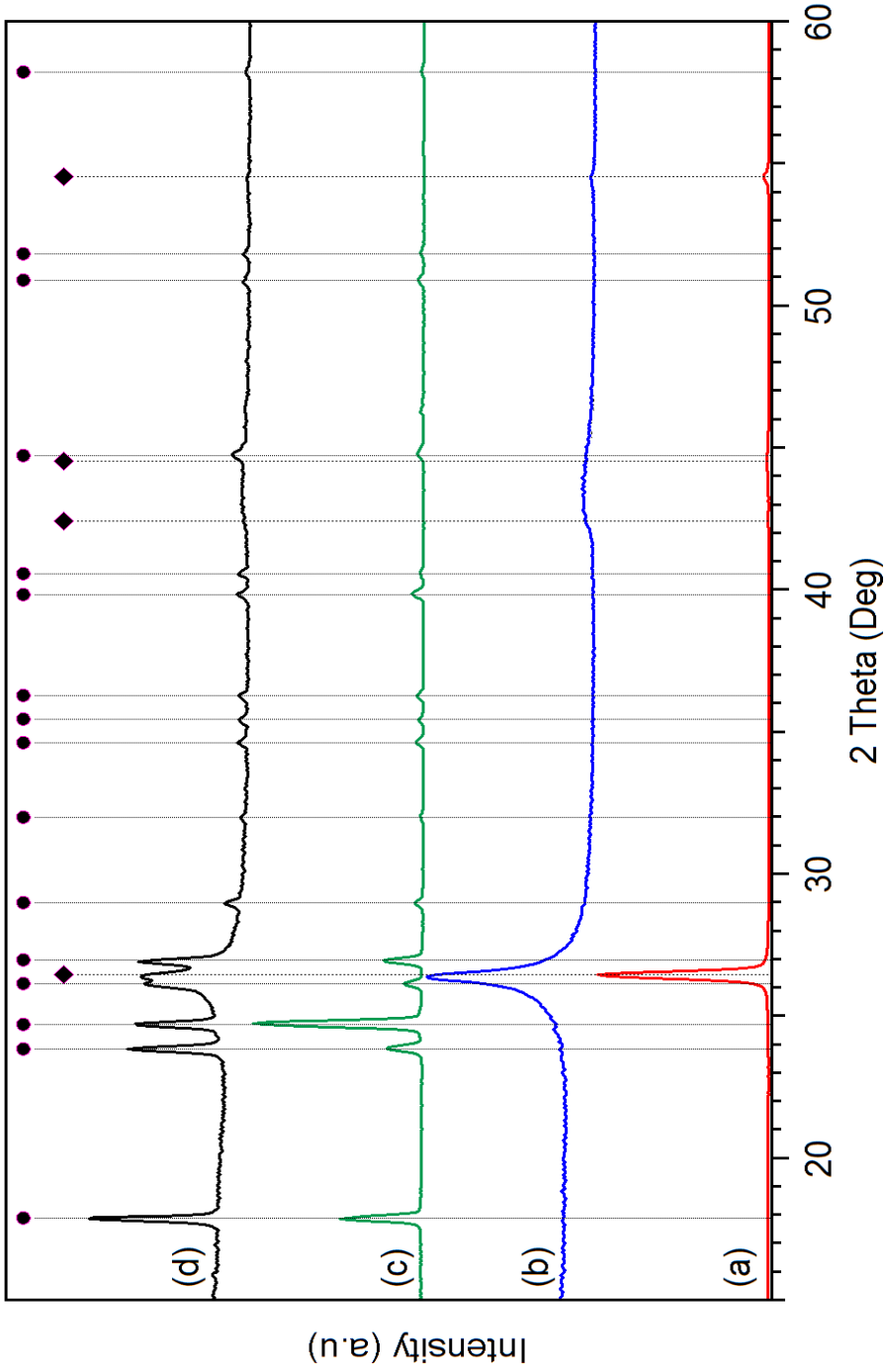

Figure 5.1 Room temperature XRD patterns of (a) as-received graphite, (b) 8 h milled graphite (Ar), (c) as-received $LiBH_4$ and (d) as-prepared graphite (Ar) + $LiBH_4$. Peak identities are indicated by dashed lines and markers; black diamonds signify reflections from graphite and black circles reflections from $LiBH_4$. The ICDD PDF2 database (2011) was used for phase identification

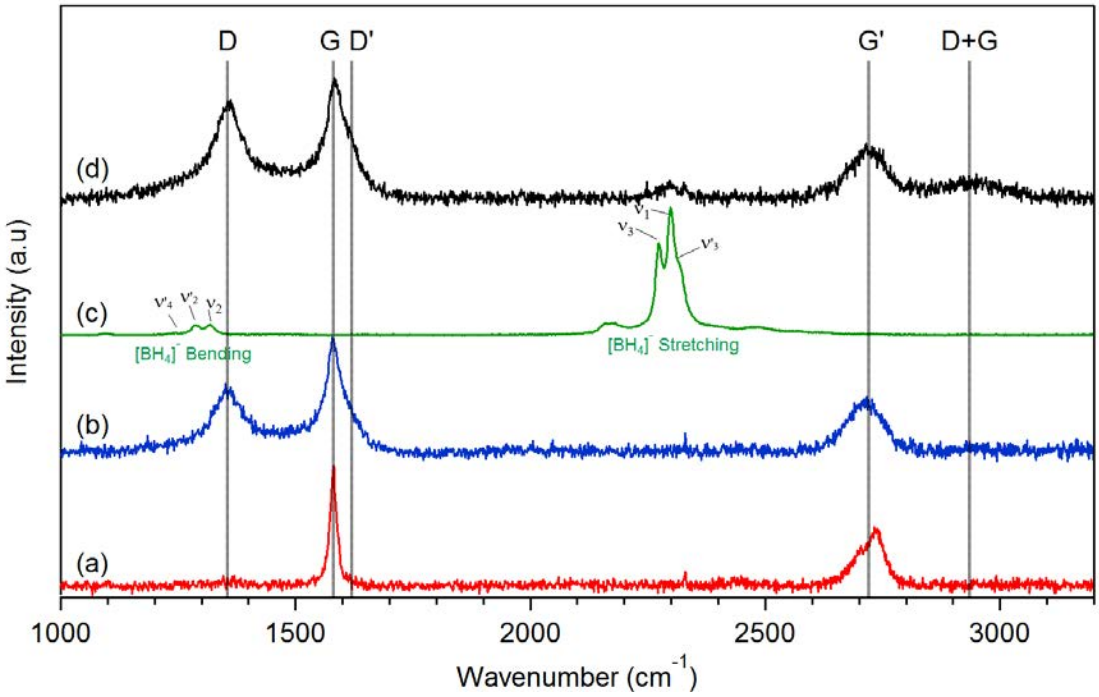

Figure 5.2 Room temperature Raman spectra of (a) as-received graphite, (b) 8 h milled graphite (Ar), (c) as-received $LiBH_4$ and (d) as-prepared graphite (Ar) + $LiBH_4$. The D, G, D', G' and D+G bands are marked by the black dashed lines (Ferrari et al., 2006)**. The $[BH_4]^-$ bending and stretching modes of $LiBH_4$ are labelled along with the origin of each vibration**

The Raman spectrum of graphite is significantly altered after 8 h of milling under Ar (Figure 5.2b) showing a new peak at 1357 cm^{-1} consistent with the breathing mode of the hexagonally arranged carbon atoms (A_{1g} symmetry) known as the D band of graphite. As discussed in Section 2.4.1.1 this band is forbidden by Raman selection rules becoming visible due to the introduction of defects within the graphitic layers. The intensity of the G band can also be seen to decrease with respect to the G' which can no longer be described by two lorentzian peaks. The shape of the G' band resembles that seen in turbostratic graphite in which the layers of graphite are stacked in random rotational orientations along the c axis (Malard et al., 2009). Another defect induced band can be seen 1620 cm^{-1} known as the D' band.

The Raman spectrum of $LiBH_4$ (Figure 5.2c) shows two prominent features corresponding to the bending and stretching of the $[BH_4]^-$ tetrahedral unit as expected for pure $LiBH_4$. Vibrations consistent with stretch of the $[BH_4]^-$ unit are observed in the as-prepared graphite (Ar) + $LiBH_4$ sample (Figure 5.2d) along with the D, G, D' and G' bands of graphite seen in the 8 h milled sample.

The in-plane correlation length of average crystallite size (La) for each graphitic sample was calculated using the generalised formula proposed by (Cançado et al., 2006) shown in Equation 2.1 using a laser energy (E_l) of 2.54 eV (λ = 488 nm). Results are shown in Table 5.2.

The calculated crystallite size for as-received graphite is 103 ± 5 nm indicating the presence of long-range order agreeing well with XRD analysis. After 8 h of milling the crystallite size can be seen to significantly decrease to 12.1 ± 0.2 nm indicating the introduction of a nano-crystalline structure and loss of long-range order, as observed by XRD as a broadening and reduction in intensity of the (002) peak. A further decrease in crystallite size is observed for the as-prepared graphite (Ar) + $LiBH_4$ sample resulting from the additional 2 h of ball milling.

Table 5.2 Location and peak area of the D and G bands of each graphitic sample from Figure 5.2

-	D Peak		G Peak		-
Sample	**Location (cm^{-1})**	**Area (a.u)**	**Location (cm^{-1})**	**Area (a.u)**	**La (nm)**
As-Received Graphite	1353 ± 8	3 ± 1	1580.3 ± 0.1	23 ± 1	120 ± 3
8 h graphite (Ar)	1357.9 ± 0.6	67 ± 1	1580.9 ± 0.3	61 ± 1	12.3 ± 0.4
As-prepared graphite (Ar) +LiBH4	1357.6 ± 0.4	102 ± 1	1584.6 ± 0.5	77 ± 2	10.1 ± 0.3

5.1.3 N_2 Adsorption Isotherms & BET

Nitrogen adsorption isotherms were carried out on as-received graphite and 8 h milled graphite (Ar) to investigate the BET surface area change as a result of ball milling under Ar, as shown in Figure 5.3.

The total N_2 uptake of the as-received graphite is < 1 wt% at 950 mbar suggesting a low surface area, whereas the 8 h milled graphite (Ar) sample exhibits superior N_2 uptake of > 25 wt% at 950 mbar showing that the surface area of the graphite has significantly increased.

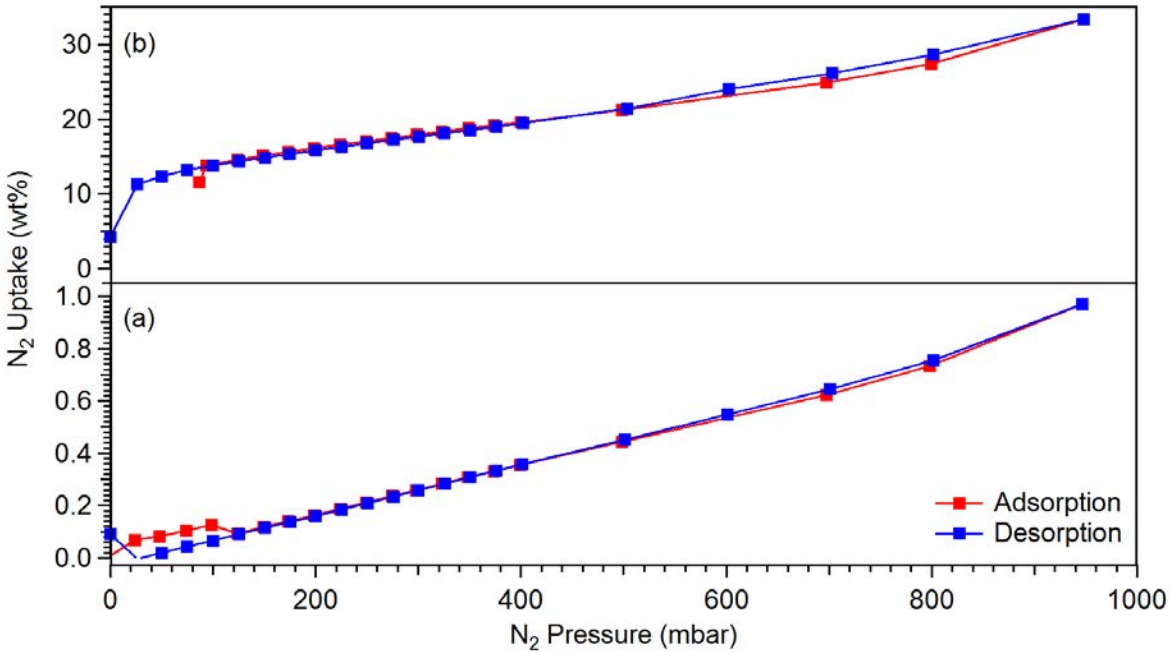

Figure 5.3 N_2 adsorption isotherms (-195 °C) for (a) as-received graphite, (b) 8 h milled graphite (Ar)

The BET surface areas for both the as-received graphite and 8 h graphite (Ar) isotherms were calculated and are shown in Figure 5.4 and Figure 5.5. The BET surface area was determined to be 15 ± 4 m^2g^{-1} for dried as-received graphite, the erratic looking behaviour below

p/p_0 = 0.1 is a result of temperature instability at the start and end of the experiment, but does not impact the BET calculations significantly.

As a result of milling under Ar for 8 h the surface of the graphite increased dramatically (by over a factor of 30) to 462 ± 3 m^2g^{-1}. This is large increase is due to the reduction in particle size caused by the high-energy ball milling technique.

This result is consistent with the ball milling of graphite under Ar, Francke et al., 2005 reported a surface area of 400 m^2g^{-1} after milling for 10 h under 1 bar Ar.

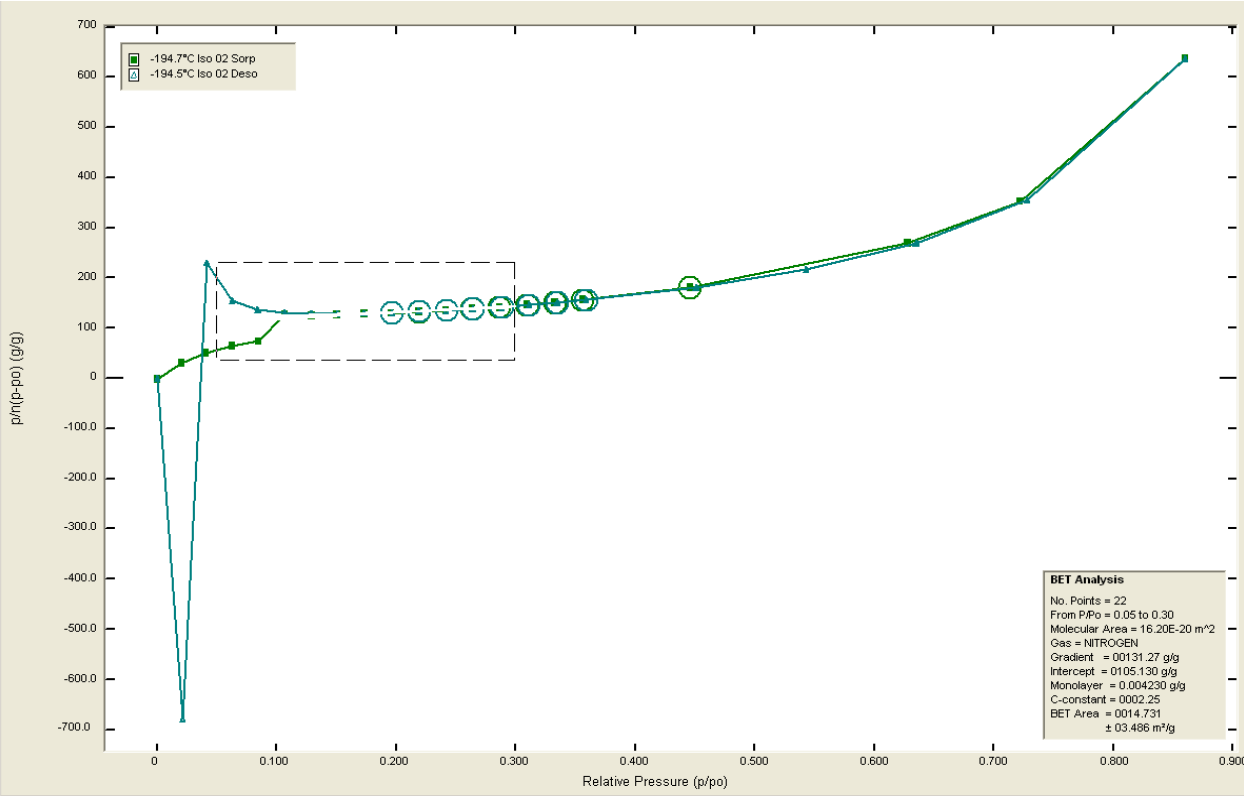

Figure 5.4 BET results for As-received graphite calculated from Figure 5.3a, the fit parameters are shown in the bottom right corner of the graph

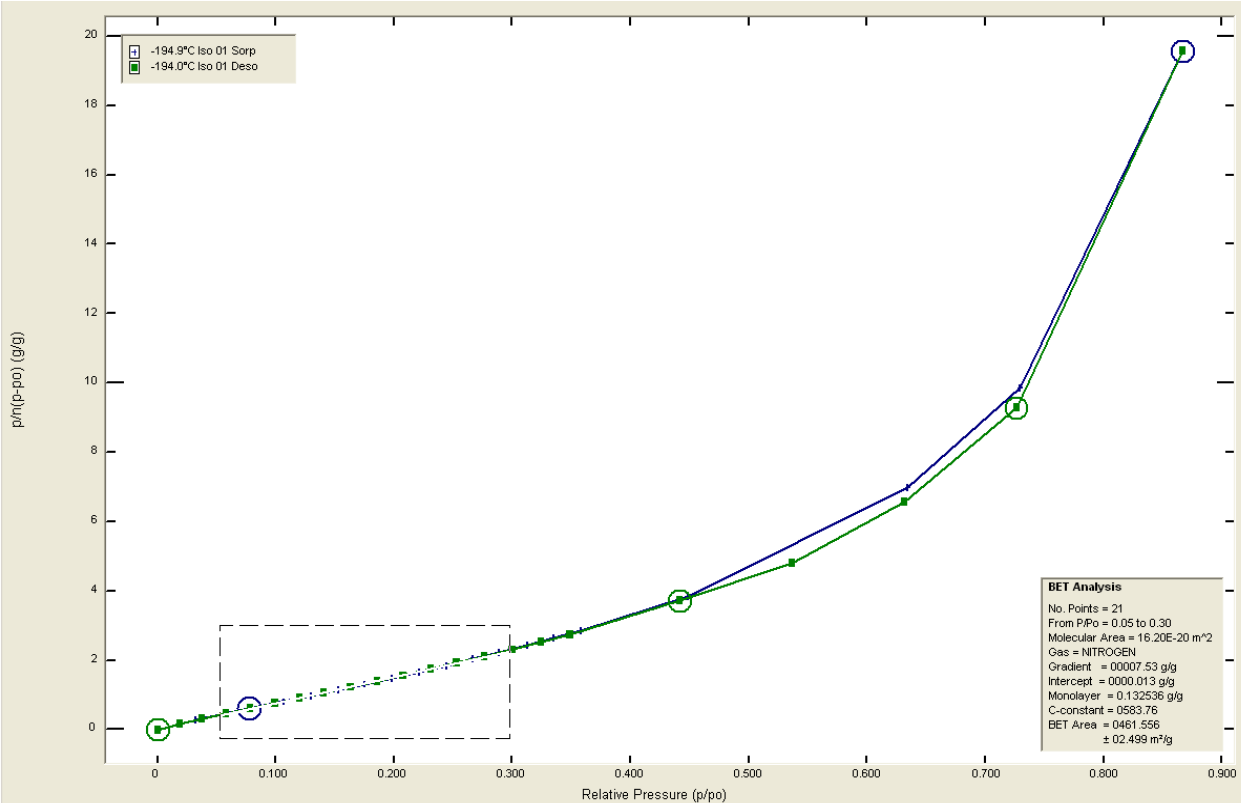

Figure 5.5 BET results for 8 h milled graphite (Ar) calculated from Figure 5.3b, the fit parameters are shown in the bottom right corner of the graph.

5.2 Thermal Decomposition

The thermal decomposition of as-prepared graphite (Ar) + $LiBH_4$ was investigated using DSC and TGA-MS shown in Figure 5.7. For comparison the 8 h milled graphite (Ar) was also studied using DSC and TGA-MS shown in Figure 5.6.

During hearing of the 8 h milled graphite (Ar) sample no events were witnessed by DSC and no hydrogen or methane detected as would be expected for the graphite milled under an inert Ar atmosphere. The linear weight loss of 0.7 ± 0.1 wt% is attributed to inaccuracies in the baseline correction during the measurement owed to the low density of the graphite.

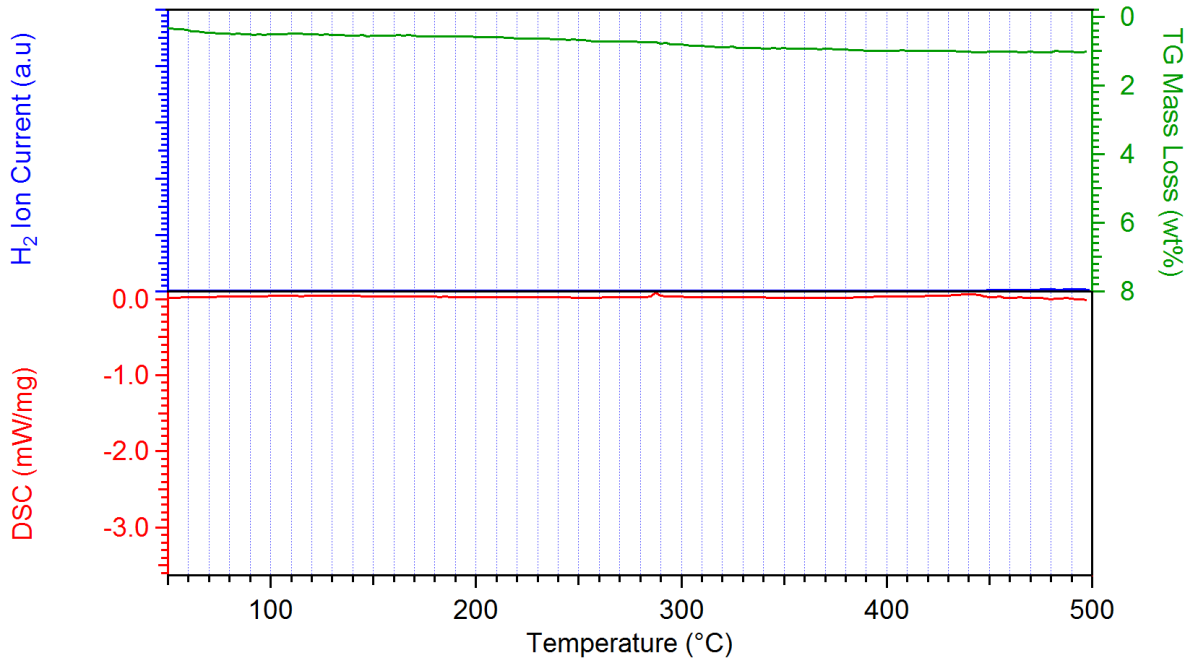

Figure 5.6 DSC-TGA-MS profile of 8 h milled graphite (Ar) heated to 500 °C at 5 °C.min^{-1} under 3 bar Ar with a flow rate of 100 ml.min^{-1}

The DSC trace from the decomposition of as-prepared graphite (Ar) + $LiBH_4$ exhibits three significant events, the first at 117 °C is the polymorphic phase transition of $LiBH_4$ from an orthorhombic crystal structure to a hexagonal structure followed by the melting of $LiBH_4$ at 284 °C. The final event is the decomposition of $LiBH_4$, the split peak nature of this event indicates a two-step reaction and is consistent with DSC traces of the decomposition of bulk $LiBH_4$ (Shao et al., 2014). The decomposition can be seen to commence immediately after melting at 290 °C with the two peaks occurring at 352 °C and 375 °C. This two-step decomposition behaviour is consistent with that reported by (Reed and Book, 2009) in which in-situ Raman spectroscopy identified the formation of $Li_2B_{12}H_{12}$ and amorphous Boron during decomposition (see Section 2.6.2).

The split peak coincides with both rapid weight loss and hydrogen release confirming that the split peak observed by DSC is the decomposition of $LiBH_4$ within the sample. The onset of bulk weight loss is 305 °C with a 4.2 ± 0.1 wt% loss between 330 °C and 380 °C, leading to a total weight loss of 7.23 ± 0.1wt% by 500 °C.

The onset of hydrogen desorption is 150 °C with bulk hydrogen release occurring just after melting between 300 °C and 400 °C. The hydrogen desorption profile appears as an asymmetric peak with the maximum hydrogen intensity occurring at 364 °C. No pronounced hydrogen desorption peak is observed in the region of $LiBH_4$ melting, a feature observed for bulk $LiBH_4$ (Figure 2.17).

Very low quantities of diborane were detected between 200 °C and 300 °C, although the signal to noise ratio is very low, a small desorption can be observed between the specified range. Diborane is a highly reactive or 'sticky gas' and as such can stick to the walls of the gas capillary line that connects the TGA to the MS. Consequently, the detection of a small quantity of diborane can indicate a much larger desorption from the sample. Diborane has been shown to thermally decompose above 250 °C (Söderlund et al., 2005) which offers an another explanation for the low quantities.

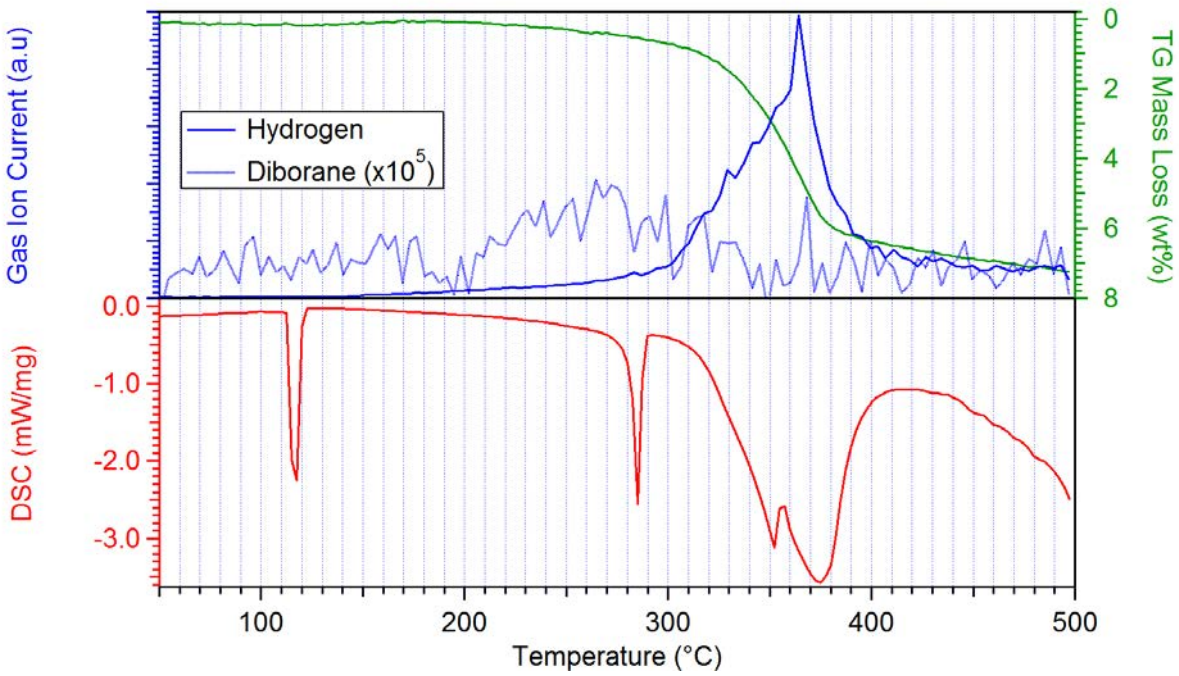

Figure 5.7 DSC-TA-MS decomposition profile of as-prepared graphite (Ar) + $LiBH_4$ heated to 500 °C at 5 °C.min^{-1} under 3 bar Ar

XRD and Raman spectroscopy measurements were carried out on a dehydrided graphite (Ar) + $LiBH_4$ sample (desorbed at 400 °C for 30 min under 3 bar He). The XRD pattern of dehydrided graphite (Ar) + $LiBH_4$ (Figure 5.9b) shows reflections consistent with nano-crystalline graphite and LiH, no other phases such as $Li_2B_{12}H_{12}$ were present in the XRD pattern indicating that all $LiBH_4$ had decomposed into LiH, or that any $Li_2B_{12}H_{12}$ formed was very low in proportion to LiH. No reflections from boron were observed, however, $LiBH_4$ is known to decompose into LiH, amorphous B (a-B) and H_2 (Section 2.6.2). LiH has been shown to react with nanostructured carbon and form Li_2C_2 (Miyaoka et al., 2009, 2011). Although no Li_2C_2 was observed in the dehydrided graphite (Ar) + $LiBH_4$ sample a large increase in the size

of the c-direction lattice parameter of 0.25 ± 0.02 Å was observed (calculated from a Pawley refinement, results are shown in Table 5.3).

The Raman spectrum of dehydrided graphite + $LiBH_4$ (Ar) (Figure 5.10b) did not show any new phases, with no significant shifts in the position of the G, D G' and D' peaks.

In situ XRD was used to help understand the decomposition pathway of the as-prepared sample. The sample was scanned during heating to 400 °C at 2 °C.min^{-1} and then cooled back to room temperature, results are shown in Figure 5.8. cDuring heating, the $LiBH_4$ undergoes a phase transition from an orthorhombic to hexagonal crystal structure between 100 °C and 125 °C as observed by DSC (Figure 5.7). At 280 °C reflections from $LiBH_4$ disappear as a result of melting and the loss of long-range order in $LiBH_4$. Reflections consistent with $Li_4B_2O_5$ becomes visible in the absence of $LiBH_4$ with Li_3BO_3 also forming at temperatures above 308 °C (onset of decomposition as seen by DSC), with both oxide phases present for the remainder off heating and cooling. No intermediates or decomposition products of $LiBH_4$ such as $Li_2B_{12}H_{12}$ or LiH are observed, however reflections from LiH are weak due to the light nature of the elements and overlap with reflections from Li_3BO_3.

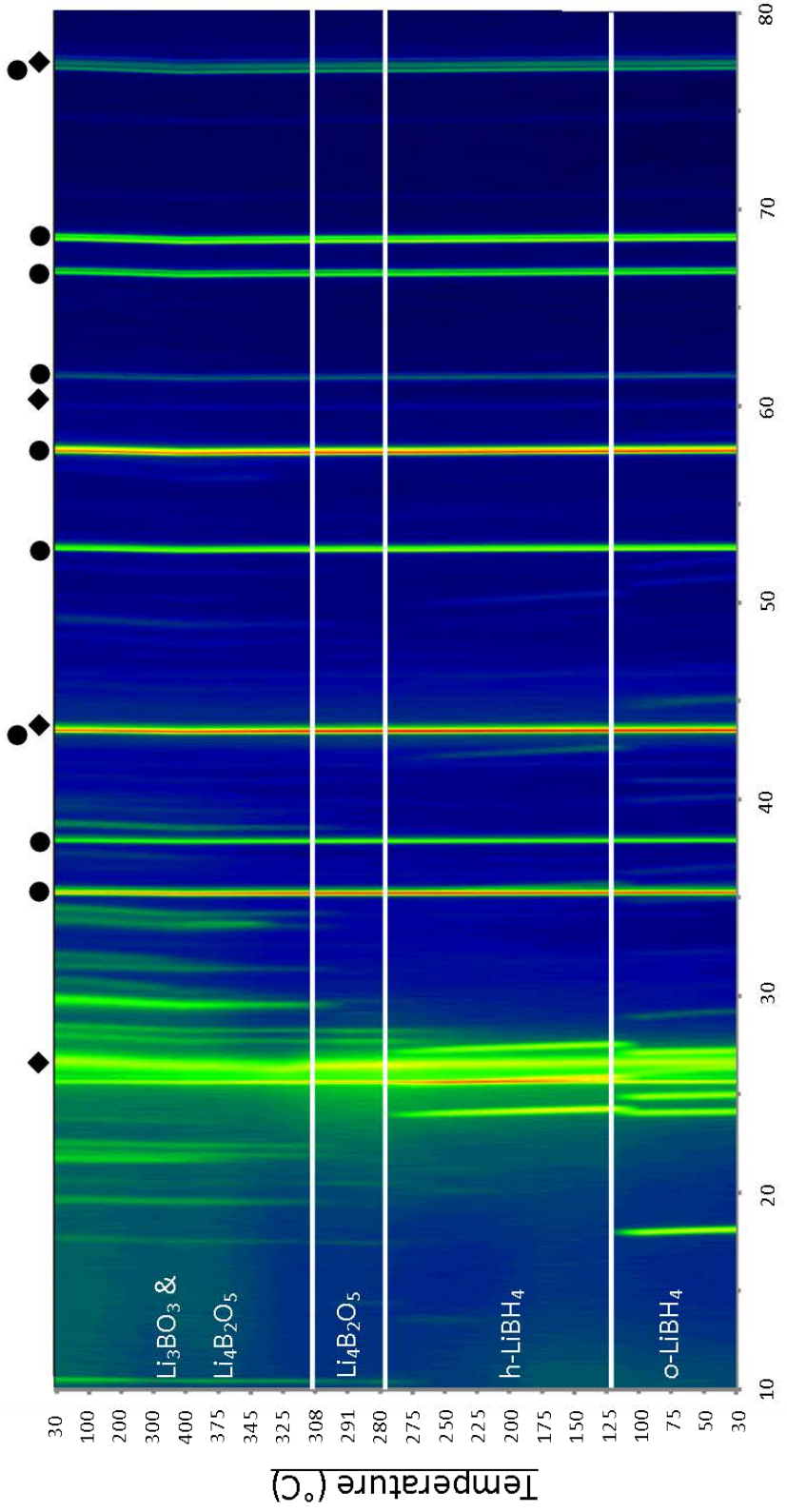

Figure 5.8 In situ XRD of as-prepared graphite (Ar) + $LiBH_4$ heated to 400 °C at 2 °C.min^{-1} under 3 bar He, intensity is indicated by a spectrum of colours where red indicates high intensity and blue indicates low intensity. Graphite reflections are marked with black diamonds, Al_2O_3 (sample holder) reflections with black circles. The ICDD PDF2 database (2011) was used for phase identification

As the sample is heated the (002) graphite peak appears to shift linearly to lower 2θ values consistent with thermal expansion of the graphite lattice, followed by contraction upon cooling.

5.3 Rehydrogenation study of Graphite (Ar) + $LiBH_4$

An as-prepared graphite (Ar) + $LiBH_4$ sample was first dehydrided under 3 bar He at 400 °C for 30 min before being rehydrided at 350 °C under 100 bar H_2 for 10 h using Sieverts apparatus and characterised using XRD, Raman Spectroscopy, and DSC-TGA-MS.

5.3.1 X-ray Diffraction

The XRD pattern of rehydrided graphite (Ar) + $LiBH_4$ has peaks consistent with orthorhombic $LiBH_4$, LiH and graphite confirming that $LiBH_4$ was successfully recombined under more moderate pressures and temperatures compared to the lowest reported for bulk $LiBH_4$ (350 °C and 155 bar H_2 (Mauron et al., 2007), recombination conditions were not optimized). The presence of LiH indicates that not all $LiBH_4$ was reformed during the 10 h hydrogen heat-treatment. It is not possible to perform quantitative phase analysis on the de/re-hydrided samples due to the nanostructure and amorphous content of the graphite along with the potential existence of a-B as a reaction product from the decomposition of $LiBH_4$.

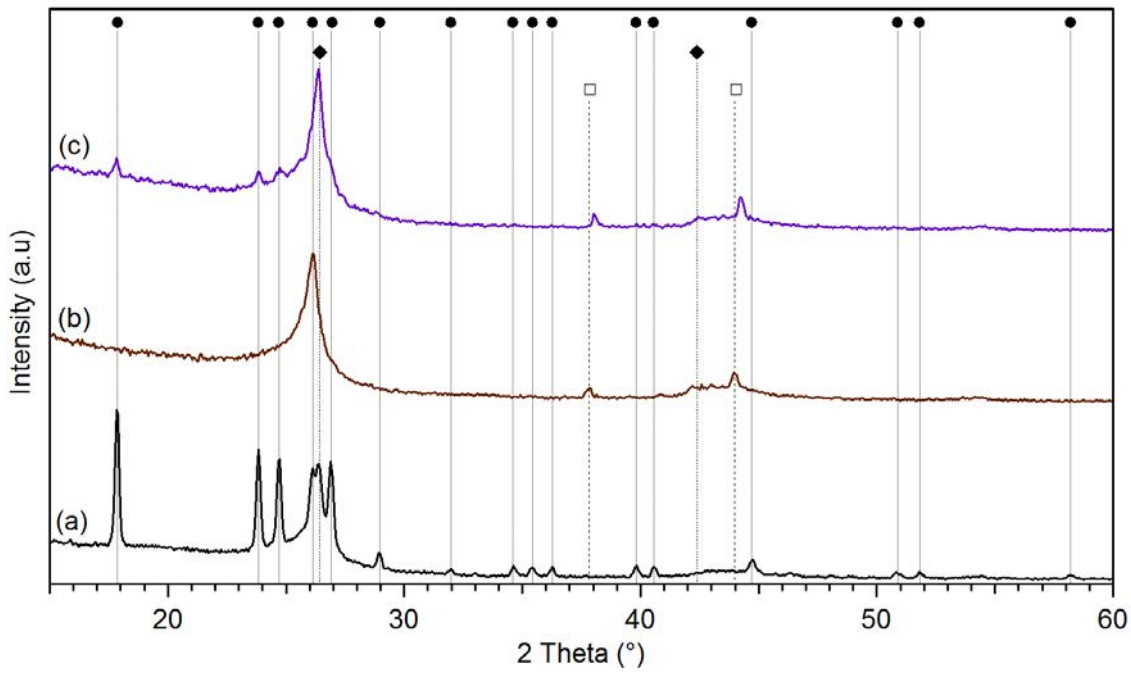

Figure 5.9 Room temperature XRD patterns of (a) as-prepared graphite (Ar) + $LiBH_4$, (b) dehydrided graphite (Ar) + $LiBH_4$ and (c) rehydrided graphite (Ar) + $LiBH_4$. The location of reflections from $LiBH_4$, graphite and LiH are indicated by the solid black circles, solid black diamonds and the clear squares respectively. The ICDD PDF2 database (2011) was used for phase identification

Table 5.3 c-direction lattice parameter determined by Pawley refinements for as prepared graphite (Ar) + $LiBH_4$, dehydrided graphite (Ar) + $LiBH_4$ and rehydrided graphite (Ar) + $LiBH_4$

Sample	c-direction lattice parameter (Å)
As-prepared graphite (Ar) + $LiBH_4$	6.727 ± 0.005
Dehydrided graphite (Ar) + $LiBH_4$	6.891 ± 0.018
Rehydrided graphite (Ar) + $LiBH_4$	6.761 ± 0.005

5.3.2 Raman Spectroscopy

Contrary to XRD results, the Raman spectra of rehydrided graphite + $LiBH_4$ (Figure 5.10c) showed no evidence of $LiBH_4$, no vibrations consistent with $[BH_4]^-$ stretching or bending were observed. The relative intensity of $LiBH_4$ to graphite reflections observed by XRD can be seen

to decrease in the rehydrided sample due to a lower $LiBH_4$ content. This reduction in $LiBH_4$ content also offers an explanation as to why the $[BH_4]^-$ stretching mode was not observed; only a small peak was observed for this vibration in the as-prepared graphite + $LiBH_4$ (Ar) sample.

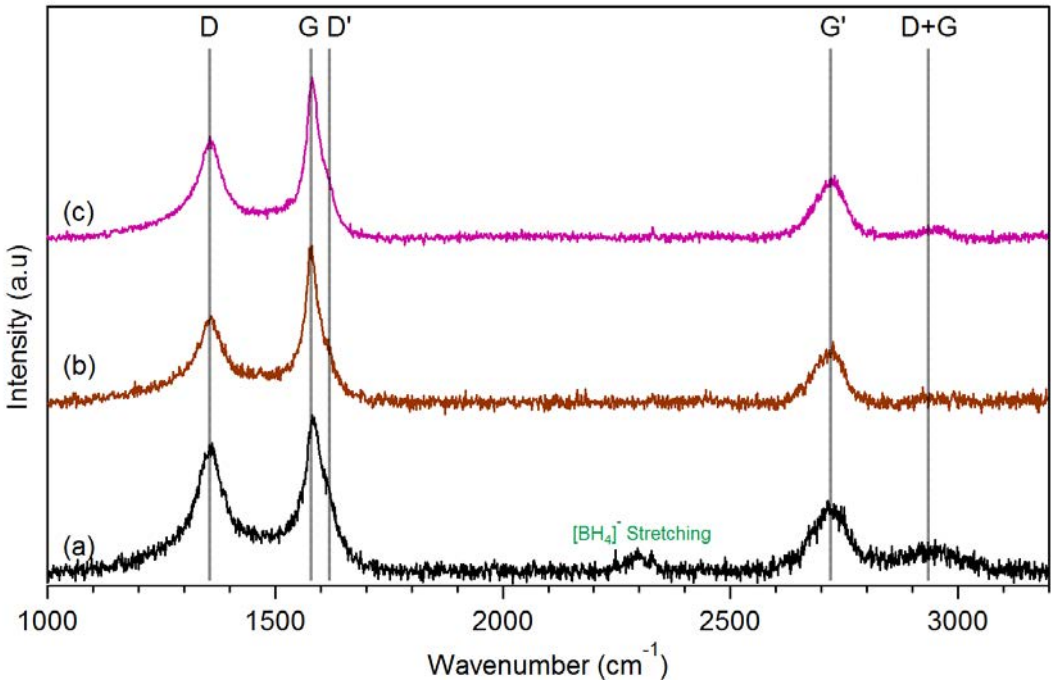

Figure 5.10 Room temperature Raman spectra of (a) as-prepared graphite (Ar) + $LiBH_4$, (b) dehydrided graphite (Ar) + $LiBH_4$ and (c) rehydrided graphite (Ar) +$LiBH_4$ measured under 100 ml.min^{-1} Ar

Table 5.4 Calculated G and D band peak fits and crystallite sizes for each graphitic sample calculated from Raman Spectra in Figure 5.10

	D Peak		G Peak		
Sample	**Location (cm^{-1})**	**Area**	**Location (cm^{-1})**	**Area**	**La (nm)**
Rehydrided graphite (Ar) + $LiBH_4$	1357.1 ± 0.5	79 ± 1	1582.3 ± 0.2	57 ± 1	9.8 ± 0.3
Dehydrided graphite (Ar) + $LiBH_4$	1358.6 ± 0.7	70 ± 1	1580.0 ± 0.3	56 ± 1	10.9 ± 0.4
As-prepared graphite (Ar) + $LiBH_4$	1357.6 ± 0.4	102 ± 1	1584.6 ± 0.5	77 ± 2	10.1 ± 0.3

5.3.3 DSC-TGA-MS

The decomposition of the rehydrided sample was investigated via DSC-TGA-MS as shown in Figure 5.11.

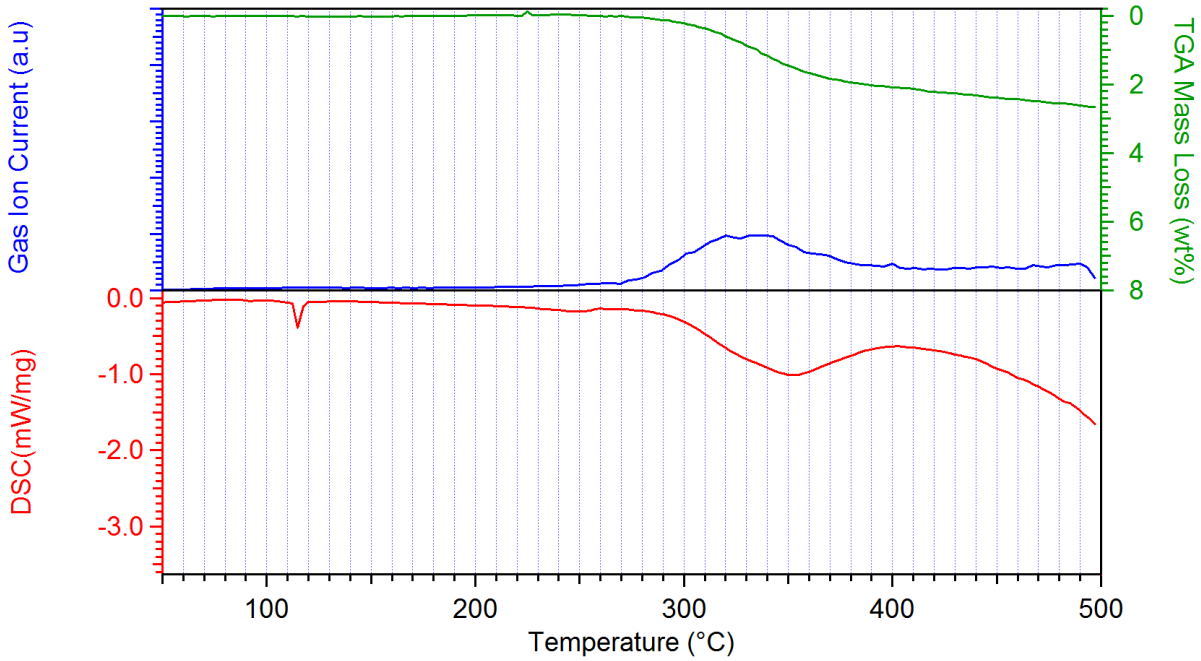

Figure 5.11 DSC-TGA-MS profile of the decomposition of rehydrided graphite (Ar) + $LiBH_4$ heated to 500 °C at 5 °C.min^{-1} under 3 bar Ar flowing at 100 ml.min^{-1}

The DSC trace of the decomposition of the rehydrided samples exhibits 3 peaks, phase change of $LiBH_4$ at 114 °C, the melting of $LiBH_4$ at 250 °C and its subsequent decomposition peaking at 352 °C, with decomposition complete by 400 °C. The change of peak shape and reduction in temperature of melting seen by DSC are consistent with $LiBH_4$ confined within nanoporous and mesoporous carbon scaffolds (Liu et al., 2011; Zhang et al., 2007) (Section 2.7.4.5). The decomposition of $LiBH_4$ occurs in the same temperature range as observed for as-prepared graphite (Ar) + $LiBH_4$ with a total weight loss of 1.88 wt% by 500 °C. The decomposition reaction no longer exhibits a clear split peak profile as seen for the as-

prepared sample, however, the asymmetric peak shape suggests there maybe be contribution from two peaks consistent with the observed decomposition of $LiBH_4$ in the as-prepared graphite (Ar) + $LiBH_4$ sample suggesting the rehydrided sample decomposes via the same two-step reaction.

No methane or diborane was detected within measurement limits during decomposition. Suggesting that either the quantity of diborane was too small to be detected or the decomposition mechanism of the $LiBH_4$ is different to that of the as-prepared sample. It is also possible to conclude that all weight loss (1.9 ± 0.1 wt%) may be attributed to the hydrogen desorption that starts shortly after melting at 270 °C with peak release occurring 330 °C, 34 °C lower than peak hydrogen desorption from the as-prepared sample.

Taking a ratio of the wt% losses of the as-prepared sample and the rehydrided sample it is possible to conclude that 37% of the initial $LiBH_4$ was successfully reformed.

5.3.4 Cyclic H_2 Uptake Stability

The cyclic stability of the as-prepared graphite (Ar) + $LiBH_4$ sample was studied over 5 de/re-hydrogenation cycles using a Sieverts apparatus to measure the isothermal H_2 uptake at 350 °C as a function of sample wt% and H_2 pressure, the results are presented in Figure 5.12. The first absorption cycle results in an uptake of 2.9 ± 0.1 wt% which is equivalent to 40 % recombination of the initial $LiBH_4$ during the absorption cycle, which is comparable to that achieved in ex situ rehydrogenation estimated from TGA mass losses. Analysis of the kinetic data of the absorption isotherms reveals that the sample was still absorbing hydrogen at the end of the cycle but the apparatus timed out, implying slow rehydrogenation kinetics of

$LiBH_4$ within the sample. Over the next 4 cycles the graphite + $LiBH_4$ continued to lose capacity, XRD data of the cycled sample (in a desorbed state) indicated the presence of graphite, LiH and Li_3BO_3 suggesting the loss in capacity is due to a combination of the formation of a stable lithium borate and slow kinetics. After 5 cycles the H_2 uptake was 2.2 ± 0.1 wt%.

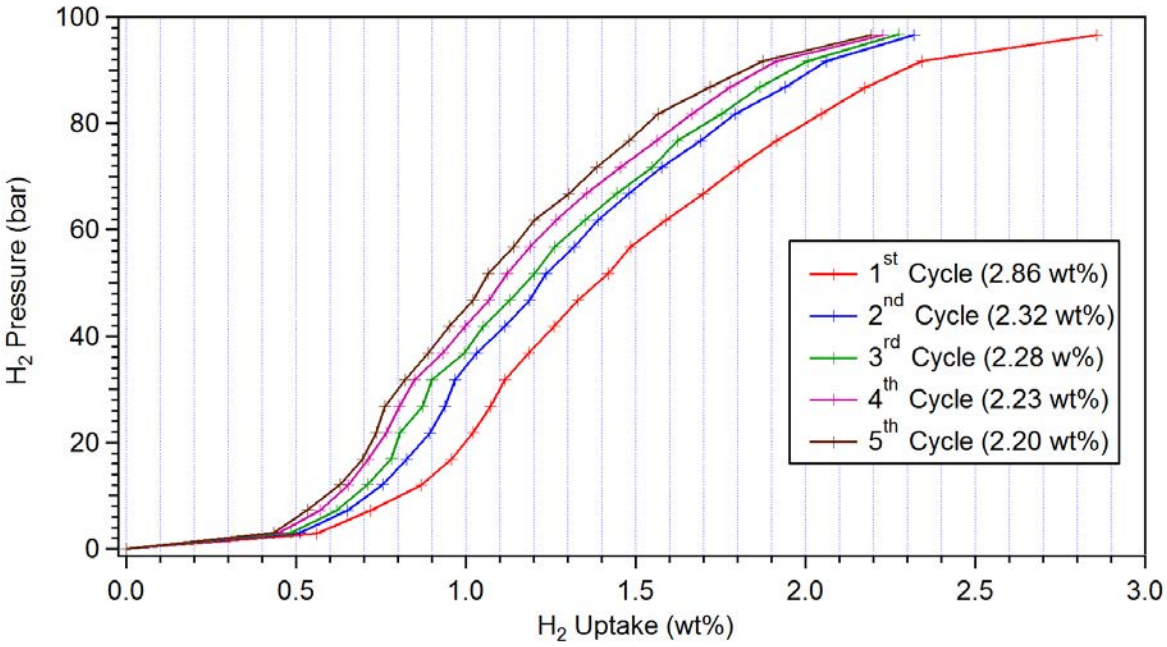

Figure 5.12 Cyclic H_2 uptake isotherms of graphite (Ar) + $LiBH_4$ measured at 350 °C as a function of H_2 pressure and uptake, the final H_2 uptake after each cycle is displayed

5.4 Discussion

Ball milling of graphite under an argon atmosphere for 8 h resulted in a large increase in surface area from 15 ± 4 m^2g^{-1} to 426 ± 3 m^2g^{-1} coupled with a the introduction of a nano-crystalline/amorphous graphite mixture observed by XRD and Raman, behaviour consistent with the literature (Francke et al., 2005). No new phases were observed by lab based XRD or

Raman spectroscopy suggesting any contamination originating from ball-milling was low of very low quantity.

DSC-TGA-MS showed no hydrogen evolution or DSC peaks for 8 h milled graphite (Ar) as would be expected for non-hydrogenated graphite. However, the effect of the milled graphite upon the decomposition of $LiBH_4$ was significant. The onset temperature of hydrogen desorption was reduced to 150 °C and peak desorption 364 °C which is over 100 °C lower than for pure $LiBH_4$ (Shao et al., 2014).

Diborane was detected between 200 °C and 300 °C, as observed by Kato et al. (2010) who reported that diborane is released from the hexagonal phase of $LiBH_4$ prior to decomposition. The extremely low quantity of diborane detected may be due to the sticky nature of the gas causing it to stick to the walls of the capillary and thus only a small amount reaching the detector.

The total theoretical wt% of H_2 in the as-prepared sample is 8.80 wt%. The direct decomposition of $LiBH_4$ into LiH, a-B and H_2 results in a theoretical weight loss of 6.60 wt%, the as-prepared graphite (Ar) + $LiBH_4$ desorbed a total of 7.3 ± 0.1 wt% of H_2 by 500 °C and as such it can be postulated that all of the $LiBH_4$ decomposed into LiH, part of which then continued to decompose into Li and H_2. This was supported by the XRD pattern of dehydrided graphite (Ar) + $LiBH_4$ which showed reflections from graphite and LiH only (any amorphous or dis-ordered phases are not visible using this technique).

Pawley refinement of the dehydrided sample indicated an expansion in the c-direction of the graphite crystal lattice of 0.13 Å, corresponding to an increase in the interlayer spacing of graphene sheets from 3.381 ± 0.003 Å to 3.446 ± 0.009 Å. This increase in the interlayer

spacing is consistent with the intercalation of Li in between the graphene sheets of graphite (Konar et al., 2015), both LiC_{27} and LiC_{36} have been shown to have average layer spacing in the region of 3.46 Å.

$LiBH_4$ was successfully reformed in a dehydrided graphite (Ar) + $LiBH_4$ sample under 350 °C and 100 bar H_2. A total of 40 % was estimated to have reformed. Cyclic uptake data showed a reduction in the H_2 capacity to 30 % of the initial value after 5 cycles. This reduction is believed to be a result of a combination of slow kinetics confirmed by the presence of LiH in the rehydrided sample and the formation of Li_3BO_3, which acts a B and Li sink reducing the quantity of B and Li available to react during recombination. Due to the amorphous nature of the B and graphite in the sample it was not possible to estimate the quantity of Li_3BO_3, LiH and $LiBH_4$ in the cycled sample using phase analysis on the XRD measurements. Although the Li_3BO_3 reduces the quantity of $LiBH_4$ in the sample, it has been shown to lower the conditions required for decomposition and recombination of $LiBH_4$ (Ma et al., 2016).

Analysis of the re-hydrided sample indicates a reduction in the c-lattice parameter of graphite to 6.761 ± 0.005 Å compared to that of the dehydrided sample (as-prepared sample 6.727 ± 0.005 Å and dehydrided sample = 6.891 ± 0.018 Å) indicating that the intercalated Li re-hydrides to form LiH outside of the graphite layers and then eventually forms $LiBH_4$. Based on these findings a possible decomposition pathway is proposed below in Equations 5.2 and 5.3.

Based on the findings in this chapter it is possible to propose a decomposition pathway. The observation of B_2H_6 indicates that $LiBH_4$ partially decomposes at 250 °C (Equation 5.2), before then decomposing via a two-step reaction through the intermediate phase $Li_2B_{12}H_{12}$.

The formation of $Li_2B_{12}H_{12}$ can either occur from the reaction with B_2H_6 (Equation 5.3) or the direct decomposition of $LiBH_4$ (Equation 5.4). After which the remaining LiH then decomposes forming lithium intercalated carbon (Equation 5.5).

$$LiBH_4 \leftrightarrow LiH + B + {}^3/_2H_2 \quad (5.1)$$

$$LiBH_4 \rightarrow LiH + BH_3 \quad (5.2)$$
$$\rightarrow LiH + B_2H_6$$

$$2LiBH_4 + 5B_2H_6 \rightarrow Li_2B_{12}H_{12} + 13H_2 \quad (5.3)$$
$$\leftrightarrow LiH + B + {}^3/_2H_2$$

$$LiBH_4 \leftrightarrow {}^1/_{12}Li_2B_{12}H_{12} + {}^5/_6LiH + {}^{13}/_{12}H_2 \quad (5.4)$$
$$\leftrightarrow LiH + B + {}^3/_2H_2$$

$$LiH + C \leftrightarrow LiC_x + H_2 \quad (5.5)$$

The addition of graphite was also found to inhibit the foaming effect observed for the decomposition of bulk $LiBH_4$, an effect observed for other additives to $LiBH_4$ such as C_{60} (Ward et al., 2013) and zeolite templated carbons (Shao et al., 2015).

In situ XRD (Figure 5.8) did not help understand the decomposition pathway of the as-prepared graphite+$LiBH_4$ sample as bulk decomposition proceeds after melting of $LiBH_4$, therefore intermediate decomposition products must crystallise out of the molten $LiBH_4$ for diffraction to occur. No intermediates were observed. The presence of $Li_4B_2O_5$ and Li_3BO_3 in the sample cooled to room temperature confirm that oxidation occurred during the experiment, the origin of which was believed to be from the apparatus as no oxidation was observed in XRD patterns of ex-situ dehydrogenated samples (Figure 5.9b). The colour of the

sample's surface was observed to change to a light grey from a carbon black on samples containing the oxide phases, as such it is believed the oxidation occurred on the surface of the sample.

Based on the absence of Li_3BO_3 in the dehydrided and rehydrided samples (Figure 5.9) it can be inferred that the graphite additive aids the decomposition and recombination of $LiBH_4$. It is believed the large homogeneous surface area provided by the graphite is believed to promote nucleation the decomposition of $LiBH_4$ resulting in the reduction in decomposition temperature.

Contrary to recent work by (Wang et al., 2016), no CH_4 was detected during the decomposition of as-prepared graphite (Ar) +$LiBH_4$. The milling conditions used by (Wang et al., 2016) were more energy intensive, 400 rpm and a ball to powder ratio of 40:1, compared to 280 rpm and 40:1 in this work. As such the effects experienced by the graphite in the same time period of 10 h will be enhanced for as result of the high energy conditions leading to a greater number of induced defects and dangling C bonds available to react with H_2 during heating, explaining why no CH_4 is observed in this work.

As discussed in Section 2.7.4.1.4, (Zhang et al., 2013) calculated that graphite fragments inserted into the $LiBH_4$ interstitial sites as a result of ball-milling led to a reduction in the decomposition temperature of $LiBH_4$. This predicted behaviour provides a possible hypothesis for the reduction in decomposition temperature along with the nature of the interaction between nano-structured graphite and the origin of B_2H_6.

6 Graphite (H_2) +$LiBH_4$

The purpose of this chapter is to investigate the hydrogen storage potential of a hydrogenated graphite and $LiBH_4$ mixture synthesised via ball milling after work by Zhang et al., (2012) reported an impressively high H_2 release of 9.3 wt% by 500 °C (Zhang et al., 2012) (see Section 2.7.4.1.4).

6.1 Characterisation of As-prepared Material

The as-received starting materials, 8 h milled graphite (H_2) and as-prepared graphite (H_2) + $LiBH_4$ were characterised by a combination of RT XRD, Raman spectroscopy and BET analysis of N_2 adsorption measurements.

6.1.1 X-Ray Diffraction

X-ray diffraction patterns of dried as-received graphite, 8 h milled graphite (H_2) and as-received $LiBH_4$ and as-prepared graphite (H_2) + $LiBH_4$ are shown in Figure 6.1.

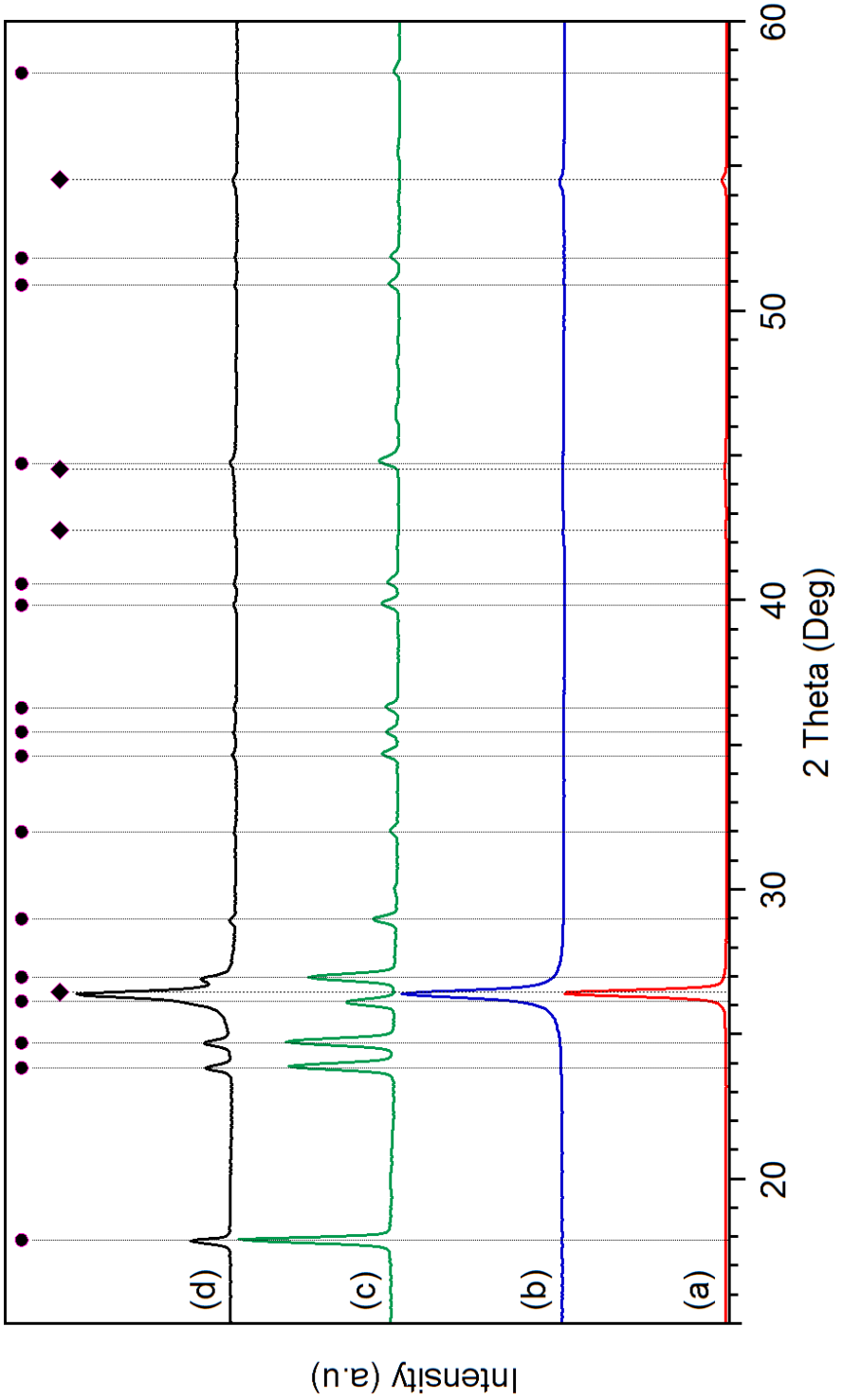

Figure 6.1 Room temperature XRD patterns of (a) dried as-received graphite, (b) 8 h milled graphite (H_2), (c) as-received $LiBH_4$ and (d) as-prepared graphite (H_2) + $LiBH_4$. Reflections associated with graphite are identified by the black diamonds, and those due to $LiBH_4$ identified by circles. The ICDD PDF2 database (2011) was used for phase identification

The XRD pattern of dried as-received graphite exhibits 4 main peaks at 26.4°, 42.4°, 44.5° and 54.5° 2θ corresponding to reflections from the (002), (010), (011) and the (004) planes respectively, as observed for crystalline graphite (identified using the ICSD PDF2 database). The most intense reflection is from the (002) peak located at 26.4° 2θ, a result of the stacking of graphene layers within graphite (Arnal et al., 2012). The 8 h milled graphite (H_2) shows the same reflections seen in the as-received graphite, but with lower peak intensities and an increase in the peak widths, most notably on the (002). Both peak broadening and reduction of intensity are consistent with the transformation of graphite from a crystalline structure to an amorphous/nano-crystalline mixture (Orimo et al., 1999).

The XRD pattern of as-prepared graphite (H_2) + $LiBH_4$ sample (Figure 6.1d) only exhibits peaks consistent with orthorhombic $LiBH_4$ (o-$LiBH_4$) and graphite indicating that no new phases were formed during milling. The low intensity WC reflections are no longer clearly visible, due to the presence of high intensity reflections from $LiBH_4$ in the same region. Pawley Refinements were carried out on the XRD patterns of the graphitic samples to study the c-direction lattice parameter at each stage of the synthesis process (since carbon atoms sit at z = 0.25 and z = 0.75 within the graphite lattice, c/2 is equal to the spacing between the graphitic sheets). The results are shown in The crystallite size can be seen to reduce by a factor of almost 5 after 8 h ball-milling in hydrogen, indicating destruction of long-range order.

Table 6.1. No expansion in the c-direction was observed indicating no intercalation (of H atoms between the graphite sheets) occurred during ball-milling. Additionally, the Scherrer equation was used to calculate the average crystallite size (L_c) in the c direction (002) based

on the width (FWHM) and peak position of the (002) peak, results are shown in The crystallite size can be seen to reduce by a factor of almost 5 after 8 h ball-milling in hydrogen, indicating destruction of long-range order.

Table 6.1. The crystallite size can be seen to reduce by a factor of almost 5 after 8 h ball-milling in hydrogen, indicating destruction of long-range order.

Table 6.1 c-direction lattice size calculated for each graphitic sample by Pawley refinements, and crystallite size of graphite calculated by the *Scherrer equation using a shape factor of K = 0.9

Sample	c-Direction Spacing (Å)	Crystallite Size* (nm)
As-received graphite	6.727 ± 0.001	52.3 ± 1.1
8 h (H_2) milled graphite	6.730 ± 0.005	13.0 ± 3.7
As-prepared graphite (H_2) + $LiBH_4$	6.728 ± 0.002	-

6.1.2 Raman Spectroscopy

Raman Spectra of the as-received materials, 8 h (H_2) milled graphite and as-received $LiBH_4$ and as-prepared graphite (H_2) +$LiBH_4$ are shown in Figure 6.2.

The Raman spectrum of as-received graphite exhibits two intense peaks, the G mode at 1581 cm^{-1} consistent with the E_{2g} stretching mode of pairs of sp^2 hybridised carbon atoms (Ferrari and Robertson, 2000), and the G' mode at 2720 cm^{-1} a result of second order double resonance scattering. Both modes are consistent with highly ordered pyrolytic graphite (Ferrari et al., 2006).

The small narrow peak seen at 2320 cm^{-1} is believed to be a measurement artefacts and not indicative of the graphite. It has been observed in a variety of different samples.

As a result of milling for 8 h, the intensity of the G band can be seen to decrease coinciding with the appearance of the D and D' bands 1352 cm^{-1} and 1616 cm^{-1}, respectively. The D band is a result of the breathing mode of A_{1g} symmetry (Ferrari and Robertson, 2000) (breathing mode of the carbon rings) and is forbidden by Raman selection criteria in defect-free graphite, only becoming active in the presence of sp^3 bonding of carbon atoms. A downshift in the position of the G band by ~4 cm^{-1} indicates the introduction of strain in the graphene sheets caused by the ball milling process (Roy et al., 2003).

The profile of the G' peak in the 8 h milled graphite (H_2) sample can be seen to change from a split peak profile to a more symmetrical singular peak at 2730 cm^{-1}. The G' band in turbostratic graphite can be described by a singular lorentzian peak located above 2700 cm^{-1}.

The Raman spectrum of as-received $LiBH_4$ Figure 6.2c exhibits two main groups of peaks, consistent with bond stretching and bond bending of the $[BH_4]^-$ tetrahedral as labelled on the graph. The broad peak located between 2140 cm^{-1} and 2200 cm^{-1} are second order phonons resulting from the bending modes of the $[BH_4]^-$ unit (Reed and Book, 2009).

The Raman spectra of the as-prepared graphite (H_2) + $LiBH_4$ (Figure 6.2d) only shows vibrations from graphite, no bands consistent with $[BH_4]^-$ stretching or bending were observed. Since the presence of $LiBH_4$ was confirmed by XRD measurements, it is possible that the absence of $[BH_4]^-$ is due to a lack of homogeneity within the sample. It is possible that $[BH_4]^-$ stretching or bending modes would be detected if a larger sample surface area was studied via Raman spectroscopy.

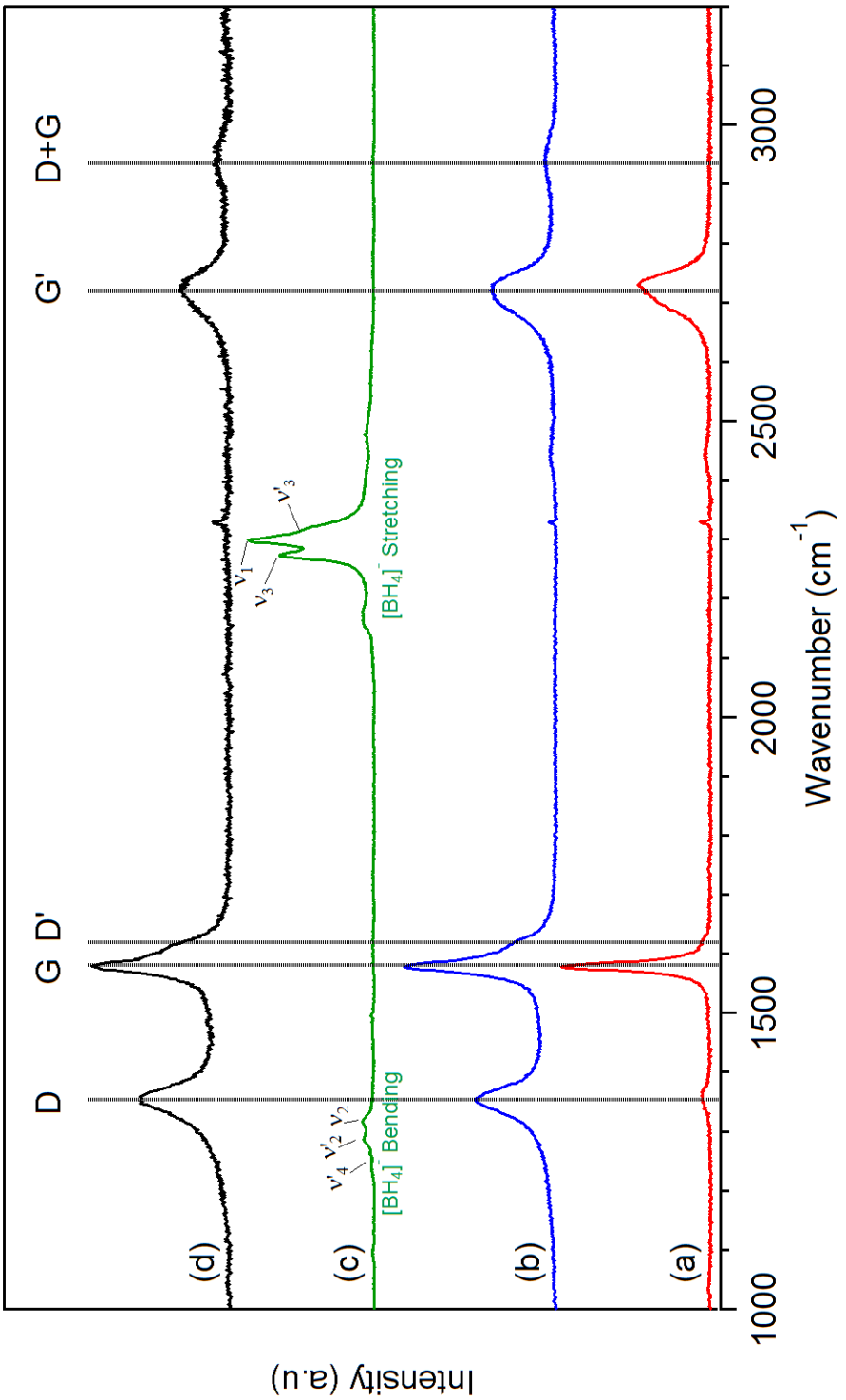

Figure 6.2 Raman spectra of (a) dried as-received graphite, (b) 8 h milled graphite (H_2), (c) as-received $LiBH_4$ and (d) as-prepared graphite (H_2) + $LiBH_4$, measured under 100 ml.min^{-1} flowing Ar. The location of the D, G, D' G' and D+G bands are indicated by the dotted black lines

Since the intensity of the G band is related to the number of sp^2 bonded C atoms, and the intensity of the D band is proportional to the number of sp^2 and sp^3 bonded C atoms, it is possible to estimate the crystallite size (L_a). This was done for each graphitic sample was calculated using Equation 2.2 (see Section 2.4.1.4) for laser excitation energy of 2.54 eV (λ = 488nm); results are shown in Table 6.2.

Table 6.2 Calculated G and D band peak fits and crystallite sizes for each graphitic sample calculated from Raman spectra in Figure 6.2

	D Peak		G Peak		
Sample	**Location (cm^{-1})**	**Area (a.u)**	**Location (cm^{-1})**	**Area (a.u)**	**La (nm)**
As-received graphite	1356.9 ± 0.9	3.5 ± 0.2	1578.4 ± 0.1	26.9 ± 0.1	103 ± 5
8 h milled graphite (H_2)	1352.2 ± 0.2	50.8 ± 0.4	1578.6 ± 0.1	45.5 ± 0.4	12.1 ± 0.2
Graphite+LiBH4	1352.2 ± 0.3	65.6 ± 0.7	1579.1 ± 0.2	48.1 ± 0.8	9.9 ± 0.2

The crystallite size L_a (calculated from the Raman spectra) can be seen to drastically reduce from 103 ± 5nm to 12.1 ± 0.2 nm after ball milling for 8 h under hydrogen. The addition of $LiBH_4$ and a further 2 h of milling, results in a small reduction in the crystallite size of the graphite to 9.9 ± 0.2 nm. The crystallite sizes calculated from the Raman spectra follow the same trend as those calculated from the XRD patterns shown in The crystallite size can be seen to reduce by a factor of almost 5 after 8 h ball-milling in hydrogen, indicating destruction of long-range order.

Table 6.1. However, the calculated crystallite size for as-received graphite is twice that of the value estimated using the Scherrer equation.

6.1.3 N_2 Adsorption Isotherms & BET

Nitrogen gas adsorption isotherms were measured for both the dried as-received graphite and 8 h milled graphite (H_2), results are displayed in Figure 6.3a and Figure 6.3b respectively. The as-received graphite can be seen to adsorb very little N_2, 0.35 wt% at 950 mbar, whereas the 8 h milled graphite (H_2) sample can be seen to adsorb 8 wt% by 950 mbar indicating that the milled sample has a larger surface area. BET analysis was carried out on each sample and the results are shown in Figure 6.4 and Figure 6.5.

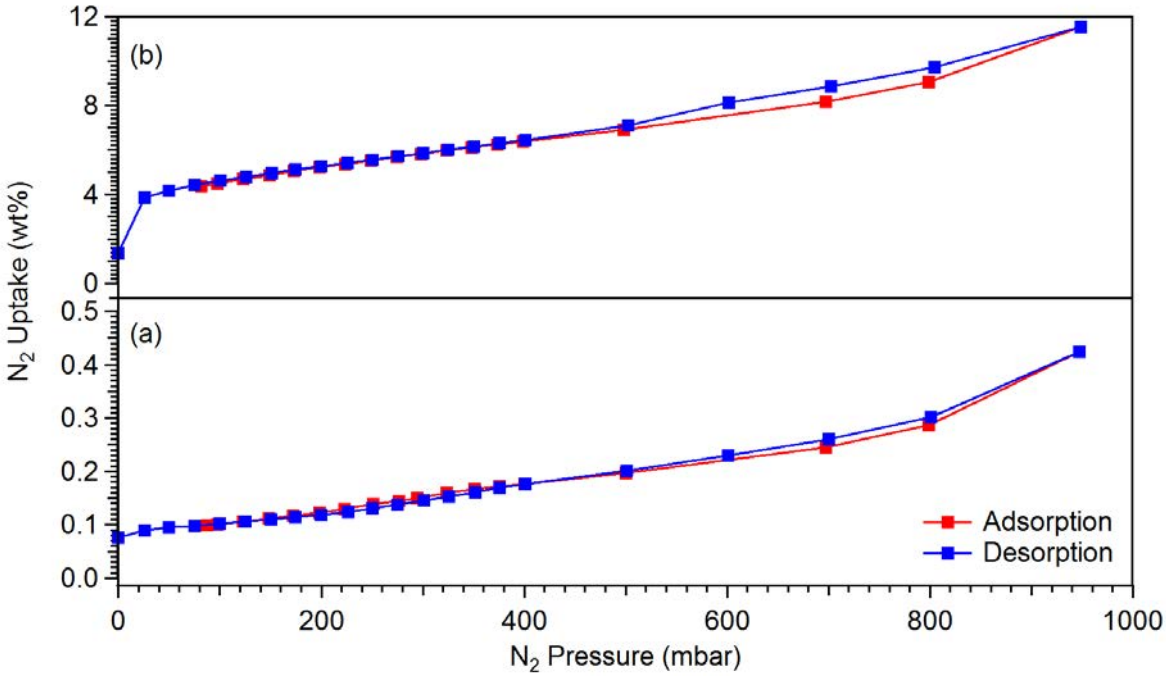

Figure 6.3 Isothermal Nitrogen adsorption measurements of (a) as-received Graphite (b) 8 h milled graphite (H_2), at -195 °C

BET analysis indicated an increase in the surface area of the graphite from 4.0 ± 0.1 m^2g^{-1} (Figure 6.4) to 150 ± 1 $m2g^{-1}$ (Figure6.5) as a result of milling for 8 h under 3 bar H_2. This large increase in surface area is a result of the reduction in the average particle size due to ball milling.

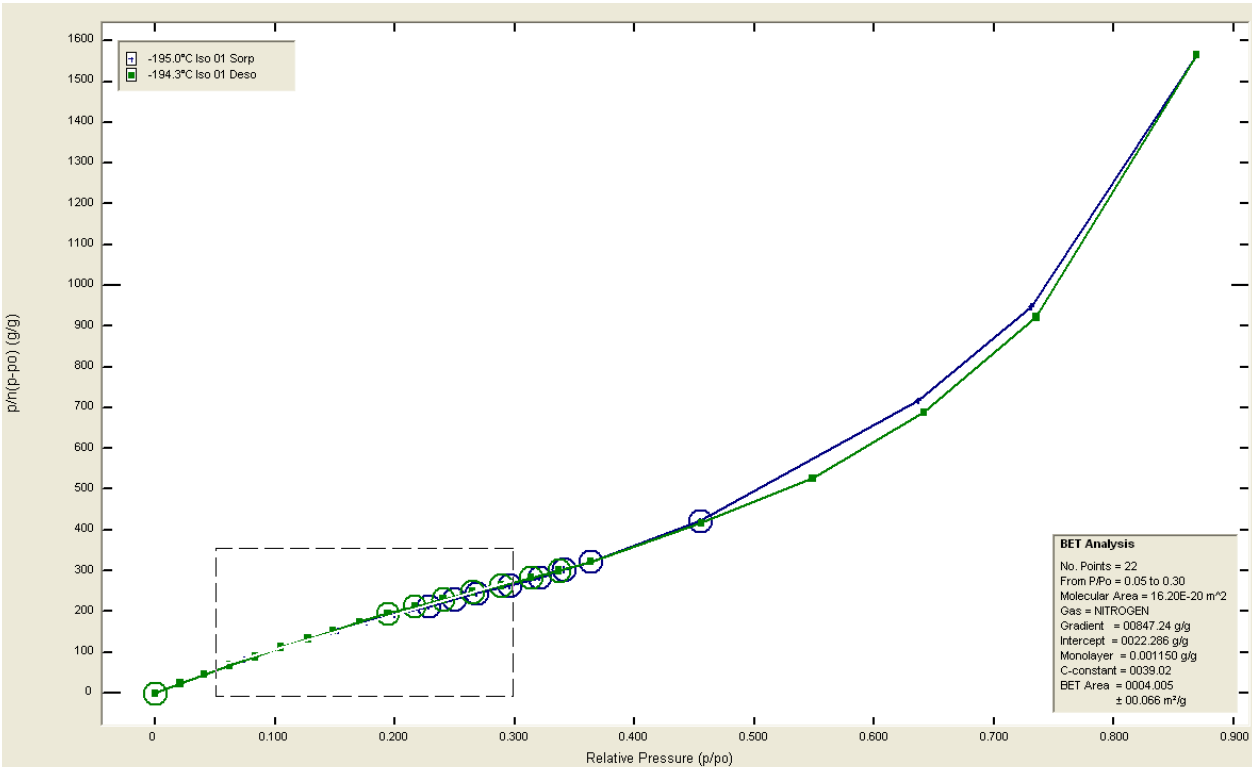

Figure 6.4 BET results for as-received graphite calculated from Figure 6.3a, the fit parameters are shown in the bottom right corner of the graph

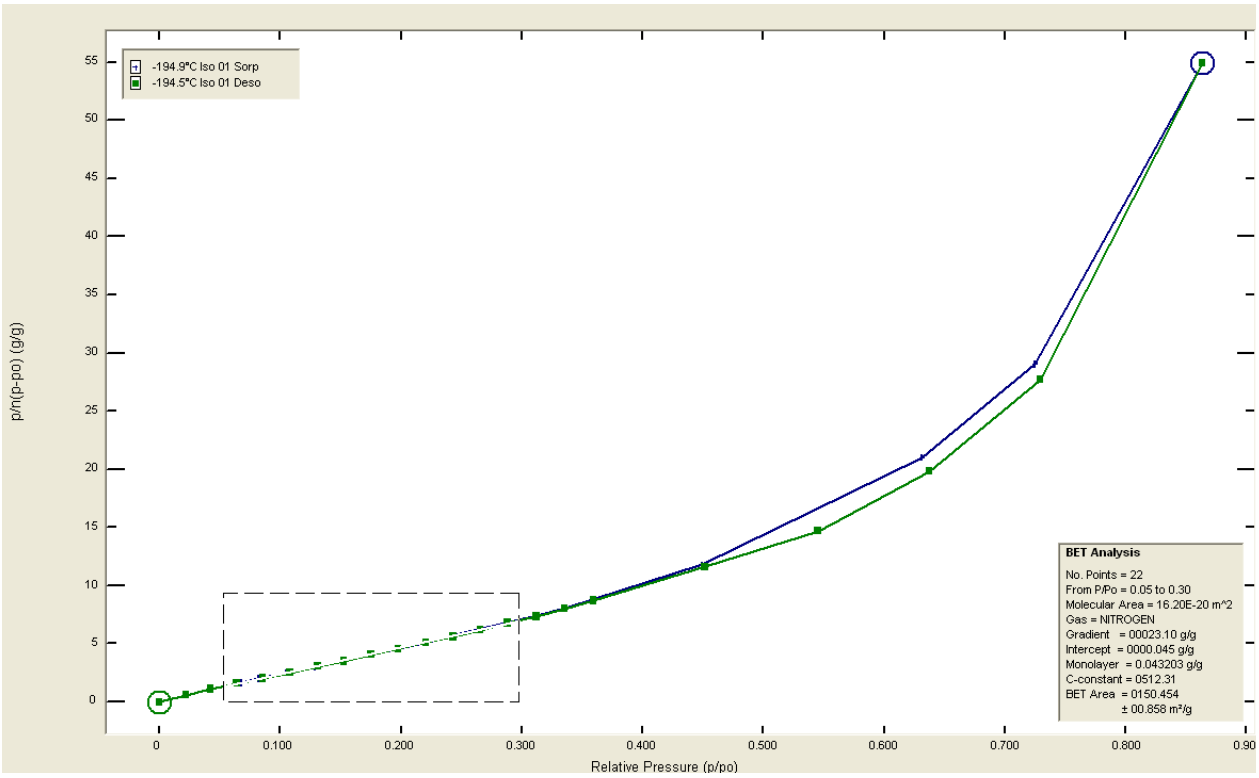

Figure 6.5 BET results for 8h milled graphite (H_2) calculated from Figure 6.3b, the fit parameters are shown in the bottom right corner of the graph

6.2 Thermal Decomposition

The thermal decomposition of the 8 h milled graphite (H_2) and as-prepared graphite (H_2) + $LiBH_4$ were studied using DSC, TGA-MS and Raman spectroscopy and XRD with the aim of understanding the effect of hydrogenated graphite upon the decomposition of $LiBH_4$.

6.2.1 8 h Milled Graphite (H_2)

Figure 6.6 shows the DSC-TGA-MS profile of 8 h milled graphite (H_2) heated to 900 °C (except DSC which is limited to 500 °C). The DSC profile exhibits no endothermic or exothermic peaks indicating that no reactions with fast kinetics occurred in the sample during heating. TGA-MS results show a small gradual weight loss of 0.3 ± 0.1 wt% between 400 °C and 900 °C coinciding with trace quantities of H_2 and CH_4 detection. The detection of H_2 suggests that the graphite was hydrogenated to some degree during milling, but not to as large an extent as reported by Zhang et al. (2012) (>2 wt% by 500 °C). The C-H bonding in the 8 h milled graphite (H_2) sample could not be investigated in this work because the interaction is very weak under visible light Raman spectroscopy (Ogita et al., 2004).

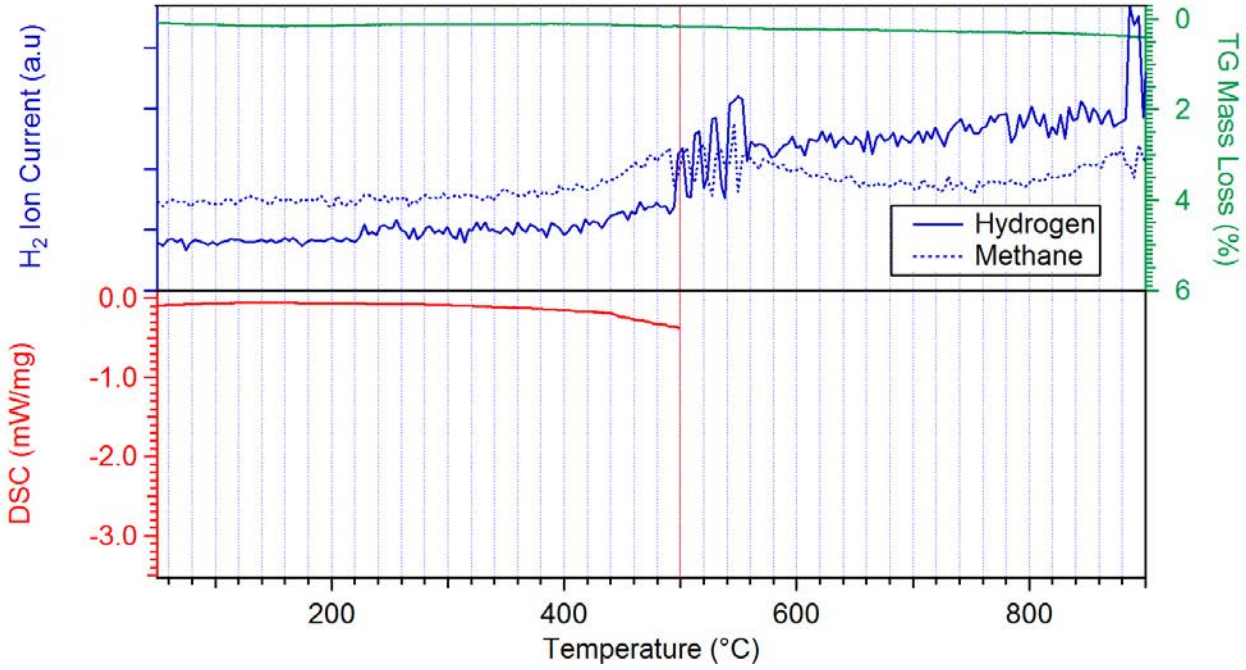

Figure 6.6 DSC-TGA-MS profile of 8 h milled graphite (H_2) heated to 900 °C at a rate of 5 °C.min^{-1} under 3 bar Ar with a constant flow rate of 100 ml.min^{-1}. The maximum temperature of the DSC is 500 °C.

6.2.2 As-prepared Graphite (H_2) + $LiBH_4$

The thermal decomposition of the as-prepared graphite (H_2) + $LiBH_4$ was studied by DSC-TGA-MS, shown in Figure 6.7. The DSC profile exhibits 3 distinct peaks, the first 114 °C is attributed to the orthorhombic to hexagonal phase transition whilst the second 287 °C is a result of the melting of $LiBH_4$. The third peak is comprised of two peaks 371 °C and 393 °C and is consistent with the decomposition of $LiBH_4$ (Shao et al., 2014). The two-step decomposition pathway is consistent with previous DSC results, however, the onset of decomposition within the as-prepared graphite (H_2) + $LiBH_4$ sample occurs almost 100°C lower than for bulk $LiBH_4$ (Shao et al., 2014; Orimo et al., 2006).

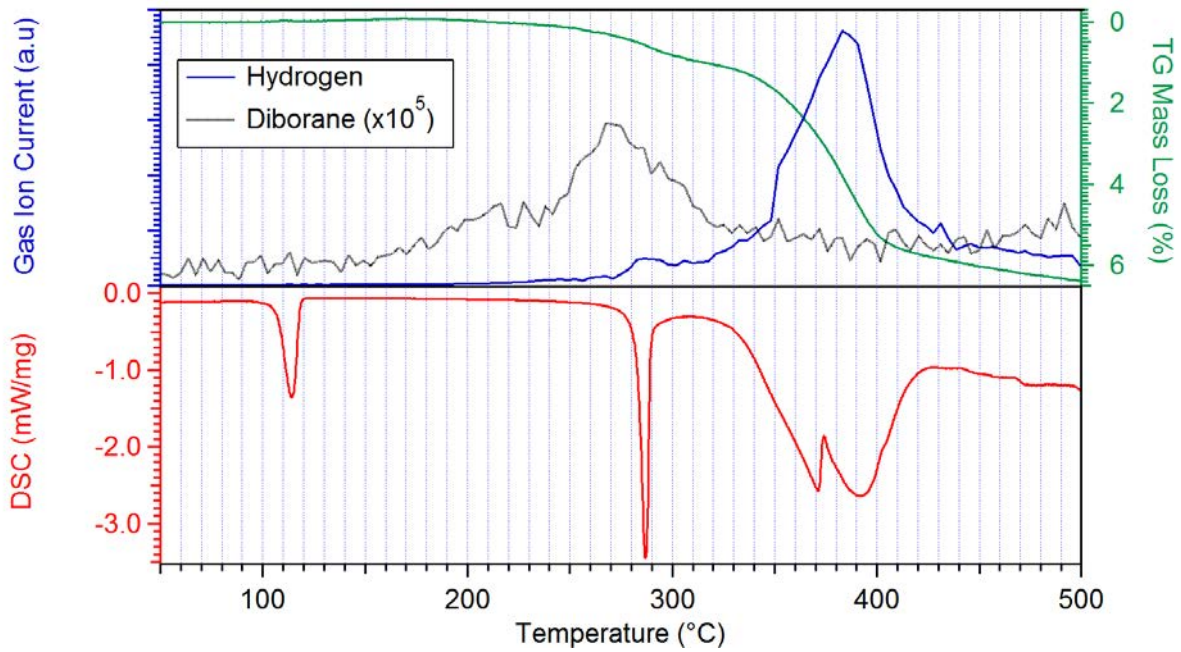

Figure 6.7 DSC-TGA-MS profile of as-prepared graphite (H_2) + $LiBH_4$ heated to 500 °C at a rate of 5 °C.min^{-1} under 3 bar Ar with a constant flow rate of 100 ml.min^{-1}

TGA-MS results of as-prepared graphite (H_2) + $LiBH_4$ heated to 500 °C (Figure 6.7) reveal the onset of H_2 desorption to be 210 °C, with two distinct peaks. The first H_2 desorption is centred around 287 °C coinciding with the melting of $LiBH_4$ seen by DSC and a weight loss of > 0.5 wt% between 270 °C and 300 °C consistent with pure $LiBH_4$ (Orimo et al., 2006). The second H_2 desorption is a result of the decomposition of $LiBH_4$ with peak H_2 desorption at 383 °C and a weight loss of 4.2 ± 0.1 wt% between 340 °C and 410 °C and a total weight loss of 6.4 ± 0.1 wt% by 500 °C. Trace amounts of methane were detected in agreement with the results for the 8 h milled graphite (H_2) sample. Diborane was also detected with an onset of 160 °C with peak B_2H_6 desorption at 270 °C. Although the detected quantity of diborane is low, a clear signal is visible. B_2H_6 release precedes H_2 desorption suggesting decomposition

of $LiBH_4$ into LiH and B_2H_6 (Equation 5.2) is the initial decomposition reaction in the as-prepared sample.

Direct decomposition of $LiBH_4$ into amorphous B (a-B), LiH and H_2 in the as-prepared graphite (H_2) + $LiBH_4$ sample would result in a theoretical weight loss of 6.6 wt% compared to 4.8 wt% from complete decomposition into $Li_2B_{12}H_{12}$. A total weight loss of 6.4 ± 0.1 wt% measured by TGA suggests that if $Li_2B_{12}H_{12}$ forms during the decomposition of $LiBH_4$, this intermediate compound continues to decompose into LiH, a-B and H_2. This two-step decomposition is consistent with the two-step reaction shown by DSC, the second decomposition peak is at 393 °C corresponding to a mass loss of 5 ± 0.1 wt%, further supporting that the two decomposition reactions are a result of $LiBH_4$ decomposition first into the intermediate $Li_2B_{12}H_{12}$ and then finally LiH, a-B and H_2.

XRD patterns of dehydrided graphite (H_2) + $LiBH_4$ (Figure 6.9b) confirmed graphite and LiH as the only crystalline products of decomposition. Raman spectroscopy measurements on the dehydrided sample (Figure 6.10b) did not show any peaks consistent with $Li_2B_{12}H_{12}$, a-B or LiH. It is believed that modes consistent with these compounds may be hidden by the graphitic modes with higher peak intensities, LiH is difficult to probe using Raman spectroscopy due high levels of photoluminescence from visible and near-infrared lasers (Acton, 2013).

A Pawley refinement of the XRD data was performed on the dehydrided sample calculated a c-direction lattice size of 6.758 ± 0.001 Å (Table 6.3), an increase of 0.030 ± 0.002 Å compared to the as-prepared sample.

To help identify the decomposition pathway of the as-prepared graphite (H_2) + $LiBH_4$ in situ XRD measurements were carried out, Figure 6.8. The as-prepared sample was heated to 400 °C at 2 °C.min^{-1} under 3 bar He flowing at 100 ml.min^{-1} and XRD patterns were collected during heating. Intense reflections from the sample holder made from Al_2O_3 are identified by black circle markers and do not shift with temperature.

Upon heating, the $LiBH_4$ under goes a phase change from o-$LiBH_4$ to h-$LiBH_4$ between 100 °C and 125 °C, as shown by DSC measurements (Figure 6.7). At 280 °C the $LiBH_4$ melts resulting in a loss in long-range order and hence reflections from $LiBH_4$ are no longer observed. A low intensity phase observed between 280 °C and 291 °C was identified as monoclinic $Li_4B_2O_5$ indicating oxidation had occurred. By 308 °C reflections from $Li_4B_2O_5$ disappeared and the more lithium-rich, lithium borate (Li_3BO_3) is observed and remains in the sample through the remaining heating and cooling. Reflections consistent with LiH cannot be distinguished due to over-lapping peaks from Li_3BO_3.

The (002) peak of graphite does not shift linearly to lower 2θ values with heating as would be expected from thermal expansion of the graphite lattice. Expansion only occurs when temperatures exceed 308 °C (near to the onset of $LiBH_4$ decomposition) where the (002) peak can be seen to rapidly shift to lower 2θ values. This behaviour is not observed during cooling in which the lattice contracts linearly over the whole temperature range. These results suggest the presence of $LiBH_4$ in the graphite sample acts to oppose the thermal expansion of the lattice as seen in previous work (Vines, 2013).

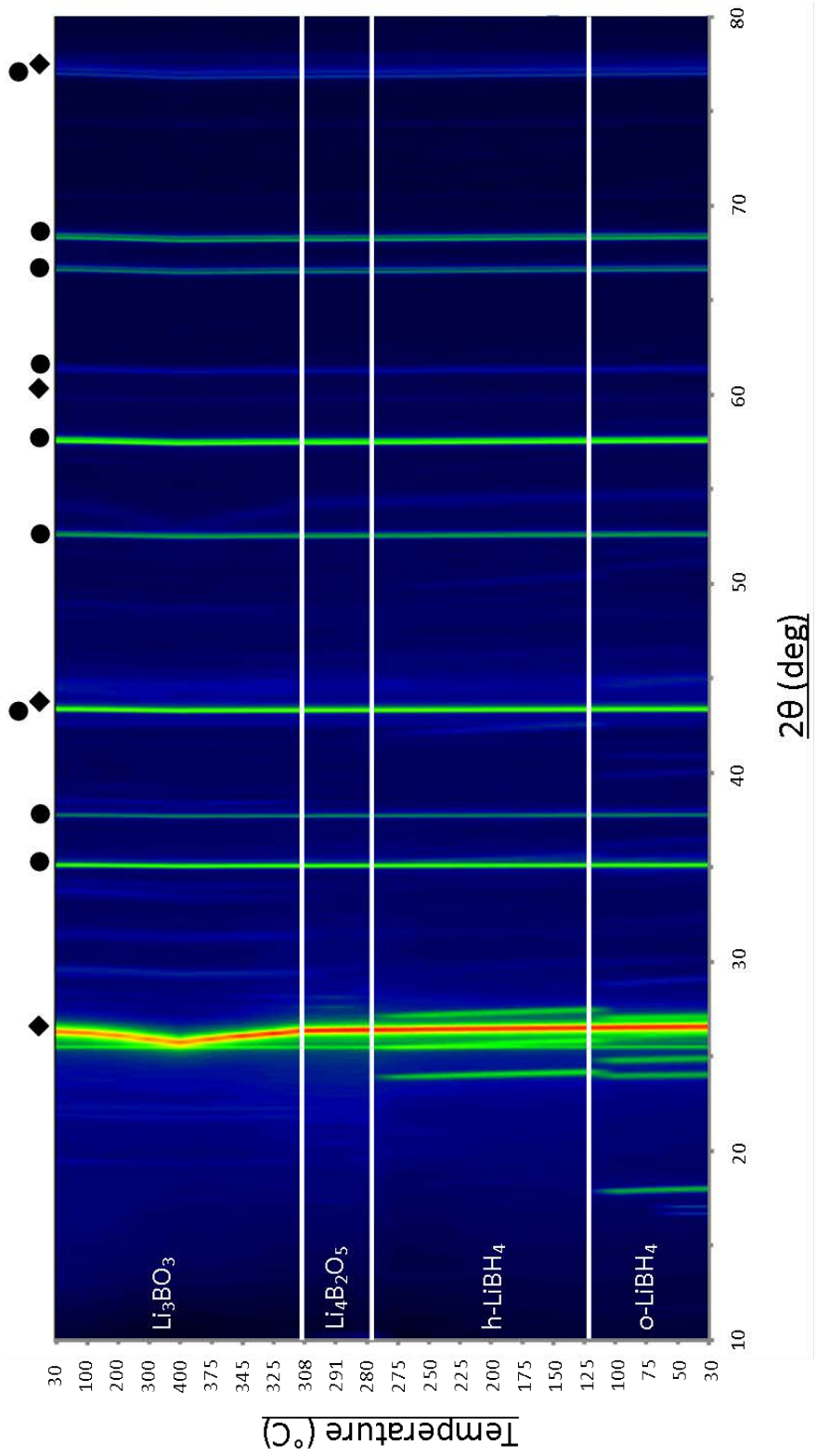

Figure 6.8 In-situ XRD results of as-prepared graphite (H_2) + $LiBH_4$ heated to 400 °C at 2 °C.min^{-1} under 3 bar He. Peak intensity is indicated by a spectrum of colours, with low intensity indicated by dark blue and high intensities indicated by red. Intense reflections consistent with graphite are indicated by black diamond markers and reflections from the Al_2O_3 sample holder indicated by black circles markers. The ICDD PDF2 database (2011) was used for phase identification

6.3 Rehydrogenation Investigation

As-prepared graphite (H_2) + $LiBH_4$ was heated to 400 °C under 3 bar He to form a dehydrided sample. An attempt was then made to rehydride the sample, by heating at 350 °C under 100 bar H_2 for 10 h.

6.3.1 X-Ray Diffraction

Figure 6.9c shows the XRD pattern of the attempt to rehydride a dehydrided sample. Reflections from crystalline $LiBH_4$, LiH and graphite are observed providing evidence that $LiBH_4$ has successfully been reformed under less extreme conditions than those reported for pure $LiBH_4$ (350 °C and 155 bar H_2 (Mauron et al., 2007)).

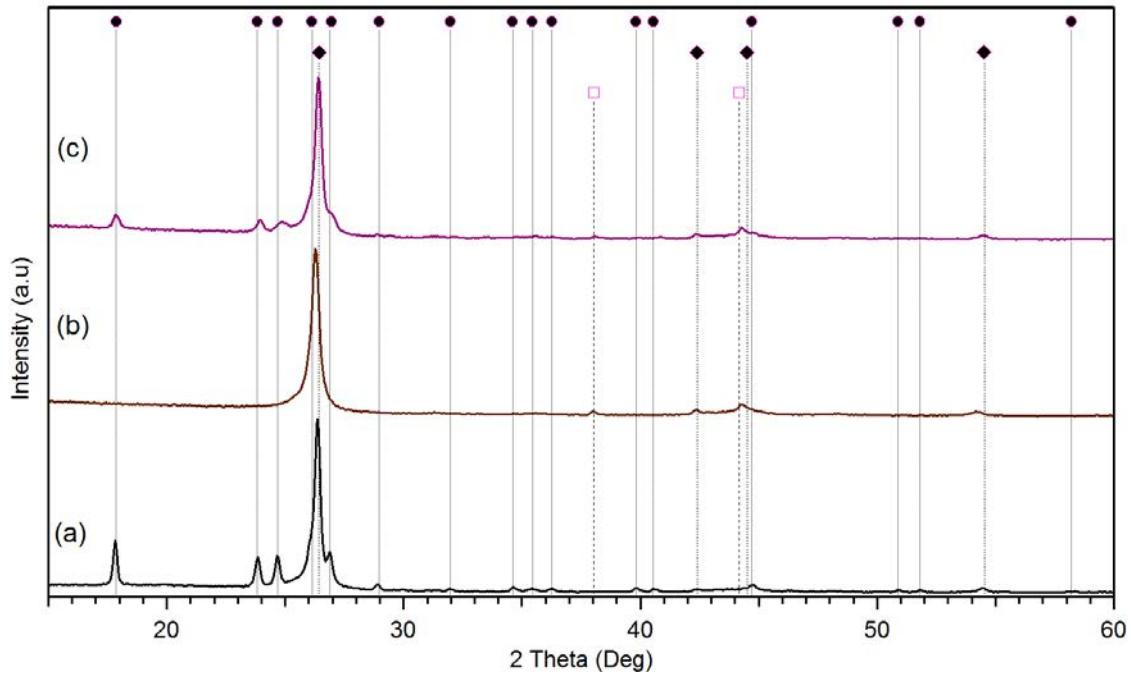

Figure 6.9 Room temperature XRD patterns of (a) as-prepared graphite (H_2) + $LiBH_4$, (b) dehydrided graphite (H_2) + $LiBH_4$ and (c) rehydrided graphite (H_2) + $LiBH_4$. Reflections from graphite are indicated by the black diamonds, $LiBH_4$ by black circles and LiH by hollow purple squares. The ICDD PDF2 database (2011) was used for phase identification

Pawley refinement calculations (Table 6.3) determined the c-plane lattice spacing of graphite in the rehydrided sample to be 6.730 ± 0.001 Å, very similar to that of the as-prepared sample indicating the c-plane spacing in graphite returns to its original value upon recombination of $LiBH_4$ after the expansion observed for the dehydrided sample.

Table 6.3 c-direction lattice spacing calculated for as-prepared and de/rehydrided graphitic samples via the Pawley refinement method

Sample	c-Direction Spacing (Å)
As-prepared graphite (H_2) + $LiBH_4$	6.728 ± 0.002
Dehydrided graphite (H_2) + $LiBH_4$	6.758 ± 0.001
Rehydrided graphite (H_2) + $LiBH_4$	6.730 ± 0.001

Quantitative phase analysis could not be performed on the rehydrided sample due to high amorphous content of graphite and potential a-B. Based on the relative peak intensities of the (101) $LiBH_4$ peak to the (002) graphite peak, an estimated 50 % of initial $LiBH_4$ was successfully reformed.

6.3.2 Raman Spectroscopy

The Raman spectrum of rehydrided graphite (H_2) + $LiBH_4$ (Figure 6.10c) is very similar to that of the as-prepared and dehydrided graphite (H_2) + $LiBH_4$ with the D, G, D' G' and D+G bands all present. The crystallite size of the rehydrided sample was calculated, and the results are shown in Table 6.1.

The crystallite size decreases after the rehydrogenation of the sample indicating that the re/de-hydrogenation processes are potentially destructive to the graphitic microstructure. As was observed for the as-prepared sample, the presence of $LiBH_4$ could not be confirmed by Raman spectroscopy, but was detected by XRD.

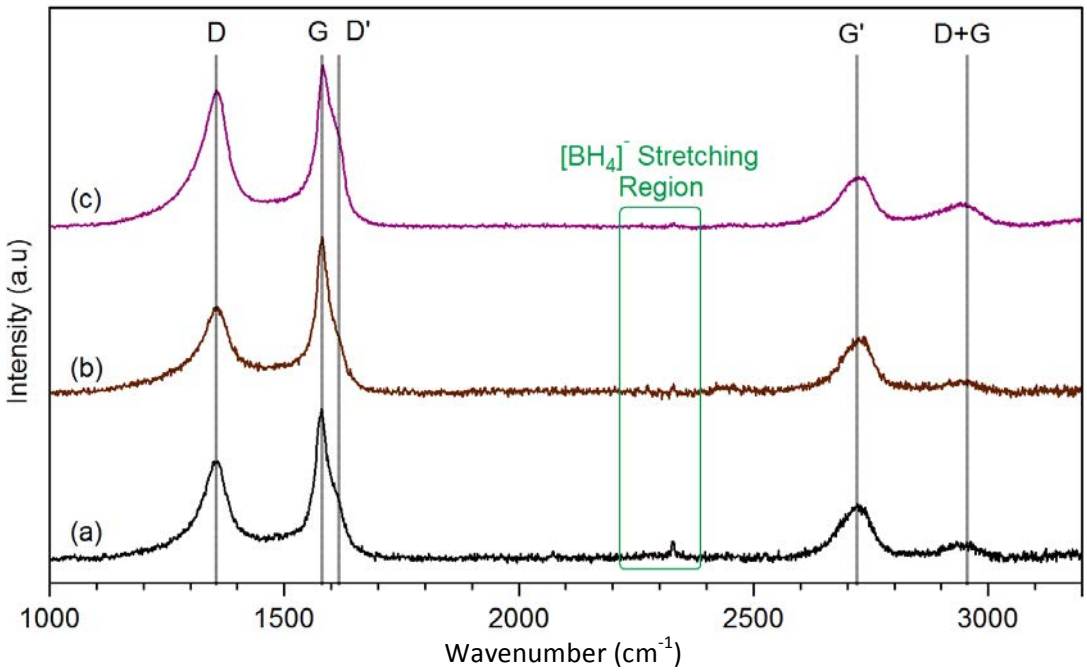

Figure 6.10 Room temperature Raman spectra of (a) as-prepared graphite (H_2) + $LiBH_4$ (b) dehydrided graphite (H_2) + $LiBH_4$ (c) rehydrided graphite (H_2) + $LiBH_4$ measured under 100 ml.min^{-1} flowing Ar. The location of the D, G, D' G' and D+G bands are indicated by the dotted black lines.

Table 6.4 Calculated G and D band peak fits and crystallite sizes for each graphitic sample calculated from Raman Spectra in Figure 6.10.

-	D Peak		G Peak		-
Sample	**Location (cm^{-1})**	**Height (a.u)**	**Location (cm^{-1})**	**Height (a.u)**	**La (nm)**
Graphite+LiBH4	1352.2 ± 0.3	65.6 ± 0.7	1579.1 ± 0.2	48.1 ± 0.8	9.9 ± 0.2
Dehydrided	1354.7 ± 0.4	71.0 ± 0.6	1580.8 ± 0.2	50.5 ± 0.7	9.6 ± 0.2
Rehydrided	1351.3 ± 0.2	94.5 ± 0.4	1584.2 ± 0.2	58.1 ± 0.7	8.3 ± 0.1

6.3.3 Thermal Decomposition

The thermal decomposition of the rehydrided sample was studied using DSC-TGA-MS, Figure 6.11. DSC measurements show three endothermic peaks as seen during the heating of the as-prepared sample. The orthorhombic to hexagonal phase transition decreases by 7 °C to 107 °C compared to the as-prepared sample along with a reduction in melting temperature to 260 °C. The shape of the melting peak can also be seen to change from a lorentzian shape to a broad asymmetric Gaussian. This result is consistent with $LiBH_4$ nano-confined in porous carbons as seen by Liu et al., (2011); Zhang et al., (2007).

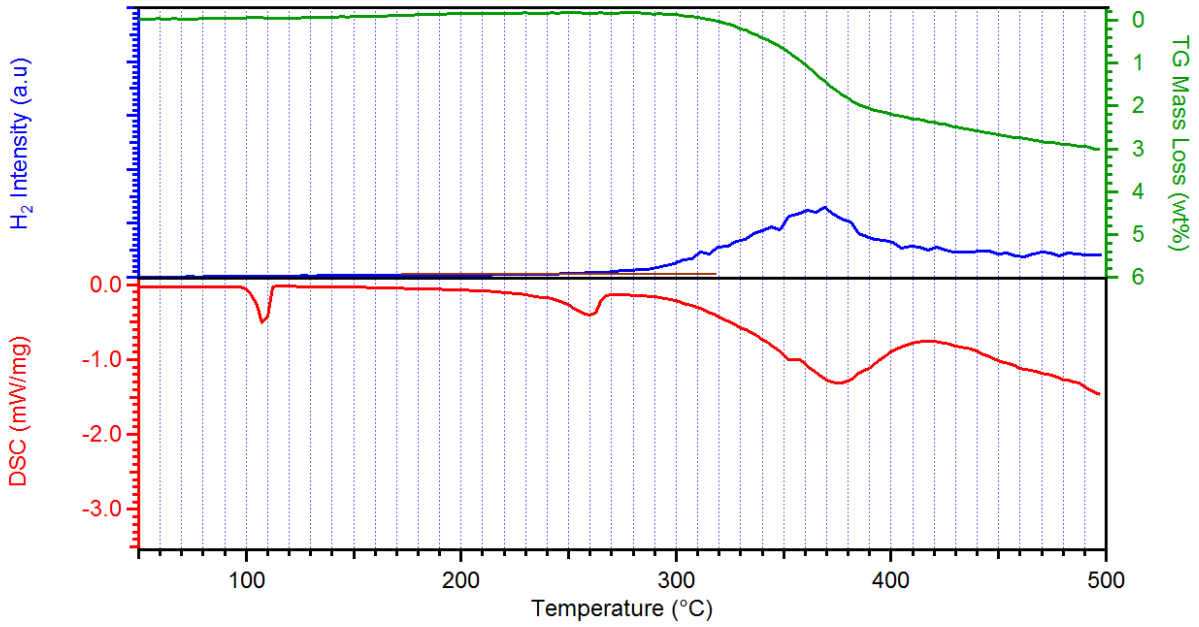

Figure 6.11 DSC-TGA-MS profile of rehydrided graphite (H_2) + $LiBH_4$ heated to 500 °C at a rate of 5 °C.min^{-1} under 3 bar Ar with a constant flow rate of 100 ml.min^{-1}

Decomposition of the rehydrided sample still proceeds through a two-step decomposition of $LiBH_4$ as observed for bulk $LiBH_4$ (Figure 2.17) and the as-prepared sample (Figure 6.7). The onset of decomposition was also found to occur 30 °C lower (at 300 °C) compared to the onset for as-prepared sample although completion of decomposition only finished 10 °C lower in the rehydrided sample.

No H_2 or wt% loss was detected as a result of melting, suggesting the state of the $LiBH_4$ within the sample has changed after cycling. A single asymmetric H_2 desorption peak was observed with an onset of 265 °C and peak H_2 release at 369 °C concurrent with the second step in the 2 step decomposition seen by DCS. A total of 3.0 ± 0.1 wt% H_2 was desorbed by 500 °C implying that 46 % of the initial storage capacity was achieved after 10 h of hydrogenation. No methane was detected during heating. Traces of diborane were detected between 200 °C and 400 °C.

Since B_2H_6 was observed in both of the as-prepared and rehydrided samples as well as both exhibiting decomposition through a two-step reaction with the majority of H_2 release occurring during the second step, the decomposition pathways are believed to be identical.

6.3.4 Cyclic H_2 Uptake Stability

The cyclic stability of the sample was studied over 5 de/re-hydrogenation cycles using a Sieverts apparatus to measure the isothermal H_2 uptake at 350 °C as a function of sample wt% and H_2 pressure, Figure 6.12. The low total H_2 uptake of the 1st cycle is a result of the unintended exposure of the sample to 25 bar H_2 at 350 °C after dehydrogenation, resulting in partial hydrogenation before cycling was commenced. The H_2 storage capacity of the

graphite (H_2) + $LiBH_4$ sample can be seen to decrease after each cycle, but appears to stabilise around 1.8 ± 0.1 wt% after 5 cycles. There is a large drop in the material's H_2 capacity from 73 % to 27 % of the initial capacity. XRD measurements on the cycled sample (in a dehydrided state) indicated oxidation has occurred during cycling with intense reflections from Li_3BO_3 being observed, along with LiH and graphite. The oxide phase may be responsible for the reduction in cyclic capacity. Quantitative phase analysis could not be completed due to high amorphous content of graphite as a result of milling and potential amorphous B from $LiBH_4$ decomposition, techniques such as quantitative NMR are required.

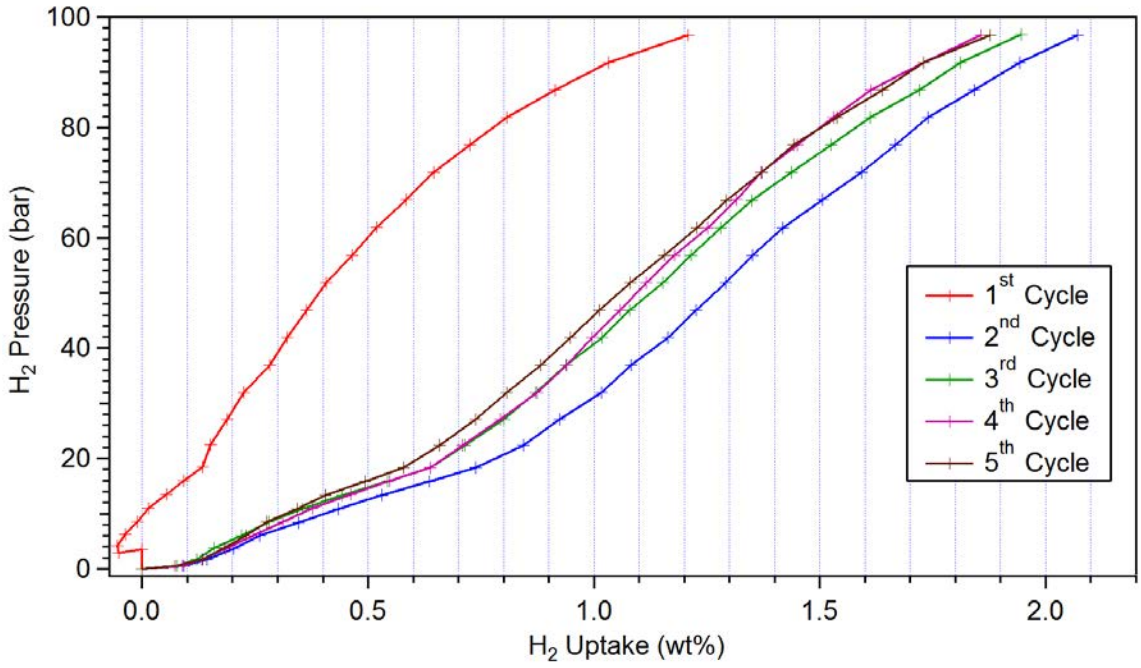

Figure 6.12 Cyclic H_2 uptake isotherms of graphite (H_2) + $LiBH_4$ measured at 350 °C as function of H_2 pressure

6.4 Discussion

Ball milling of graphite under a H_2 atmosphere induces nano-crystallinity and defects into the graphite lattice as confirmed by XRD and Raman spectroscopy measurements; this behaviour is well documented in the literature (Orimo et al., 1999; Huang et al., 2007; Chen et al., 2003; Zhang et al., 2009; Fukunaga et al., 2004). TGA-MS results of 8 h milled graphite (H_2) indicated a very small hydrogen desorption of 0.3 ± 0.1 wt% when heated to 500 °C which is 1.2 wt% less than that achieved by (Zhang et al., 2012) under the same milling conditions. Three separate batches of sample were milled under these conditions with none of the 8 h milled graphite (H_2) samples desorbing >0.5 wt%. Since the presence of C-H bonding could not be probed with the characterisation equipment available (UV Raman is required to detect $sp^3C\text{-}H_x$ vibrations (Ferrari and Robertson, 2001)) the term hydrogenated graphite must be used with caution. Since hydrogen was successfully detected by MS during heating of 8 h milled graphite (H_2) the graphite can be considered partially hydrogenated.

The addition of partially hydrogenated graphite to $LiBH_4$ successfully lowered the decomposition temperature of bulk $LiBH_4$ by almost 100 °C, suggesting the graphite catalyses the decomposition and recombination of $LiBH_4$. The presence of diborane was confirmed by MS; the onset of B_2H_6 desorption occurred just after the orthorhombic to hexagonal phase transformation of $LiBH_4$ with peak desorption occurring just before melting, agreeing with work by Kato et al. (2010) who found the majority of B_2H_6 was desorbed from the solid hexagonal phase of $LiBH_4$. B_2H_6 is a possible intermediate in the decomposition of $LiBH_4$ and

as such the H_2 released before bulk decomposition may originate from an interaction between $LiBH_4$ and B_2H_6 (Equation 5.3).

The small quantity of H_2 detected during the heating of the 8 h milled graphite (H_2) sample allows for the assumption that any significant quantity of hydrogen desorbed from the as-prepared sample originated from $LiBH_4$. The as-prepared sample desorbed a total of 6.4 wt% H_2 (and trace B_2H_6) by 500 °C through a two-step reaction consistent with the decomposition of pure $LiBH_4$. Only LiH and graphite were observed in the dehydrided sample with no $Li_2B_{12}H_{12}$ detected at any stage. Pawley refinement on the XRD pattern of dehydrided graphite (H_2) + $LiBH_4$ revealed an expansion in the c-direction from 6.728 ± 0.002 Å to 6.758 ± 0.001 Å, suggesting possible formation of LiC_{72} (Konar et al., 2015) resulting from the intercalation of Li in between the sheets of carbon atoms in the graphite.

In situ XRD measurements were unable to identify the presence of any intermediate phases during decomposition with only reflections from oxide phases visible after the melting of $LiBH_4$ as they crystallize out of the molten $LiBH_4$ during decomposition. As such the intermediate decomposition pathway of the as-prepared graphite (H_2) + $LiBH_4$ sample could not be confirmed, however, since a small quantity of B_2H_6 was detected before bulk decomposition, it is possible the decomposition first proceeds through Equations 5.2 and 5.3 giving rise to the evolution of B_2H_6 and H_2 before rapid decomposition occurs through either the decomposition of $Li_2B_{12}H_{12}$ formed from Equation 5.3 or Equation 5.4. Finally some LiH is then believed to further decompose and intercalate within the graphite sheets, Equation 5.5.

Li and H are both very light elements resulting in a low cross section scattering factor; LiH reflections have a low intensity in XRD. Along with the low levels of detected B_2H_6 and

formation of Li_3BO_3, this helps to explain why no LiH reflections are seen in the in situ data. Li_3BO_3 has been shown to catalyse the decomposition and recombination of $LiBH_4$ improving the reaction kinetics associated with each process (Ma et al., 2016), see Section 2.7.2.4.

Recombination of $LiBH_4$ was achieved at a lower pressure than has been so far reported for $LiBH_4$ (Mauron et al., 2007) supporting the argument that the graphite acts catalyse the decomposition and recombination of $LiBH_4$. An estimated 46-50% of the initial $LiBH_4$ was reformed under 100 bar H_2 at 350 °C.

Similar results were achieved in a graphite +$LiBH_4$ sample milled under Ar for 1 h (Fang et al., 2010b). A decrease in the decomposition temperature of the $LiBH_4$ of 40 °C was observed, with a total of 9.9 wt% desorbed by 500 °C from the $LiBH_4$ in the sample. Rehydrogenation found to be possible under 100 bar H_2 at 400 °C, however, the cyclic capacity was also found to reduce by over 70% after one cycle.

7 Activated Carbon + $LiBH_4$

In this chapter the hydrogen storage properties of $LiBH_4$ added to activated carbon are studied in order to help understand the influence on of pore structure and surface area of materials added to $LiBH_4$.

7.1 Characterisation of As-Prepared Sample

The starting materials, non-PM AC+$LiBH_4$ and PM AC+$LiBH_4$ were characterised by XRD, Raman spectroscopy and N_2 adsorption isotherms with BET surface area analysis; PM=pre-melted.

7.1.1 X-Ray Diffraction

Figure 7.1 shows the XRD patterns of AC, as-received $LiBH_4$, non PM AC+$LiBH_4$ and PM AC+$LiBH_4$. The XRD pattern of AC is as expected, two broad peaks consistent with the amorphous structure of activated carbon. As-received $LiBH_4$ shows reflections consistent with orthorhombic $LiBH_4$ (o-$LiBH_4$), and no other crystalline phases.

After hand mixing, the non-PM AC+$LiBH_4$ sample does not exhibit any new peaks, confirming that hand-mixing of AC and $LiBH_4$ does not result in any solid state reactions, but forms a

mixture of the two materials. The intensity of the broad peaks produced by AC can be seen to decrease due to the high relative intensity of reflections from o-$LiBH_4$.

After the pre-melting process, the intensity of these broad peaks increases relative to those of $LiBH_4$ suggesting a change in the structure of mixture. A reduction in the long-range ordering of the $LiBH_4$ due to potential confinement within the amorphous porous structure of AC or coating of the surface of the AC scaffold offer explanations for this. No new phases are seen after melt-infiltration indicating that hand-mixing of AC and $LiBH_4$ followed by pre-melting under a H_2 back pressure is a viable way to produce a mixture of $LiBH_4$ confined within the structure of AC.

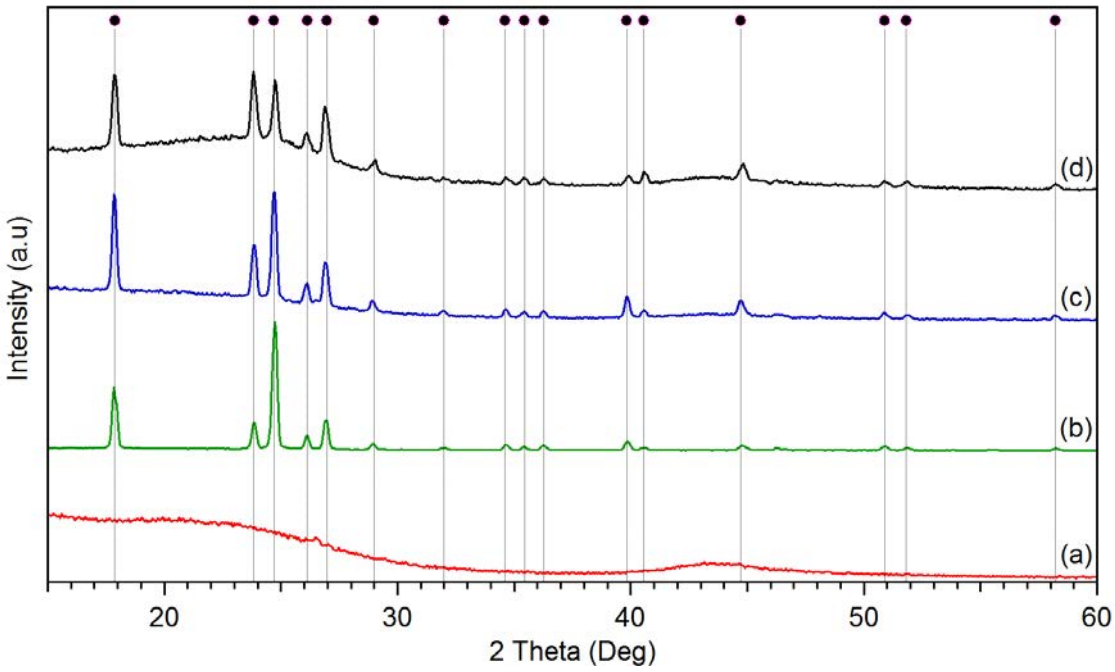

Figure 7.1 Room temperature XRD patterns of (a) dried AC, (b) as-received $LiBH_4$, (c) Non-PM AC+$LiBH_4$ and (d) PM AC+$LiBH_4$. Reflections consistent with $LiBH_4$ are indicated by the dashed lines and black circles. The ICDD PDF2 database (2011) was used for phase identification

7.1.2 Raman Spectroscopy

Figure 7.2 shows the Raman spectra of AC, as-received $LiBH_4$, non PM AC+$LiBH_4$ and PM AC+$LiBH_4$. The Raman spectrum of AC shows two large peaks located at 1351 cm^{-1} and 1600 cm^{-1}. The first peak was identified as the D mode of graphite, a forbidden Raman transition only permitted in the presence of defects within the sheets of carbon atoms.

The Raman spectrum of as-received $LiBH_4$ shows vibrations consistent with the bending and stretching of $[BH_4]^-$ tetrahedral units within $LiBH_4$ as labelled on the graph. After hand mixing these vibrations are no longer visible in the Raman spectrum of Non-PM AC+$LiBH_4$, and return after the pre-melting process providing evidence that the pre-melting process created a homogeneous mixture of AC and $LiBH_4$. It was not possible to estimate the crystallite size of the AC as a good fit of the D and G band could not be achieved with the high contribution from the D' band and high intensity between the D and G/D' peaks making peak fit analysis with the available software tools impossible.

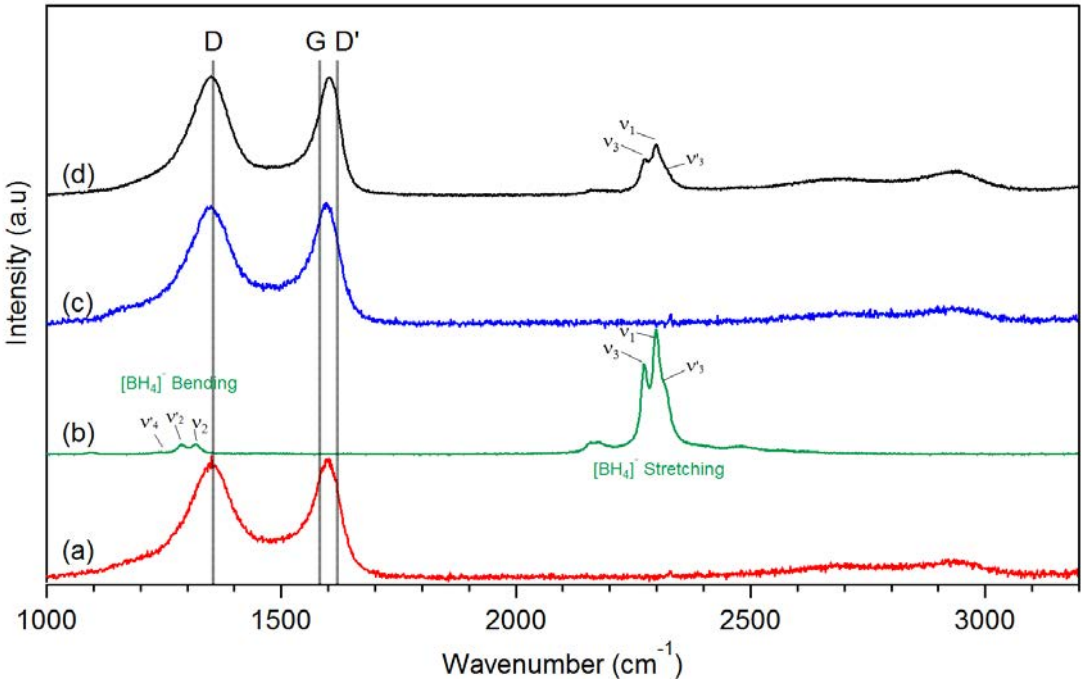

Figure 7.2 Room temperature Raman spectra of (a) dried AC, (b) as-received $LiBH_4$, (c) Non-PM AC+$LiBH_4$ and (d) PM AC+$LiBH_4$. The D, G, and D' bands are marked by the black dashed lines. The $[BH_4]^-$ bending and stretching modes of $LiBH_4$ are labelled along with the origin of each vibration

7.1.3 N_2 Adsorption Isotherm & BET

The nitrogen gas (N_2) adsorption isotherm of AC was measured at -195 °C, Figure 7.4. The AC sample was found to adsorb 42.9 wt% N_2 at 950 mbar. The adsorption data point at 65 mbar, 25.3 wt% does not fit with the adsorption trend due to an experimental error in which the sample temperature did not reach -195 °C before the measurement was started. BET analysis on the N_2 adsorption isotherm is shown in Figure 7.4. The BET surface area was calculated to be 958 ± 16 m^2g^{-1}, which lies within the expected range for commercially available activated carbons (500-1500 m^2g^{-1}, (Varin et al., 2009)).

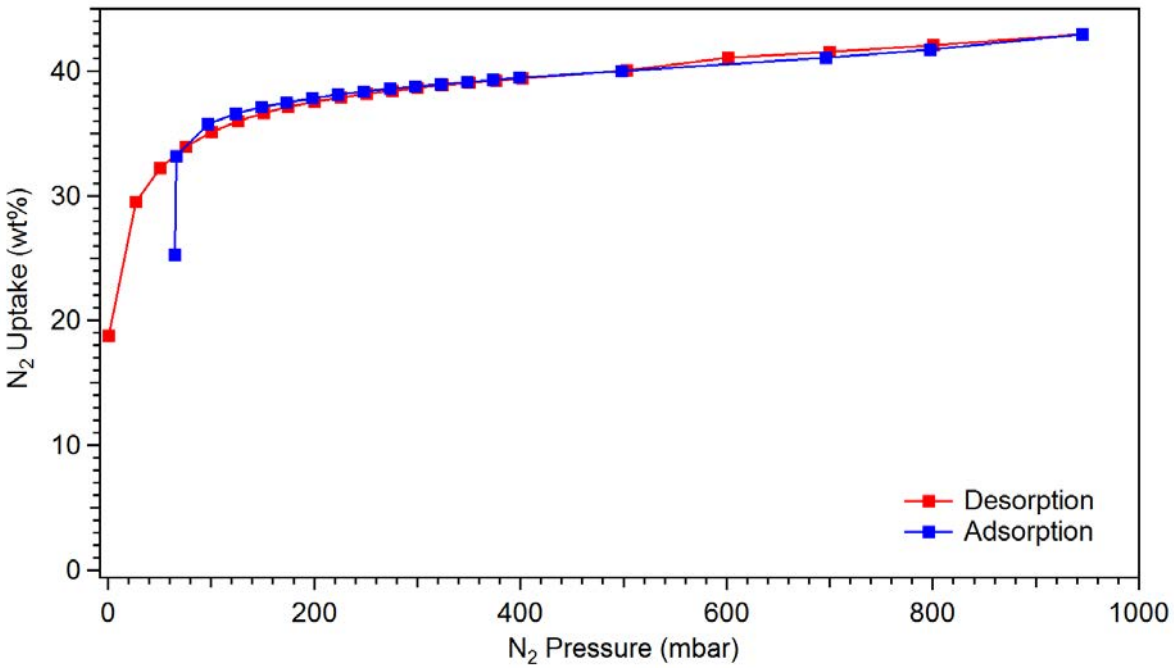

Figure 7.3 N_2 adsorption and desorption isotherm of dried AC at -195 °C

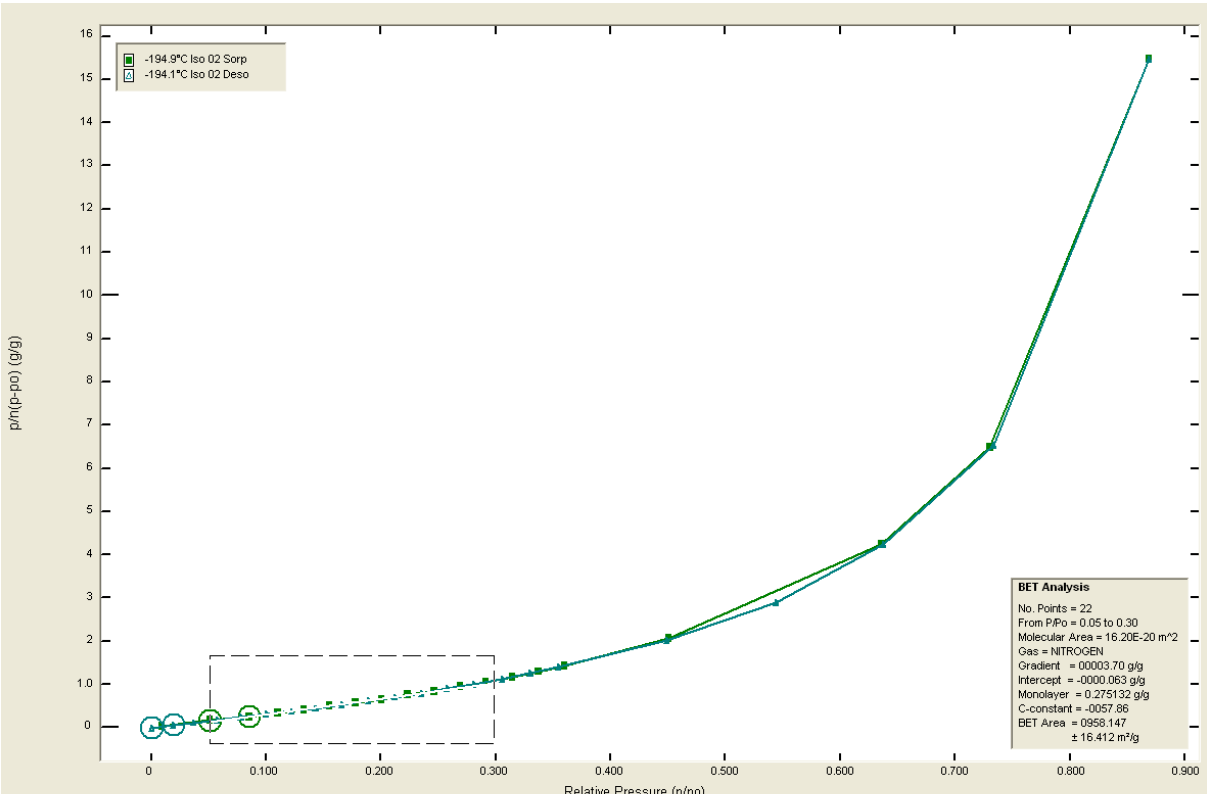

Figure 7.4 BET Analysis for dried AC calculated from Figure 7.3, the fit parameters are shown in the bottom right corner of the graph

7.2 Thermal Decomposition

The thermal decomposition of non-PM AC+$LiBH_4$ and PM AC+$LiBH_4$ were studied by DSC-TGA-MS. PM AC+$LiBH_4$ was investigated further using XRD, Raman and in-situ XRD.

7.2.1 DSC-TGA-MS

7.2.1.1 Non-PM AC+$LiBH_4$

The thermal decomposition of non-PM AC+$LiBH_4$ was investigated by DSC-TGA-MS, results are shown in Figure 7.5. The DSC profile closely resembles that for the decomposition of bulk $LiBH_4$ (Shao et al., 2014), 3 endothermic peaks corresponding to the orthorhombic to hexagonal phases change at 117 °C, melting at 288 °C and finally decomposition of $LiBH_4$ through a two step process ca. 380 °C. The two-step decomposition peak has minima at 376 °C and 393 °C.

The TGA-MS trace reveals two regions of rapid weight loss, the first occurs between 270 °C and 290 °C and results in a weight loss of 0.7 ± 0.1 wt%. This mass loss coincides with the melting of $LiBH_4$ and the release of H_2 and trace quantities of B_2H_6 (4 orders of magnitude lower than H_2). The sample then continues to lose weight steadily up to 360 °C desorbing a further 1 wt% H_2. This sustained release is then followed by the second and largest H_2 desorption peak at 393 °C, resulting in a further mass loss of 3.8 ± 0.1 wt% between 360 °C and 410 °C, after which the sample continues to slowly release H_2 desorbing a total of 7.5 ± 0.1 wt% by 500 °C. If it is assumed that all wt% loss is attributed to H_2 evolution, 85% of the total H_2 in the sample is desorbed by 500 °C indicating a significant improvement on

bulk $LiBH_4$ which desorbs less than half of its capacity by 500 °C (Züttel et al., 2003; Yu et al., 2010).

Although only trace quantities of B_2H_6 were detected, it is possible that larger quantities were released during the decomposition. B_2H_6 is a sticky gas and can adsorb onto the surface of the exhaust pipes, resulting in only a small quantity being detected.

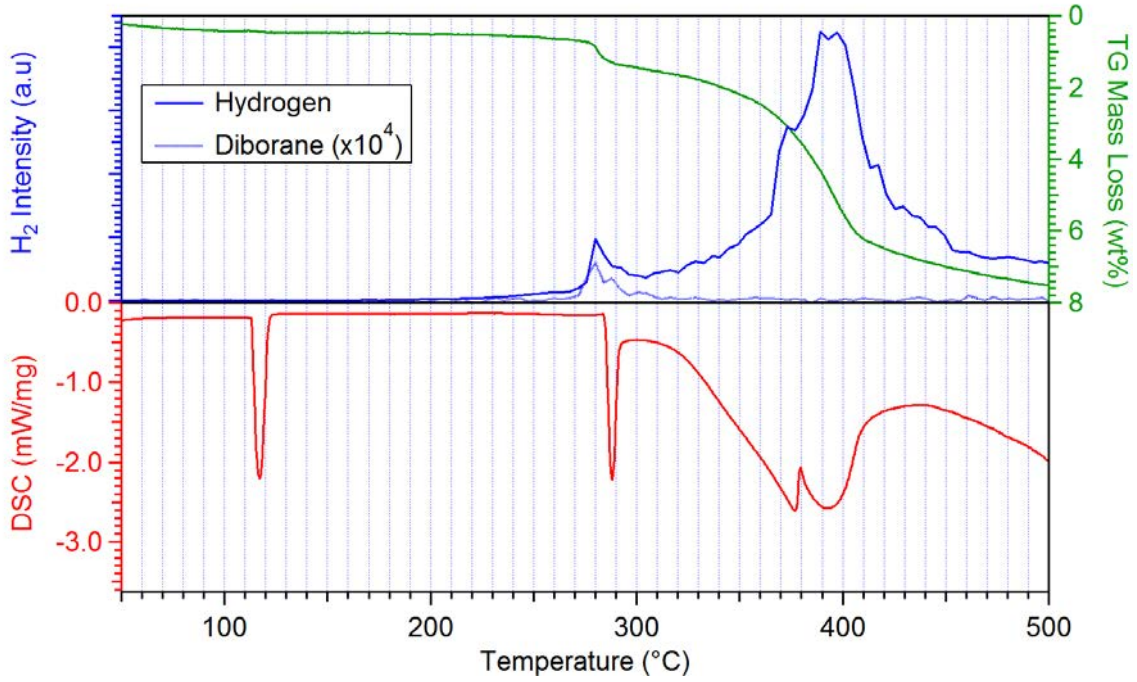

Figure 7.5 DSC-TGA-MS profile of Non-PM AC+$LiBH_4$ heated to 500 °C at 5 °C.min^{-1} under 3 bar Ar with a flow rate of 100 ml.min^{-1}

7.2.1.2 PM AC+$LiBH_4$

The thermal decomposition of PM AC+$LiBH_4$ was investigated by DSC-TGA-MS, results are shown in Figure 7.6. The DSC profile exhibits the same three endothermic peaks, seen in the DSC profile of non-PM AC+$LiBH_4$. The orthorhombic to hexagonal phase change at 117 °C, melting at 285 °C and the two-step decomposition of $LiBH_4$ ca. 389 °C with minima 386 °C

and 400 °C. After the pre-melting process, the melting temperature of $LiBH_4$ was found to decrease by 3 °C, whilst the location of the decomposition peak increased by 7-8 °C.

The TGA-MS trace reveals a single H_2 desorption 383 °C with an onset of 250 °C, 125 °C lower than that observed for bulk $LiBH_4$ (Shao et al., 2014). A total of 1.1 wt% is desorbed by 350 °C at which point the sample starts to rapidly desorb H_2, 3.5 ± 0.1 wt% between 350 °C and 400 °C with peak H_2 desorption occurring at 383 °C, 10 °C lower than the non-PM AC+$LiBH_4$. The sample continues to release H_2 at steady rate, desorbing a total of 5.9 ± 0.1 wt% by 500 °C, 1.6 ± 0.1 wt% less than non-PM AC+$LiBH_4$. On the other hand, no B_2H_6 was detected.

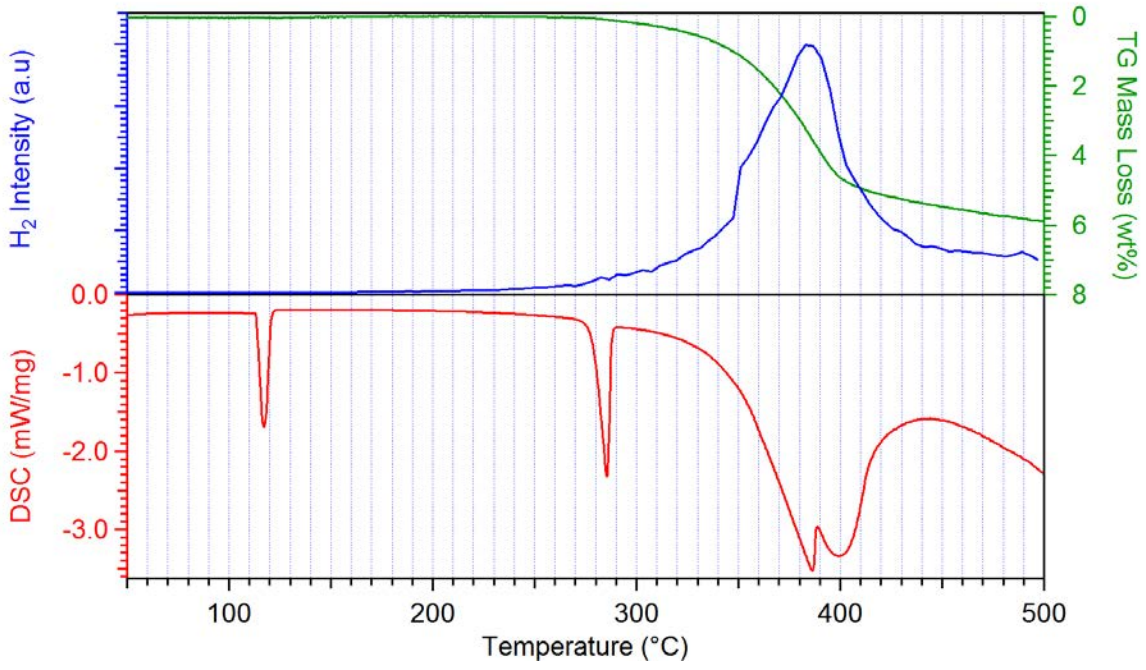

Figure 7.6 DSC-TGA-MS profile of PM AC+$LiBH_4$ heated to 500 °C at 5 °C.min^{-1} under 3 bar Ar with a flow rate of 100 ml.min^{-1}

7.2.2 X-Ray Diffraction

The XRD pattern of PM AC+$LiBH_4$ dehydrided at 400 °C under 3 bar Ar is shown in Figure 7.8b. No crystalline $LiBH_4$ remains in the sample after heating to 400 °C, confirming that the split peak seen in Figure 7.6 ca. 389 °C results from the decomposition of $LiBH_4$. After dehydrogenation, reflections from LiH are present, along with weak reflections consistent with Li_3BO_3 indicating partial oxidation of the sample during decomposition. No Li-C compounds were observed. Li_3BO_3 has been shown to improve decomposition and recombination kinetics of $LiBH_4$ (Ma et al., 2016).

Taking into account the 5.9 ± 0.1 wt% H_2 desorbed by the PM AC+$LiBH_4$ coupled with the presence of LiH in the dehydrided sample, it can be concluded that the majority of $LiBH_4$ in the sample decomposed via reaction (2) in Table 7.1, with some $LiBH_4$ reacting with oxygen to form stable Li_3BO_3.

Table 7.1 Expected H_2 Desorption in wt% for different possible decomposition pathways of $LiBH_4$

-	Reaction Pathway	H_2 Release (wt%)
(1)	$LiBH_4 \rightarrow Li + B + 2H_2$	8.80
(2)	$LiBH_4 \rightarrow LiH + B + {}^{3}/_{2}H_2$	6.60
(3)	$LiBH_4 \rightarrow {}^{5}/_{6}LiH + {}^{1}/_{12}Li_2B_{12}H_{12} + {}^{13}/_{12}H_2$	4.77

7.2.3 Raman Spectroscopy

The Raman spectrum of PM AC+$LiBH_4$ dehydrided at 400 °C under 3 bar Ar is shown in Figure 7.9. No vibrations originating from the bending of stretching of $[BH_4]^-$ tetrahedral units are seen in the spectrum, agreeing with XRD and DSC-TGA-MS that $LiBH_4$ within the sample decomposed by 400 °C. No new peaks are present in the spectrum.

The location of the D band in the dehydrided PM AC+$LiBH_4$ can be seen to down shift. This weakening of the sp^3 C-C bond maybe be a possible side effect of LiH or B sat in vacant sites, destabilising the C-C bonds.

7.2.4 In-situ X-Ray Diffraction

To further understand the decomposition pathway of $LiBH_4$ in the PM AC+$LiBH_4$ sample, the sample was studied by in-situ XRD. The sample was heated to 400 °C at 2 °C.min^{-1} and XRD measurements taken a regular temperature intervals, results are shown in Figure 7.7. Reflections from the Al_2O_3 sample holder are marked by black circles. By 125 °C the $LiBH_4$ can be seen to have undergone the orthorhombic to hexagonal phase transition observed by DSC (Figure 7.6), reflections from hexagonal $LiBH_4$ (h-$LiBH_4$) then persist up to 280 °C, their linear down shift is attributed to the thermal expansion of the $LiBH_4$ lattice. Upon melting, reflections from $LiBH_4$ disappear, as its long-range ordering is lost. Peaks consistent with the oxide phase Li_4 B_2O_5 are observed immediately after melting. Upon decomposition of the $LiBH_4$ at 325 °C, the more lithium rich Li_3BO_3 and LiO_2 phases appear, and remain in the sample through the remainder of the heating and cooling cycle.

It is clear that the sample heavily oxidised during decomposition, consequently the in-situ XRD results do not offer much insight into the decomposition pathway of $LiBH_4$ within PM AC+$LiBH_4$.

On the other hand, no $Li_2B_{12}H_{12}$ was observed by Raman spectroscopy or XRD, and LiH was identified by XRD. $LiBH_4$ was not found to react with the carbon scaffold, no Li_2C_2 was observed by XRD. It is therefore possible to conclude that $LiBH_4$ decomposes via reaction pathway (1) forming LiH and amorphous Boron. The presence of amorphous B could not be confirmed, however, its presence maybe implied by the formation of LiH and detection of H_2.

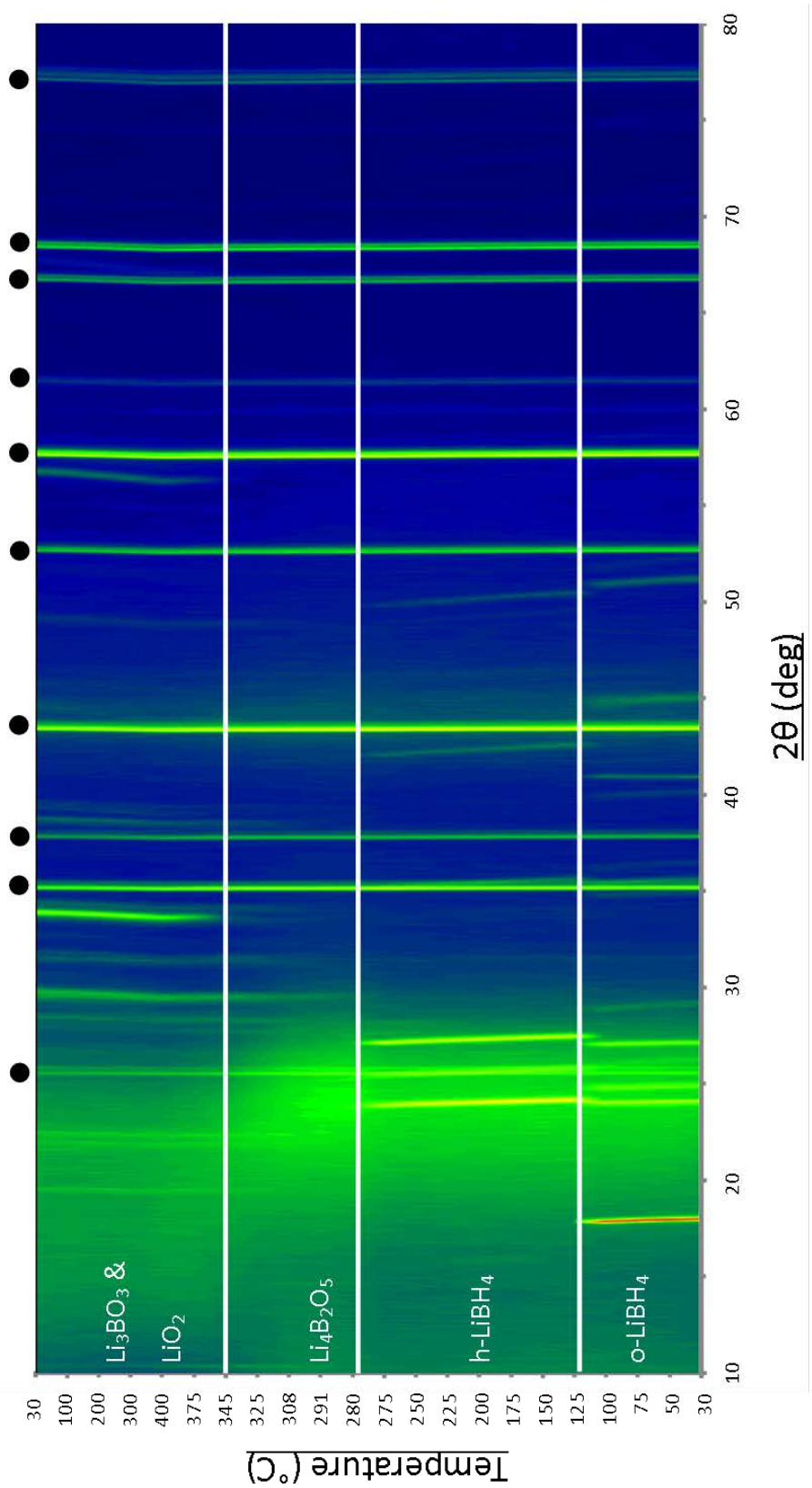

Figure 7.7 In situ XRD of PM AC+ LiBH4 heated to 400 °C at 2 °C.min-1 under 3 bar He, intensity is indicated by a spectrum of colours where red indicates high intensity and blue indicates low intensity. Reflections from the Al2O3 sample holder are marked with black circles. The ICDD PDF2 database (2011) was used for phase identification

7.3 Rehydrogenation investigation

PM AC+$LiBH_4$ was heated to 400 °C under 3 bar He to create a dehydrided sample, this sample was then rehydrided at 350 °C under 100 bar H_2 for 10 h, resulting in the sample referred to as rehydrided PM AC+$LiBH_4$.

7.3.1 X-Ray Diffraction

The rehydrided PM AC+$LiBH_4$ sample was studied by room temperature XRD, Figure 7.8. Strong reflections from o-$LiBH_4$ can be seen in the in the XRD pattern of rehydrided PM AC+$LiBH_4$ confirming the successful recombination of $LiBH_4$ under 350 °C and 100 bar H_2. Reflections from LiH are still present indicating that not all the $LiBH_4$ was successfully recombined during the 10 h process. Small quantities of Li_3BO_3 were also identified. The B contained within the oxide phase is unable to react with LiH within the sample to form $LiBH_4$, providing an explanation as to why some LiH remains in the rehydrided sample. As previously discussed Li_3BO_3 has been shown to improve the reaction kinetics of both decomposition and recombination of $LiBH_4$ (Ma et al., 2016) increasing H_2 uptake by a factor of 3 under 400 °C, as such the presence of Li_3BO_3 should not be ignored.

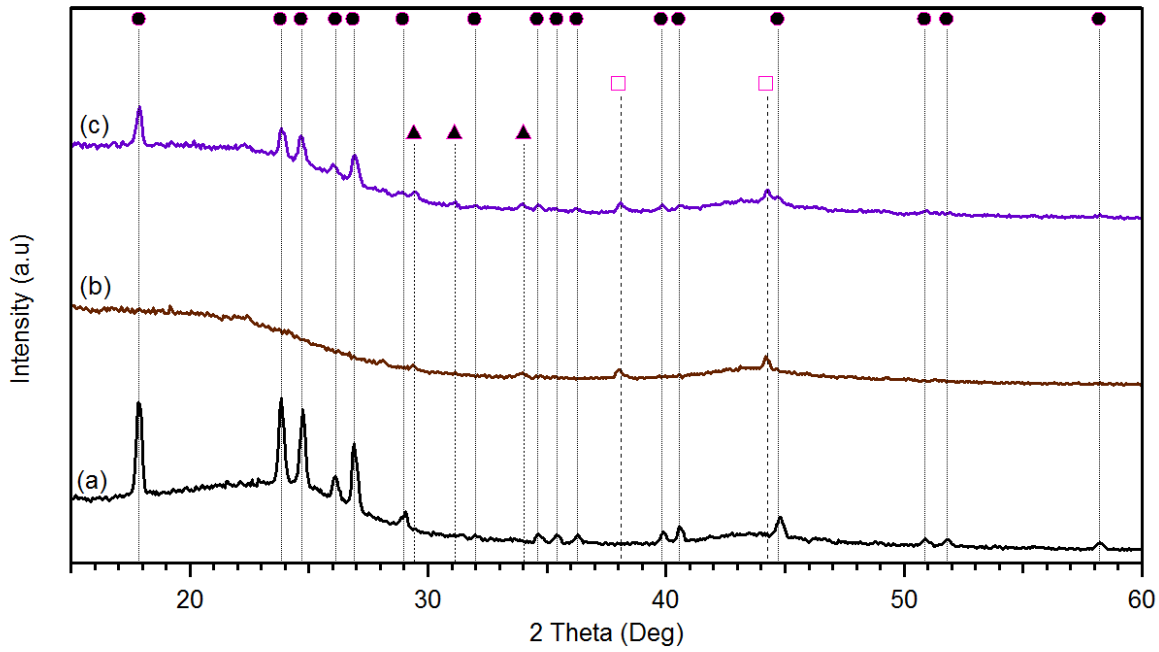

Figure 7.8 Room temperature XRD patterns of (a) PM AC+$LiBH_4$, (b) dehydrided PM AC+$LiBH_4$ and (c) rehydrided PM AC+$LiBH_4$. Reflections consistent with $LiBH_4$, LiH and Li_3BO_3 are indicated by black circles, hollow purple squares and black triangles respectively. The ICDD PDF2 database (2011) was used for phase identification

7.3.2 Raman Spectroscopy

The rehydrided PM AC+$LiBH_4$ sample was studied by room temperature Raman spectroscopy, Figure 7.9. Although the presence of $LiBH_4$ was identified by XRD, no vibrations from $[BH_4]^-$ tetrahedral units are visible in the Raman spectrum of rehydrided PM AC+$LiBH_4$ suggesting a lack of long rang order in the reformed $LiBH_4$. A number of different areas were measured by Raman spectroscopy on the rehydrided PM AC+$LiBH_4$, none of which showed vibrations from $LiBH_4$.

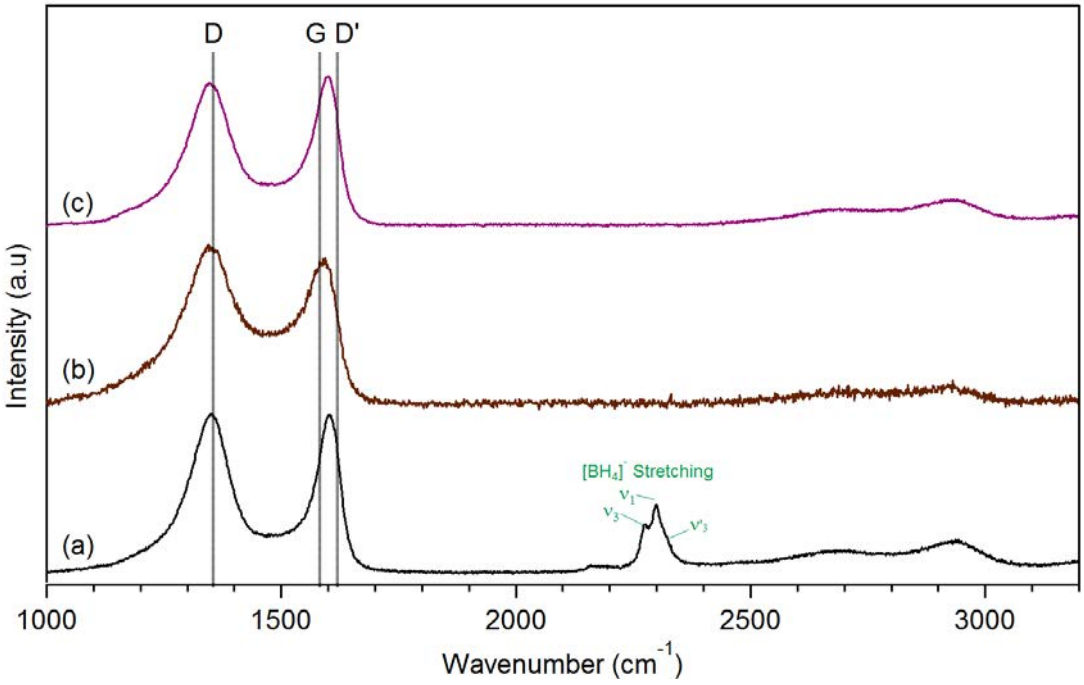

Figure 7.9 Room temperature Raman spectra of (a) PM AC+LiBH$_4$, (b) dehydrided PM AC+LiBH$_4$ and (c) rehydrided PM AC+LiBH$_4$. The D, G, and D' bands are marked by the black dashed lines. The [BH$_4$]$^-$ bending and stretching modes of LiBH$_4$ are labelled along with the origin of each vibration

7.3.3 DSC-TGA-MS

The thermal decomposition of rehydrided PM AC+LiBH$_4$ was investigated by DSC-TGA-MS, Figure 7.10. The DSC trace exhibits 3 endothermic peaks, the phase change from o-LiBH$_4$ to h-LiBH$_4$ at 117 °C, the melting of LiBH$_4$ at 266 °C and a singular asymmetric peak associated with the decomposition of LiBH$_4$ commencing immediately after melting with a minima at 353 °C.

The onset of H_2 desorption occurs at 250 °C coinciding with the onset of melting and the onset of wt%. H_2 desorption reaches its peak value at 338 °C with the sample desorbing 2.1 wt% by 370 °C, followed by a sustained H_2 release as seen for both PM AC+LiBH$_4$ and

non-PM AC+$LiBH_4$ resulting in a total of 3.4 ± 0.1 wt% H_2 being desorbed by 500 °C. No B_2H_6 was detected during decomposition.

Compared to PM AC+$LiBH_4$, $LiBH_4$ in the rehydrided sample melts over 20 °C lower, consistent with $LiBH_4$ confined within CMK (Zhang et al., 2007). Peak H_2 desorption also occurs 45 °C lower suggesting the state of the $LiBH_4$ in the rehydrided sample is different to that of as-prepared PM AC+$LiBH_4$.

By comparing the total wt% loss of PM AC+$LiBH_4$ and the rehydrided sample, 59% of the total $LiBH_4$ was reformed at 350 °C and 100 bar. The lowest conditions reported for recombination of bulk $LiBH_4$ is 350 °C and 155 bar H_2 (Mauron et al., 2007).

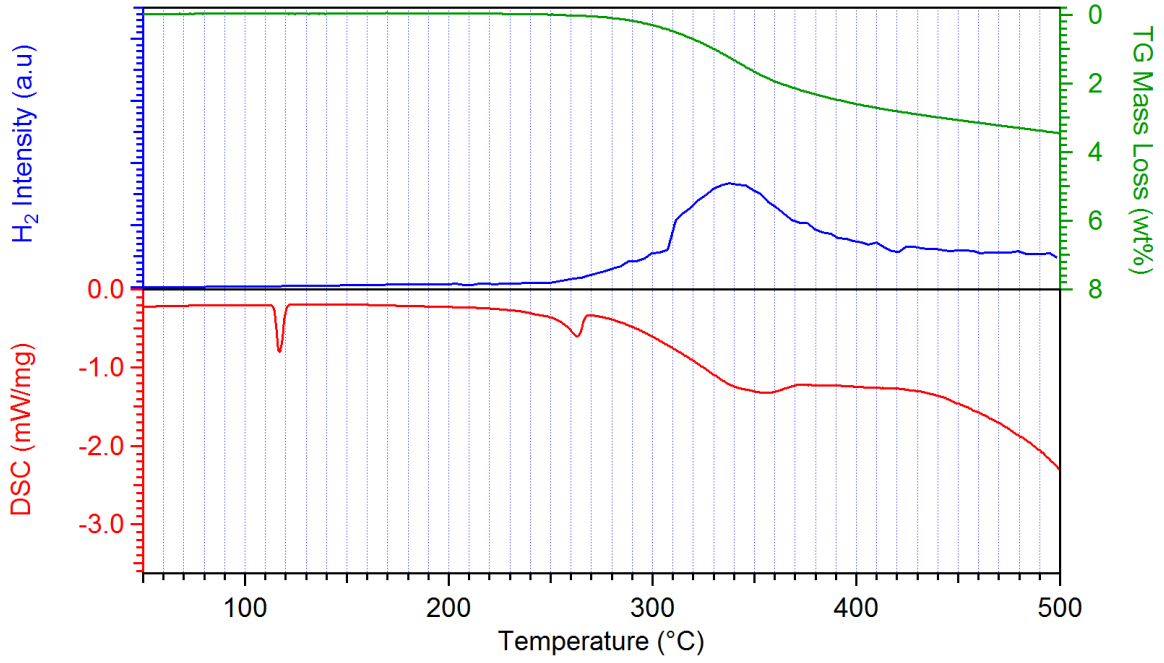

Figure 7.10 DSC-TGA-MS profile of rehydrided PM AC+$LiBH_4$ heated to 500 °C at 5 °C.min^{-1} under 3 bar Ar flowing at 100 ml.min^{-1}

7.3.4 Cyclic Uptake

The cyclic stability of the sample was studied over 5 re/de-hydrogenation cycles using a Sieverts apparatus to measure isothermal H_2 uptake at 350 °C as a function of the sample weight and H_2 pressure, Figure 7.11.

After 5 cycles, the sample was found to absorb 2.3 ± 0.1 wt% H_2, corresponding to 38% of the original capacity identified by TGA. The capacity was found to steadily decrease over cycling indicating degradation of the sample occurred. It is also evident from the isotherms that the sample was still absorbing H_2, this offers an explanation for the reduced capacity observed after one cycle, compared to that achieved by external hydrogenation (Figure 7.10). The shape of the adsorption isotherm suggests the rehydrogenation process is kinetically limited with the isotherm appearing to reach an adsorption plateau at 95 bar H_2. A two-step rehydrogenation process may also be inferred with two distinct adsorption gradients above and below 50 bar H_2. The first adsorption step corresponds to a H_2 uptake of 1 ± 0.1 wt% and is most likely a result of the reformation of LiH from fully decomposed $LiBH_4$.

7.4 Discussion

The pre-melting of AC + $LiBH_4$ has been shown to produce a homogenous mixture of the two compounds without the formation of any new phases as well as to suppress the release of B_2H_6 and H_2 upon melting. It is possible that the pre-melting process results in a layer $LiBH_4$ coating the surface of the activated carbon and becoming confined within its amorphous pore structure altering the decomposition mechanism of $LiBH_4$ compared to bulk $LiBH_4$).

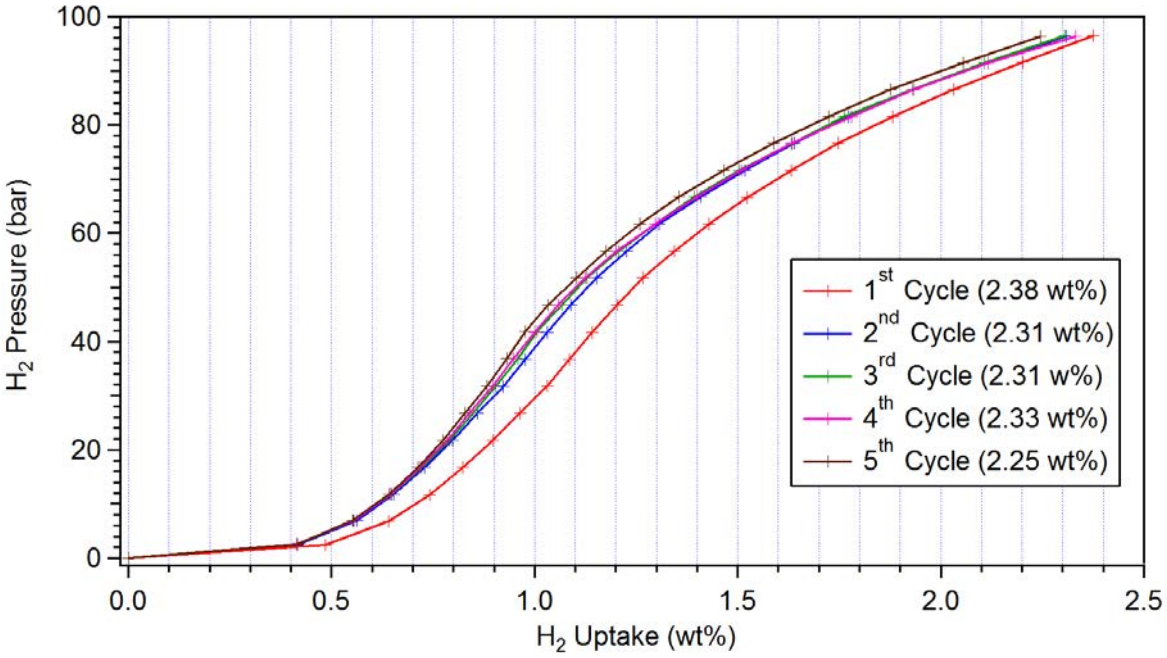

Figure 7.11 Cyclic H_2 uptake isotherms of PM AC+$LiBH_4$ measured at 350 °C as a function of H_2 pressure and uptake, the final H_2 uptake after each cycle is displayed

These results suggest that eliminating hydrogen evolution at melting helps to prevent B_2H_6 release and consequently that the two events are linked. With the absence of B_2H_6 production during the decomposition of PM AC + $LiBH_4$ it is clear the initial reaction pathway differs after the pre-melting process but both samples release the majority of their H_2 through a two step reaction (as shown by DSC) consistent with the decomposition of bulk LiBH4 just below 400 °C. The proposed decomposition pathway for the non-PM AC + $LiBH_4$ sample is shown in Equations 5.1 and 5.2, whilst the decomposition pathway for PM AC + $LiBH_4$ is shown in Equation 5.3.

The higher wt% loss observed for the non-PM AC + $LiBH_4$ sample can be attributed to the further decomposition of LiH into Li and H_2 with a small contribution from the production of the heavier B_2H_6 desorbed upon melting or the decomposition of LiH into H_2.

The addition of the activated carbon to $LiBH_4$ is also shown to reduce the temperatures and pressures required to recombine $LiBH_4$ to more moderate conditions of 350 °C and 100 bar H_2, with close to 60% (Figure 7.10) of its desorbed capacity being restored over 10 h. The loss in capacity is believed to be due to a combination of slow kinetics indicated by H_2 absorption isotherms and presence of LiH in the rehydrided sample and also the formation of the stable oxide phase Li_3BO_3, which was shown to form upon melting by in-situ XRD Figure 7.7.

No CH_4 was detected during decomposition indicating no chemical reaction took place between the AC additive and $LiBH_4$ during decomposition. Consequently the destabilisation of $LiBH_4$ must come from an interaction between the surface of the AC and $LiBH_4$, such as the confinement of $LiBH_4$ inside the amorphous pores that in turn induces nano-sizing effects or an interaction directly with the surface of the AC. The pre-melting of the AC + $LiBH_4$ mixture under a H_2 over pressure appears to suppress the release of H_2 and B_2H_6 upon melting, this behaviour has been observed for $LiBH_4$ confined within porous scaffolds (Liu et al., 2011). As discussed above XRD and Raman spectroscopy on the PM AC + $LiBH_4$ sample showed evidence for the creation of a homogenous mixture which maximises the AC surface to $LiBH_4$ contact which further enhances the proposed destabilising surface interactions.

When comparing the DSC-TGA-MS profile of as-prepared and rehydrided PM AC + $LiBH_4$ (Figure 7.6 and Figure 7.10 respectively) it is clear that the both the melting and decomposition of the reformed $LiBH_4$ occurs much lower than in the as-prepared sample. Melting occurs 19 °C lower in a small asymmetric peak followed by a single asymmetric decomposition peak at 353 °C almost 50 °C lower than for the as-prepared sample. These

large observed reductions infer that the $LiBH_4$ is in a different state in the rehydrided sample. This behaviour has been observed for $LiBH_4$ confined within nanoporous carbon (Zhang et al., 2007) indicating that the reformed $LiBH_4$ is nano-sized and thus maybe contained within the amorphous pore structure of the AC additive.

8 Zeolite Templated Carbon + $LiBH_4$

In this chapter results of work on $LiBH_4$ pre-melted into a zeolite templated carbon to investigate the effect of a high surface area, highly porous and carbon scaffold with a defined pore structure on the hydrogen storage properties of $LiBH_4$ are presented and discussed.

8.1 Characterisation of As-Prepared Sample

The as-received materials, Non-PM ZTC+$LiBH_4$ and PM ZTC+$LiBH_4$ were characterised by XRD, Raman spectroscopy and N_2 adsorption isotherms (BET); PM=pre-melted.

8.1.1 X-ray Diffraction

Room temperature XRD patterns for the as-received $LiBH_4$, dried ZTC, Non-PM ZTC+$LiBH_4$ and PM ZTC+ $LiBH_4$ are shown in Figure 8.1. The XRD pattern of as-received ZTC (Figure 8.1a) exhibits a single peak located at 6.4° 2θ corresponding to the presence of long range ordering within the amorphous structure with a periodicity of 1.2 nm (Paredes et al., 2005).

As-received $LiBH_4$ (Figure 8.1b) showed reflections consistent with the low temperature orthorhombic phase of $LiBH_4$ and no crystalline impurities. The hand-mixing of ZTC and $LiBH_4$ results in a physical mixture of the two materials, as indicated by the presence of reflections of both ZTC and o-$LiBH_4$ in the pre-infiltrated sample (Figure 8.1c).

After pre-melting of the hand mixed ZTC + $LiBH_4$ at 300 °C under 10 bar H_2, all peaks associated with o-$LiBH_4$ can be seen to have disappeared indicating that the $LiBH_4$ lost its long-range order (Figure 8.1d). The long-range order of the ZTC can also been seen to decrease after melt-infiltration, shown as a significant reduction in the intensity of the peak 6.4° 2θ.

A small peak located at 10.6° 2θ is present after melt-infiltration, corresponding to a d spacing of 0.9 nm. It is therefore possible to conclude that this peak does not arise from ZTC, intercalation of $LiBH_4$ within the ZTC structure would result in a downshift to larger d spacing. The origin of this peak could not be identified.

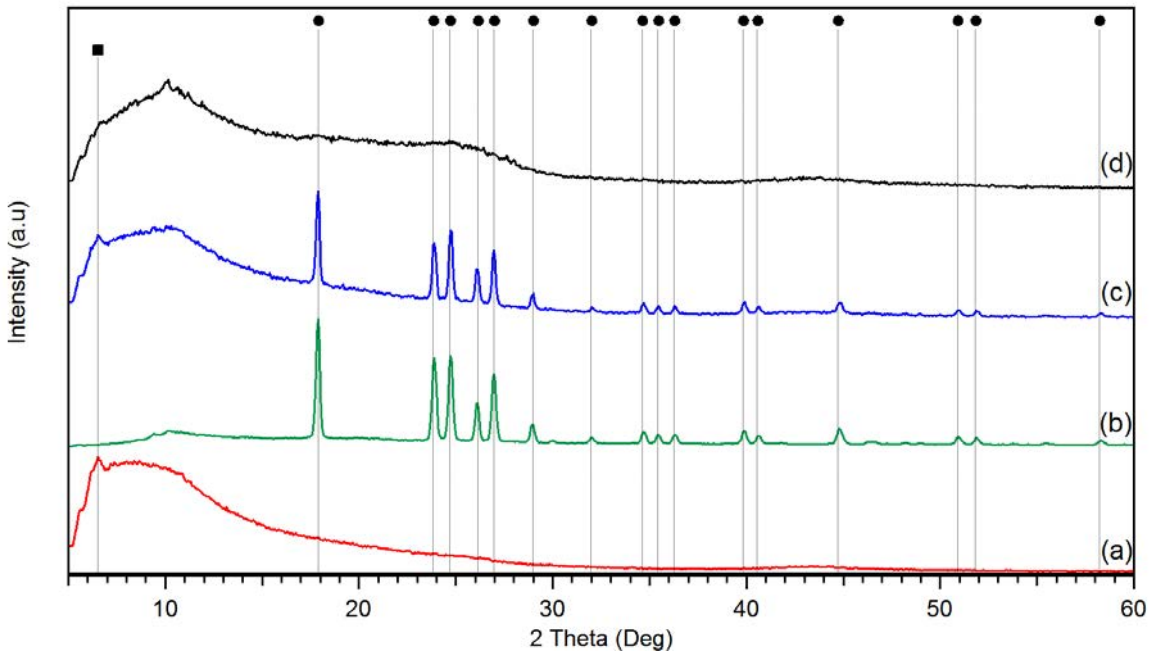

Figure 8.1 Room temperature XRD patterns of (a) ZTC, (b) As-received $LiBH_4$, (c) non-PM ZTC+$LiBH_4$ and (d) PM ZTC+$LiBH_4$. Peak identities are indicated by dashed lines and markers; black circles signify reflections from o-$LiBH_4$ and the black square a reflection from the ZTC. The ICDD PDF2 database (2011) was used for phase identification

8.1.2 Raman Spectroscopy

Raman spectra of the as-received $LiBH_4$, dried ZTC, non-PM ZTC+$LiBH_4$ and PM ZTC+$LiBH_4$ are shown in Figure 8.2. The Raman spectrum of dried ZTC shows two broad peaks located at 1350 cm^{-1} and 1600 cm^{-1}. The first peak is consistent with the D band of graphite and forbidden in defect free graphite originating from the breathing mode of the carbon rings, whilst the second peak can be attributed to a combination of the G and D' bands of graphite which originate from the E_{2g} stretching mode of pairs of sp^2 hybridised carbon atoms (Ferrari and Robertson, 2000) and second order double resonance scattering respectively. The Raman spectrum of dried ZTC resembles that of activated carbon Figure 6.2a.

The Raman spectrum of as-received $LiBH_4$ Figure 8.2b exhibits two main groups of peaks, consistent with bond stretching and bond bending of the $[BH_4]^-$ tetrahedral anion as labelled on the graph. The broad peak located between 2140 cm^{-1} and 2200 cm^{-1} are second order phonons resulting from the bending modes of the $[BH_4]^-$ unit (Reed and Book, 2009).

Once added to the ZTC, $LiBH_4$ is no longer visible by Raman Spectroscopy, even though its presence is confirmed by XRD (Figure 8.1c). This is believed to be a result of carbon's higher cross-sectional scattering factor compared to that of $LiBH_4$, the low intensity $[BH_4]^-$ stretching and bending modes are hidden behind the higher intensity scattering from ZTC (this is the same as seen with the graphite (Ar) + $LiBH_4$ sample (Figure 6.2d)).

After infiltration the peak visible at 1600 cm^{-1} resulting from the G+D' bands appears to downshift to lower wavenumbers, suggesting a destabilisation in C-C bonding within the ZTC.

The small narrow peak seen at 2320 cm^{-1} is believed to be a measurement artefact and not indicative of the ZTC sample. It has been observed in a variety of different samples. Peak fitting of the D and G bands in the ZTC samples could not be carried out due to the high background between the two bands (1400-1500 cm^{-1}) makeing peak fitting inaccurate.

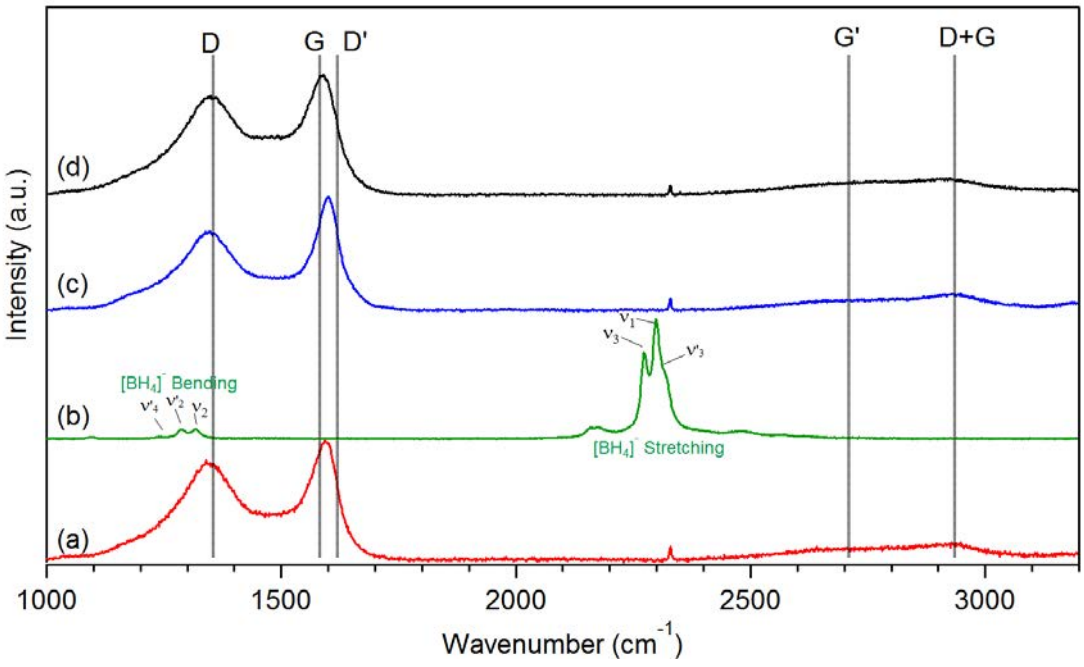

Figure 8.2 Room temperature Raman Spectra of (a) ZTC, (b) $LiBH_4$, (c) Non-PM ZTC+$LiBH_4$ and (d) PM ZTC+$LiBH_4$. The D, G, D', G' and D+G bands are marked by the black dashed lines. The $[BH_4]^-$ bending and stretching modes of $LiBH_4$ are labelled along with the origin of each vibration

8.1.3 N_2 Adsorption Isotherms & BET

A nitrogen gas adsorption isotherm was measured for as-received ZTC, Figure 8.3. The ZTC was found to adsorb an impressive 123 wt% N_2 at -195 °C under 950 mbar N_2, indicating a very large surface area. BET surface analysis was carried out on the N_2 adsorption isotherm in Figure 8.3, results are shown in Figure 8.4. The BET surface area of dried ZTC was calculated to be 2745 ± 32 m^2g^{-1}, as expected for ZTCs (Nishihara et al., 2009).

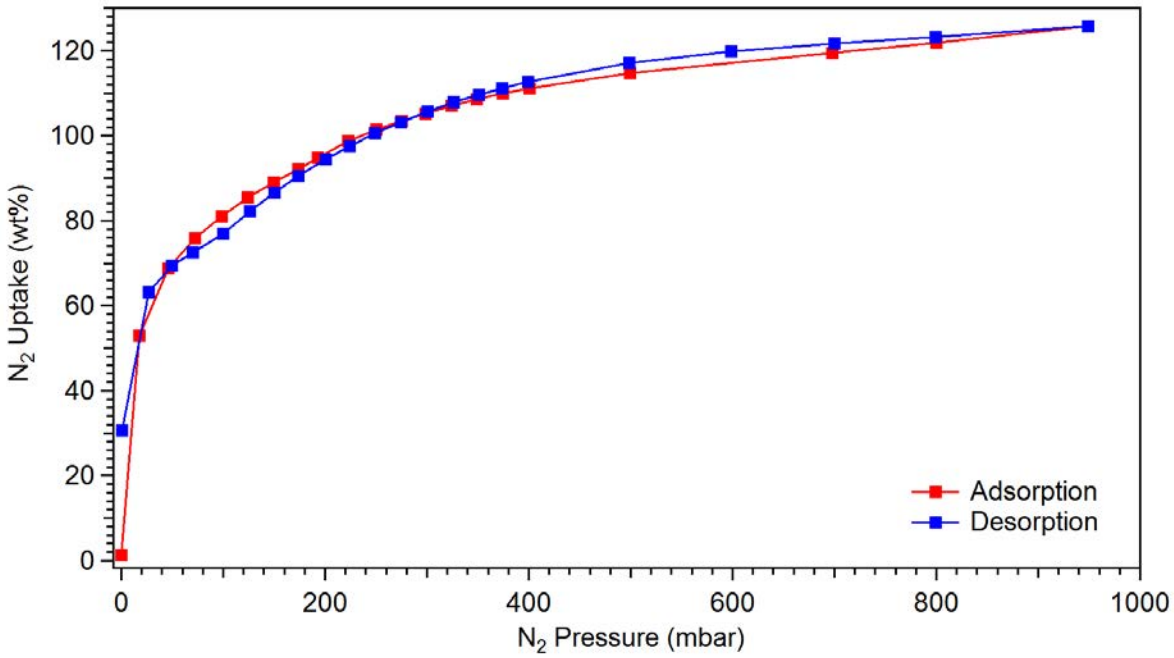

Figure 8.3 N_2 adsorption isotherm (-195 °C) of dried ZTC

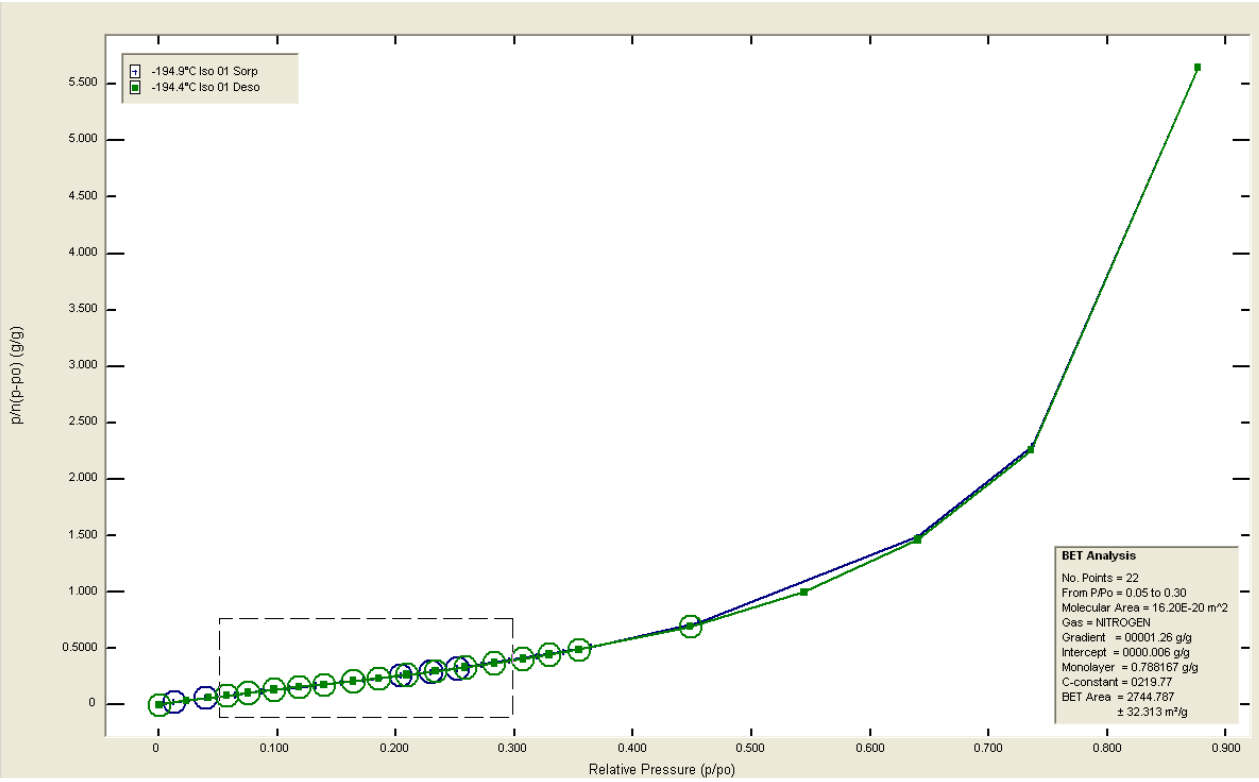

Figure 8.4 BET analysis of the ZTC N_2 adsorption isotherm shown in Figure 8.3, fit parameters are shown in the bottom right corner of the graph

8.2 Thermal Decomposition

The thermal decomposition pathway of non-PM ZTC+$LiBH_4$ and PM ZTC+$LiBH_4$ were investigated through DSC-TGA-MS, with PM ZTC+$LiBH_4$ further investigated using XRD and Raman spectroscopy.

During the decomposition of both infiltrated and non-infiltrated ZTC+$LiBH_4$ samples, no foaming (which is synonymous with thermal decomposition of $LiBH_4$) was observed. This is consistent with $LiBH_4$ mixed with the high surface materials and scaffolds reported in this thesis. This phenomenon has also been observed in other works in which $LiBH_4$ has been nano-confined in ZTC (Shao et al., 2015).

8.2.1 Non-PM ZTC + $LiBH_4$

The thermal decomposition of non-PM ZTC+$LiBH_4$ was investigated by DSC-TGA-MS, shown in Figure 8.5. The DSC trace shows three main endothermic events, the first at 115 °C is consistent with the phase transition from orthorhombic $LiBH_4$ (o-$LiBH_4$) to hexagonal $LiBH_4$ (h-$LiBH_4$). The second feature is comprised of three peaks, two endothermic peaks located at 281 °C and 287 °C followed by a sharp exothermic peak at 289 °C. The third feature is a broad split endothermic peak with minima at 341°C and 361 °C, consistent with the peak shape for the decomposition of bulk $LiBH_4$ but more than 100 °C lower.

The TGA-MS profile of non-PM ZTC+$LiBH_4$ indicates the onset of hydrogen desorption to be 200 °C resulting to a small mass loss of 0.4 ± 0.1 wt% between 200 °C and 280 °C.

The sample then desorbs H_2 rapidly around melting (280 °C) with an observed mass loss of 2.1 ± 0.1 wt% occurring between 280 °C and 320 °C. The rate of wt% loss then increases as bulk decomposition of $LiBH_4$ takes place (as indicated by DSC) with peak H_2 desorption at 340 °C, corresponding to a weight loss of 3.7 ± 0.1 wt% between 320 °C and 370 °C. Overall non-PM ZTC+$LiBH_4$ desorbs over 7.2 ± 0.1 wt% H_2 by 500 °C. A very small quantity of diborane was detected during decomposition, with the same onset temperature as H_2 suggesting the B_2H_6 might play a role in the decomposition pathway. Previously, B_2H_6 has been shown to release during the orthorhombic to hexagonal phases change of $LiBH_4$, not in the region of melting (Kato et al., 2010).

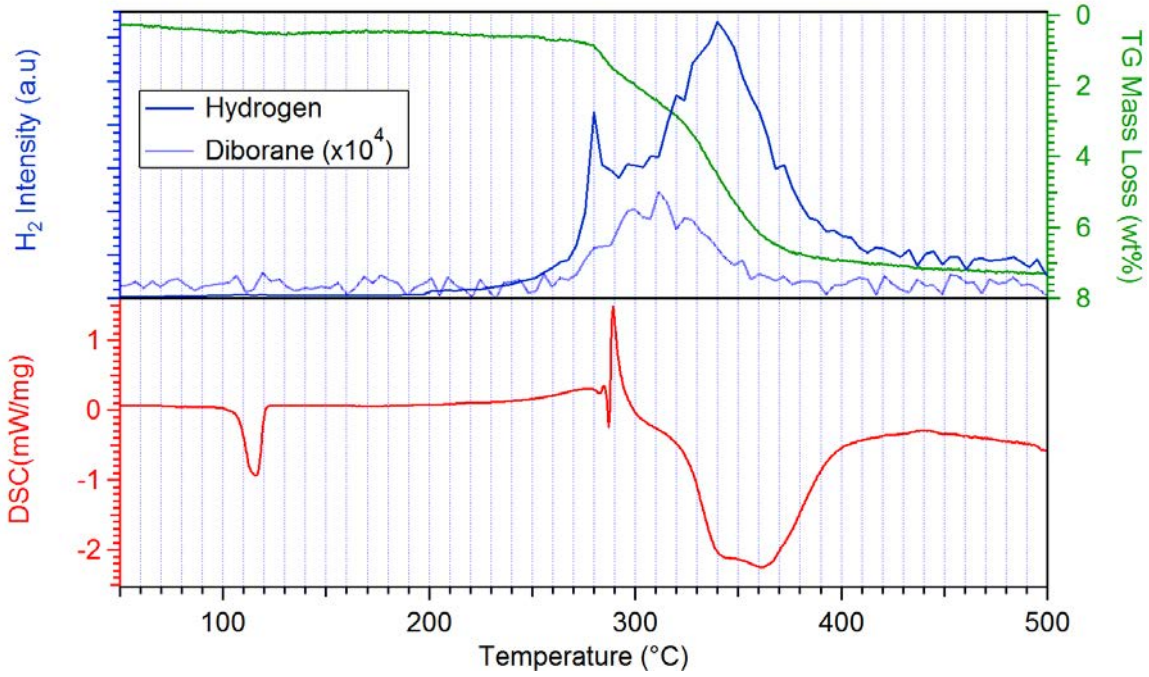

Figure 8.5 DSC-TGA-MS profile of Non-PM ZTC+$LiBH_4$ heated to 500 °C at 5 °C.min^{-1} under 3 bar Ar with a flow rate of 100 ml.min^{-1}

8.2.2 PM ZTC + $LiBH_4$

The thermal decomposition of PM ZTC+$LiBH_4$ was initially investigated by DSC-TGA-MS, shown in Figure 8.6. The sample can be seen to desorb 5.8 ± 0.1 wt% by 500 °C with 1.2 ±

0.1 wt% desorbed by 310 °C, followed by a rapid weight loss of 3.4 ± 0.1 wt% between 310 °C and 370 °C in conjunction with a large hydrogen desorption at 335 °C. The onset of hydrogen desorption occurs at an impressively low 130 °C.

The DSC trace of PM ZTC+$LiBH_4$ shows a single asymmetric endothermic peak with a minimum ca. 342 °C. This peak endothermic peak corresponds to a significant weight loss and large hydrogen desorption and can therefore be attributed to the decomposition of $LiBH_4$ within the sample. No peaks consistent with a phase change or melting observed for pure $LiBH_4$ were observed. No diborane was detected during decomposition.

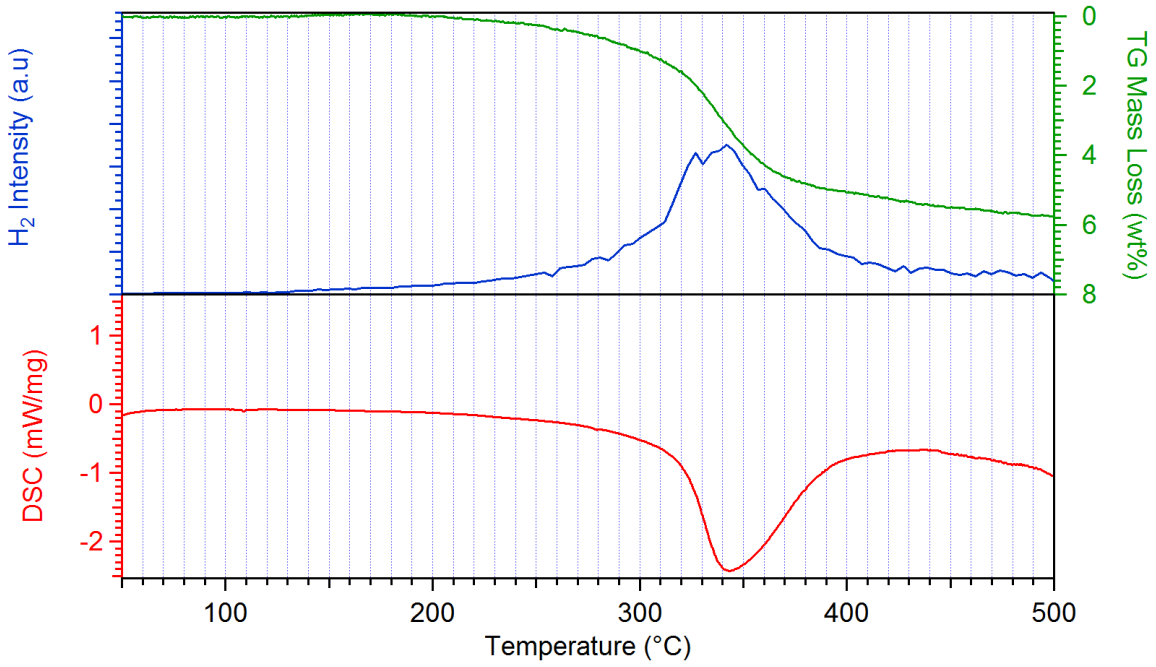

Figure 8.6 DSC-TGA-MS profile of PM ZTC+$LiBH_4$ heated to 500 °C under 3 bar Ar with a flow rate of 100 ml.min^{-1}

With the aim of further understanding the decomposition pathway of PM ZTC + $LiBH_4$, room temperature XRD and Raman spectroscopy measurements were carried out on dehydrided

PM ZTC+$LiBH_4$ desorbed at 400 °C for 30 min under 3 bar He. The XRD pattern of dehydrided PM ZTC+$LiBH_4$ (Figure 8.7b) exhibits a number of small peaks that are consistent with Li_3BO_3 indicating partial oxidation occurred during decomposition. The unknown peak observed in the as-prepared PM ZTC+$LiBH_4$ sample at 10.6° 2θ disappears after dehydrogenation. No other crystalline phases were observed by XRD, the decomposition products of $LiBH_4$ are likely to be confined within the pores of the ZTC structure and thus have short-range order.

The Raman spectrum of dehydrided PM ZTC+$LiBH_4$ (Figure 8.8b) did not show any new bands, only those observed in PM ZTC+$LiBH_4$ sample were observed. A small upshift in the G+D' band is seen suggesting: an increase in the C-C bond stability after dehydrogenation; or an increase in the D' band relative to the G band resulting from an increase in the number of sp^3 bonded carbon atoms and consequent decrease in the number of sp^2 bonded carbon atoms.

8.3 Rehydrogenation Investigation

An attempt was made to rehydride a dehydrided PM ZTC+$LiBH_4$ sample at 350 °C under 100 bar H_2 for 10 h using Sieverts apparatus and characterised using XRD, Raman spectroscopy and DSC-TGA-MS.

8.3.1 X-Ray Diffraction

The XRD pattern of the attempt to rehydride a dehydrided PM ZTC+$LiBH_4$ sample is shown in Figure 8.7c. The pattern exhibits peaks consistent with crystalline Li_3BO_3, their relative

intensities can be seen to be greater compared to that of the dehydrided sample (Figure 8.7b) suggesting the sample has been further oxidised during rehydrogenation. No peaks consistent with crystalline $LiBH_4$ can be seen after rehydrogenation. Quantitative analysis on Li_3BO_3 is not possible, expected phases such as B, $LiBH_4$ and ZTC are not observed due to their short-range ordering or amorphous nature.

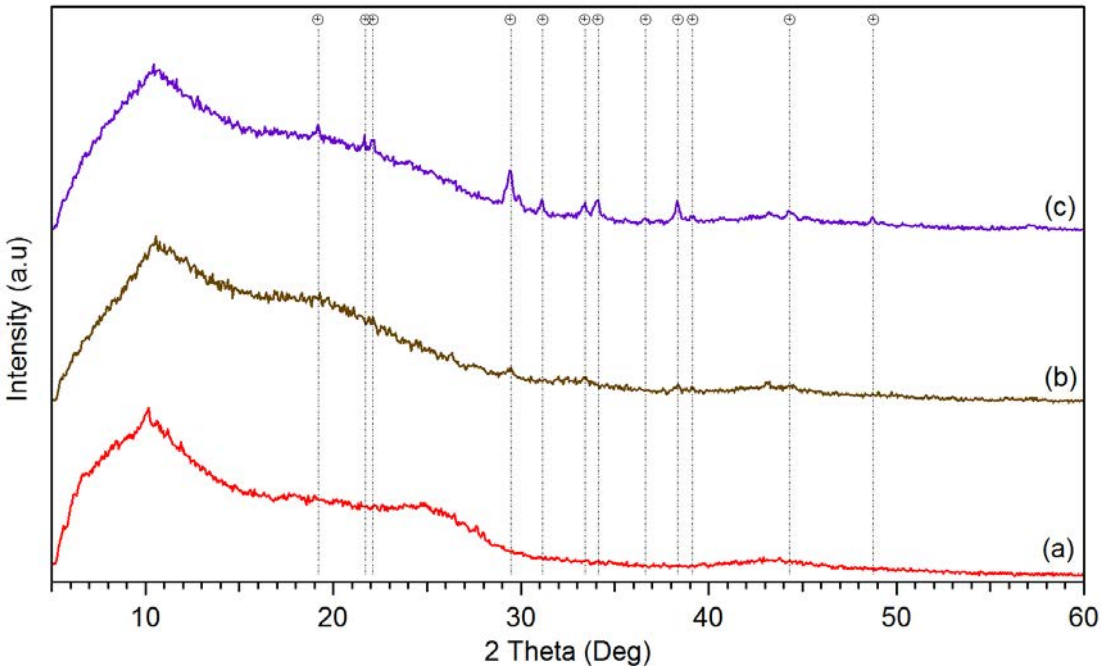

Figure 8.7 Room temperature XRD patterns of (a) PM ZTC+$LiBH_4$, (b) dehydrided PM ZTC+$LiBH_4$ and (c) rehydrided PM ZTC+$LiBH_4$. The location of reflections from Li_3BO_3 are indicated by the dotted lines labelled with clear circles containing a cross. The ICDD PDF2 database (2011) was used for phase identification

8.3.2 Raman Spectroscopy

The rehydrided PM ZTC+$LiBH_4$ sample was studied via Raman spectroscopy, results are shown in Figure 8.8. No vibrations consistent with $[BH_4]^-$ bending or stretching modes were observed in the rehydrided sample, only vibrations consistent with those observed for ZTC in

the dehydrided and PM ZTC+$LiBH_4$ are seen. Accurate peak fitting could not be carried out on the rehydrided sample.

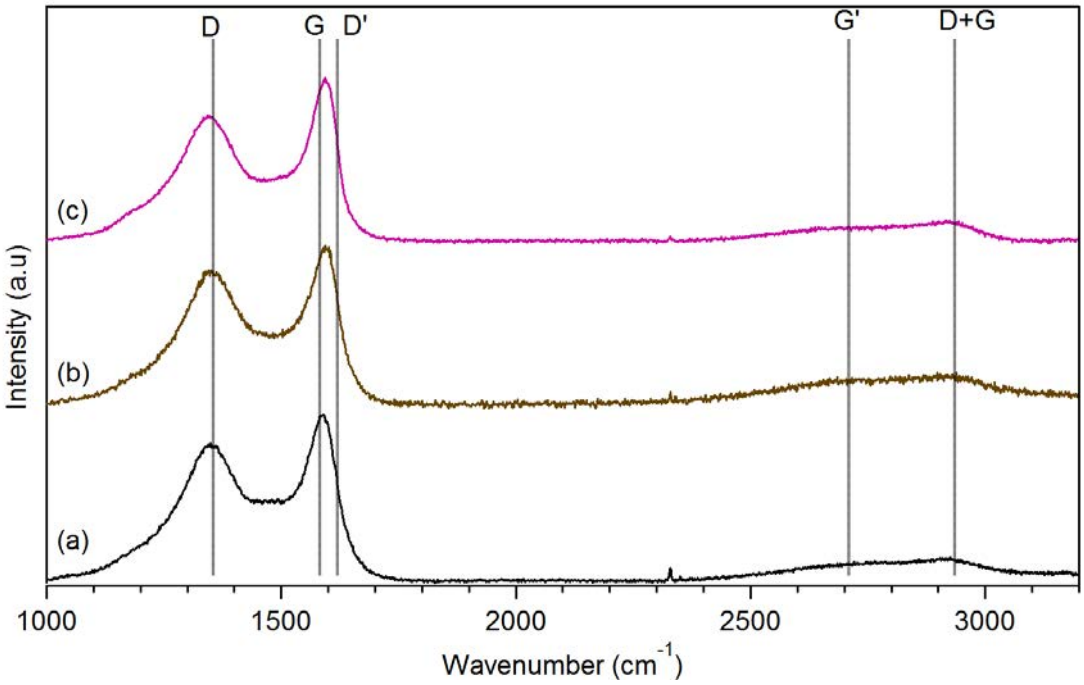

Figure 8.8 Room temperature Raman spectra of (a) PM ZTC+$LiBH_4$, (b) dehydrided PM ZTC+$LiBH_4$ and (c) rehydrided ZTC+$LiBH_4$

8.3.3 DSC-TGA-MS

The decomposition of rehydrided PM ZTC+$LiBH_4$ was investigated by DSC-TGA-MS, Figure 8.9. As seen for as-prepared PM ZTC+$LiBH_4$, the rehydrided sample exhibits a single hydrogen desorption event. Small quantities of hydrogen can be seen to be desorbed from < 100 °C, with peak desorption at 320 °C. This hydrogen desorption corresponds to a weight loss of 2.4 ± 0.1 wt% between 270 °C and 370 °C, with the sample desorbing a total of 3.4 ± 0.1 wt% hydrogen by 500 °C. The same single asymmetric endothermic peak observed by DSC for as-prepared PM ZTC+$LiBH_4$ is observed for the rehydrided sample, and is at 330 °C.

No diborane was detected. Comparing the wt% loss between the as-prepared and rehydrided samples, it can be estimated that 59 % of the initial hydrogen capacity was achieved upon rehydrogenation.

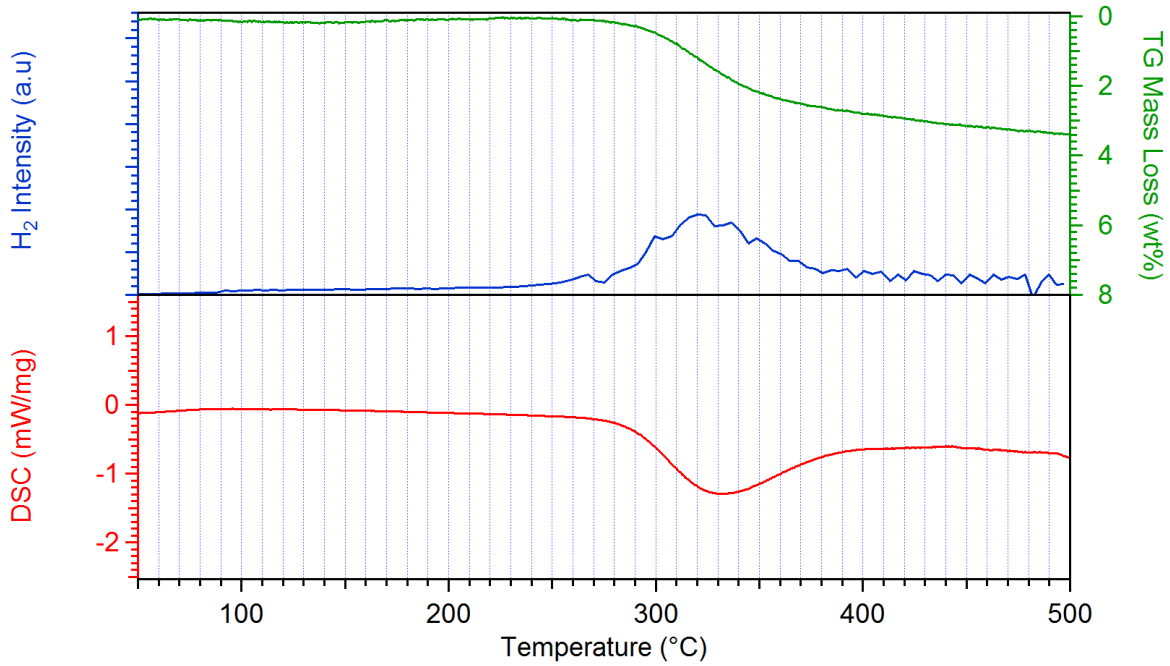

Figure 8.9 DSC-TGA-MS profile of rehydrided PM ZTC+LiBH$_4$ heated to 500 °C at 5 °C.min^{-1} under 3 bar Ar with a flow rate of 100 ml.min^{-1}

8.3.4 Cyclic H_2 Uptake

The cyclic uptake of PM ZTC+LiBH$_4$ was studied over 5 de/re-hydrogenation cycles using a Sieverts apparatus to measure the isothermal uptake at 350 °C as function of sample wt% and H_2 pressure, Figure 8.10. During the first hydrogen absorption cycle, PM ZTC+LiBH$_4$ absorbed 3.7 ± 0.1 wt% corresponding to 63 % of its initial hydrogen desorption. The hydrogen absorption capacity can be seen to slightly decrease over the following to cycles before steadily climbing. These results suggest that the cyclic capacity of PM ZTC+LiBH$_4$ may stablilize around 3.2 -3.3 wt% (55-57 % of the samples initial hydrogen release).

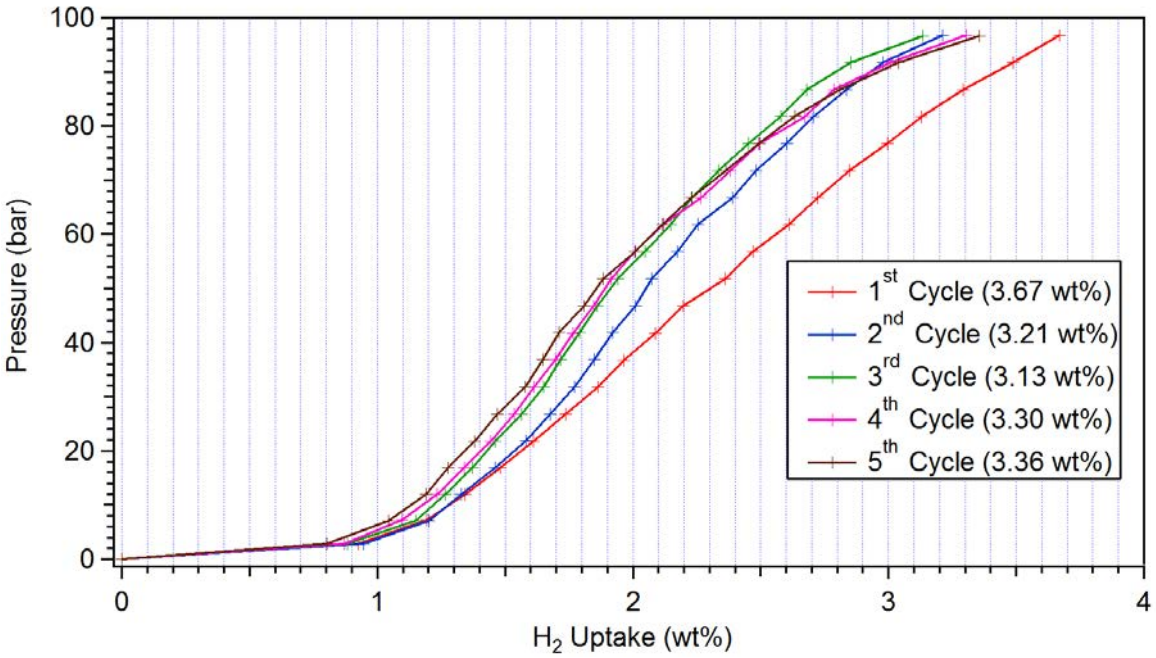

Figure 8.10 Cyclic H_2 uptake isotherms of PM ZTC+$LiBH_4$ measured at 350 °C as a function of H_2 pressure and uptake, the final H_2 uptake after each cycle is displayed

8.4 Discussion

Zeolite templated carbon with a surface area of 2745 ± 32 m^2g^{-1} was hand mixed with $LiBH_4$ at a molar ratio of 2:1 (ZTC:$LiBH_4$) before being pre-heated at 300 °C under 5 bar H_2 for 30 min. A non melt-infiltrated ZTC+$LiBH_4$ sample was studied by XRD, Raman spectroscopy and DSC-TGA-MS for comparison. XRD of as-received ZTC (Figure 8.1a) showed a single peak at 6.4 ° 2θ indicating long-range order with a period of 1.2 nm was present. The Raman spectra of as-received ZTC (Figure 8.2a) showed evidence of the D, G, D', G' and D+G bands observed in amorphous carbon. After pre-heating, XRD (Figure 8.1d) confirmed the loss of long-range ordering in $LiBH_4$, indicated by the disappearance of reflections from orthorhombic $LiBH_4$ observed in the non PM ZTC+$LiBH_4$ sample. This loss in long-range ordering is believed to be due to the confinement of $LiBH_4$. No new phases were observed by

Raman spectroscopy or after mixing and infiltration; the origin of the small peak at 10 ° 2θ is unknown, no match could be found for this phases in the ICDD PDF2 database (2011), LiOH, $LiBH_4.H_2O$, LiH, Li_2C were all ruled out.

DSC-TGA-MS results of non PM ZTC+$LiBH_4$ indicated a total wt% loss of greater than 7.2 ± 0.1 wt% H_2 by 500 °C. Work by Kato et al. (2010) reported evidence of diborane release during the orthorhombic to hexagonal phase transformation, in this work diborane was detected during the first stages of decomposition, suggesting it might play a part in the decomposition pathway of $LiBH_4$ in non PM ZTC+$LiBH_4$. The extremely low quantity of detected diborane may be due to the sticky nature of the gas, causing it to stick to the wall of the gas capillary. The DSC measurement of the decomposition of Non-PM ZTC+$LiBH_4$ exhibits a trace not seen for pure $LiBH_4$ after melting 287 °C. The melting of pure $LiBH_4$ is an endothermic reaction 285 °C seen as a single sharp peak by DSC (Shao et al., 2014), however, for the Non-PM ZTC+$LiBH_4$ sample this endothermic melting peak is followed rapidly by a sharp exothermic reaction 290 °C. The exact reason for this exothermic peak is not clear, but may be a result of melt-infiltration of $LiBH_4$ into the ZTC framework, the exothermic reactions have also been observed after melting in $LiBH_4$ confined in nanoporous carbons (Brun et al., 2010; Liu et al., 2010). Brun et al., (2010) speculated that his exothermic peak might arise from a surface reaction between $LiBH_4$ and -OH or -COOH groups on the pore surface.

The decomposition of $LiBH_4$ can be seen to follow shortly after in a two-step process as seen for pure $LiBH_4$, over 100 °C lower than bulk $LiBH_4$. From TGA, bulk decomposition can be seen to finish well below 400 °C confirming that the high surface area ZTC framework

destabilizes the decomposition of $LiBH_4$. The Non PM ZTC+$LiBH_4$ sample was not investigated by XRD or Raman spectroscopy after decomposition so the composition of phases is unknown. However, based on a wt% loss of 7.2 ± 0.1 wt%, the two-step decomposition reaction observed by DSC and presence of B_2H_6 two potential decomposition pathways can be proposed; Equations 5.2 and 5.3 occurring at melting followed by Equation 8.1 shortly after.

$$LiBH_4 \leftrightarrow {}^{1}/_{12}Li_2B_{12}H_{12} + {}^{5}/_{6}LiH + {}^{13}/_{12}H_2 \leftrightarrow LiH + B + {}^{3}/_{2}H_2 \leftrightarrow Li + B + 2H_2 \qquad (8.2)$$

As shown in Table 8.1, a mass loss of 7.2 wt% indicates that all the $LiBH_4$ in the sample decomposed in LiH, B and H_2 and just under half of the remaining LiH decomposes into its constituent parts.

Table 8.1 Expected H_2 Desorption in wt% for different possible decomposition pathways of $LiBH_4$

-	Reaction Pathway	H_2 Release (wt%)
(1)	**$LiBH_4 \rightarrow Li + B + 2H_2$**	8.80
(2)	**$LiBH_4 \rightarrow LiH + B + {}^{3}/_{2}H_2$**	6.60
(3)	**$LiBH_4 \rightarrow {}^{5}/_{6}LiH + {}^{1}/_{12}Li_2B_{12}H_{12} + {}^{13}/_{12}H_2$**	4.77

DSC-TGA-MS results of PM ZTC+$LiBH_4$ showed no large endothermic peaks consistent with the orthorhombic to hexagonal phase change or melting of $LiBH_4$ were observed; two very small endothermic bumps are just visible at 114 °C and 279 °C. These residual peaks may be attributed to a very small quantity of non-confined $LiBH_4$, suggesting over-filling of the porous ZTC structure. The disappearance of these two peaks from the DSC trace during heating are consistent with nano-confined $LiBH_4$ (Shao et al., 2015; Liu et al., 2010; Zhang et

al., 2007) agreeing well with XRD results that $LiBH_4$ has been confined within the porous ZTC scaffold after the pre-melting step.

MS results (Figure 8.6) showed that PM ZTC+$LiBH_4$ released H_2 at an impressively low 120 °C (74 °C lower than was observed for densified $LiBH_4$+ZTC by (Shao et al., 2015)), with bulk desorption at 335 °C occurring in a single step with no B_2H_6 detected; consistent with nano-confined $LiBH_4$ (Shao et al., 2015; Liu et al., 2010). The PM ZTC+$LiBH_4$ desorbed 5.8 ± 0.1wt% by 500 °C, 1.4 ± 0.1 wt% less than its Non-PM counterpart, this reduction in weight loss may originate from a combination of no B_2H_6 evolution (1 M of B_2H_6 is greater than 13 times heavier than 1M of H_2) and the partial decomposition of $LiBH_4$ during the pre-melting process; the onset of hydrogen evolution from the Non-PM ZTC+$LiBH_4$ sample occurred 190 °C lower than for bulk $LiBH_4$ (375 °C), as such, the 5 bar H_2 overpressure applied during the melt-infiltration process may not have been enough to fully supress hydrogen evolution.

The XRD of pattern of dehydrided PM ZTC+$LiBH_4$ also provides a possible explanation for the decrease in mass loss. Small peaks resulting from monoclinic Li_3BO_3 are the only crystalline phase observed indicating the sample has been exposed to a small quantity of oxygen during decomposition. The oxygen present in the dehydrided sample will therefore increase the overall sample weight reducing the relative H_2 wt% in the sample. It was unclear if the sample oxidation was homogenous throughout the sample or whether it was a surface reaction.

Li_3BO_3 has been shown to improve the reaction kinetics of decomposition and recombination of $LiBH_4$, and as such may play a role in the decomposition and recombination reactions after its formation on first dehydrogenation. In-situ XRD on

PM AC+$LiBH_4$ showed evidence for the formation of Li_3BO_3 upon melting, this reaction may be responsible for the exothermic peak directly after melting in the DSC profile of PM ZTC+$LiBH_4$.

No B or LiH were detected by XRD in the dehydrided, the products of decomposition are believed to remain confined within the ZTC pores and thus limit their long-range order.

With the absence of B_2H_6 during heating, the decomposition pathway of PM ZTC+$LiBH_4$ is believed to differ slightly to that of non-PM ZTC+$LiBH_4$. With no in-situ decomposition measurements and a single decomposition peak seen by DSC the only decomposition pathway that can be inferred is direct decomposition of $LiBH_4$ into LiH, B and H_2 shown in Equation 5.1.

In work by Shao et al. 2015, NMR measurements identified the presence of amorphous B and $Li_2B_{12}H_{12}$ in dehydrided, densified ZTC+$LiBH_4$. As such it is possible to speculate that although the overall decomposition of $LiBH_4$ followed Equation 5.1, $Li_2B_{12}H_{12}$ should still be considered a possible intermediate (Equation 5.4).

The decrease in hydrogen desorption temperature and consequent reduction in decomposition temperature of $LiBH_4$ within the ZTC framework may result from an increase in the mobility of the BH_4^- anion resulting from nano-confinement (Verkuijlen et al., 2012; Liu et al., 2013), Shane et al. (2010) have shown by NMR that a smaller pore size acts to further increase its mobility.

The cyclic H_2 uptake investigation of PM ZTC+$LiBH_4$ indicates a stable H_2 capacity of 3.3 ± 0.1 wt% (Figure 8.10), approximately half the total capacity of the as-prepared sample (5.8 ±

0.1 wt%, Figure 8.6). $Li_2B_{12}H_{12}$ is a known possible intermediate in the decomposition of $LiBH_4$ and due to its high stability acts as a B sink reducing the cyclic capacity of $LiBH_4$. Li_3BO_3 identified by XRD although has been shown to increase the recombination reaction kinetics also acts as a B sink.

The presence of $LiBH_4$ could not be confirmed in the rehydrided PM ZTC+$LiBH_4$ sample by XRD or Raman spectroscopy, Figure 8.1c and Figure 8.8c respectively, however, it may be inferred through analysis of hydrogen uptake. If only partial recombination to LiH had been achieved during rehydrogenation, then the maximum wt% uptake which could be achieved is 2.2 ± 0.1 wt% (see Table 8.1), however, TGA-MS of rehydrided PM ZTC+$LiBH_4$ showed a hydrogen capacity of 3.4 wt%. Thus is it possible to speculate that $LiBH_4$ was successfully reformed at 350 °C under 100 bar H_2, a significant improvement on the lowest reported recombination conditions for bulk $LiBH_4$ (600 °C under 155 bar H_2 (Mauron et al., 2007)), and under a lower pressure reported by Shao et al. (2015) to recombine densified ZTC+$LiBH_4$ (120 bar H_2 at 260 °C). Further studies are needed for the optimization of the required rehydrogenation conditions of PM ZTC+$LiBH_4$).

It is clear from the cyclic uptake measurements (Figure 8.10) that the sample was still absorbing H_2 at 350 under 100 bar and thus the maximum hydrogen capacity was not achieved in any of the cycles during the measurement. From this it is possible to conclude that whilst the hydrogen absorption kinetics of $LiBH_4$ are improved by the ZTC framework (in agreement with results seen by Shao et al. (2015)) and possibly the small quantity of Li_3BO_3, they are still limited. Further investigation is required to identify if the reaction is critically limited by the recombination conditions of the material itself.

9 Porous Silicon + $LiBH_4$

As discussed in Section 2.7.4.5.1, the confinement of $LiBH_4$ within porous silica has been shown to reduce the onset of H_2 desorption from $LiBH_4$ to 150 °C (Ngene et al., 2010), however, the decomposition products of $LiBH_4$ were found to react with the SiO_2 scaffold and eliminate the possibility of reversibility. In order to investigate if reversibility can be achieved without the presence of O atoms in the host porous material, $LiBH_4$ was mixed with porous silicon (PS). It is also possible to investigate the effect of a silicon porous host vs a carbon porous hosts that are more commonly investigated (see Section 2.7.4.5).

9.1 Characterisation of Porous Silicon

The structure of as-received PS was characterised by XRD, Raman, SEM and N_2 adsorption isotherms for BET surface analysis.

9.1.1 XRD

The room temperature XRD patterns of as-received PS and Sigma Aldrich silicon nano-powder used for comparison are shown in Figure 9.1.

The XRD pattern of as-received PS exhibits peaks consistent with cubic crystalline silicon. The Si peaks in the PS sample can be seen to be wider than the crystalline silicon nano-powder, consistent with previous XRD patterns of PS (Russo et al., 2011; Nayef, 2013).

The relative peak intensities in the PS sample Figure 9.1a can be seen to differ from that of the crystalline comparison sample Figure 9.1b. The most obvious of which is the intensity of the (004) plane reflections at 69.1° 2θ, which can be seen to greatly increase in the porous silicon sample. The reasoning behind this increase is not known and was not observed in previous XRD of PS (Russo et al., 2011). One reason for this may be the fabrication process discussed in (Section 2.5) that results in pore growth in the (001) plane direction. The increased intensity in the (004) plane reflections may be a by-product of preferential ordering in the (001) plane arising from the electrochemical etching process.

Pseudo Reitveld refinements were carried out on the XRD patterns as-received PS and crystalline nano-powder silicon shown in Figure 9.1, results are shown in Table 9.1. The errors on calculated values for the porous silicon are larger than the crystalline comparison sample due to the peak broadening observed in the porous silicon sample, resulting in a poorer fit, reflected in the goodness of fit (gof) values of the two samples. (A perfect fit would give a gof of 1). Density, lattice parameter and consequent volume of the unit cell with the two samples can be seen to be identical within errors to one another.

Table 9.1 Pseudo Reitveld Refinement results for XRD patterns in Figure 9.1. Cell parameters are listed for both samples.

	Porous Silicon	Nano-powder Silicon Comparison
Cell Mass	224.683	224.683
Cell Volume (Å)	160.7 ± 0.3	160.5 ± 0.1
Density g/cm3	2.32 ± 0.01	2.32 ± 0.1
Lattice Parameter (Å)	5.44 ± 0.01	5.43 ± 0.01
Goodness of Fit (gof)	3.119	1.701

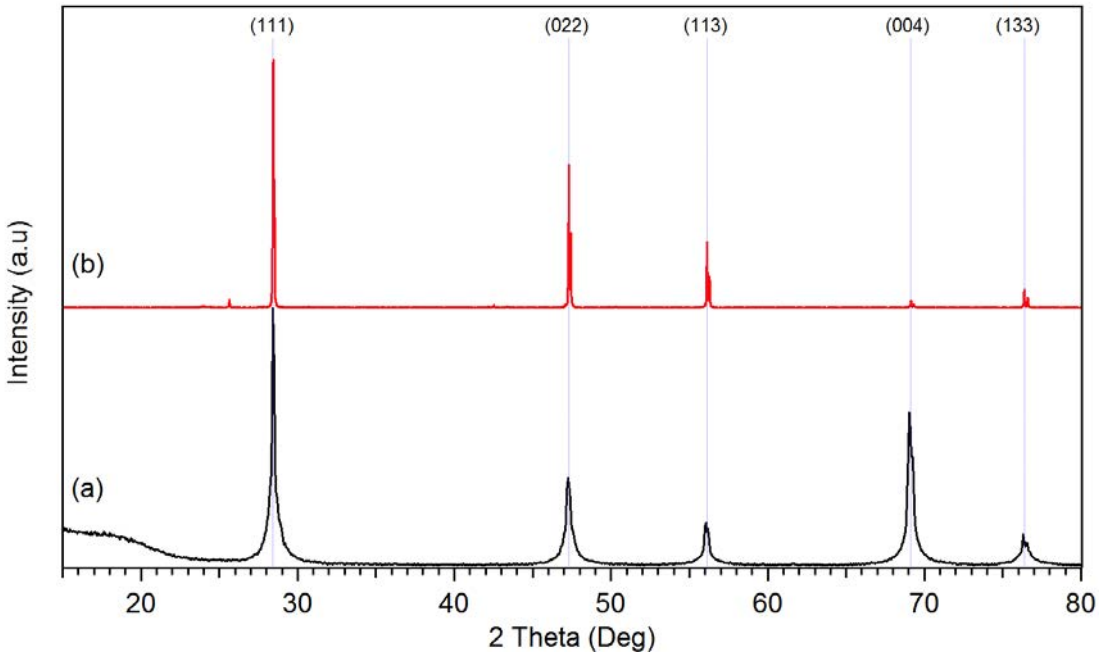

Figure 9.1 Room temperature XRD patterns of (a) as-received PS and (b) Sigma Aldrich silicon nano powder comparison. The corresponding reflections from Si planes are indicated by the solid grey lines. The ICDD PDF2 database (2011) was used for phase identification

9.1.2 Raman Spectroscopy

As-received PS and the CS comparison were studied by room temperature Raman spectroscopy (Figure 9.2), the internal Si standard using for calibration of Raman spectrometer is also included as a highly crystalline silicon comparison.

As shown in Figure 9.2c, highly crystalline silicon exhibits the symmetric TO mode originating from Si-Si bond at 520 cm^{-1}, whilst the Raman spectrum of amorphous silicon exhibits a broad peak at 430 cm^{-1} (Veprek et al., 1981).

The Raman spectra of CS shows three peaks, located at 300 cm^{-1}, 516 cm^{-1} and 958 cm^{-1} originating from the second order transverse acoustic (2TA) mode, transverse optical (TO)

mode and second order transverse optical (2TO) mode of crystalline silicon, respectively. A small shoulder on the low energy side of the TO band indicates the presence of a small quantity amorphous-like content (Iqbal et al., 1980).

The amorphous silicon content in the PS sample (Figure 9.2a) can be seen to be higher, indicated by a reduction in the relative intensity of the TO mode and an increase in the width of the shoulder associated with amorphous Si. A downshift in the TO band of 5 cm^{-1} is observed compared to the highly crystalline CS, consistent with the literature (Salcedo et al., 1999).

PS is fabricated by electrochemical etching of Si wafers. The amorphous content observed in the PS sample is believed to be due to the introduction of pores and defects, resulting in a reduction in the crystallinity of the sample, agreeing with the XRD results of the PS shown in Figure 9.1a. The electrochemical etching process results in a surface layer of hydrogenated silicon species (SiH_x), the presence of SiH, SiH_2 and SiH_3 were confirmed by Raman spectroscopy, with clear peaks at 2087 cm^{-1}, 2112 cm^{-1} and 2137 cm^{-1} corresponding to SiH (2088 cm^{-1}), SiH_2 (2110 cm^{-1}) and SiH_3 (2137 cm^{-1}) (Lysenko et al., 2005).

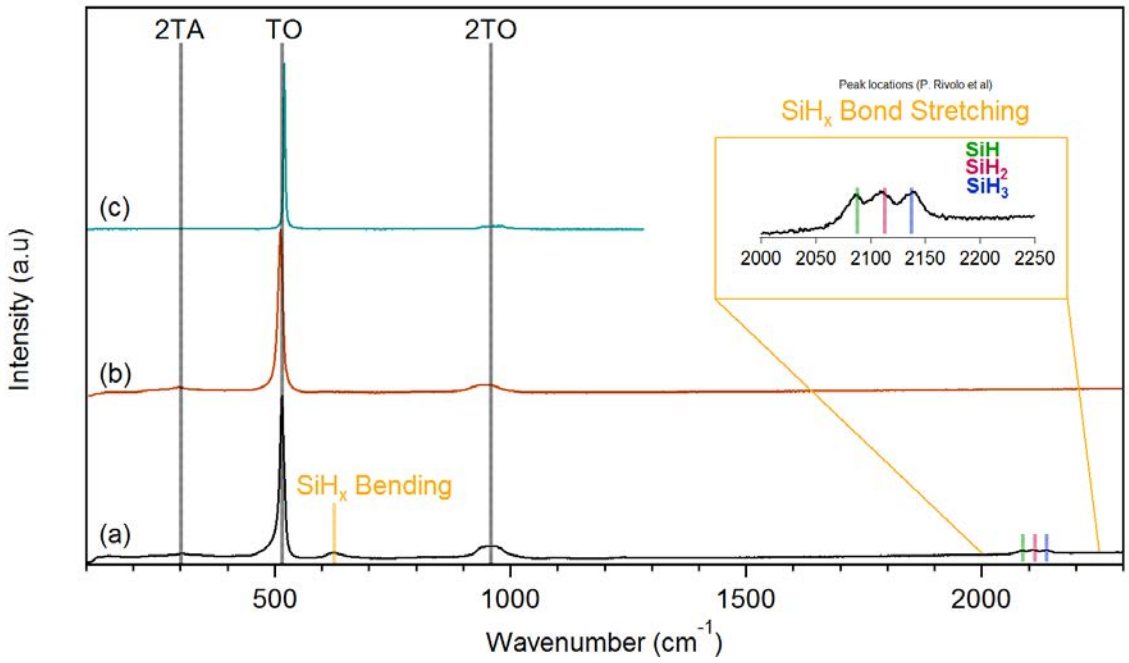

Figure 9.2 Room temperature Raman spectra of (a) as-received PS, (b) Sigma Aldrich silicon nano-powder comparison and (c) single crystal Si calibration standard measured under 100 ml.min^{-1} flowing Ar. SiH_x bending and stretch modes are indicated by the corresponding coloured bands, the 2TA, TO and 2TO Raman modes of crystalline Si are identified by the black dotted lines and corresponding labels

9.1.3 SEM-EDS

SEM-EDS was carried out on the surface and a perpendicular edge in order to characterise the structure and composition of as-received PS, results are shown in Figure 9.3. EDS analysis was in agreement with XRD and Raman spectroscopy analysis that no other elements (such as oxygen or fluoride, possible contaminants from the fabrication process) were present, although due to their light atomic weight and subsequent light electron cloud, these elements can be hard to detect via EDS, based on this same premise, Hydrogen cannot be detected via EDS either.

Neither the surface or edge of the PS wafer was polished prior to the SEM image was taken, this was to protect the hydrogen terminated surface and avoid forming Si dangling bonds

which would react with oxygen instantaneous. Consequently there are varying levels of focus across the images, but the features are still clearly visible.

Figure 9.3a shows the edge of a PS wafer snapped in half revealing the elongated pores, propagating in the (001) plane consistent with the fabrication of PS (Sailor, 2011b).

Figure 9.3b shows an SEM image of the surface of a PS wafer, open pores can clearly be seen with a diameter ranging from 20-50 nm. It is therefore possible to classify the PS sample as being mesoporous ($2 \geq x \geq 50$ nm) in conjunction with the IUPAC guidelines for pore size classification (Haber, 1991). Since the pores in PS form in a tube like structure in the (001) direction, it can be assumed that all pores must be open.

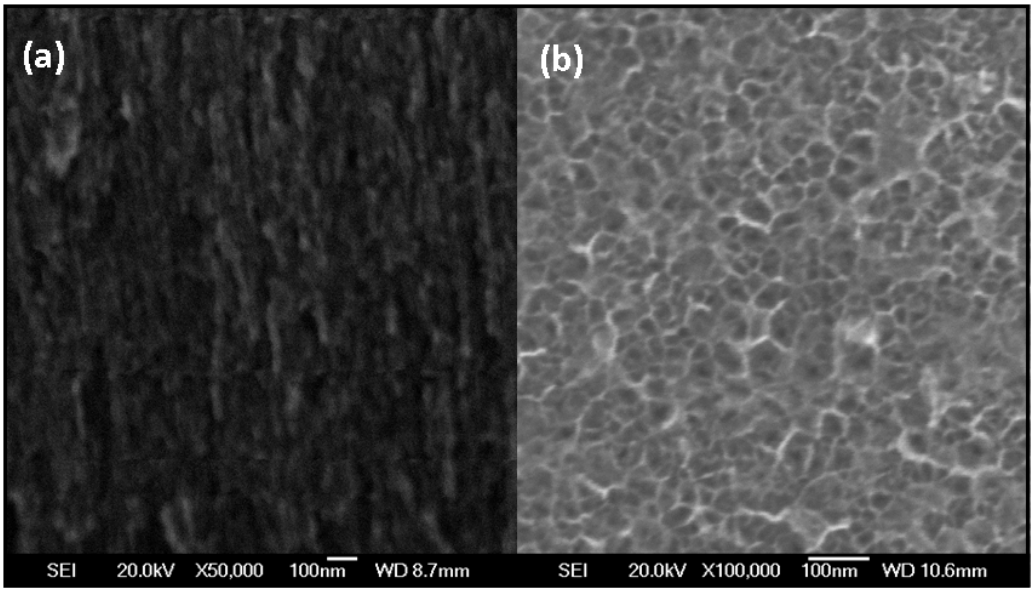

Figure 9.3 SEM image of the a) an edge of a PS wafer with showing pore orientation in the (001) plane, b) the surface of a PS wafer showing open pores

9.1.4 N_2 Adsorption Isotherms and BET

The surface of PS was investigated using BET analysis (Figure 9.5) of N_2 adsorption isotherms to determine the surface area of the as-received PS sample. Figure 9.4a shows the N_2 adsorption isotherm at -195 °C under 950 mbar N_2, a total of 35 wt% N_2 was adsorbed to the surface of as-received PS, corresponding a BET surface area of 280 ± 2 m^2g^{-1} which lies within the expected range of surface areas for porous silicons of between 9 and 429 m^2g^{-1} (Petrova et al., 2000).

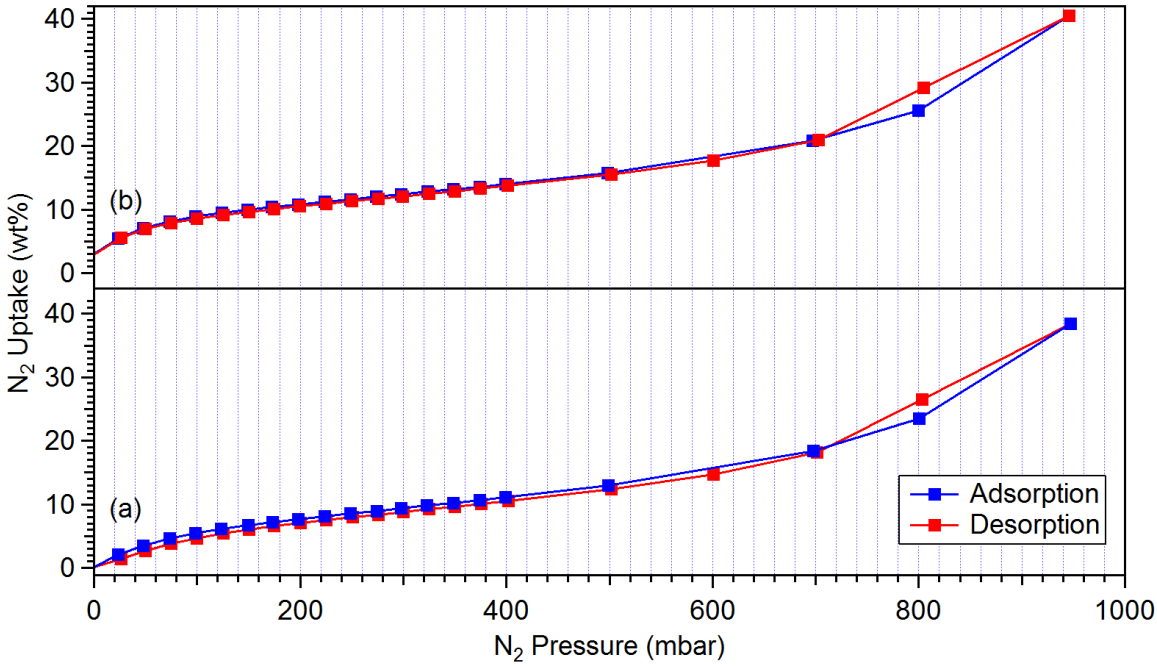

Figure 9.4 N_2 Adsorption isotherms (-195 °C) of (a) as-received PS and (b) PS pre-heated to 400 °C for 30 min under vacuum (10^{-6} mbar) and then cooled to -195 °C to remove H_2 surface

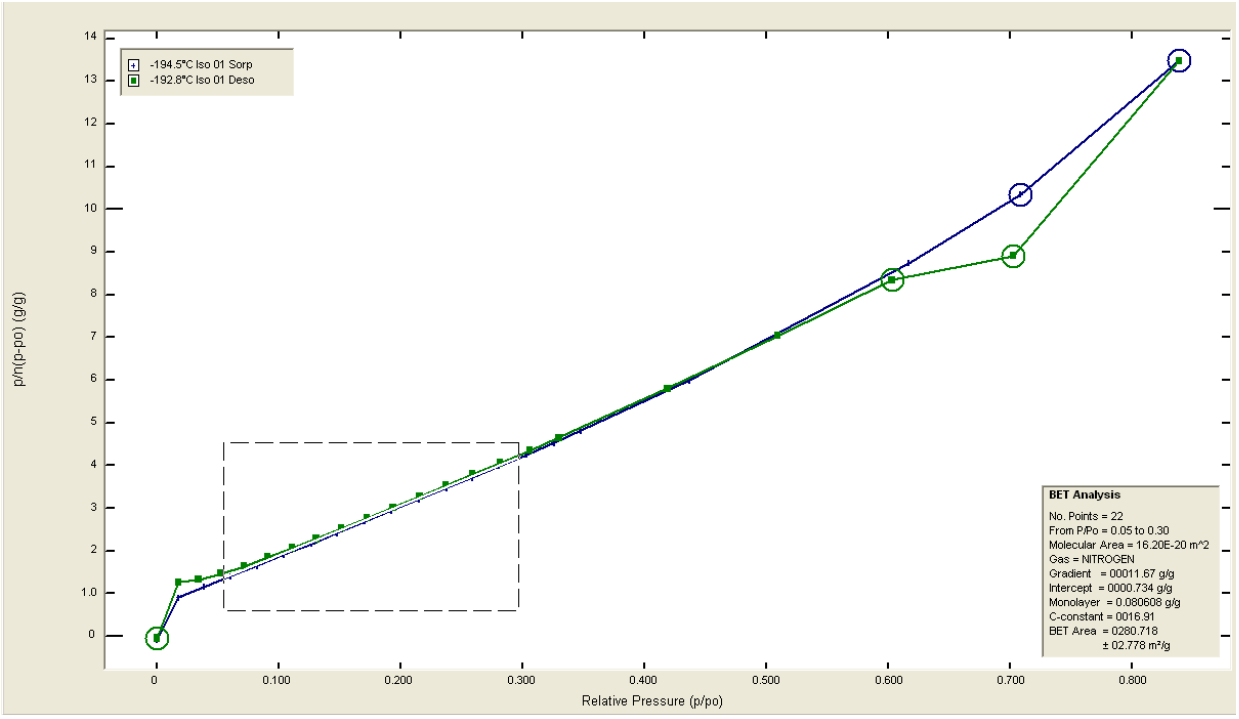

Figure 9.5 BET analysis of the as-received PS N_2 adsorption isotherm shown in Figure 9.4a, the fit parameters are shown in the bottom right corner of the graph

9.2 Thermal Decomposition of Porous Silicon

The thermal decomposition of hydrogenated silicon species (SiH_x) was investigated via in-situ Raman spectroscopy and DSC-TGA-MS. The surface area was recalculated by BET analysis of N_2 adsorption isotherms after heating.

9.2.1 In-situ Raman Spectroscopy

In Raman spectroscopy the energy of the incident laser often causes a shift in the peak location, as the excitation wavelength of the incident laser is increased, the power density of the area being measured increases. This causes localised heating and a change in the power

density of the area being measured, seen as a down-shift in the wavenumber (Zhang, 2012). This same phenomenon is seen when the temperature of the sample is independently increased. Opposed to the laser increasing the power density of the area being measured, the independent heating of the sample causes a change, seen as a downshift in peak location.

The relative intensity of Raman modes also decreases with increasing temperature, due to more energetic thermal vibration of the molecules. This both reduces the Raman scattering factor of the molecules and reduces the number of electrons in the ground state which can be Raman scattered. In Figure 9.6 the intensity of the 2TA, TO and 2TO modes can all be seen to decrease with increasing temperature.

In-situ Raman spectroscopy measurements were carried from out from room temperature to 500 °C at 2 °C.min^{-1} under 100 ml.min^{-1} flowing Ar, as described in Section 4.3.2.3. Figure 9.6 shows in-situ Raman spectroscopy measurements between 150 cm^{-1} – 1650 cm^{-1}, the 2TA, TO and 2TO modes of Si can be seen at 300 cm^{-1}, 516 cm^{-1} and 958 cm^{-1} with vibrations consistent with the wagging mode of SiH at 626 cm^{-1} (Tuyen et al., 2001).

Vibrations from the SiH wagging mode at 626 cm^{-1} disappear around 300 °C suggesting the thermal decomposition of the SiH and the evolution of hydrogen.

Figure 9.7 shows in-situ Raman spectroscopy measurements in the range of 1250 cm^{-1} - 2850 cm^{-1}. Due to the low relative intensities of the SiH_x stretching modes to the background (resulting from the low density of hydrogen atoms on the top surface of the PS flakes).

The intensity of the SiH_x stretching modes decreases with increasing temperature as discussed above, however, their intensity can be seen to drastically decrease after 250 °C and disappear around 300 °C, as seen in Figure 9.6. The apparent reduction and increase in intensity ca. 100 °C and 240 °C is an artificial artefact caused by thermal expansion of the Si lattice. To increase the rate of data capture, auto-focusing of the laser on the sample surface was carried out every 5 scans.

Room temperature Raman spectra of PS after heating to 400 °C showed no peaks consistent with SiH_x wagging or stretching modes. Areas of the sample not directly irradiated by the excitation laser were also scanned after heating and revealed no evidence for the existence of SiH_x, confirming that thermal decomposition of the SiH_x species was successful under 400 °C and atmospheric Ar.

Lysenko et al. 2005 reported that PS begins to desorb H_2 from 190 °C, with SiH decomposing at temperatures in excess of 450 °C, over 150 °C higher than observed in this work. This large reduction in temperature may originate from localised heating of the sample from the excitation laser. Laser irradiation (LI) has been shown to be a viable way of desorbing H_2 from the SiH_x species from PS (Tuyen et al., 2001). Effort was made to minimalise the laser exposure time on the sample to limit the effect of localised heating as much as possible.

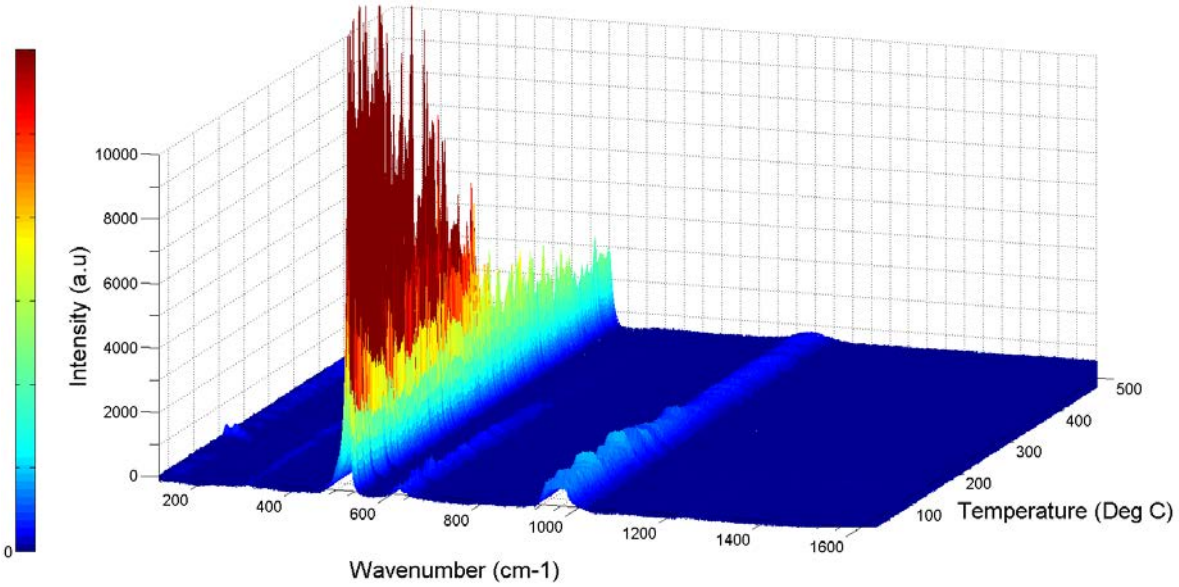

Figure 9.6 3-dimensional graph of in-situ Raman spectroscopy measurements on as-received PS heated to 500 °C at 2 °C.min^{-1} under 100 ml.min^{-1} flowing Ar. Intensity is indicated by colour chart, with dark blue being low intensity and red representing regions of high intensity

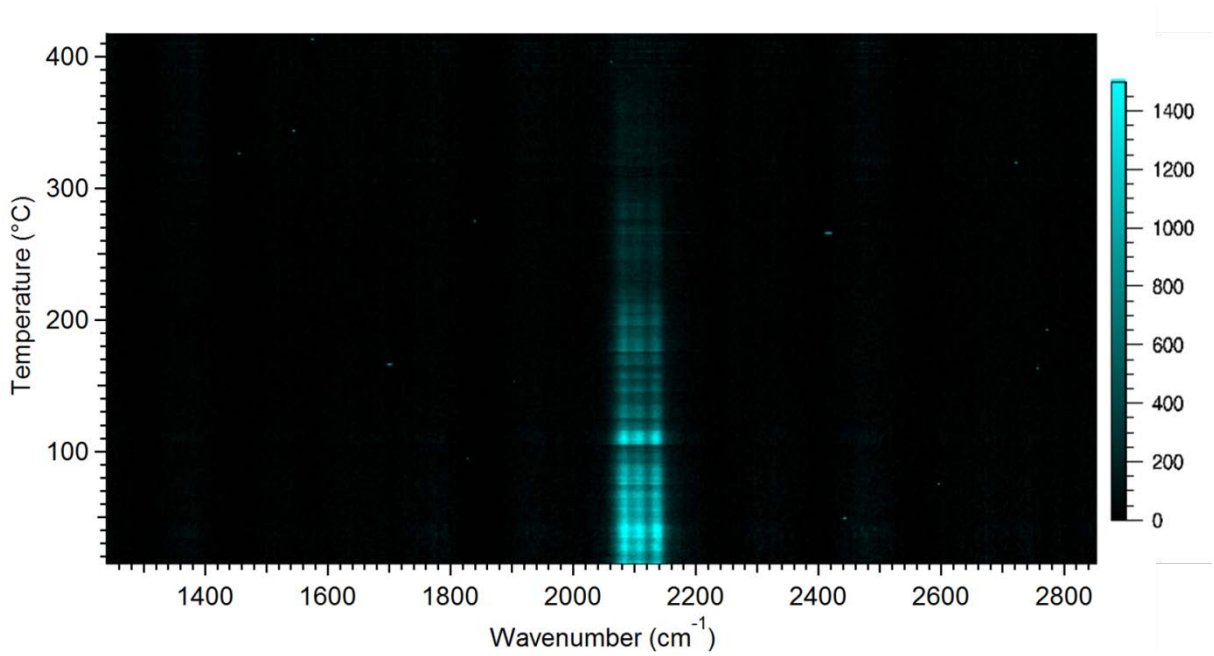

Figure 9.7 In-situ Raman spectroscopy measurements of PS heated to 400 °C at 2 °C.min^{-1} under 100 ml.min^{-1} flowing Ar, intensity is indicated by colour. Black indicates areas of low intensity and bright aqua indicates areas of high intensity

9.2.2 N_2 adsorption isotherms & BET

PS heated to 400 °C at 5 °C.min^{-1} and cooled to RT was investigated using BET analysis of N_2 adsorption isotherms to determine the surface area after heating. Figure 9.4b shows the N_2 adsorption isotherm of pre-heated PS at -195 °C under 950 mbar N_2, a total of 38 wt% N_2 was adsorbed to the surface of as-received PS, corresponding a BET surface area of 332 ± 2 m^{2}g^{-1}. BET analysis results and fit parameters are shown in Figure 9.8.

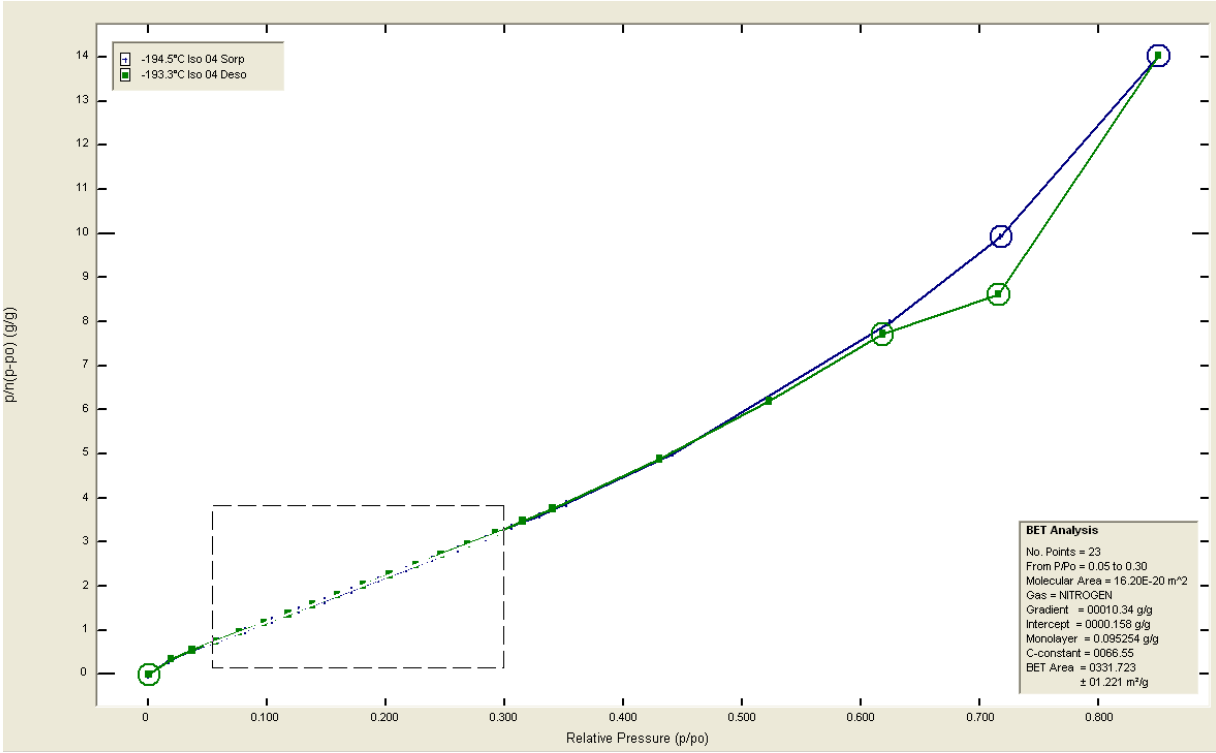

Figure 9.8 BET analysis of thermally decomposed PS N_2 adsorption isotherms shown in Figure 9.4b, the fit parameters are shown in the bottom right corner of the graph

9.2.3 DSC-TGA-MS

The thermal decomposition of SiH_x species on the surface of as-received PS was further investigated by DSC-TGA-MS, Figure 9.9. DSC measurements could only be carried out up to 500 °C (maximum temperature). A small endothermic peak can be seen at 345 °C indicating

an endothermic reaction with an onset of 300 °C. This endothermic reaction occurs concurrently with a defined H_2 desorption at 314 °C and small weight loss of 0.2 ± 0.1 wt%, followed by a prolonged H_2 desorption and steady wt% loss completing by 700 °C. As-received PS desorbed a total of 0.2 ± 0.1 wt% by 650 °C, after which the weight loss appears to decrease. There are two possible reasons for this decrease. Firstly, due to the extremely small wt% values being measured, any baseline line variations will result in large fluctuations in the measured wt% loss. Secondly, if the sample had been exposed to air, when the SiH_x species decomposed, dangling Si bonds would have readily reacted with any oxygen (Tuyen et al., 2001). H_2 was the only gas desorbed during thermal decomposition of the SiH_x species up to 850 °C.

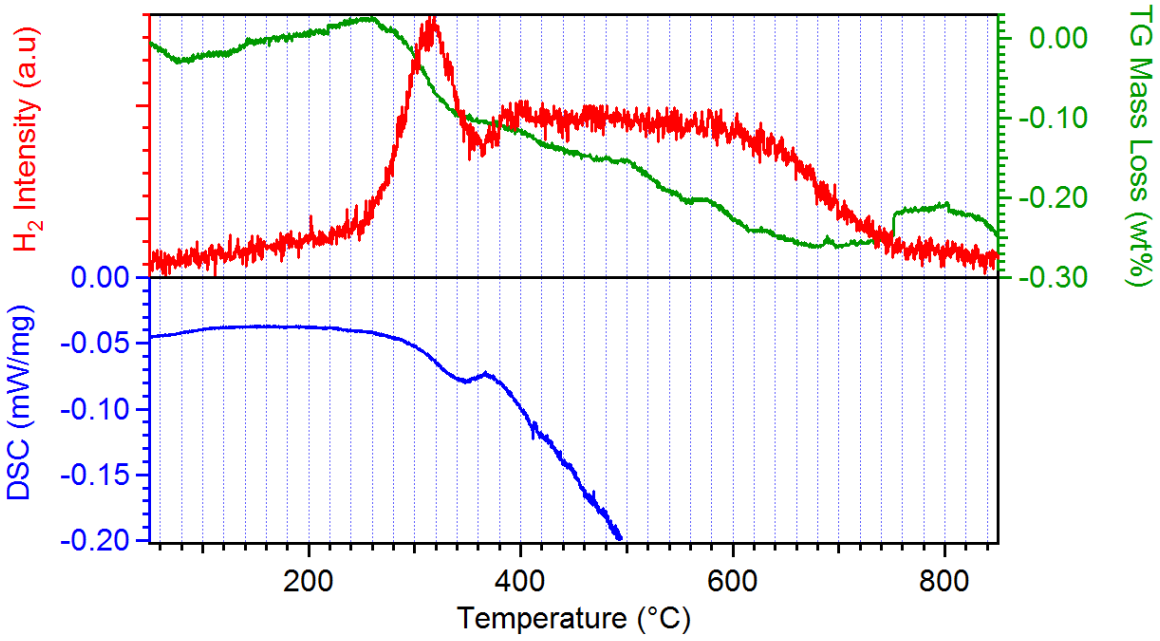

Figure 9.9 DSC-TGA-MS profile of as-received PS to 850 °C at 5 °C.min^{-1} under 3 bar Ar and a flow rate of 100 ml.min^{-1}

9.3 Characterisation of Porous Silicon + $LiBH_4$

The structure of Non PM-PS+$LiBH_4$ and PM-PS+$LiBH_4$ were investigated by room temperature XRD and Raman spectroscopy. It was not possible to conduct N_2 adsorption isotherms and BET analysis on either sample as sample loading could not be carried out under inert conditions. As such sample oxidation could not be prevented and results would not be considered reliable.

9.3.1 XRD

Room temperature XRD patterns of as-received PS, as-received $LiBH_4$, hand-mixed PS+$LiBH_4$ and PM-PS+$LiBH_4$ are shown in Figure 9.11, peak locations consistent with reflections from orthorhombic $LiBH_4$ (o-$LiBH_4$) and Si are indicated by the black circles and triangles, respectively. The XRD pattern of hand-mixed PS+$LiBH_4$ (Figure 9.11c) shows reflections consistent with o-$LiBH_4$ and cubic Si only, indicating that the hand-mixing process simply created a mixture of the two materials; no additional phases are observed.

The XRD pattern of PM-PS+$LiBH_4$ (Figure 9.11d) shows reflections from cubic silicon and with very weak reflections consistent with o-$LiBH_4$ present. This reduction of intensity of o-$LiBH_4$ is consistent with the loss of long-range order in $LiBH_4$ resulting from the confinement $LiBH_4$ within porous scaffolds (Shao et al., 2014). The presence of weak reflections from o-$LiBH_4$ suggests that not all the $LiBH_4$ was successfully nano-confined with the PS due to over-filling.

The lattice parameter of cubic silicon was calculated by pseudo-Reitveld refinement for as-received PS, hand-mixed PS+LiBH4 and PM PS+$LiBH_4$, results are shown in Figure 9.10. No expansion of the Si lattice was observed within errors as a result of $LiBH_4$ addition and melt-infiltration.

The crystallite size of as-received PS, hand-mixed PS+$LiBH_4$ and PM PS+$LiBH_4$ were calculated using the Scherrer equation, results are shown in Table 9.2. A reduction in crystallite size is observed after the pre-melting, however, as discussed in Section 2.4.1.4 a number of factors can affect the result given by the Scherrer equation such as stress/strain, which cannot be ruled out here.

Table 9.2 Crystallite sizes of as-received PS, hand-mixed PS+$LiBH_4$ and PM PS+$LiBH_4$, calculated by the Scherrer equation

Sample	Calculated crystallite sizes for each PS sample
As-received PS	32.7 ± 0.7 nm
Hand-mixed PS+$LiBH_4$	30.2 ± 0.6 nm
PM PS+$LiBH_4$	24.5 ± 4 nm

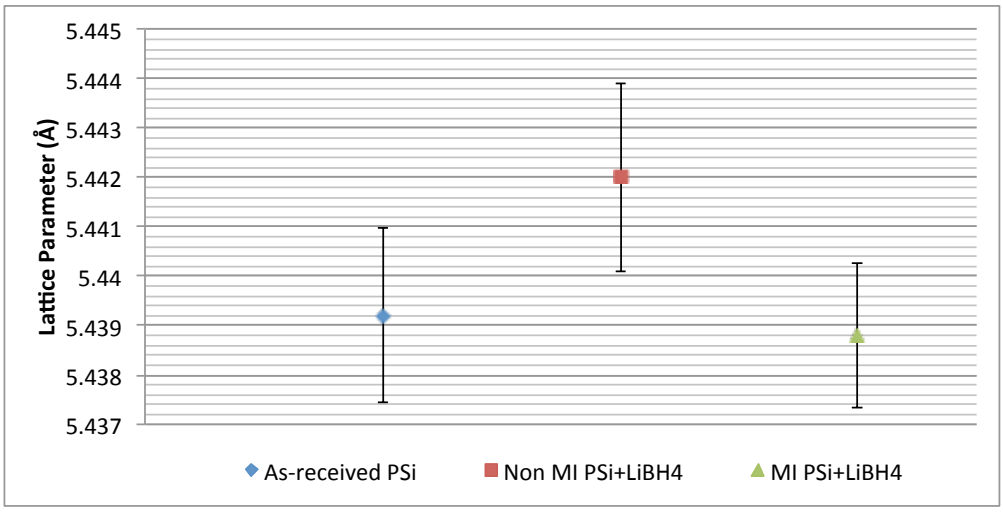

Figure 9.10 Lattice Parameter of cubic silicon in As-received PS, Non PM-PS+$LiBH_4$ and PM-PS+$LiBH_4$ calculated by pseudo Reitveld refinement

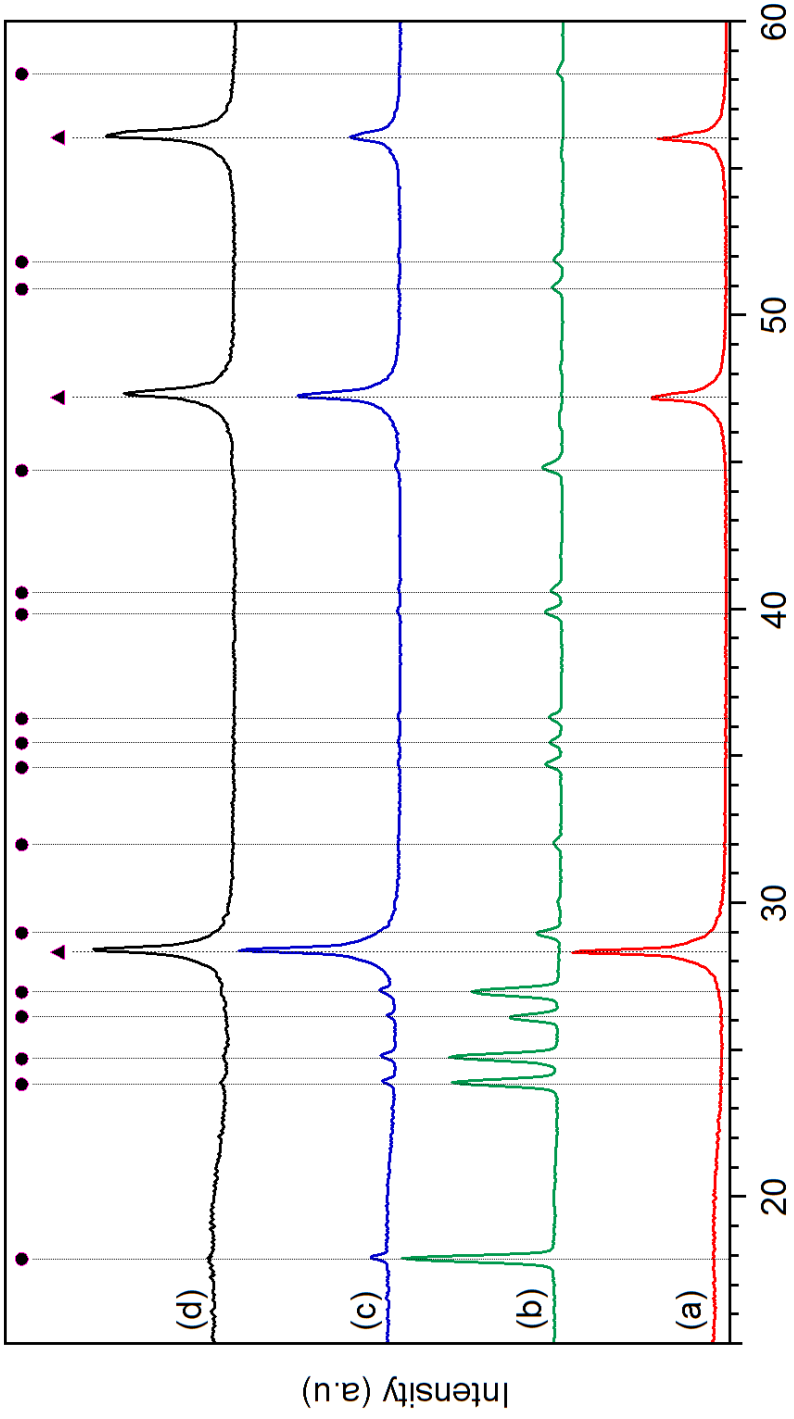

Figure 9.11 Room temperature XRD patterns of (a) as-received PS, (b) as-received $LiBH_4$, (c) Hand-mixed PS+$LiBH_4$ and (d) PM-PS+$LiBH_4$. Reflections from $LiBH_4$ and Silicon are indicated by the dotted lines and black circles and triangles respectively. The ICDD PDF2 database (2011) was used for phase identification

9.3.2 Raman Spectroscopy

Raman spectroscopy measurements of as-received PS, as-received $LiBH_4$, hand-mixed PS+$LiBH_4$ and PM-PS+$LiBH_4$ are shown in Figure 9.12. The Raman spectrum of as-received $LiBH4_4$ Figure 9.10b shows two features: the $[BH_4]^-$ bending vibrations at 1300 cm^{-1} and the $[BH_4]^-$ stretching vibrations at 2300 cm^{-1}.

After hand-mixing of PS+$LiBH_4$ both phases remain, the intensity of the $[BH_4]^-$ vibrations appears to decrease as the TO mode of silicon is so dominant.

After melt-infiltration, the Raman spectrum of PS+$LiBH_4$ (Figure 9.10) no longer shows vibrations from SiH_x species, suggesting they decomposed during the infiltration process (295 °C). As shown in Section 9.2 the SiH_x species on the surface of PS decomposed at 300 °C whilst subject to laser irradiation during the Raman spectroscopic measurement. The width of the TO mode can also be seen to change, the lower wavenumber shoulder can be seen to broaden, indicating an increase in the amorphous Si content within the sample.

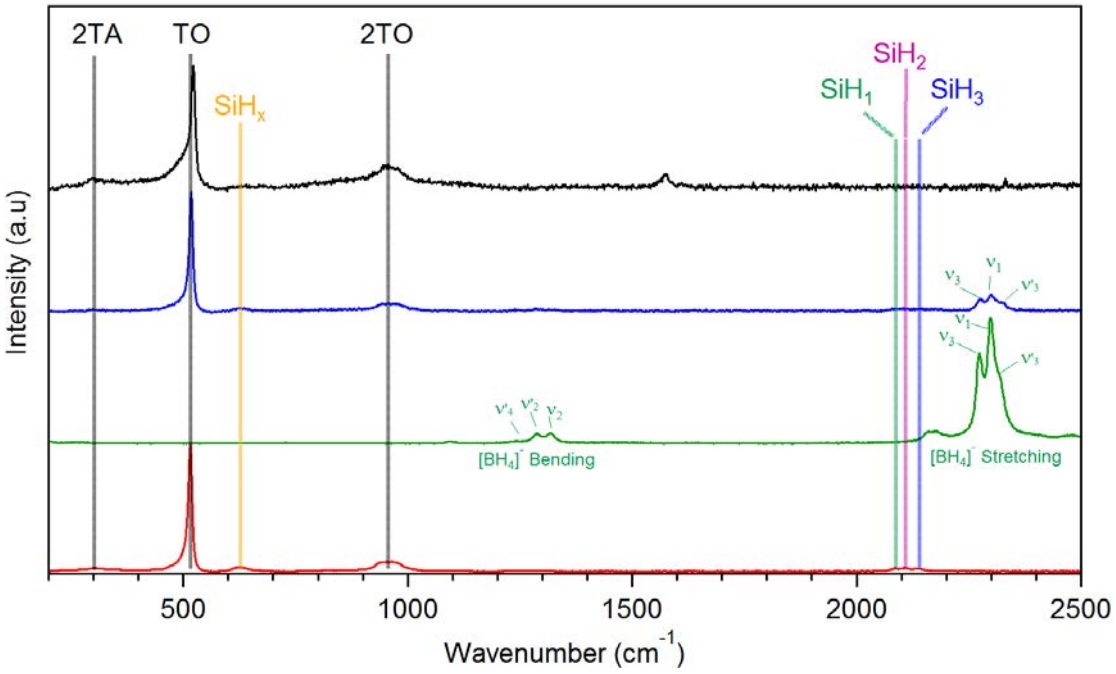

Figure 9.12 Room temperature Raman spectra of (a) as-received PS, (b) as-received $LiBH_4$, (c) Hand-mixed PS+$LiBH_4$ and (d) PM-PS+$LiBH_4$ under 100 ml.min^{-1} flowing Ar. SiH_x Peak origins are labelled accordingly. Measurements were carried out under an excitation wavelength of 488 nm

9.4 Thermal Decomposition

The thermal decomposition of hand-mixed PS+$LiBH_4$ and PM-PS+$LiBH_4$ were investigated by DSC-TGA-MS.

9.4.1 DSC-TGA-MS

The DSC-TGA-MS profile of hand-mixed PS+$LiBH_4$ heated to 500 °C at 5 °C.min^{-1} under 3 bar Ar is shown in Figure 9.13. The DSC trace shows 4 distinct endothermic peaks, the first at 114 °C is consistent with the orthorhombic to hexagonal phase transition of $LiBH_4$ followed by the melting of $LiBH_4$ at 285 °C.

The final two peaks located at 352 °C and 414 °C are consistent with decomposition of $LiBH_4$ with the first peak resulting from decomposition of $LiBH_4$ confined within the PS mesopores and the second at 414 °C resulting from the decomposition of excess bulk $LiBH_4$ not confined within the PS scaffold. This behaviour is consistent with the over loading of $LiBH_4$ within porous frameworks (Liu et al., 2011). It is possible that upon melting, the molten $LiBH_4$ proceeds to melt-infiltrate in to Si mesopores filling the pores. The newly confined $LiBH_4$ then continues to decompose giving rise to the first endothermic DSC peak located at 352 °C, followed by the decomposition of the remaining un-confined $LiBH_4$ at 414 °C.

The H_2 desorption profile of non-PM PS+$LiBH_4$ shows an onset temperature of 110 °C followed by two distinct peaks at 80 °C and 333 °C. The wt% loss from the sample is directly linked to the desorption of gas, 3 different gradients can clearly be seen indicating 3 differing rates of desorption. The first gradient is the steepest of the two and coincides with the first H_2 desorption peak corresponding to a mass loss of 1.2 ± 0.1 wt% by 290 °C, the rate of wt% loss then reduces before remaining constant up to 350 °C. This second wt% loss gives rise to the second H_2 desorption peak and a further wt% loss of 2.4 ± 0.1 wt% by 370 °C. The sample then continues to lose weight up to 500 °C at which point the sample has lost a total of 4.4 ± 0.1 wt%.

This hydrogen desorption behaviour supports the observations seen by DSC. As soon as the $LiBH_4$ melts, the sample melt infiltrates into the PS. The $[BH_4]^-$ ion mobility is greatly increased by both melting and nano-confinement resulting in the lower decomposition temperatures of $LiBH_4$ within the sample. Consequently the first H_2 desorption can be

attributed to the melting of $LiBH_4$ and the second to the nano-confinement effects experienced by the newly confined $LiBH_4$ in the PS mesopores.

Remaining $LiBH_4$ which was not infiltrated into the PS scaffold, possibly due to pore capacity being exceed, then proceeds to decompose at temperatures in excess of 390 °C, consistent with the decomposition of bulk $LiBH_4$ (Shao et al., 2014).

Both diborane (B_2H_6) and silane (SiH_4) were observed during thermal decomposition of non-PM PS+$LiBH_4$. Although the quantities were very low relative the measured H_2 desorption, the evolution of these two gases are major draw backs in the potential use of silicon based materials mixed with $LiBH_4$; B_2H_6 can be poisonous to fuel cells whilst SiH_4 is highly pyrophoric.

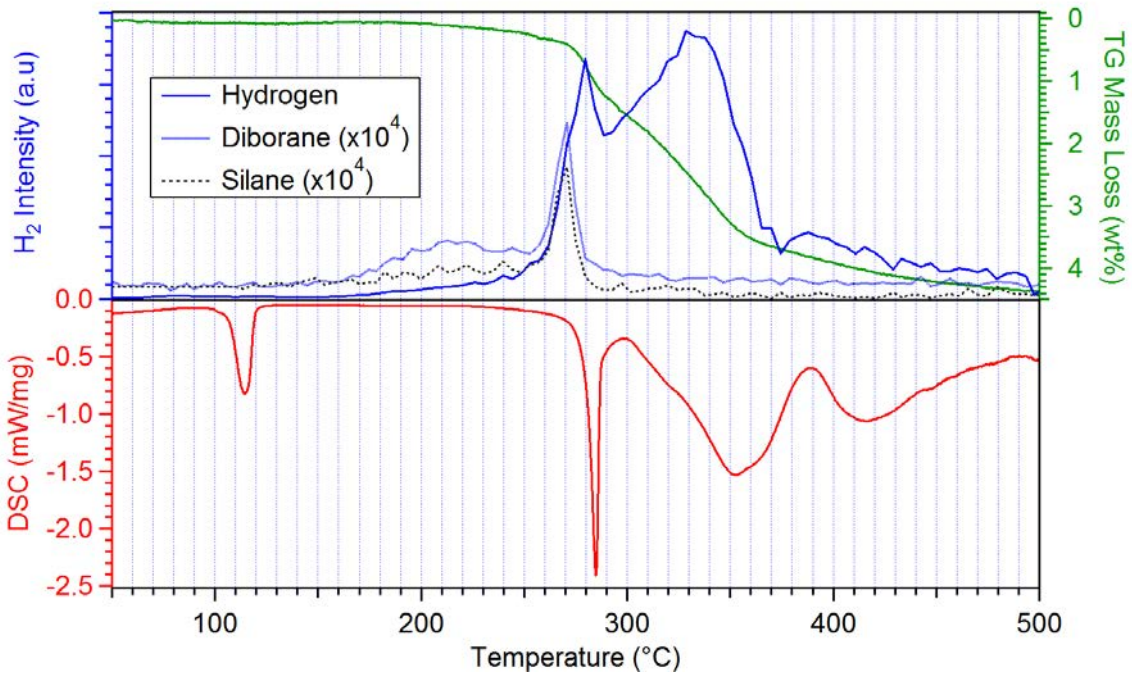

Figure 9.13 DSC-TGA-MS profile of Hand-mixed PS+$LiBH_4$ heated to 500 °C at 5 °C.min^{-1} under 3 bar Ar and a flow rate of 100 ml.min^{-1}

Figure 9.14 shows the DSC-TGA-MS profile of PM-PS+$LiBH_4$ heated to 500 °C at 5 °C.min^{-1} under 3 bar Ar. The DSC profile of PM-PS+$LiBH_4$ shows a number of endothermic peaks. The peak at 109 °C is indicative of polymorphic phase transition of $LiBH_4$ from an orthorhombic to hexagonal crystal structure. The next two peaks at 258 °C and 279 °C are a result of the melting of nano-confined and bulk $LiBH_4$ respectively, suggesting the pores were over loaded during the melt-infiltration process and some bulk $LiBH_4$ remained un-confined. This result agrees with the DSC for non-PM PS+$LiBH_4$ (Figure 9.13) that indicated at pore over filling after melting.

The final two endothermic peaks provide further evidence for over loading the pore capacity of PS. The first peak at 353 °C is consistent with the decomposition of nano-confined $LiBH_4$, whilst the second peak split peak with minima located at 415 °C and 424 °C is consistent with the decomposition of pure $LiBH_4$. The decomposition of the non-confined $LiBH_4$ within the sample still precedes over 40 °C lower than is observed for pure $LiBH_4$ indicating that the PS surface has an influence upon the decomposition of $LiBH_4$.

The onset of H_2 desorption occurs at an impressively low 120 °C with peak desorption occurring at 336 °C. A small shoulder can be seen on the right of the H_2 desorption peak and is accredited to the decomposition on un-confined $LiBH_4$. The sample desorbed 2.8 ± 0.1 wt% H_2 by 500 °C, with no SiH_4 or B_2H_6 being detected.

It is clear from the H_2 desorption profile of PM-PS+$LiBH_4$ that the sample begins to desorb H_2 over 100 °C below the melting point of the nano-confined $LiBH_4$, suggesting the $[BH_4]^-$ ion mobility is greatly improved when confined within the PS mesopores.

Both the shape and downshift in location of the of the phase change and melting peaks are consistent with work by Liu et al. 2011 who studied the thermal decomposition of $LiBH_4$ nano-confined within nano-porous carbons.

PS did not desorb any SiH_x during heating, PM-PS+$LiBH_4$ did not desorb any B_2H_6 or SiH_4 during decomposition, whereas non-PM PS+$LiBH_4$ was shown to desorb both B_2H_6 and SiH_4 at melting suggesting SiH_4 is released as a result of a reaction between B_2H_6 and the PS surface.

Compared to the non-PM PS+$LiBH_4$ sample, the melt-infiltrated sample desorbed almost 1.6 wt% less by 500 °C. It is clear from the DSC that the decomposition of $LiBH_4$ is completed by 500 °C, suggesting that either the PM sample follows a different reaction pathway with heavier products, or more simply, the 10 bar H_2 overpressure applied during the pre-melting process of PS+$LiBH_4$ was not adequate to suppress the decomposition of $LiBH_4$, a 3 bar H_2 over pressure has been shown to supress the decomposition of bulk $LiBH_4$ (Pinkerton et al., 2007). Since the non-PM PS+$LiBH_4$ sample was found to rapidly desorb H_2 above 260 °C, it is believed that the $LiBH_4$ began to decompose during the melt-infiltration due to the effect of nano-confinement and the PS scaffold upon $LiBH_4$.

9.4.2 XRD

The XRD pattern of dehydrided PM-PS+$LiBH_4$ is shown in Figure 9.16. No reflections from o-$LiBH_4$ are observed confirming the excess $LiBH_4$ not confined within the PS scaffold was decomposed. No reflections consistent LiH are observed in the dehydrided sample, however, LiH is difficult to detect by XRD since the measurement relies upon the interaction between

X-Rays and the atom's electron cloud, which for light elements, is less populated compared to heavier atoms.

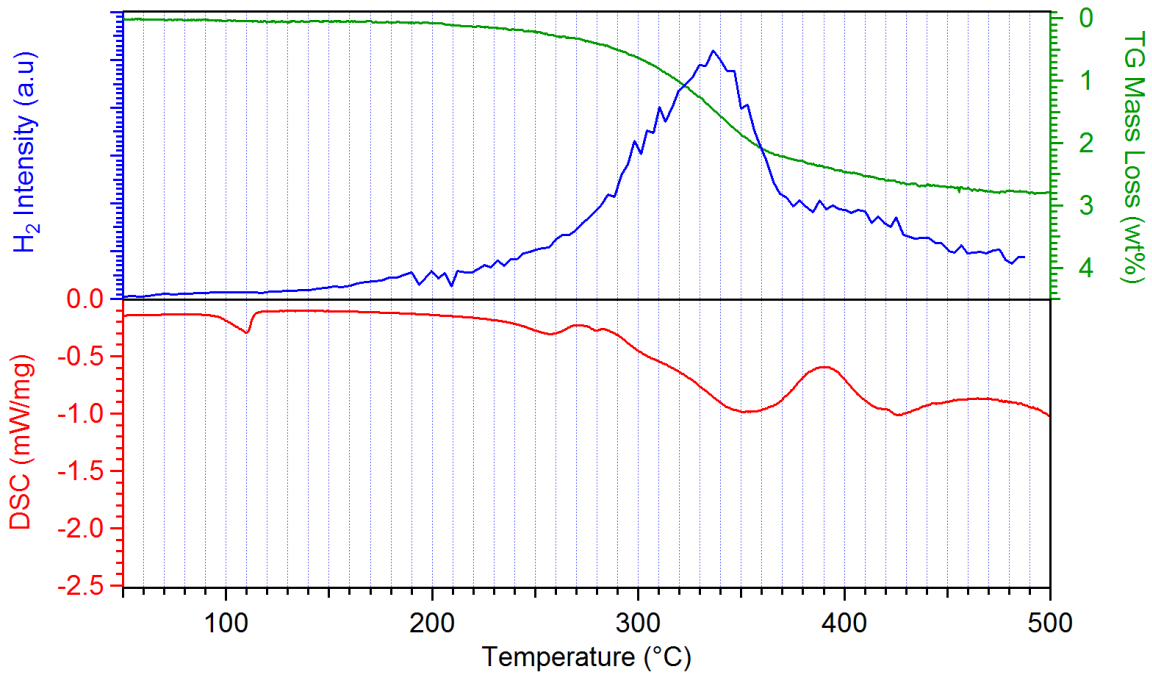

Figure 9.14 DSC-TGA-MS profile of PM-PS+LiBH$_4$ heated to 500 °C at 5 °C.min^{-1} under 3 bar Ar and a flow rate of 100 ml.min^{-1}

Decomposition products will also be confined within the pores thus eliminating any long-range order, making them even harder to detect by XRD. Cubic silicon is still observed in the dehydrided sample, however the relative intensity of the (004) can be seen to further increase after heating. This may be a result of the crystal growth along the direction of pore propagation caused by annealing of the Si during decomposition.

9.4.3 Raman Spectroscopy

The Raman spectrum of dehydrided PM-PS+LiBH$_4$ is shown in Figure 9.18, no new phases are observed after dehydrogenation. The intensity of the 2TA mode can be seen to decrease

after heating, along with an increase in the shoulder peak associated with the amorphous content, suggesting the dehydrided samples has a higher amorphous content that the as-prepared PM PS+$LiBH_4$ sample. The vibrations located at 1580 cm^{-1} observed in the PM-PS+$LiBH_4$ are believed to be a measurement artefact as previously discussed, and are not present in the dehydrided or rehydrided Raman spectra.

9.4.4 In-situ XRD

To help understand and identify the decomposition mechanism of PM-PS+$LiBH_4$, in-situ XRD measurements were carried out at regular intervals up to 400 °C at a heating rate of 2 °C.min^{-1} under 3 bar He with a flow rate of 100 ml.min^{-1}, results are shown in Figure 9.15.

Prior to heating at 30 °C the PM-PS+$LiBH_4$ sample exhibits reflections consistent with o-$LiBH_4$, PS and the Al_2O_3 sample holder. After 125 °C the $LiBH_4$ can be seen to undergo a phase transition to h-$LiBH_4$ followed by the disappearance of reflections consistent with h-$LiBH_4$ by 275 °C resulting from melting of $LiBH_4$ and subsequent loss of long range ordering. Between 275 °C and 291 °C reflections from monoclinic SiO_2 are observed. Above 291 °C Li_2O is also observed remaining in the sample for the rest of the measurement. During cooling a new phase is detected at 100 °C, this phase is yet to be identified, but phases containing Li, Si and O in the ICSD PDF2 database have been ruled out. It is clear from these results that the PM-PS+$LiBH_4$ sample heavily oxidised during heating, highlighting the samples high reactivity with oxygen.

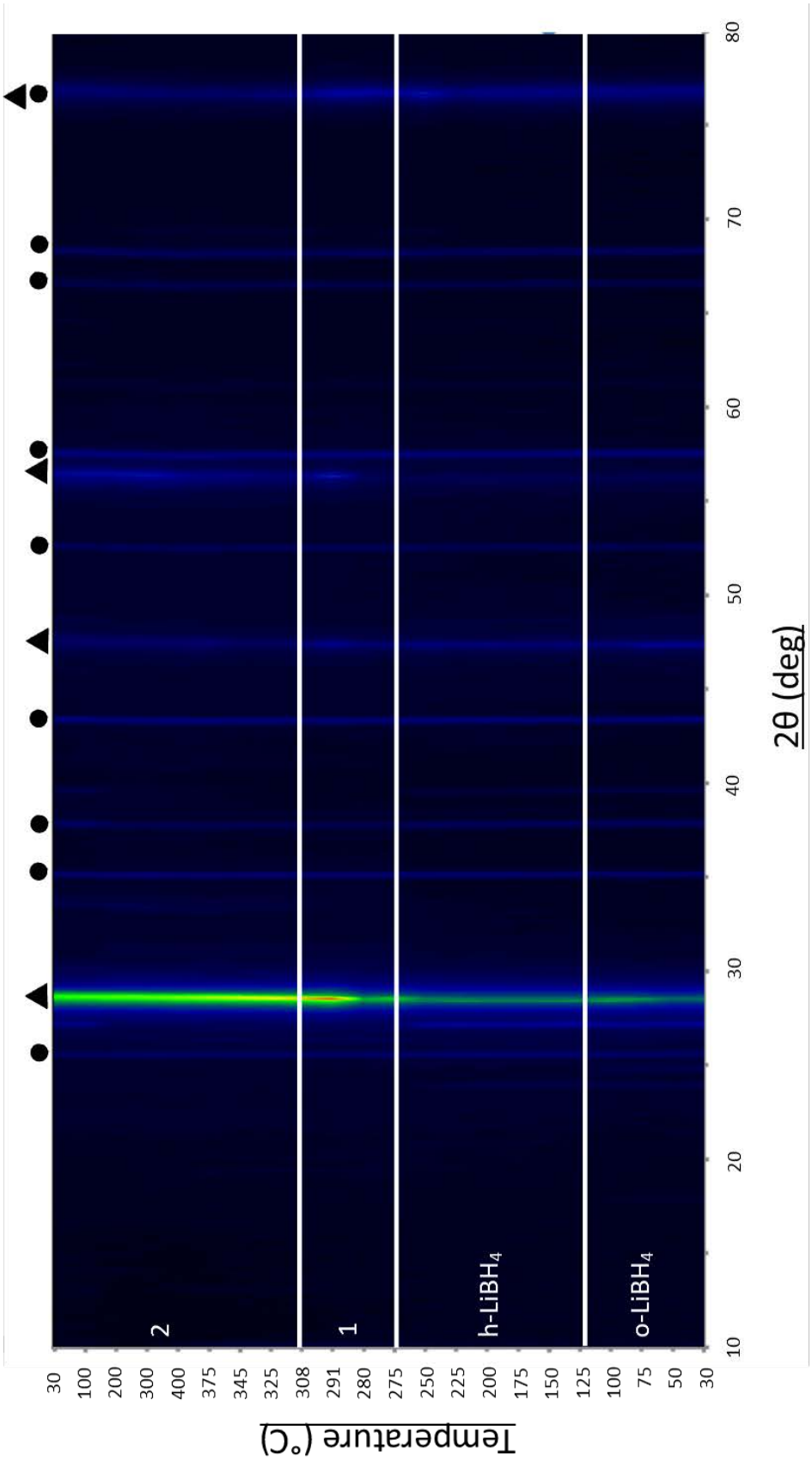

Figure 9.15 In-situ XRD of PM-PS+LiBH4 heated to 400 °C at 2 °C.min^{-1} under 3 bar He with a flow rate of 100 ml.min^{-1}. Black circles and black triangles indicate the location of reflections from the AlO_2 sample holder and cubic Si respectively. The ICDD PDF2 database (2011) was used for phase identification

9.5 Rehydrogenation of Porous Silicon + $LiBH_4$

Dehydrided PM-PS+$LiBH_4$ was rehydrided at 350 °C under 100 bar H_2 for 10 h using Sieverts apparatus and characterised using XRD, Raman spectroscopy and DSC-TGA-MS.

9.5.1 XRD

Rehydrided PM-PS+$LiBH_4$ was studied by XRD, Figure 9.16c. No reflections consistent with o-$LiBH_4$ are present, cubic silicon is the only phase that can be identified. After rehydrogenation the reflections from the (004) plane of Si at 69.1 ° 2θ can be seen to reduce. This could be a result of a reduction in the long-range order in the (004) direction caused by the reformation of $LiBH_4$ with in the pores of the PS scaffold. Two low intensity peaks located at 33° 2θ and 38 ° 2θ are just visible on the rehydrided sample, the origin of these peaks is unknown.

The lattice parameter of cubic silicon in the rehydrided PM-PS+$LiBH_4$ was calculated using Pseudo-Reitveld refinement, results are shown in Figure 9.17. The lattice parameter can be seen to return to its original size (within errors) after rehydrogenation.

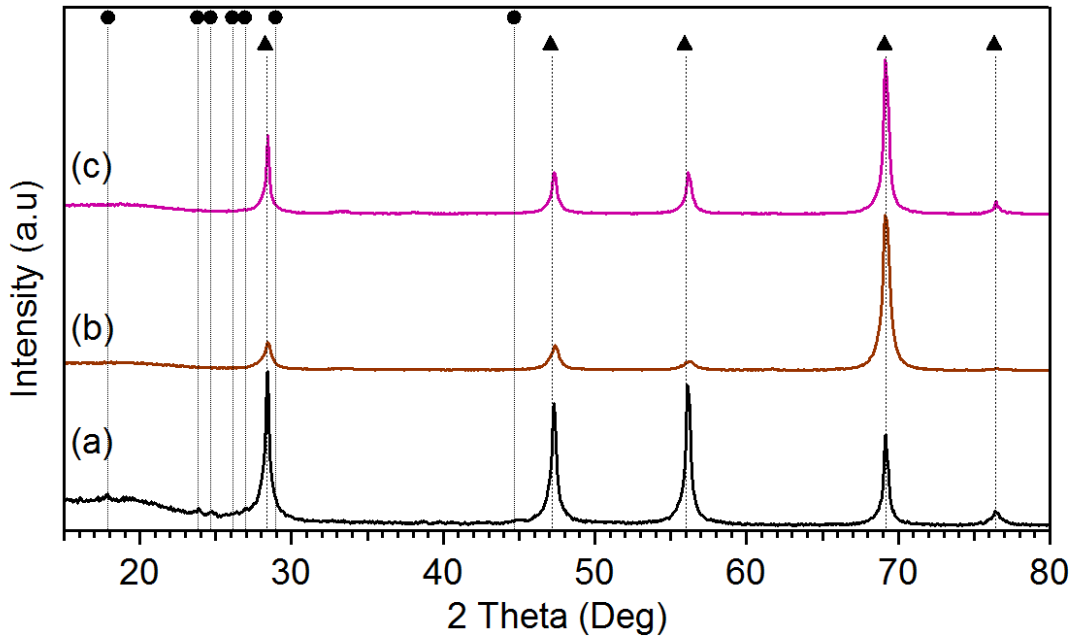

Figure 9.16 Room temperature XRD patterns of a) PM-PS+LiBH$_4$ b) dehydrided PM-PS+LiBH$_4$ and c) rehydrided PM-PS+LiBH$_4$. Reflections consistent with o-LiBH$_4$ and cubic Si are indicated by the black circles and triangles, respectively.

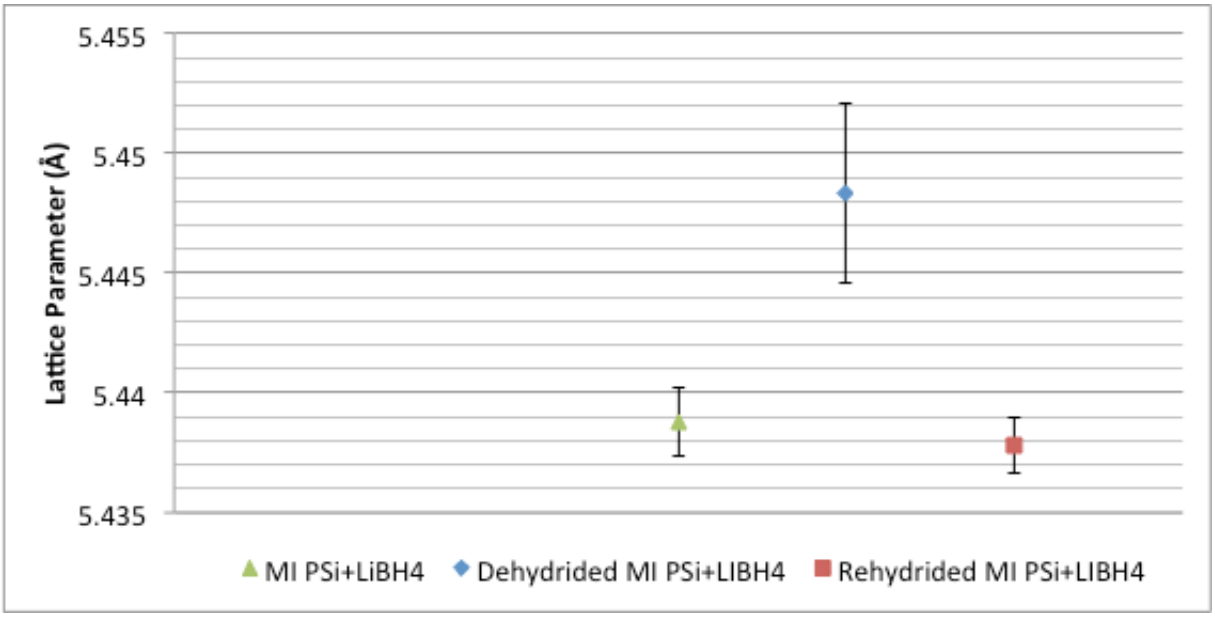

Figure 9.17 Lattice Parameter of cubic silicon in PM-PS+LiBH$_4$, dehydrided PM-PS+LiBH$_4$ and rehydrided PM-PS+LiBH4, calculated by pseudo Reitveld refinement

9.5.2 Raman

The Raman spectrum of rehydrided PM-PS+$LiBH_4$ is shown in Figure 9.18c. No new vibrations are observed in the Raman spectrum after rehydrogenation, only the 2TA, TO and 2TO modes of Si are seen. No vibrations consistent with the $[BH_4]^-$ tetrahedral structure of $LiBH_4$ or SiH_x modes are visible.

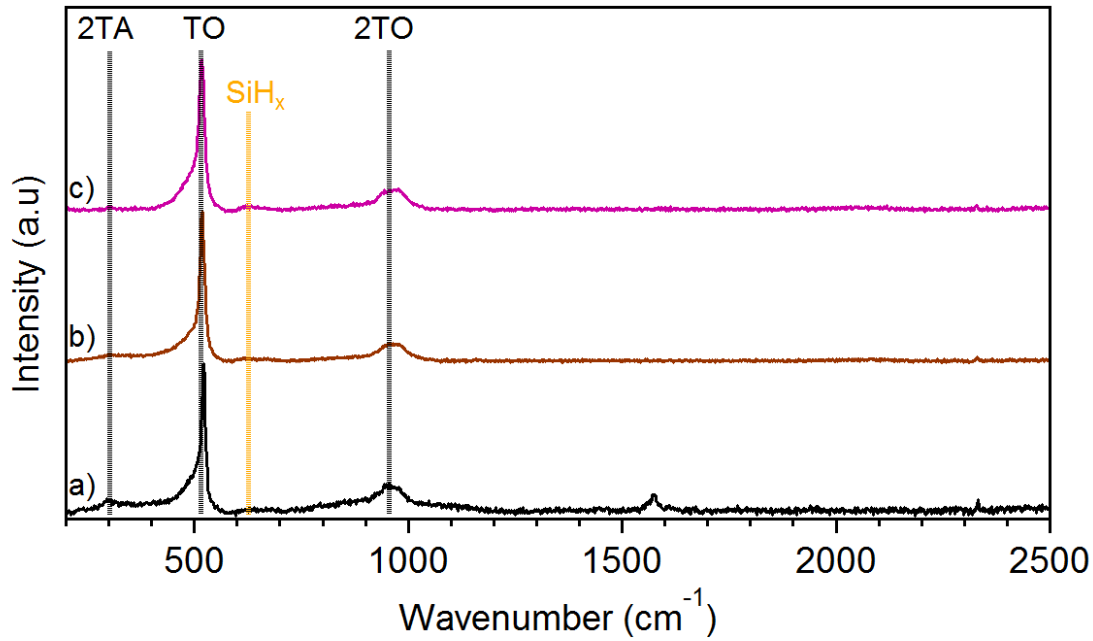

Figure 9.18 Room temperature Raman spectra of a) PM-PS+$LiBH_4$ b) dehydrided PM-PS+$LiBH_4$ and c) rehydrided PM-PS+$LiBH_4$. The 2TA, TO and 2TO modes of Silicon are indicated by the dotted lines.

9.5.3 DSC-TGA-MS

The thermal decomposition of rehydrided PM-PS+$LiBH_4$ was investigated by DSC-TGA-MS, shown in Figure 9.19. The DSC trace exhibits a single endothermic event with a minima located at 330 °C, no peaks consistent with an orthorhombic to hexagonal phase change or melting of $LiBH_4$ are observed. The single endothermic peak is believed to be the

decomposition of reformed $LiBH_4$ confined within the PS scaffold. 0.9 wt% H_2 was desorbed by 500 °C indicating that only 32% of the initial capacity was restored after rehydrogenation.

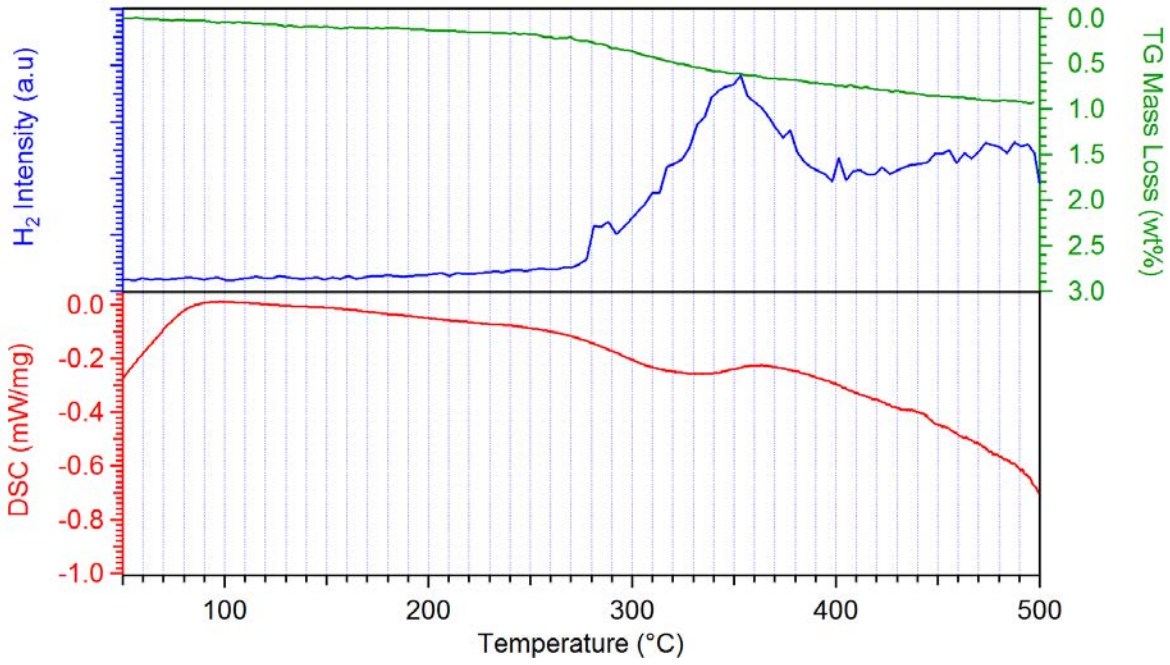

Figure 9.19 DSC-TGA-MS profile of rehydrided PM-PS+$LiBH_4$ heated to 500 °C at 5 °C.min^{-1} under 3 bar Ar and a flow rate of 100 ml.min^{-1}

9.5.4 Cyclic Uptake

The cyclic stability of PM-PS+$LiBH_4$ was studied over 5 de/re-hydrogenation cycles using Sieverts apparatus to measure the isothermal H_2 uptake at 350 °C as function of sample wt% and H_2 pressure, Figure 9.20. On the first uptake cycle, PM-PS+$LiBH_4$ absorbed 1.3 ± 0.1 wt% H_2, corresponding to 46 % of the original H_2 quantity desorbed by 500 °C. The H_2 uptake can be seen to gradually increase during cycling, 1.1 ± 0.1 wt% was achieved after 5 cycles, corresponding to 40 % of the original H_2 desorption from the as-prepared sample.

The first uptake cycle can be seen to start just above 3 bar, opposed to 0 bar. This was caused by an experimental error in which the chamber was not fully evacuated after decomposition of the as-prepared sample before the measurement began. This error is not believed to have drastically altered the conditions and as such the total uptake is regarded as a valid value.

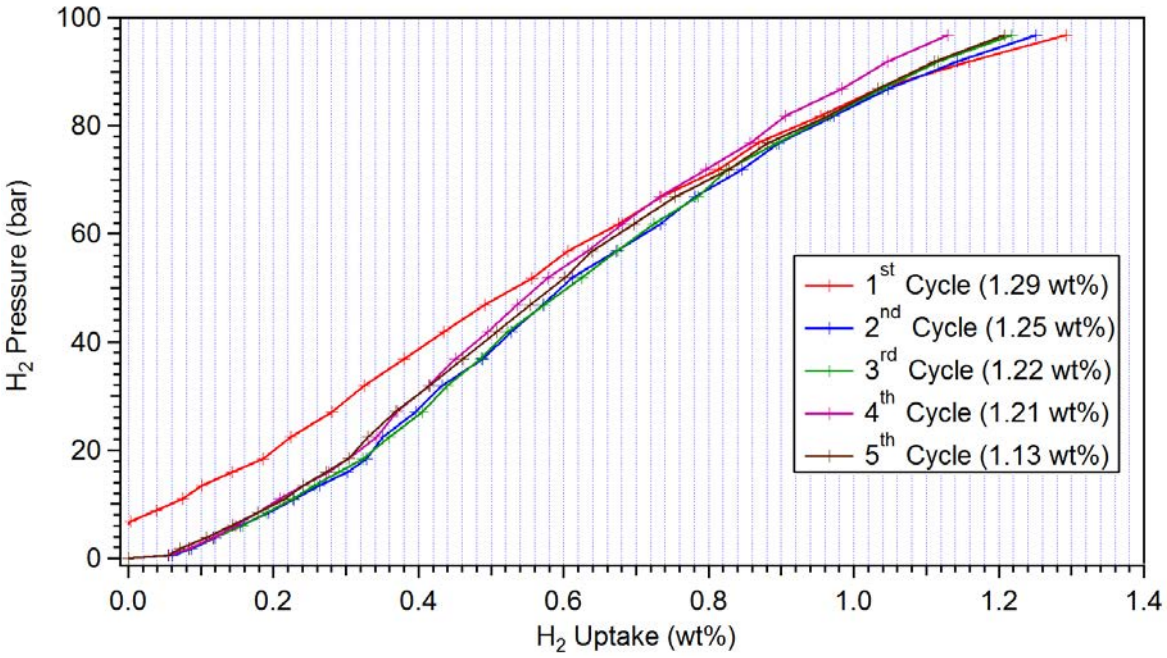

Figure 9.20 Cyclic H_2 uptake isotherms of PM-PS+$LiBH_4$ measured at 350 °C as a function of H_2 pressure and uptake, the final H_2 uptake after each cycle is displayed

9.6 Discussion

As-received PS was first characterised by room temperature XRD and Raman spectroscopy, which revealed broad reflections consistent with silicon as expected for PS (Diaz-Guerra and Montone, 2002) with a small amorphous content indicated by a shoulder on the TO Raman mode of Silicon (Iqbal et al., 1980). The Scherrer equation calculated the crystallite size of

between 28 nm and 40 nm. SEM allowed the PS to be characterised as mesoporous with an estimated pore range of 20 nm to 50 nm.

DSC-TGA-MS (Figure 9.9) has shown the onset of H_2 desorption to be below 250 °C supporting in-situ Raman spectroscopy results (Figure 9.6 & Figure 9.7) indicate that SiH_x species start to decompose around 250 °C. Previous work by Lysenko et al. 2005 saw a similar shaped H_2 desorption with a defined peak ca. 344 °C followed by a prolonged desorption, accrediting the defined H_2 desorption peak to the decomposition of SiH_2, and the wider desorption resulting from the decomposition of SiH. The room temperature Raman spectra of PS heated to 500 °C did not show any evidence for the existence of SiH_x species.

A total of 0.2 ± 0.1 wt% H_2 was desorbed by 500 °C equating to a hydrogen concentration of 61 $mmolg^{-1}$, consistent with a previous reported value of 66 $mmolg^{-1}$ for PS with a calculated crystallite size of 2 nm (Lysenko et al., 2005).

The surface area of PS was found to increase by over 50 m^2g^{-1} after thermal decomposition of SiH_x species on the surface of as-received PS (Figure 9.5 and Figure 9.8) from 280 ± 2 m^2g^{-1} to 332 ± 2 m^2g^{-1}. This increase in surface area may be caused by the removal of the top layer of H_2 during heating, with the removal of this coating exposing a larger surface area and in-turn opening up defects that could previously not be accessed by the N_2 molecules.

The pre-melting of PS+$LiBH_4$ is believed to have produced $LiBH_4$ confined within the porous scaffold of PS as indicated by loss of long range order of $LiBH_4$ in the XRD pattern of PM-PS+$LiBH_4$. Weak reflections from o-$LiBH_4$ and the DSC decomposition profile both suggest that some $LiBH_4$ remained unconfined indicating over-filling of the pores, with the remaining

$LiBH_4$ creating a surface layer on the PS. The unconfined PS was still shown to decompose over 40 °C lower than bulk $LiBH_4$ providing evidence of a surface interaction between $LiBH_4$ and PS resulting in the destabilisation of $LiBH_4$.

Nano-scale effects resulting from a larger surface energy experienced by smaller particles, only occurs when particles sizes are in the range of 2 nm, thus requiring an equivalent pore size to achieve this (Fichtner, 2011). Subsequently, the observed reduction in the decomposition temperature along with required temperatures and pressures for rehydrogenation of $LiBH_4$ within the pre-melted within the PS scaffold is believed to be due to improved $[BH_4]^-$ ion mobility and prevention of product agglomeration resulting in improved kinetics.

After pre-melting, PS + $LiBH_4$ did not desorb any detectable levels of B_2H_6 or SiH_4 agreeing with previous work in the literature that the nano-confinement of $LiBH_4$ suppresses the formation of B_2H_6 and influences the decomposition pathway (Liu et al., 2011).

In-situ XRD did not give any further insight into the decomposition pathway of PM-PS+$LiBH_4$ due to the observed aggressive reaction with oxygen, ideally this results would be repeated with the source of oxygen contamination eliminated. Consequently the decomposition pathway can only be speculated based on TGA-MS results.

Non-PM PS+$LiBH_4$ was shown to desorb small quantities of SiH_4 and B_2H_6 that were not observed during the heating of pure PS, indicating that a chemical reaction between $LiBH_4$ the Porous Silicon additive occurred during heating. The SiH_4 evolution was accompanied with an intense H_2 desorption as the $LiBH_4$ melted, consistent with the behaviour seen for

B_2H_6 evolution from non-PM ZTC+$LiBH_4$. With no SiH_4 or B_2H_6 detected during the heating of as-received or PM PS+$LiBH_4$ the release of SiH_4 can be inferred to result from a reaction between B_2H_6 and PS. Proposed decomposition pathways for non-PM PS+$LiBH_4$ is shown in Equations 5.2 and 5.3 and Equation 5.4, with Equations 9.1, 9.2 and 9.3 a side reaction which occurs when BH_3 reacts with the Si surface exposed after the thermal decomposition of SiH_4 species.

$$LiBH_4 \rightarrow LiH + BH_3 \quad (9.1)$$
$$SiH_x \rightarrow Si + {}^{x}/_{2}H_2 \quad (9.2)$$
$$3Si + 4BH_3 \rightarrow 3SiH_4 + 4B \quad (9.3)$$

PM-PS+$LiBH_4$ was found to desorb a total of 2.79 wt% H_2 with no SiH_4 or B_2H_6 observed, suggesting the decomposition pathway of $LiBH_4$ in the pre-melted sample is different to that of non-PM PS+$LiBH_4$. The decomposition pathway of PM PS+$LiBH_4$ is unknown, however, if the assumption that partial decomposition of $LiBH_4$ occurred during pre-melting resulting in the loss of some capacity, it can be assumed that $LiBH_4$ decomposed into LiH, amorphous B and H_2, Equation 5.4.

The confinement of $LiBH_4$ in PS has been shown to be an effective way to destabilize the decomposition of $LiBH_4$ reducing the temperature of the decomposition by over 110 °C. The sample was shown to be effectively recharged with 41% of its original H_2 capacity after 5 cycles, under 100 bar H_2 and 350 °C, although the reformation of $LiBH_4$ in the rehydrided sample could not be confirmed. Although confinement of $LiBH_4$ in PS has been shown to greatly reduce the required temperatures for H_2 evolution, its use as on-board storage material is limited. The limited H_2 content in wt% and loss of capacity after 5 cycles prevent it from being considered as a possible candidate.

10 General Discussion

The addition of each additive to $LiBH_4$ was found to suppress the aggressive foaming effect observed during the decomposition of bulk $LiBH_4$ that originates from the rapid release of H_2 from the liquid phases of $LiBH_4$ during decomposition. This foaming effect poses difficulties with the containment of the complex borohydride during dehydrogenation as demonstrated by the pictures published Ward et al., (2013) showing decomposed $LiBH_4$ inside a glass tube. None of the samples studied in this work demonstrated any evidence of foaming during decomposition. A possible explanation for the elimination of this foaming effect is an interaction between the liquid $LiBH_4$ and the surface of the additive, in which the surface tension between the liquid $LiBH_4$ and additive's surface suppresses the foaming effect. Alternatively, the reduction of H_2 onset temperatures aids a longer less aggressive initial desorption. The suppression of foaming helps to keep the decomposition products in close proximity preventing agglomeration and separation of the products promoting reversibility.

In this work, the quantity of H_2 desorbed from graphite milled under 3 bar H_2 for 8 h reported by Zhang et al., (2012) could not be replicated under the same conditions. Since small quantities (<0.5 wt%) of H_2 were detected via TGA-MS during the heating of the graphite milled under 3 bar H_2, this sample can be regarded as partially hydrogenated graphite. The surface area of 8 h graphite (Ar) was measured to be 462 m^2g^{-1} compared to 150 m^2g^{-1} for 8 h graphite (H_2) providing evidence that the 8 h graphite (H_2) sample was indeed milled under a H_2 over pressure; milling graphite under Ar is known to introduce

greater levels of disorder and particle size reduction whereas milling under H_2 is known to supress these effects (Section 2.4.2).

Peak H_2 desorption from graphite (Ar) + $LiBH_4$ was found to occur at 365 °C, 102 °C lower than for pure $LiBH_4$, whilst peak H_2 desorption from graphite (H_2) + $LiBH_4$ occurred at 381 °C suggesting that the structure of the carbon additive plays a role in the destabilisation of the $LiBH_4$. XRD measurements on the dehydrided samples displayed reflections consistent with LiH along with down shifts in the location of reflections from the 002 plane to lower 2θ values inferring an expansion in the c direction of the graphite unit cell. Subsequent Pawley refinements on these XRD patterns indicated an increase in the interlayer spacing of C atoms after decomposition in both samples, 0.065 ± 0.009 Å for the dehydrided graphite (Ar) + $LiBH_4$ sample and 0.015 ± 0.001 Å for dehydrided graphite (H_2) + $LiBH_4$ sample. These observed expansions are consistent with the intercalation of Li in between the layers of carbon atoms and correspond to the formation of LiC_{36} (Dahn, 1991; Konar et al., 2015) and LiC_{72} (Konar et al., 2015) respectively. This evidence of Li intercalation below 500 °C suggests that some of the LiH in both graphite-based samples was destabilized by the nanostructured graphite decomposing over 100 °C below bulk LiH, consistent with results reported Miyaoka et al., 2009 for a ball milled graphite+LiH system.

The greater level of deformation achieved by milling under Ar vs H_2 in this work is believed to result in greater fragmentation of the graphite sheets in turn leading to a greater number of edges in which Li is able to enter the graphite. The graphite (Ar) + $LiBH_4$ sample desorbed the largest amount of H_2 (7.3 wt%) whilst forming a more lithium rich intercalation compound compared to the graphite (H_2) + $LiBH_4$ sample (6.4 wt%). The graphite milled

under Ar was shown to have a higher amorphous content and greater ratio of sp^3 to sp^2 C bonds via XRD and Raman spectroscopy, consequently it can be concluded that the higher the level of amorphisation of the graphite, the greater the destabilization effect on $LiBH_4$ and LiH.

Trace quantities of B_2H_6 were detected for both graphite-based samples between 200 and 300 °C above which B_2H_6 is known to thermally decompose. The presence of B_2H_6 below the melting temperature of $LiBH_4$ suggests that some of the $LiBH_4$ underwent a solid-state reaction. DFT calculations carried out by Wang et al., 2016 predicted that graphite fragments inserted into the interstitial sites of $LiBH_4$ resulted in the formation of BH_3 complexes reducing the decomposition temperature of $LiBH_4$ and offering a mechanism for B_2H_6 production. It is therefore proposed that both graphite samples followed a similar reaction pathway, with some $LiBH_4$ decomposing via either reaction 5.2 and 5.3 between 200-300 °C followed by the decomposition of the remaining $LiBH_4$ into LiH, B and H_2 via equations 5.1 and 5.4. After which some of the LiH decomposed via reaction 5.5. Although no $Li_2B_{12}H_{12}$ was detected, both DSC profiles show clear 2-step decomposition pathway suggesting the formation and decomposition of an intermediary compound. Reed and Book, 2009 carried out a study on the decomposition of $LiBH_4$ using in-situ Raman spectroscopy demonstrating that $LiBH_4$ decomposes through two competing reactions, the direct decomposition (Equation 5.1) into LiH, B and H_2 and decomposition into the known intermediate $Li_2B_{12}H_{12}$ (first half of Equation 5.4). Based on the wt% of H_2 desorbed from both graphite samples it can be inferred that even if $Li_2B_{12}H_{12}$ was formed during decomposition it must have further decomposed into LiH, B and H_2 (Equation 5.4), no

evidence for the presence of this intermediary was observed via XRD or Raman spectroscopy.

The presence of reflections from o-$LiBH_4$ in the PM AC+$LiBH_4$ sample (Figure 7.2d) coupled with the DSC profile during decomposition (Figure 10.1) which both show no significant loss in order after the pre-melting step, indicate that the majority of $LiBH_4$ was not nanoconfined within the porous structure of the AC at 300 °C for 30 min under 10 bar H_2. This may be a result of either the slow impregnation of $LiBH_4$ into the AC via capillary action or more likely due to the size of the pores not resulting in a significant loss of order. Unfortunately, the pore structure of the AC could not be investigated by TEM, so the pore-size and morphology is unknown. The pre-melting of the AC+$LiBH_4$ sample was shown to supress the evolution of B_2H_6 during thermal decomposition resulting in the PM AC+$LiBH_4$ decomposing via 2 possible reaction pathways, Equation 5.1 and Equation 5.4. The presence of a two-step decomposition mechanism between 350 °C and 420 °C in the DSC profile suggests that the AC+$LiBH_4$ sample decomposes via the same bulk decomposition mechanism as the graphite based samples. This decomposition between 350 °C and 400 °C is consistent with $LiBH_4$ incorporated into AC (pore size < 2 nm) via pre-melting reported by (Gross et al., 2008), no DSC results were published for this sample.

The DSC trace of the decomposition of the non-PM ZTC+$LiBH_4$ sample (Figure 8.6) shows a sharp exothermic peak immediately after the melting of $LiBH_4$ peak ca. 290 °C. No exothermic reactions occur during the decomposition of bulk $LiBH_4$ (Figure 2.17), as such, the exothermic peak observed for the non-PM ZTC+$LiBH_4$ must originate from an interaction between the porous scaffold and liquid phase $LiBH_4$. To the best of my knowledge the

presence of an exothermic peak immediately after the melting of $LiBH_4$ into a porous scaffold as not been reported, and was not observed during the decomposition of non-PM PS+$LiBH_4$. The density of solid phase $LiBH_4$ is 0.666 $gmol^{-1}$, although a value for the density of liquid phase $LiBH_4$ could not be found in the literature, one possible explanation for this exothermic reaction is the contraction of $LiBH_4$ after infiltration into the porous scaffold. No such exothermic peak was observed during the decomposition of PM ZTC+$LiBH_4$ suggesting that the exothermic reaction occurred during the pre-melting treatment. PM ZTC+$LiBH_4$ desorbed 5.8 wt% $LiBH_4$ by 500°C exhibiting the lowest H_2 desorption onset of any sample in this work (136 °C) and the second lowest peak H_2 desorption (339 °C), see Table 10.2. The profile of the endothermic peak associated the decomposition of $LiBH_4$ emulates a single asymmetric peak, different to the clear split-peak decomposition associated with bulk $LiBH_4$ Figure 2.17, this behaviour is consistent with $LiBH_4$ confined within porous carbon scaffolds with a pore size of < 4nm (Shao et al., 2014, 2015; Liu et al., 2011). The broad asymmetric DSC decomposition peak suggests that $LiBH_4$ may be sat in a wide range of different energy sites and may still decompose through a two-step reaction, resulting in decomposition over a wide temperature range. Due to the loss of long range order originating in the confinement of reaction products in the ZTC pores, XRD and Raman spectroscopy did not identify any decomposition products, however, a weight loss of 5.8 wt% corresponds to the decomposition of $LiBH_4$ into LiH, B and H, as such the decomposition is of PM ZTC+$LiBH_4$ is believed to proceed via Equation 5.1.

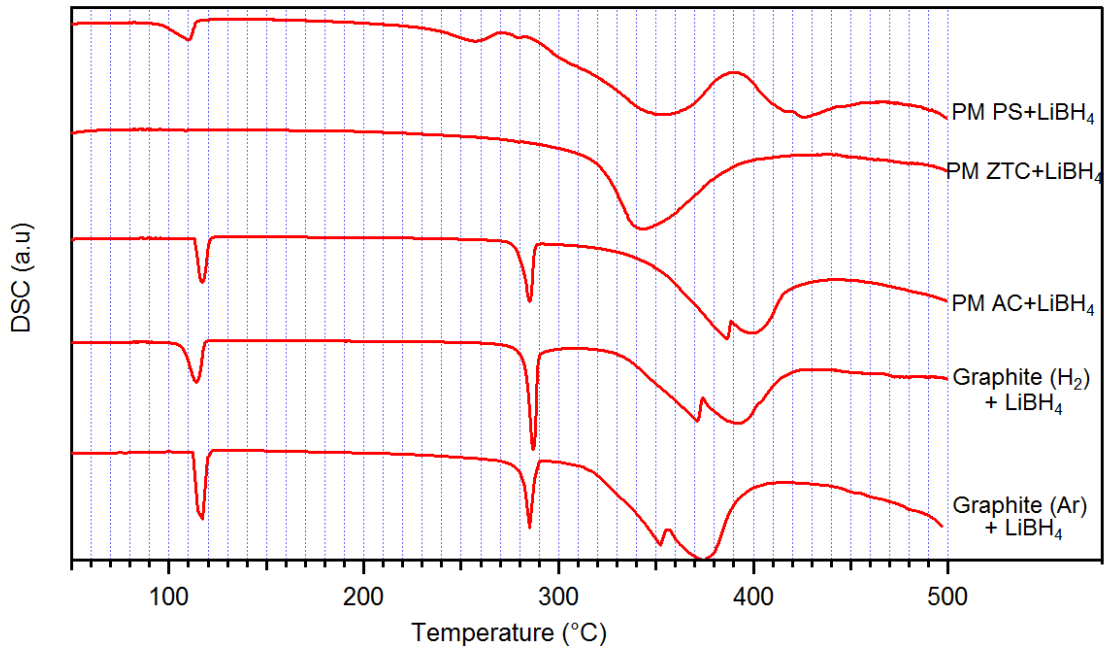

Figure 10.1 DSC profile of each sample heated to 500 °C at 5 °C.min^{-1} under 3 bar Ar and a flow rate of 100 ml.min^{-1} for easy comparison

The DSC profile of PM PS+$LiBH_4$ (Figure 9.14) also displays an asymmetric decomposition peak ca. 336 °C consistent with the nano-confinement of $LiBH_4$ as discussed above, followed by a two-step decomposition ca. 420 °C owed to decomposition of $LiBH_4$ resulting from over filling. The PM PS+$LiBH_4$ sample is believed to follow the same decomposition pathway as the PM ZTC+$LiBH_4$ (Equation 5.1), however, the formation of intermediate compounds cannot be ruled out.

The absence of CH_4 during decomposition of $LiBH_4$ in any of the carbon-based samples implies that the carbon additives do no chemically react with $LiBH_4$ during its decomposition into LiH B and H_2. Non-PM PS+$LiBH_4$ desorbed small quantities of SiH_4 and B_2H_6 that were not observed during the heating of pure PS indicating that a chemical reaction between $LiBH_4$ and the Porous Silicon additive occurred during heating. The SiH_4 and B_2H_6 evolution

was accompanied with an intense H_2 desorption as the $LiBH_4$ melted, consistent with the behaviour seen for B_2H_6 evolution from non-PM ZTC+$LiBH_4$. No B_2H_6 evolution was detected for any of the samples in the work exposed to the pre-melting process offering evidence that this step alters the decomposition mechanism of $LiBH_4$. No SiH_4 or B_2H_6 was detected during the decomposition of as-received PS or PM PS+$LiBH_4$ inferring the evolution of SiH_4 arises from a reaction between B_2H_6 and PS.

The pre-melting step is believed to create an intimate relationship between $LiBH_4$ and the surface of the additive, the nature of this interaction between the additive surface and $LiBH_4$ should be further explored to understand its influence on the suppression of B_2H_6 desorption. Confinement of $LiBH_4$ within porous scaffolds has been reported to suppress B_2H_6 evolution (Liu et al., 2011), however, it may be in the pre-melting/melt-infiltration process that results in the suppression of B_2H_6 evolution.

Figure 10.2 shows the a plot of the H_2 onset and peak decomposition temperatures, no correlation between additive surface area and the H_2 onset temperature or decomposition temperature of $LiBH_4$ is observed. The onset of H_2 desorption and peak H_2 release appear independent of the BET surface area of the additives. A decrease in the onset temperature does appear to correlate to a reduction in the decomposition temperature of $LiBH_4$ indicating the additives destabilized the entire decomposition mechanism of $LiBH_4$. This finding agrees well with results published for $LiBH_4$ confined within porous carbon scaffolds, shown in Table 10.1.

Table 10.1 Decomposition temperatures, H_2 onset temperatures, pore size and surface areas of carbon additives to $LiBH_4$

Carbon Additive	Pore Size (nm)	Surface Area (m^2g^{-1})	H_2 Onset (°C)	Peak H_2 Desorption (°C)	Source
Carbon Aerogel	25	810	-	390	(Gross et al., 2008)
Carbon Aerogel	13	770	-	381	(Gross et al., 2008)
Mesoporous carbon	3.8	1321	205	342	(Shao et al., 2014)
CMK-3	3.5	997	209	346	(Shao et al., 2015)
Nanoporous Hard Carbon	2	594	220	339	(Liu et al., 2010)
Activated Carbon	<2	1200	-	375	(Gross et al., 2008)
ZTC	1.4	3309	194	332	(Shao et al., 2015)

The DSC decomposition profiles of each sample are shown in Figure 10.1. Both PM ZTC+$LiBH_4$ and PM PS+$LiBH_4$ decompose at the lowest temperatures, 339 °C and 336 °C respectively suggesting that a small pore size results in the greatest destabilization of $LiBH_4$. Values in the literature also follow the same trend as shown in Table 10.1. Aside from activated carbon, the smaller the pore size, the lower the decomposition temperature of $LiBH_4$. Gross et al., 2008 reported a reduction in the both the activation energy of hydrogen desorption and increase in desorption kinetics with decreasing pore size for carbon aerogels further supporting this hypothesis.

It appears that a defined pore structure, in the nanometre range, is more important that a high surface area when considering possible additives to $LiBH_4$. This result may arise from the nano-sizing of $LiBH_4$ induced by confinement within a nanoporous structure and offers an explanation as to why graphite (Ar) + $LiBH_4$ has the third lowest peak H_2 desorption

temperature of 385 °C. The nanostructured graphite additive has a much high level of disorder compared to the equivalent milled under H_2, leading to fewer defects and pore like structures in which $LiBH_4$ can be confined. Also, as suggested by (Wang et al., 2016) the nanostructured graphite acts as a milling aid in the $LiBH_4$ ball milling step which will lead to a greater reduction in particle size of $LiBH_4$ reducing H_2 diffusion distances and improving desorption kinetics. In order to isolate the effect of nano-sizing vs the influence of the surface chemistry between the additives and $LiBH_4$, $LiBH_4$ particles in the size range of a few nanometres would need fabricating which poses extreme difficulties since ball milling of metal hydrides only leads to particles sizes in the range of 100-200 nm (Liu et al., 2010).

Each of the 5 additive materials (4 carbon and 1 silicon) were all found to reduce the decomposition temperature of $LiBH_4$ and promote reversibility, suggesting that the destabilization of $LiBH_4$ arises from an interaction between the additive surface and the $LiBH_4$ and not a chemical reaction with the host material itself. All the samples were rehydrided under 95 bar H_2 at 350 °C, Table 10.3 shows their initial H_2 storage capacities and their equivalent capacitates after 5 cycles. The two graphite-based samples (graphite H_2 + $LiBH_4$ and graphite Ar + $LiBH_4$) performed the worst with a reduction of initial capacity by over 73% and 70% respectively. The confinement of $LiBH_4$ in porous scaffolds has been reported to aid recombination of $LiBH_4$ (Shao et al., 2015; Gross et al., 2008) which agrees well with work in this thesis in which the PM ZTC+$LiBH_4$ and PM PS+$LiBH_4$ samples performed the best maintaining 57% and 42% of their initial storage capacities.

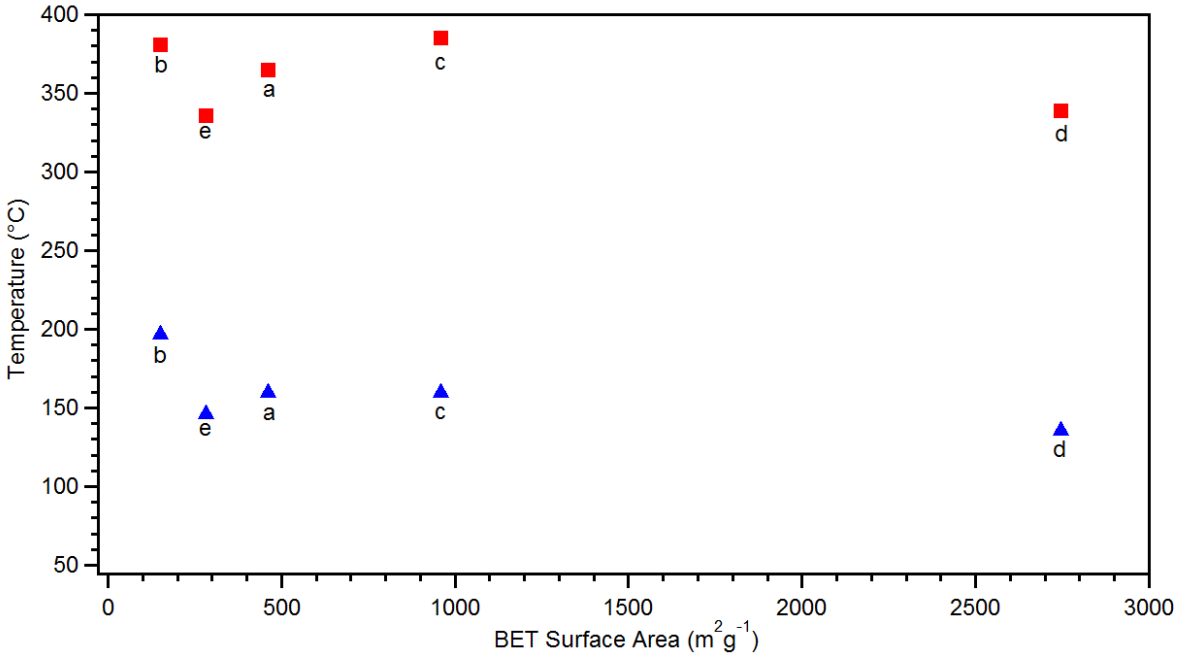

Figure 10.2 H_2 onset temperature (blue triangles) and peak H_2 desorption temperatures (red squares) as a function of the BET surface area for each sample; a) graphite (Ar) + $LiBH_4$, b) graphite (H_2) + $LiBH_4$, c) activated carbon + $LiBH_4$, d) zeolite templated carbon + $LiBH_4$ and e) porous silicon + $LiBH_4$

The confinement of $LiBH_4$ helps to prevent agglomeration and subsequent separation of the decomposition products of $LiBH_4$, helping to keep reactants in close proximity and minimise diffusion lengths. It is clear that nano-confinement of $LiBH_4$ within porous scaffolds helps to unlock the potential of $LiBH_4$ reducing decomposition temperatures and promoting reversibility. Recently, the incorporation of a NbF_5 catalyst into a mesoporous scaffold with $LiBH_4$ has been shown to reduce to reduce onset of H_2 desorption to 150 °C with peak desorption at 309 °C corresponding to a total H_2 desorption of 6.5 wt%. This dual approach of catalyst and nano-confinement offers a promising approach in the destabilization of $LiBH_4$ through nano-confinement. Recently, a $LiBH_4$-MgH_2 nano-composite with a particle size of ~10 nm dispersed onto graphene sheets was reported to complete 25 cycles without any

degradation to its 8.9 wt% H_2 desorption at 350 °C (Xia et al., 2016). However, mass production of this storage material is not currently economically viable.

As discussed in Section 1.6, the United States DoE targets for a hydrogen storage system for applications on light-duty vehicles are a 7.5 wt% H_2 capacity with a storage medium lifetime of 1500 cycles. The theoretical H_2 capacities of the carbon-based samples in this work (8.8 wt%) only just surpass the target wt% for the entire system, so even with impressive H_2 evolution of up to 7.3 wt%, higher storage capacities are required to meet the DoE Ultimate Fleet targets. In order to achieve the target wt% for a system, the ratio of additive to $LiBH_4$ needs optimizing, however, the greatest limiting factor of $LiBH_4$ based storage materials is the cyclic stability of the samples. The cause behind large reduction in capacity observed for all 5 samples (see Table 10.3) needs understanding in order to improve the hydrogen storage properties of $LiBH_4$ destabilized by non-reactive additives. This observed reduction in capacity is a common problem in $LiBH_4$ based storage materials. Shao et al., 2015 reported the formation of the stable intermediate $Li_2B_{12}H_{12}$ after rehydrogenation of a ZTC+$LiBH_4$ sample under 260 °C and 120 bar H_2 observed by Nuclear Magnetic Resonance spectroscopy (NMR), this phase was not observed via XRD. The formation of $Li_2B_{12}H_{12}$ under similar conditions to those used in this work (95 bar H_2 and 350 °C) suggests that the formation of this stable intermediary might be responsible for the large losses in H_2 capacity over cycling.

Table 10.2 Comparison table summarizing the effect on the hydrogen storage properties of $LiBH_4$ mixed with different additives. *Calculated using the BET Method **(Musyoka et al., 2015) ***Measured by SEM

	Additive	Structure	Pore Size	*Surface Area (m^2g^{-1})	H_2 Onset (°C)	Decomposition Peak (°C)	Weight loss (% of H_2 Content)	Reformed $LiBH_4$ (% of first desorption)	Rehydrided Decomposition Peak (°C)
a	Graphite (Ar)	Nanocrystalline /amorphous	N/A	462	160	365	82	37	352
b	Graphite (H_2)	Nanocrystalline /amorphous	N/A	150	197	381	73	46	375
c	Activate Carbon	Amorphous	Wide range of pore size	959	160	385	67	59	353
d	Zeolite Templated Carbon	Amorphous periodicity of 1.2 nm	Well defined 1-2 nm **	2745	136	339	66	59	330
e	Porous Silicon	Crystalline	20-50 nm ***	282	146	336	30	46	330

Table 10.3 H_2 capacity of initial H_2 desorption and uptake after 5 cycles for each sample

	Sample	Theoretical H_2 Capacity (wt%)	H_2 release at 500 °C (wt%)	H_2 capacity after 5 cycles (wt%)	Normalised H_2 storage capacity after 5 cycles
a	Graphite (Ar) + $LiBH_4$	8.8	7.3 ± 0.1	2.2 ± 0.1	0.30
b	Graphite (H_2) + $LiBH_4$	8.8	6.4 ± 0.1	1.8 ± 0.1	0.27
c	PM AC + $LiBH_4$	8.8	5.9 ± 0.1	2.3 ± 0.1	0.38
d	PM ZTC + $LiBH_4$	8.8	5.8 ± 0.1	3.3 ± 0.1	0.57
e	PM PS + $LiBH_4$	5.2	2.7 ± 0.1	1.1 ± 0.1	0.42

11Conclusions

The main aim of this thesis was to examine the effect of stable additives on the H_2 storage properties of $LiBH_4$ such as H_2 onset temperatures, decomposition temperatures and suppression of B_2H_6 evolution. In particular the effects of porous versus non-porous additives were investigated. Five different additives were added to $LiBH_4$ at a molar ratio of 2:1 (additive to $LiBH_4$): nanostructured graphite, partially hydrogenated graphite, activated carbon, zeolite templated carbon and porous silicon.

- Graphite is a cheap and abundant material that when ball milled under 3 bar Ar was found to desorb 7.3 wt% H_2 by 500 °C. Milling the graphite under Ar was found to induce a higher level of amorphisation than milling under 3 bar H_2 which in turn lead to higher H_2 desorption, higher cyclic stability and a lower decomposition temperature. The addition of graphite milled under Ar resulted in a decrease of 102 °C in the decomposition temperature compered to that for bulk $LiBH_4$.
- Porous additives were found to have a greater effect on decomposition of $LiBH_4$ as well as promoting cyclic stability, believed to result from the confinement of reaction products. Zeolite templated carbon and porous silicon were found to lower the decomposition temperature of $LiBH_4$ by 128 °C and 131 °C respectively.
- No correlation between surface area and decomposition temperature was observed agreeing with results published for carbon additives to $LiBH_4$.
- The confinement of $LiBH_4$ within porous scaffolds via melt-infiltration was found to offer an effective way of altering the decomposition pathway of $LiBH_4$ in order to

suppress the evolution of B_2H_6. Further investigation is needed to understand whether it is the pre-melting step or the incorporation of the $LiBH_4$ within the porous scaffold that causes this change in reaction pathway.

- The addition of each material to $LiBH_4$ at a molar a ratio of 2:1 (additive:$LiBH_4$) was found to suppress of the aggressive foaming of $LiBH_4$ during decomposition, believed to arise from a reduced decomposition temperature and surface tension between the liquid $LiBH_4$ and additive.

Although $LiBH_4$ shows great promise as a hydrogen storage material (owing to its high H_2 content), none of the materials studied in this work meet the Ultimate Fleet targets set out by the United States DoE (Section 1.6). Further advancements are required to improve cyclic stability whilst optimising the additive ratio.

12 Future Work

- Further studies into the hydrogenation of graphite through ball milling should be carried out in order to optimise the milling conditions (RPM, ball-to-powder ratio, milling media) required for graphite hydrogenation. UV Raman spectroscopy should be used to identify and quantify the $sp^3C\text{-}H_x$ stretching modes (around 2920 cm^{-1} (Ferrari and Robertson, 2001)) on hydrogenated graphite samples.
- The pre-melting (30 min at 300 °C under 10 bar H_2) of $LiBH_4$ within ZTC and PS has been shown to an effective mechanism for reducing the decomposition temperature of $LiBH_4$. These two porous additives resulted in the two lowest $LiBH_4$ decomposition temperatures in this work, consequently further investigation should be carried out to find the optimum pore size for a porous additive to $LiBH_4$, for this a wider range of pore sizes should be studied.
- TEM and pore size analysis should used to improve the understanding of the pore size and shape of porous additives to $LiBH_4$ and confirm the occurrence of nano-confinement.
- Currently there has been no investigation into the optimisation of conditions required to achieve recombination of $LiBH_4$. A study should be carried out to find the minimum conditions required for $LiBH_4$ reformation and the optimum conditions under which $LiBH_4$ can be reformed with the aim of reaching times comparable to that outlined in the US DoE Ultimate Fleet targets (3 minutes).

- The greatest drawback observed for all $LiBH_4$ samples investigated in this study was the large decrease in H_2 capacity observed over 5 cycles. The reason behind this should be explored including understanding the state of $LiBH_4$ in the dehydrided and rehydrided samples along with studying the effects of the application of varying temperatures and H_2 pressures during recombination in order to improve the cyclic performance.
- Further investigations should be made into the effect of pore size vs high surface additives in order to help understand their respective influences on the decomposition of $LiBH_4$. Nuclear magnetic resonance, transmission electron microscopy and small angle neutron scattering will help aid phase determination in nanoconfined samples that cannot be probed by XRD or Raman.

13 References

Acton, Q.A. (2013) **Issues in Acoustic and Ultrasound Technology: 2013 Edition**. ScholarlyEditions

Adhikari, S. and Fernando, S. (2006) Hydrogen membrane separation techniques. **Industrial & Engineering Chemistry Research**, 45 (3): 875–881

Aladekomo, J.B. and Bragg, R.H. (1990) Structural transformations induced in graphite by grinding: Analysis of 002 X-ray diffraction line profiles. **Carbon**, 28 (6): 897–906

Aoki, M., Miwa, K., Noritake, T., Kitahara, G., Nakamori, Y., Orimo, S. and Towata, S. (2005) Destabilization of LiBH4 by mixing with LiNH2. **Applied Physics A: Materials Science and Processing**, 80 (7): 1409–1412

Arnal, C., Alzueta, M.U., Millera, a. and Bilbao, R. (2012) Experimental and Kinetic Study of the Interaction of a Commercial Soot with NO at High Temperature. **Combustion Science and Technology**, 184 (July): 1191–1206

Au, M., Spencer, W., Jurgensen, A. and Zeigler, C. (2008) Hydrogen storage properties of modified lithium borohydrides. **Journal of Alloys and Compounds**, 462 (1–2): 303–309

Baerlocher, C., McCusker, L.. and Olson, D.. (2007) **Atlas of Zeolite Framework Types**. 6th ed. Elevier

Balat, M. (2010) Thermochemical Routes for Biomass-based Hydrogen Production. **Energy Sources, Part A: Recovery, Utilization, and Environmental Effects**, 32 (15): 1388–1398

Baldi, A., Gonzalez-Silveira, M., Palmisano, V., Dam, B. and Griessen, R. (2009) Destabilization of the Mg-H System through Elastic Constraints. **Physical Review Letters**, 102 (22): 226102

Bevan, A.I., Züttel, A., Book, D. and Harris, I.R. (2011) Performance of a metal hydride store on the “Ross Barlow” hydrogen powered canal boat. **Faraday Discussions**, 151 (March 2005): 353

Blanchard, D., Nale, A., Sveinbjörnsson, D., Eggenhuisen, T.M., Verkuijlen, M.H.W., Suwarno, Vegge, T., Kentgens, A.P.M. and De Jongh, P.E. (2015) Nanoconfined LiBH4 as a fast lithium ion conductor. **Advanced Functional Materials**, 25 (2): 184–192

Branauer, S. (1945) **The Adsorption of Gases Vapors, Volume 1, Physical Adsoprtion**. Princeton University Press

Brinkman, N., Eberle, U., Formanski, V., Grebe, P.U.D. and Matthé, R. (2012) **Vehicle Electrification – Quo Vadis ?** Österreichischer Verein für Kraftfahrzeugtechnik (ÖVK)

Broom, D.P. (2011) **Hydrogen Storage Materials: The Characterisation of Their Storage Properties**. Springer-Verlag London

Browning, D.J., Gerrard, M.L., Lakeman, J.B., Mellor, I.M., Mortimer, R.J. and Turpin, M.C. (2002) Studies into the Storage of Hydrogen in\rCarbon Nanofibers: Proposal of a\rPossible Reaction Mechanism. **Nano Letters**, 2 (3): 201–205

Brun, N., Janot, R., Sanchez, C., Deleuze, H., Gervais, C., Morcrette, M. and Backov, R. (2010) Preparation of LiBH4@carbon micro–macrocellular foams: tuning hydrogen release through varying microporosity. **Energy & Environmental Science**, 3 (6): 824

Brunauer, S., Emmett, P.H. and Teller, E. (1938) Adsorption of Gases in Multimolecular Layers. **Journal of the American Chemical Society**, 60 (2): 309–319

Busby, R.L. (2005) **Hydrogen and Fuel Cells: A Comprehensive Guide**. PenWell Books

Cahen, S., Eymery, J.-B., Janot, R. and Tarascon, J.-M. (2009) Improvement of the LiBH4 hydrogen desorption by inclusion into mesoporous carbons. **Journal of Power Sources**, 189 (2): 902–908

Cançado, L., Pimenta, M., Saito, R., Jorio, a., Ladeira, L., Grueneis, a., Souza-Filho, a., Dresselhaus, G. and Dresselhaus, M. (2002) Stokes and anti-Stokes double resonance Raman scattering in two-dimensional graphite. **Physical Review B**, 66 (3): 1–5

Cançado, L., Takai, K. and Enoki, T. (2006) General equation for the determination of the crystallite size L a of nanographite by Raman spectroscopy. **Applied Physics …**, 163106 (May 2013): 90–93

Cançado, L.G., Takai, K., Enoki, T., Endo, M., Kim, Y. a., Mizusaki, H., Speziali, N.L., Jorio, a. and Pimenta, M. a. (2008) Measuring the degree of stacking order in graphite by Raman spectroscopy. **Carbon**, 46 (2): 272–275

Capurso, G., Agresti, F., Crociani, L., Rossetto, G., Schiavo, B., Maddalena, A., Lo Russo, S. and Principi, G. (2012) Nanoconfined mixed Li and Mg borohydrides as materials for solid state hydrogen storage. **International Journal of Hydrogen Energy**, 37 (14): 768–773

CDC (2015) **International Chemical Safety Cards (ICSC): SILANE** [online]. Available from: http://www.cdc.gov/niosh/ipcsneng/neng0564.html [Accessed 21 September 2016]

Chalk, S.G. and Miller, J.F. (2006) Key challenges and recent progress in batteries, fuel cells, and hydrogen storage for clean energy systems. **Journal of Power Sources**, 159: 73–80

Chambers, A., Park, C., Baker, R.T.K. and Rodriguez, N.M. (1998) Hydrogen storage in graphite nanofibers. **Journal of Physical Chemistry B**, 102 (22): 4253–4256

Chen, D.M., Ichikawa, T., Fujii, H., Ogita, N., Udagawa, M., Kitano, Y. and Tanabe, E. (2003) Unusual hydrogen absorption properties in graphite mechanically milled under various hydrogen pressures up to 6 MPa. **Journal of Alloys and Compounds**, 354 (1–2): 5–9

Chen, X.H., Yang, H.S., Wu, G.T., Wang, M., Deng, F.M., Zhang, X.B., Peng, J.C. and Li, W.Z. (2000) Generation of curved or closed-shell carbon nanostructures by ball-milling of graphite. **Journal of Crystal Growth**, 218 (1): 57–61

Cockcroft, J.K. (2006) **Whole Pattern Fitting I. Pawley Method** [online]. Available from: http://pd.chem.ucl.ac.uk/pdnn/solve1/pawley.htm [Accessed 13 May 2017]

Dahn, J.R. (1991) Phase diagram of LixC6. **Physical Review B**, 44 (17): 9170–9177

Davis, J.. (ed.) (2001) **Surface Engineering for Corrosion and Wear Resistance**. ASM International

Dian, J., Macek, A., Nižňanský, D., Němec, I., Vrkoslav, V., Chvojka, T. and Jelínek, I. (2004) SEM and HRTEM study of porous silicon - Relationship between fabrication, morphology and optical properties. **Applied Surface Science**, 238 (1–4 SPEC. ISS.): 169–174

Diaz-Guerra, C. and Montone, A. (2002) Structural and cathodoluminescence study of mechanically milled silicon. **Semiconductor …**

Dillon, A.C., Jones, K.M., Bekkedahl, T.A., Kiang, C.H., Bethune, D.S. and Heben, M.J. (1997) Storage of hydrogen in single-walled carbon nanotubes. **Nature**, 386 (6623): 377–379

DoE (2015) **Target Explanation Document: Onboard Hydrogen Storage for Light-Duty Fuel Cell Vehicles**

Dolan, M.D. (2010) Non-Pd BCC alloy membranes for industrial hydrogen separation. **Journal of Membrane Science**, 362 (1–2): 12–28

Dubey, R. and Gautam, D. (2009) Synthesis and Characterization of Nanocrystalline Porous Silicon Layer for Solar Cells Applications. **Journal of Optoelectronic and Biomedical …**, 1 (1): 8–14

Dunlap, R.A. (2013) **Sustainable Energy**. Cengage Learning

EIA (2013) International Energy Outlook 2013. **US Energy Information Administration (EIA)**

Fakiolu, E. (2004) A review of hydrogen storage systems based on boron and its compounds. **International Journal of Hydrogen Energy**, 29 (13): 1371–1376

Fang, Z.-Z., Kang, X.-D., Wang, P., Li, H.-W. and Orimo, S.-I. (2010a) Unexpected dehydrogenation behavior of LiBH4/Mg(BH4)2 mixture associated with the in situ formation of dual-cation borohydride. **Journal of Alloys and Compounds**, 491 (1–2): L1–L4

Fang, Z.-Z.Z., Kang, X.-D.D. and Wang, P. (2010b) Improved hydrogen storage properties of LiBH4 by mechanical milling with various carbon additives. **INTERNATIONAL JOURNAL OF HYDROGEN ENERGY**, 35 (15): 8247–8252

Felderhoff, M., Weidenthaler, C., von Helmolt, R. and Eberle, U. (2007) Hydrogen storage: the remaining scientific and technological challenges. **Physical chemistry chemical physics : PCCP**, 9 (21): 2643–2653

Ferrari, A. and Robertson, J. (2000) Interpretation of Raman spectra of disordered and

amorphous carbon. **Physical Review B**, 61 (20): 14095–14107

Ferrari, A. and Robertson, J. (2001) Resonant Raman spectroscopy of disordered, amorphous, and diamondlike carbon. **Physical Review B**, 64 (7): 1–13

Ferrari, A.C., Meyer, J.C., Scardaci, V., Casiraghi, C., Lazzeri, M., Mauri, F., Piscanec, S., Jiang, D., Novoselov, K.S., Roth, S. and Geim, a. K. (2006) Raman spectrum of graphene and graphene layers. **Physical Review Letters**, 97 (18): 1–4

Fichtner, M. (2011) Nanoconfinement effects in energy storage materials. **Physical chemistry chemical physics : PCCP**, 13 (48): 21186–95

Francke, M., Hermann, H., Wenzel, R., Seifert, G. and Wetzig, K. (2005) Modification of carbon nanostructures by high energy ball-milling under argon and hydrogen atmosphere. **Carbon**, 43 (6): 1204–1212

Friedrichs, O., Remhof, a., Hwang, S.-J. and Züttel, a. (2010) Role of Li 2 B 12 H 12 for the Formation and Decomposition of LiBH 4. **Chemistry of Materials**, 22 (10): 3265–3268

Fronasiero, P. and Graziani, M. (2011) **Renewable Resources and Renewable Energy: A Global Challenge**. Second Edi. CRC Press

Fukunaga, T., Itoh, K., Orimo, S., Aoki, K., Nagano, K., Mizutani, U., Wakayama, H. and Fukushima, Y. (2004) Structural change of graphite subjected to mechanical milling. **Materials Science and Engineering B-Solid State Materials for Advanced Technology**, 108 (1–2): 105–113

Goldstein, J. (2003) **Scanning Electron Microscopy and X-ray Microanalysis**. 3rd ed. Plenum

Gross, A.F., Vajo, J.J., Van Atta, S.L. and Olson, G.L. (2008) Enhanced Hydrogen Storage Kinetics of LiBH 4 in Nanoporous Carbon Scaffolds. **The Journal of Physical Chemistry C**, 112 (14): 5651–5657

Haber, J. (1991) MANUAL ON CATALYST CHARACTERIZATION. **International Union of Pure and Applied Chemistry**, 63 (9): 1127–1246

Hodkiewicz, J. (2010) **Characterizing Carbon Materials with Raman Spectroscopy** [online]. Available from: http://www.thermoscientific.com/content/dam/tfs/ATG/CAD/CAD Documents/Application & Technical Notes/Molecular Spectroscopy/Raman/Raman Instruments/D19504~.pdf [Accessed 11 June 2014]

Holladay, J.D., Hu, J., King, D.L. and Wang, Y. (2009) An overview of hydrogen production technologies. **Catalysis Today**, 139 (4): 244–260

Holzwarth, U. and Gibson, N. (2011) The Scherrer equation versus the “Debye-Scherrer equation”. **Nature nanotechnology**, 6 (9): 534

Huang, J.Y. (1999) HRTEM and EELS studies of defects structure and amorphous-like graphite induced by ball-milling. **Acta Materialia**, 47 (6): 1801–1808

Huang, Z., Calka, A. and Liu, H. (2007) Effects of milling conditions on hydrogen storage properties of graphite. **Journal of Materials Science**, 42 (14): 5437–5441

Huot, J., Liang, G., Boily, S., Van Neste, A. and Schulz, R. (1999) Structural study and hydrogen sorption kinetics of ball-milled magnesium hydride. **Journal of Alloys and Compounds**, 293: 495–500

Ichikawa, T., Chen, D.M., Isobe, S., Gomibuchi, E. and Fujii, H. (2004) Hydrogen storage properties on mechanically milled graphite. **Materials Science and Engineering: B**, 108 (1–2): 138–142

Ichikawa, T., Isobe, S. and Fujii, H. (2005) **Hydrogen desorption properties of lithium-carbon-hydrogen system**. Sendai, JAPON: Japan Institute of Metals

Ichikawa, T., Miyaoka, H. and Kojima, Y. (2011) "Hydrogen Storage Properties of Hydrogenated Graphite and Lithium Hydride Nanoomposite." In Reddy, B. (ed.) **Advances in Diverse Industrial Applications of Nanocomposites**. InTech. p. 550

IEA (2006) **Hydrogen Production and Storage: R&D Priorities and Gaps**.

IPPC (2007) **Climate Change 2007 - Mitigation of Climate Change**. Cambridge University Press

Iqbal, Z., Webb, A.P. and Vepřek, S. (1980) Polycrystalline silicon films deposited in a glow discharge at temperatures below 250 °C. **Appl. Phys. Lett.**, 36 (2): 163

de Jongh, P.E., Allendorf, M., Vajo, J.J. and Zlotea, C. (2013) Nanoconfined light metal hydrides for reversible hydrogen storage. **MRS Bulletin**, 38 (6): 488–494

Kato, S., Bielmann, M., Borgschulte, A., Zakaznova-Herzog, V., Remhof, A., Orimo, S.-I. and Züttel, A. (2010) Effect of the surface oxidation of LiBH4 on the hydrogen desorption mechanism. **Physical chemistry chemical physics : PCCP**, 12: 10950–10955

Khaligh, A. (2010) Battery, Ultracapacitor, Fuel Cell, and Hybrid Energy Storage Systems for Electric, Hybrid Electric, Fuel Cell, and Plug-In Hybrid Electric Vehicles: State of the Art. **IEEE Transactions on Vehicular Technology**, 59 (6): 2806–2814

Knight, D.S. and White, W.B. (1989) Characterization of diamond films by Raman spectroscopy. **Journal of Materials Research**, 4 (2): 385–393

Kojima, Y., Kawai, Y., Kimbara, M., Nakanishi, H. and Matsumoto, S. (2004) Hydrogen generation by hydrolysis reaction of lithium borohydride. **International Journal of Hydrogen Energy**, 29 (12): 1213–1217

Konar, S., Häusserman, U. and Svensson, G. (2015) Intercalation Compounds from LiH and Graphite: Relative Stability of Metastable Stages and Thermodynamic Stability of Dilute Stage Id. **Chemistry of Materials**, 27 (7): 2566–2575

Kostka, J., Lohstroh, W., Fichtner, M. and Hahn, H. (2007) Diborane Release from LiBH 4 /Silica-Gel Mixtures and the Effect of Additives. **The Journal of Physical Chemistry C**,

111 (37): 14026–14029

Kothari, R., Buddhi, D. and Sawhney, R.L. (2008) Comparison of environmental and economic aspects of various hydrogen production methods. **Renewable and Sustainable Energy Reviews**, 12 (2): 553–563

Kou, H., Sang, G., Zhou, Y., Wang, X., Huang, Z., Luo, W., Chen, L., Xiao, X., Yang, G. and Hu, C. (2014) Enhanced hydrogen storage properties of LiBH4 modified by NbF5. **International Journal of Hydrogen Energy**, 39 (22): 11675–11682

Lebeau, K., Van Mierlo, J., Lebeau, P., Mairesse, O. and Macharis, C. (2012) The market potential for plug-in hybrid and battery electric vehicles in Flanders: A choice-based conjoint analysis. **Transportation Research Part D: Transport and Environment**, 17 (8): 592–597

Li, C., Peng, P., Zhou, D.W. and Wan, L. (2011) Research progress in LiBH4 for hydrogen storage: A review. **International Journal of Hydrogen Energy**, 36: 14512–14526

Lim, K.L., Kazemian, H., Yaakob, Z. and Daud, W.R.W. (2010) Solid-state materials and methods for hydrogen storage: A critical review. **Chemical Engineering and Technology**, 33 (2): 213–226

Liu, X., Majzoub, E.H., Stavila, V., Bhakta, R.K., Allendorf, M.D., Shane, D.T., Conradi, M.S., Verdal, N., Udovic, T.J. and Hwang, S.-J. (2013) Probing the unusual anion mobility of LiBH4 confined in highly ordered nanoporous carbon frameworks via solid state NMR and quasielastic neutron scattering. **Journal of Materials Chemistry A**, 1 (34): 9935

Liu, X., Peaslee, D., Jost, C., Baumann, T. and Majzoub, E. (2011) Systematic pore-size effects of nanoconfinement of LiBH4: elimination of diborane release and tunable behavior for hydrogen storage applications. **Chemistry of Materials**, pp. 1331–1336

Liu, X., Peaslee, D., Jost, C.Z. and Majzoub, E.H. (2010) Controlling the decomposition pathway of LiBH4 via confinement in highly ordered nanoporous carbon. **Journal of Physical Chemistry C**, 114 (33): 14036–14041

Lowell, S., Shields, J.E., Thomas, M.A. and Thommes, M. (2004) **Characterization of Porous Solids and Powders: Surface Area, Pore Size and Density**. Particle Technology Series. Dordrecht: Springer Netherlands

Lysenko, V., Bidault, F., Alekseev, S., Zaitsev, V., Barbier, D., Turpin, C., Geobaldo, F., Rivolo, P. and Garrone, E. (2005) Study of porous silicon nanostructures as hydrogen reservoirs. **The journal of physical chemistry. B**, 109 (42): 19711–8

Lysenko, V., Vitiello, J., Remaki, B., Barbier, D. and Skryshevsky, V. (2004) Nanoscale morphology dependent hydrogen coverage of meso-porous silicon. **Applied Surface Science**, 230 (1–4): 425–430

Ma, Y., Li, Y., Liu, T., Zhao, X., Zhang, L., Han, S. and Wang, Y. (2016) Enhanced hydrogen storage properties of LiBH4 generated using a porous Li3BO3 catalyst. **Journal of Alloys**

and Compounds, 689: 187–191

Maekawa, H., Matsuo, M., Takamura, H., Ando, M., Noda, Y., Karahashi, T. and Orimo, S.I. (2009) Halide-stabilized LiBH4, a room-temperature lithium fast-ion conductor. **Journal of the American Chemical Society**, pp. 894–895

Malard, L.M., Pimenta, M. a., Dresselhaus, G. and Dresselhaus, M.S. (2009) Raman spectroscopy in graphene. **Physics Reports**, 473 (5–6): 51–87

Manilov, a. I. and Skryshevsky, V. a. (2013) Hydrogen in porous silicon — A review. **Materials Science and Engineering: B**, 178 (15): 942–955

Matsuo, M., Nakamori, Y., Orimo, S.I., Maekawa, H. and Takamura, H. (2007) Lithium superionic conduction in lithium borohydride accompanied by structural transition. **Applied Physics Letters**, 91 (22): 5–8

Matsuoka, K., Yamagishi, Y., Yamazaki, T., Setoyama, N., Tomita, A. and Kyotani, T. (2005) Extremely high microporosity and sharp pore size distribution of a large surface area carbon prepared in the nanochannels of zeolite Y. **Carbon**, 43 (4): 876–879

Mauron, P., Buchter, F., Friedrichs, O., Remhof, A., Bielmann, M., Zwicky, C.N., Züttel, A. and Zuttel, A. (2007) Stability and Reversibility of LiBH4. **The Journal of Physical Chemistry B**, 112 (3): 906–910

Mernagh, T.P., Cooney, R.P. and Johnson, R. a. (1984) Raman spectra of Graphon carbon black. **Carbon**, 22 (1): 39–42

Miyaoka, H., Ichikawa, T. and Kojima, Y. (2009) The reaction process of hydrogen absorption and desorption on the nanocomposite of hydrogenated graphite and lithium hydride. **Nanotechnology**, 20 (20): 204021

Miyaoka, H., Ishida, W., Ichikawa, T. and Kojima, Y. (2011) Synthesis and characterization of lithium-carbon compounds for hydrogen storage. **Journal of Alloys and Compounds**, 509 (3): 719–723

Mohan, S.V. and Pandey, A. (2013) "1. Biohydrogen Production: An Introduction." In **Biohydrogen**. Elsevier B.V. pp. 1–24

Mosegaard, L., Moller, B., Jorgensen, J.-E., Filinchuk, Y., Cerenius, Y., Hanson, J.C., Dimasi, E., Besenbacher, F. and Jensen, T.R. (2008) Reactivity of LiBH4: In Situ Synchrotron Radiation Powder X-ray Diffraction Study. **The Journal of Physical Chemistry C**, 112 (4): 1299–1303

Musyoka, N.., Ren, J., Langmi, H.., Rogers, D.E.., North, B.., Mathe, M. and Bessarabov, D. (2007) Synthesis of templated carbons starting from clay and clay-derived zeolites for hydrogen storage applications. **International journal of energy research**, 31 (August 2007): 135–147

Musyoka, N.M., Ren, J., Langmi, H.W., North, B.C. and Mathe, M. (2015) A comparison of

hydrogen storage capacity of commercial and fly ash-derived zeolite X together with their respective templated carbon derivatives. **International Journal of Hydrogen Energy**, 40 (37): 12705–12712

Nakagawa, T., Ichikawa, T., Hanada, N., Kojima, Y. and Fujii, H. (2007) Thermal analysis on the Li–Mg–B–H systems. **Journal of Alloys and Compounds**, 446–447 (0): 306–309

Nayef, U.M. (2013) **Fabrication and Characteristics of Porous Silicon for Photoconversion**., (April)

Nersesian, R.L. (2015) **Energy for the 21st Century: A Comprehensive Guide to Conventional and Alternative Sources**. Taylor & Francis Group

Ngene, P., Adelhelm, P., Beale, A.M., de Jong, K.P. and de Jongh, P.E. (2010) LiBH4/SBA-15 nanocomposites prepared by melt infiltration under hydrogen pressure: synthesis and hydrogen sorption properties. **The Journal of Physical Chemistry C**, 114 (13): 6163–6168

Nishihara, H., Yang, Q.H., Hou, P.X., Unno, M., Yamauchi, S., Saito, R., Paredes, J.I., Martínez-Alonso, A., Tascón, J.M.D., Sato, Y., Terauchi, M. and Kyotani, T. (2009) A possible buckybowl-like structure of zeolite templated carbon. **Carbon**, 47 (5): 1220–1230

NMSEA (2015) **Electrolysis: Obtaining hydrogen from water: The Basis for a Solar-Hydrogen Economy** [online]. Available from: http://www.nmsea.org/Curriculum/7_12/electrolysis/electrolysis.htm [Accessed 25 May 2015]

Ogita, N., Yamamoto, K., Hayashi, C., Matsushima, T., Orimo, S., Ichikawa, T., Fujii, H. and Udagawa, M. (2004) Raman scattering and infrared absorption investigation of hydrogen configuration state in mechanically milled graphite under H2 gas atmosphere. **Journal of the Physical Society of Japan**, 73 (3): 553–555

Ohba, N., Miwa, K., Aoki, M., Noritake, T., Towata, S.I., Nakamori, Y., Orimo, S.I. and Züttel, A. (2006) First-principles study on the stability of intermediate compounds of LiBH4. **Physical Review B - Condensed Matter and Materials Physics**, 74 (7): 1–7

Orimo, S.-I.I., Nakamori, Y., Ohba, N., Miwa, K., Aoki, M., Towata, S.I., Züttel, A. and Zuttel, A. (2006) Experimental studies on intermediate compound of LiBH4. **Applied Physics Letters**, 89 (2): 21920–21923

Orimo, S., Majer, G., Fukunaga, T., Züttel, A., Schlapbach, L. and Fujii, H. (1999) Hydrogen in the mechanically prepared nanostructured graphite. **Applied Physics Letters**, 75 (20): 3093

Orimo, S., Matsushima, T., Fujii, H., Fukunaga, T. and Majer, G. (2001) Hydrogen desorption property of mechanically prepared nanostructured graphite. **Journal of Applied Physics**, 90 (3): 1545–1549

Paredes, J.I., Martínez-Alonso, a., Yamazaki, T., Matsuoka, K., Tascon, J.M.D. and Kyotani, T.

(2005) Structural investigation of zeolite-templated, ordered microporous carbon by scanning tunneling microscopy and raman spectroscopy. **Langmuir**, 21 (19): 8817–8823

Parker, S.F. (2010) Spectroscopy and bonding in ternary metal hydride complexes—Potential hydrogen storage media. **Coordination Chemistry Reviews**, 254 (3–4): 215–234

Pecharsky, V.K. and Zavalij, P.Y. (2009) **Fundamentals of Powder Diffraction and Structural Characterization of Materials**. 1st ed. Boston, MA: Springer US

Petrova, E.., Bogoslovskaya, K.., Balagurov, L.. and Kochoradze, G.. (2000) Room temperature oxidation of porous silicon in air. **Materials Science and Engineering: B**, 69–70: 152–156

Pinkerton, F.E. and Meyer, M.S. (2008) Reversible hydrogen storage in the lithium borohydride-calcium hydride coupled system. **Journal of Alloys and Compounds**, 464 (1–2): 4–7

Pinkerton, F.E., Meyer, M.S., Meisner, G.P., Balogh, M.P. and Vajo, J.J. (2007) Phase Boundaries and Reversibility of LiBH 4 /MgH 2 Hydrogen Storage Material. **The Journal of Physical Chemistry C**, 111 (35): 12881–12885

Reed, D. and Book, D. (2009) In-situ Raman study of the thermal decomposition of LiBH4. **Materials Resource Society Proceedings**, 1216: 2–8

REN21 (2011) **Renewables 2014 Global Status Report**.

Roduner, E. (2006) Size matters: why nanomaterials are different. **Chemical Society reviews**, 35 (7): 583–592

Rosi, N.., Eckert, J., Eddaoudi, M., Vodak, D.., Kim, J., O'Keeffe, M. and Yaghi, O.. (2003) Hydrogen Storage in Microporous Metal-Organic Frameworks. **Science**, 300 (May): 1127–1129

Rouqerol, J., Avnir, D., Fairbridge, C.., Everett, D.., Haynes, J.., Pernicone, N., Ramsay, J.D.., Sing, K.S.. and Unger, K.. (1994) Recommendations for the characterization of porous solids. **Pure and Applied Chemistry**, 66 (8): 1739–1758

Rowsell, J.L.C., Millward, A.R., Park, K.S. and Yaghi, O.M. (2004) Hydrogen Sorption in Functionalized Metal-Organic Frameworks. **Journal of the American Chemical Society**, 126 (18): 5666–5667

Roy, D., Chhowalla, M., Wang, H., Sano, N., Alexandrou, I., Clyne, T.W. and Amaratunga, G. a J. (2003) Characterisation of carbon nano-onions using Raman spectroscopy. **Chemical Physics Letters**, 373 (1–2): 52–56

Russo, L., Colangelo, F., Cioffi, R., Rea, I. and De Stefano, L. (2011) A mechanochemical approach to porous silicon nanoparticles fabrication. **Materials**, 4 (6): 1023–1033

Sailor, M.J. (2011a) "Fundamentals of Porous Silicon Preparation." In **Porous Silicon in Practice**. Wiley-VCH Verlag GmbH & Co. KGaA. pp. 1–42

Sailor, M.J. (2011b) **Porous Silicon in Practice: Preparation, Characterization and Applications**. 1st ed. Wiley-VCH Verlag GmbH & Co. KGaA

Salcedo, W.J., Fernandez, F.J.R. and Rubimc, J.C. (1999) Influence of Laser Excitation on Raman and Photoluminescence Spectra and FTIR Study of Porous Silicon Layers. **Brazilian Journal of Physics**, 29 (4): 751–755

Saldan, I. (2011) A prospect for LiBH4 as on-board hydrogen storage. **Central European Journal of Chemistry**, 9 (5): 761–775

Schlapbach, L. and Züttel, A. (2001) Hydrogen-storage materials for mobile applications. **Nature**, 414 (November): 353–358

Schlesinger, H.I. and Brown, H.C. (1940) Metallo Borohydrides. III. Lithium Borohydride. **Journal of the American Chemical Society**, 62 (12): 3429–3435

Semrock (2016) **Green Photonics Raman Spectroscopy** [online]. Available from: https://www.semrock.com/green-photonics-raman-spectroscopy.aspx [Accessed 30 April 2016]

Shane, D.T., Corey, R.L., McIntosh, C., Rayhel, L.H., Bowman, R.C., Vajo, J.J., Gross, A.F. and Conradi, M.S. (2010) LiBH 4 in carbon aerogel nanoscaffolds: An NMR study of atomic motions. **Journal of Physical Chemistry C**, 114 (9): 4008–4014

Shao, H., Xin, G., Zheng, J., Li, X. and Akiba, E. (2012) Nanotechnology in Mg-based materials for hydrogen storage. **Nano Energy**, 1 (4): 590–601

Shao, J., Xiao, X., Fan, X., Huang, X., Zhai, B., Li, S., Ge, H., Wang, Q. and Chen, L. (2015) Enhanced hydrogen storage capacity and reversibility of LiBH4 nanoconfined in the densified zeolite-templated carbon with high mechanical stability. **Nano Energy**, 15: 244–255

Shao, J., Xiao, X., Fan, X., Zhang, L., Li, S., Ge, H., Wang, Q. and Chen, L. (2014) **Low-Temperature Reversible Hydrogen Storage Properties of LiBH 4 : A Synergetic Effect of Nanoconfinement and Nanocatalysis**.

Shim, J.-H., Lim, J.-H., Rather, S., Lee, Y.-S., Reed, D., Kim, Y., Book, D. and Cho, Y.W. (2010) Effect of Hydrogen Back Pressure on Dehydrogenation Behavior of LiBH 4 -Based Reactive Hydride Composites. **The Journal of Physical Chemistry Letters**, 1 (1): 59–63

Shriver, D.., Atkins, P.. and Langford, C.. (1994) **Inorganic Chemistry**. 2nd ed. Oxford University Press

Smith, C.I., Miyaoka, H., Ichikawa, T., Jones, M.O., Harmer, J., Ishida, W., Edwards, P.P., Kojima, Y. and Fuji, H. (2009) Electron Spin Resonance Investigation of Hydrogen Absorption in Ball-Milled Graphite. **Journal of Physical Chemistry C**, 113 (14): 5409–5416

Smith, E. and Dent, G. (2005) **Modern Raman Spectroscopy: A Practical Approach**. John

Wiley & Sons, Ltd

Söderlund, M., Mäki-Arvela, P., Eränen, K., Salmi, T., Rahkola, R. and Murzin, Y.D. (2005) Catalyst Deactivation in Diborane Decomposition. **Catalysis Letters**, 105 (3): 191–202

Speight, J.D. (2011) "Hydrogen as a Fuel: The Hydrogen Cycle." In Züttel, A., Borgschulte, A. and Schlapbach, L. (eds.) **Hydrogen As A Future Energy Carrier**. John Wiley & Sons, Ltd. pp. 43–69

Stavila, V., Klebanoff, L., Vajo, J. and Chen, P. (2013) "Development of On-Board Reversible Complex Metal Hydrides for Hydrogen Storage." In Klebanoff, L. (ed.) **Hydrogen Storage Technology: Materials and Applications**. CRC

Takahashi, K., Hattori, K., Yamazaki, T., Takada, K., Matsuo, M., Orimo, S., Maekawa, H. and Takamura, H. (2013) All-solid-state lithium battery with LiBH4 solid electrolyte. **Journal of Power Sources**, 226: 61–64

Tuinstra, F. and Koenig, L. (1970) Raman Spectrum of Graphite. **The Journal of Chemical Physics**, 53 (1970): 1126–1130

Tuyen, L.T.T., Tam, N.T.T., Quang, N.H., Nghia, N.X., Khang, D.D. and Khoi, P.H. (2001) Study on hydrogen reactivity with surface chemical species of nanocrystalline porous silicon. **Materials Science and Engineering: C**, 15 (1–2): 133–135

Uhlir, A. (1956) Electrolytic Shaping of Germanium and Silicon. **Bell System Technical Journal**, 35 (2): 333–347

UN (2015) World Population Prospects: The 2015 Revision, Key Findings and Advance Tables. **Department of Economic and Social Affairs, Population Devision**

Ushizawa, K., N.-Gamo, M., Kikuchi, Y., Sakaguchi, I., Sato, Y. and Ando, T. (1999) Surface-enhanced Raman spectroscopic study of hydrogen and deuterium chemisorption on diamond (111) and (100) surfaces. **Physical Review B**, 60 (8): R5165–R5168

Vajo, J. (2011) nfluence of nano-confinement on the thermodynamics and dehydrogenation kinetics of metal hydrides. **Current Opinion in Solid State and Materials Science**, 15 (2): 52–61

Vajo, J.J., Skeith, S.L. and Mertens, F. (2005) Reversible Storage of Hydrogen in Destabilized LiBH 4. **The Journal of Physical Chemistry B**, 109 (9): 3719–3722

Varin, R.A., Czujko, T. and Wronski, Z.S. (2009) **Nanomaterials for Solid State Hydrogen Storage**. Fuel Cells and Hydrogen Energy. Boston, MA: Springer US

Veprek, S., Iqbal, Z., Oswald, H.R. and Webb, A.P. (1981) Properties of polycrystalline silicon prepared by chemical transport in hydrogen plasma at temperature between 80 and 400°C. **Journal of Physics C: Solid State Physics**, 14: 295–308

Verkuijlen, M.H.W., Ngene, P., De Kort, D.W., Barré, C., Nale, A., Van Eck, E.R.H., Van Bentum, P.J.M., De Jongh, P.E. and Kentgens, A.P.M. (2012) Nanoconfined LiBH4 and

enhanced mobility of Li+ and BH4- studied by solid-state NMR. **The Journal of Physical Chemistry C**, 116 (42): 22169–22178

Vines, J.E. (2013) **Nanocarbon-Hydride Composites for Hydrogen Storage**. University of Birmingham

Walker, G. (2008) **Solid-State Hydrogen Storage**. 1st ed. Walker, G. (ed.). Woodhead Publishing Ltd

Wang, K., Kang, X., Ren, J. and Wang, P. (2016) Nanostructured graphite-induced destabilization of LiBH4 for reversible hydrogen storage. **Journal of Alloys and Compounds**, 685: 242–247

Ward, P.A., Teprovich, J.A., Peters, B., Wheeler, J., Compton, R.N. and Zidan, R. (2013) Reversible Hydrogen Storage in a LiBH 4 –C 60 Nanocomposite. **The Journal of Physical Chemistry C**, 117 (44): 22569–22575

Watt, I.M. (1997) **The Principles and Practice of Electron Microscopy**. Cambridge University Press

Weidenthaler, C. and Felderhoff, M. (2010) "Complex Hydrides." In Hirscher, M. (ed.) **Handbook of Hydrogen Storage**. Wiley-VCH Verlag GmbH & Co. KGaA. p. 353

Wellons, M.S., Berseth, P.A. and Zidan, R. (2009) Novel catalytic effects of fullerene for LiBH(4) hydrogen uptake and release. **Nanotechnology**, 20 (20)

Weng, B., Wu, Z., Li, Z., Yang, H. and Leng, H. (2011a) Enhanced hydrogen generation by hydrolysis of LiBH4 doped with multiwalled carbon nanotubes for micro proton exchange membrane fuel cell application. **Journal of Power Sources**, 196 (11): 5095–5101

Weng, B., Wu, Z., Li, Z., Yang, H. and Leng, H. (2011b) Hydrogen generation from noncatalytic hydrolysis of LiBH4/NH3BH3 mixture for fuel cell applications. **International Journal of Hydrogen Energy**, 36 (17): 10870–10876

Wong-Foy, A.., Matzger, A.. and Yaghi, O.. (2006) Exceptional H2 Saturation Uptake in Microporous Metal-Organic Frameworks. **Journal of the American Chemical Society**, 128 (11): 3494–3495

Xia, G., Tan, Y., Wu, F., Fang, F., Sun, D., Guo, Z., Huang, Z. and Yu, X. (2016) Graphene-wrapped reversible reaction for advanced hydrogen storage. **Nano Energy**, 26: 488–495

Yan, Y., Remhof, A., Hwang, S.-J., Li, H.-W., Mauron, P., Orimo, S. and Züttel, A. (2012) Pressure and temperature dependence of the decomposition pathway of LiBH4. **Physical Chemistry Chemical Physics**, 14 (18): 6514–6519

Yang, Z., Xia, Y. and Mokaya, R. (2007a) Enhanced hydrogen storage capacity of high surface area zeolite-like carbon materials. **Journal of the American Chemical Society**, 129 (6): 1673–1679

Yang, Z., Xia, Y. and Mokaya, R. (2007b) **Enhanced Hydrogen Storage Capacity of High Surface Area Zeolite-like Carbon Materials**., (3): 1673–1679

Young, R.A. (1995) **The Rietveld Method**. Oxford University Press

Yu, X.B., Grant, D.M. and Walker, G.S. (2010) **Low-Temperature Dehydrogenation of LiBH 4 through Destabilization with TiO 2**., pp. 11059–11062

Yürüm, Y., Taralp, A. and Veziroglu, T.N. (2009) Storage of hydrogen in nanostructured carbon materials. **International Journal of Hydrogen Energy**, 34 (9): 3784–3798

Zaluska, a., Zaluski, L. and Ström-Olsen, J.O. (1999) Nanocrystalline magnesium for hydrogen storage. **Journal of Alloys and Compounds**, 288 (1–2): 217–225

Zhang, S.-L. (2012) "Theoretical Fundamentals of Raman Scattering in Nanostructures." In **Raman Spectroscopy and its Application in Nanostructures**. 1st ed. John Wiley & Sons, Ltd

Zhang, Y., Bevan, A. and Book, D. (2012) Hydrogen desorption behaviour of a ball-milled graphite - LiBH4 composite. **MRS Proceedings**, 1386: mrsf11-1386-d02-02

Zhang, Y. and Book, D. (2011a) Effect of Milling Conditions on the Purity of Hydrogen Desorbed from Ball-milled Graphite. **The Journal of Physical Chemistry C**, 115 (51): 25285–25289

Zhang, Y. and Book, D. (2011b) Hydrogen storage properties of ball-milled graphite with 0.5 wt% Fe. **International Journal of Energy Research**

Zhang, Y., Ding, H., Liu, C., Zhang, S. and Huang, S. (2013) Significant effects of graphite fragments on hydrogen storage performances of LiBH4: A first-principles approach. **International Journal of Hydrogen Energy**, 38 (31): 13717–13727

Zhang, Y., Mann, V., Reed, D., Walton, A., Harris, I.R. and Book, D. (2009) Hydrogen storage properties of nanostructured graphite-based materials. **Sustainable Power Generation and Supply, 2009. SUPERGEN '09**, pp. 1–4

Zhang, Y., Zhang, W.-S.S., Wang, A.-Q.Q., Li-Xian, S., Fan, M.-Q.Q., Chu, H.-L.L., Sun, J.-C.C., Zhang, T., Li-Xian Sun, Fan, M.-Q.Q., Chu, H.-L.L., Sun, J.-C.C. and Zhang, T. (2007) LiBH4 nanoparticles supported by disordered mesoporous carbon: Hydrogen storage performances and destabilization mechanisms. **INTERNATIONAL JOURNAL OF HYDROGEN ENERGY**, 32 (16): 3976–3980

Zhao, D., Feng, J., Huo, Q., Melosh, N., Fredrickson, G., Chmelka, B. and Stucky, G. (1998) Triblock copolymer syntheses of mesoporous silica with periodic 50 to 300 angstrom pores. **Science**, 279 (5350): 548–52

Züttel, A. (2003) Materials for hydrogen storage. **Materials Today**, 6 (9): 24–33

Züttel, A. (2011) "Hydrogen Storage." In Züttel, A., Borgschulte, A. and Schlapbach, L. (eds.) **Hydrogen As A Future Energy Carrier2**. John Wiley & Sons, Ltd. pp. 165–263

Züttel, A. and Borgschulte, A. (2007) No Title. **International Symposium on H2 Energy**

Züttel, A., Wenger, P., Rentsch, S., Sudan, P., Mauron, P. and Emmenegger, C. (2003) LiBH4 a new hydrogen storage material. **Journal of Power Sources**, 118 (1–2): 1–7